INTEGRATED NONLINEAR MODELLING OF FLOATING WIND TURBINE

By

Sudhir Jagdale

M.Tech. in Offshore Engineering

Supervisor

Prof. Qingwei Ma

A thesis submitted to

City, University of London

for the degree of

Doctor of Philosophy

School of Mathematics, Computer Science and Engineering

City, University of London

May 2019

CONTENTS

ABSTRACT

Locating wind turbines on floating platforms offshore would allow tapping an immense wind resource available in a deep sea. A realisation of this potential, however, requires cost-effective floating platform designs that can compete with other energy sources. To reduce the large capital cost associated with construction, the design of such platforms will need a reliable and sophisticated design tool that can perform load and response analysis in a comprehensive and fully integrated manner. This thesis presents an integrated nonlinear model for performing load and response analysis of a tension-leg-platform wind turbine that is being considered as a most promising concept to harness wind energy in a moderately deep sea (80m to 200m). It presents the formulation for evaluating various external loads acting on each component of a floating wind turbine considering nonlinear interaction among them. The formulations for various external loads and the motions are developed and solved, and the results are used to demonstrate the significance of the hybrid hydrodynamic model suggested in this thesis as the main contribution. The most discerning feature of the hybrid hydrodynamic model is, it employs fully nonlinear potential theory for wave kinematic prediction and non-diffracting potential theory for wave force calculation. This feature enables to study the nonlinear loads and responses of the floating wind turbine subjected to extreme waves resulting from the nonlinear evolution in a random sea environment which linear and second order wave theories fail to predict, as evidenced by many experimental studies. The model predicts the responses of a floating wind turbine for the given environmental condition which could be time history of wind speed and wave surface derived either from existing site-specific spectra or record of an actual arriving storm event. Therefore, the model can be used to analyse structure during both pre and post construction stage. During the pre-construction stage, the model can be used to optimize the structure's geometry whereas, during the post-construction stage, the model can be used for predicting costly wind turbine's performance under actual storm event, to issue warning for planning its evacuation or arranging precautionary measures, to minimize damages to it and its supporting structure including station-keeping system. Thus, the model can be used for optimizing CAPEX as well as OPEX and hence the LCOE for the concerned floating wind turbine system.

ACKNOWLEDGEMENT

First, I would like to express my sincere gratitude to my supervisor Prof. Qingwei Ma for his continuous support, insight and guidance during this research study. His enthusiasm and motivation have been a source of inspiration to improve and learn something new every day. My sincere thank goes to Dr. Shiqiang Yan, Dr. Jinghua Wang, and Dr. Juntao Zhao for their expert advice throughout this research study. I would also like to thank City library and IT department for providing the excellent computing facility that made this thesis possible. I would also like to thank Dr. Andrew Goupee from the University of Maine for supplying me experimental data to validate the numerical model developed and presented in this thesis.

I am grateful to have Professor Pandeli Temarel from University of Southampton and Professor Cedric D'Mello from City, University of London as my examiners. I would like to thank them for their time, dedication, and insightful comments to improve the content of this thesis.

I also thank my wife, my parents and my brothers for their unconditional support and endless patience, without which this work would not have been completed. Finally, I would like to take this opportunity to thank my lovely daughter Sunidhi and son Sidhant to whom I dedicate this thesis.

DECLARATION

No portion of the work referred to in this thesis has been submitted in support of an application for other degree or qualification of this or any other university or other institutes of learning. I grant powers of discretion to the City, University of London Library to allow this thesis to be copied in whole or in part without any reference to me. This permits a single copy to be made for study purpose subject to the normal condition of acknowledgement.

LIST OF FIGURES

LIST OF TABLES

LIST OF SYMBOLS

$\overrightarrow{F_{aero}}/\overrightarrow{M_{aero}}$	Aerodynamic forces/moments due to wind
ρ_a	Air density
AG	Airgap
ω	Angular frequency
$\vec{L}$	Angular momentum of the body
a	Axial induction factor
a_{skew}	Axial induction factor with skewed wake
Υ	Azimuth angle
α_b	Blade angle of attack
dr	Blade element length or annulus width
β_b	Blade pitch angle
L_c	Carrier wave length
T_c	Carrier wave period
H	Characteristic wave height
L_0	Characteristic wave length
T_0	Characteristic wave period
c	Chord length
ψ	Coning angle
F_{tip}	Correction for losses at blade tip
F_{hub}	Correction for losses at hub
u_c, v_c	Current velocity in x and y direction
h_d	Draft of the platform hull
C_d, C_l	Drag and Lift coefficient
$\overrightarrow{F_{drag}}$	Drag force
$\varepsilon_1, \varepsilon_2$	Error
ε_{tol}	Error tolerance
(α, β, γ)	Euler angles (roll, pitch and yaw)
$\overrightarrow{a_w}$	Flow acceleration (temporal + convective)
u, v, w	Flow velocity in x, y, and z direction (includes wave and current)
$\overrightarrow{u_w}$	Flow velocity
$d\overrightarrow{f_1}$	Force per unit immersed length
$\overrightarrow{F_{gravity}}/\overrightarrow{M_{gravity}}$	Forces/moments due to gravity
f	Frequency
R_{hub}	Hub radius

$\overrightarrow{F_{hydro}}/\overrightarrow{M_{hydro}}$	Hydrodynamic forces/moments due to waves and current
i, j	Indices
$\overrightarrow{F_{inertia}}$	Inertia force
ϕ_{inf}	Inflow angle
$\vec{P}$	Linear momentum of the body
r	Local radius of blade element
X_e	Location of extreme wave evolution from wave maker
$[M]\ and\ [I]$	Mass and inertia matrix
$\overline{V_w}$	Mean wind speed
$\Delta T''$	Normalised period bandwidth
B	Number of blades
N_c	Number of components
N_e	Number of elements
L_p	Peak wave length
T_p	Peak wave period
ΔT	Period bandwidth
$\emptyset$	Phase angle
$\overrightarrow{F_2}/\overrightarrow{F_{bp}}$	Point force at an immersed end of member
$\overrightarrow{F_3}/\overrightarrow{F_{int}}$	Point force at wave surface intersection
$\overrightarrow{r_p}$	Position vector
P_0	Power
α_{shear}	Power law coefficient
$\overrightarrow{a_r}$	Relative flow acceleration (flow acceleration – member acceleration)
$\overrightarrow{u_r}$	Relative flow velocity (flow velocity – member velocity)
$V_{w,rel}$	Relative wind speed
$\overrightarrow{F_{moor}}/\overrightarrow{M_{moor}}$	Restoring forces/moments due to mooring system
V_R	Resultant velocity
$\vec{\theta}$	Rotational motion $\{\theta_{roll}, \theta_{pitch}, \theta_{yaw}\}$
a'	Rotational or tangential induction factor
$\vec{\Omega}$	Rotational velocity of body around its centre of gravity
ω_{rot}	Rotor rotational speed
R_{tip}	Rotor tip radius
ρ_s	Seawater density
H_s	Significant wave height
S_p	Significant wave steepness
σ_r	Solidity ratio

$S(f)$	Spectral density function
σ_{V_w}	Standard deviation of wind speed variation around its mean
T	Thrust
C_T	Thrust coefficient
dT	Thrust of element or annulus
T_e	Time of extreme wave evolution
h	Time step size
Q	Torque
dQ	Torque of element or annulus
F_c	Total correction factor
$\vec{F}$	Total external force acting on the body at its centre of gravity
$\vec{N}$	Total external moment acting on the body about its centre of gravity
TF	Transfer function
$[B]$	Transformation matrix relating angular velocities to time derivatives of Euler angles
$\vec{X}$	Translational motion
$\overrightarrow{U_c}$	Translational velocity of body at its centre of gravity
$\overrightarrow{\Delta_{turbine}}$	Turbine displacement
I_{turb}	Turbulence intensity
$[V]$	Velocity gradient matrix
V_{hub-ip}/V_{hub-op}	Velocity of hub in and out of rotor plane
ϕ	Velocity potential
χ	Wake skew angle
d	Water depth
amp	Wave amplitude
q	Wave group steepness
u_w, v_w, w_w	Wave induced flow velocity in x, y, and z direction
k	Wave number
ε	Wave steepness
η	Wave surface
dT_{drag}	Wind drag force on tower element

LIST OF TECHNICAL TERMS

AEP	Annual Energy Production
BEM	Blade Element and Momentum
BFI	Benjamin Feir Index
CAPEX	Capital Expenditure
CFD	Computational Fluid Dynamic
DES	Detached Eddy Simulation
DNS	Direct Numerical Simulation
FAST	Fatigue, Aerodynamics, Structures, and Turbulence
FNPT	Fully Nonlinear Potential Theory
FWT	Floating Wind Turbine
HAWC2	Horizontal Axis Wind turbine simulation Code 2nd generation
HOS	Higher Order Spectral
LCOE	Levelized Cost of Electricity
LES	Large Eddy Simulation
NDPT	Non-Diffracting Potential Theory
NIMBY	Not In My Back Yard
NLSE	Non-Linear Schrödinger equation
N-S	Navier-Stokes
OPEX	Operating Expenditure
RANS	Reynolds Averaged Navier Stokes
RNA	Rotor Nacelle Assembly
RNL	RISØ National Laboratory
TLPWT	Tension-Leg-Platform Wind Turbine

1 INTRODUCTION

1.1 Motivation

Climate change and the need to manage dwindling fossil fuel reserves are the biggest challenges faced by energy suppliers worldwide. The growing awareness about environmental concern uplifts the use of renewable energy to make these challenges manageable. Wind energy is the world's fastest-growing, non-polluting, inexhaustible renewable energy source and has become an integrated part of modern power production in many countries. According to Global Wind Energy Council (2018), the worldwide wind power generation capacity has crossed 539GW in 2017, growing by 52.5GW over the preceding year and covers almost 5% of the global electricity demand (11.6% in EU). This trend is expected to continue with falling cost of wind turbines and an urgent international need to tackle CO2 emission to prevent climate change.

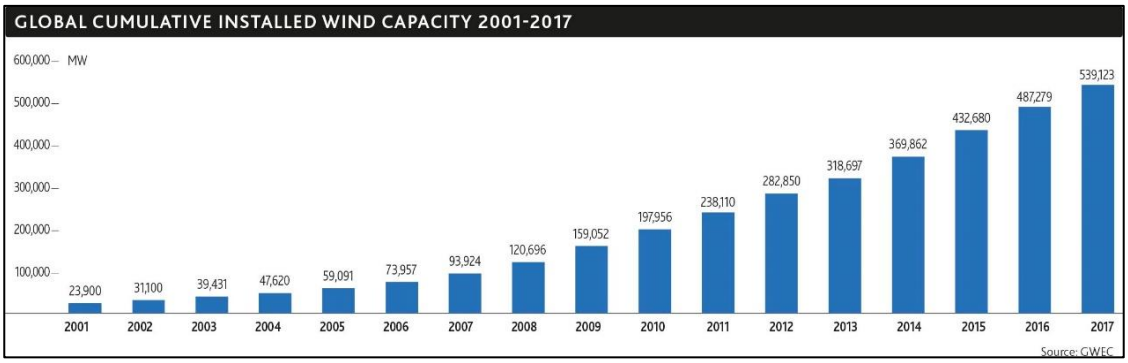

Figure 1.1.1 Global cumulative installed wind capacity for year 2001-2017

Future onshore wind farm developments are hampered by concerns such as turbine noise, aesthetic (visual) impact and scarcity of land for turbine placement near major population or energy load centre (coastal cities) where energy cost and demand are high. Locating wind turbines offshore alleviate these concerns and offers advantages such as higher and steadier wind speed, and availability of larger area sites than onshore. The offshore wind farm development began in shallow water area by placing wind turbines on fixed (seabed mounted) structures. However, most of the global offshore wind resource is available in the location where water is much deeper and deploying wind turbines on a fixed support structure becomes economically infeasible. Therefore, it is strongly desired to develop a cost-effective floating platform system to support the wind turbine in a deep sea. A major disadvantage of using a floating platform to support wind turbine is a large inertia loading acting on the tall tower caused by wind and wave excitation. When wind turbines will be deployed offshore, they will be in numbers and will be more vulnerable due to strong environmental loading during storm or hurricane. It may cause significant platform motions which may affect turbines performance and structural strength of the supporting tower and platform. Hence, optimal low-cost platform designs are possible only when the environmental loads acting on it and the resulting motions are predicted accurately.

During the recent past, a large wave appearing during storm event started drawing great attention of oceanographers and design engineers, as they have been overlooked in the past due to their rare in-situ observation. Thanks to the recent progress in gathering and analysing storm sea data by Ward (1979); Patterson (1974); Buckley and Stavovy (1981); Buckley (1983), and Rosenthal and Lackner (2008) which has been a significant contribution to the research community studying extreme waves and their loadings on marine structures. For example, an analysis of data from the Gulf of Mexico hurricane Camille (Patterson, 1974) and a storm off Irish Coast (Buckley, 1983) revealed that some of the large waves contained in the sample time history were steep on their forward face and greatly elevated as shown in Figure 1.1.2. Such wave is often termed as Extreme Transient Wave (also known as Rogue wave, freak wave, monster wave, episodic wave, killer wave, and abnormal wave).

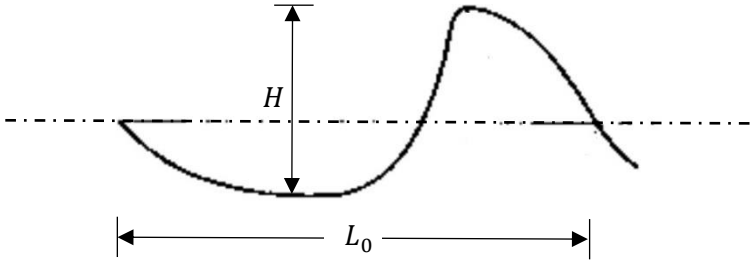

Figure 1.1.2 Extreme Transient Wave

The probability of occurrence of such wave is higher than expected as per traditional statistical theories (Kharif, et al., 2009) and increasing marine accidents involving them being reported recently (Liu, 2007; Nikolkina & Didenkulova, 2012). Although such waves are recurring event along the continental margin, an origin of it is not fully understood. It is believed that a shoaling mechanism, wind-wave interaction, a random phase relationship between waves (i.e., wave-wave interaction), and an opposing shear current could be the plausible reason behind it. To study these phenomena, such waves have been generated in a several wave tanks and reported by researchers such as (Longuet-Higgins, 1974; Takezawa & Hirayama, 1977; Kjeldsen, 1982; Mansard & Funke, 1982; Kraft & Kim, 1987; Rapp & Melville, 1990; Kim, et al., 1990; 1992; Clauss & Kuehnlein, 1994). Kinematic measurements made by Kim et al. (1990) for a laboratory generated extreme transient wave having equivalent size and asymmetric properties as those found in hurricane Camille indicated crest velocity 64% greater than the phase velocity just prior to breaking. Based on the measurements, he proposed that severely asymmetric extreme transient wave to be selected as a design wave to avoid severe underestimation of wave loads. Zou and Kim (2000) further studied the response of a tension leg platform to such extreme transient wave and found pronounced ringing and springing response.

The response of a floating wind turbine to such extreme transient wave can also be studied experimentally. However, they are expensive, and for each setup, one model can be tested. Although the experiments can provide beneficial and irreplaceable results, a systematic

investigation with different wind-wave parameters and the structure configurations are practically impossible. Contrary to this, numerical modelling is a relatively easier and cheaper option with recent advancements in computing technologies. Once the methodology and computer codes are established, many different analysis runs can be easily performed.

1.2 Statement of the problem

A development of numerical model for simulating responses of floating wind turbine to extreme wave requires simulation codes for both wind turbine and moored floating platform, and currently, state of the art codes for both are existing separately. Wind turbine simulation codes are used to model and simulate wind turbine behaviour whereas floating platform simulation codes are used to analyse wave structure interaction and to simulate structures responses. In the past, several attempts have been made to simulate the floating wind turbine responses by extending either wind turbine or floating platform simulation codes or by combining both through the numerical coupling scheme. For example, extended wind turbine simulation codes include, Bladed by GL Garrad Hassan (2003), Flex5 by RNL (2007), FAST by NREL (2009) and HAWC2 by RNL (2015) whilst extended moored floating platform simulation codes include, SIMO/RIFLEX by MARINTEK (2008; 2010), and 3D float by UMB (2011). The combined codes include FAST coupled with SML and WAMIT (Jonkman, 2007), Charm3D (Shim & Kim, 2008), and TimeFloat (Roddier, et al., 2009; Cermelli, et al., 2009), and HAWC2 coupled with SIMO/RIFLEX (Skaare, et al., 2007; Larsen & Hanson, 2007).

All the afore-mentioned simulation codes consist of a state-of-the-art aerodynamic model for fix bottom wind turbine which is applicable to floating wind turbines by incorporating the interaction between the wind turbine and floating platform. However, all the afore-mentioned simulation codes consist of a hydrodynamic model that follows either Morison's equation or diffraction theory for wave force evaluation where linear or second order wave theory is employed for wave kinematic prediction. Such approaches are insufficient for analysing floating wind turbine responses to extreme waves since they are highly nonlinear and the effect of nonlinearity on the floating wind turbine responses could be significant. As such extreme waves do not arise as part of the regular wave train but occur as an individual event within a random sea. If one considers a narrow-banded spectrum in deep water, frequency dispersion provides a plausible explanation for the evolution of extreme wave. There are growing evidences that an individual height (crest to trough) of an extreme wave in a random record may be higher (more frequently) than predicted by the Rayleigh distribution based on the linear wave assumption. This is supported by various full-scale observations (Kjeldsen, 1990; Sand, et al., 1990; Skourup, et al., 1996; Yasuda, et al., 1998), laboratory observations (Phillips, 1981; Stansberg, 1993; 1998a; Onorato, et al., 2006; Xia, et al., 2015), and numerical simulations (Mori & Yasuda, 2000; Gibson & Swan, 2007; Goullet & Choi, 2011). In contrast to non-Rayleigh extreme crest height, which is

more frequent and to some extent (for low significant wave steepness $H_s/L_p < 0.02$ as per Hu and Zhao 1993) can be described by second-order wave model, non-Rayleigh wave heights must be described by higher-order wave model.

This thesis presents an integrated nonlinear model for simulating responses of floating wind turbine by incorporating higher-order wave model. The model aims to incorporate state of the art nonlinear wave kinematic and force model that enables it to simulate extreme wave and its interaction with the floating wind turbine.

2 LITERATURE REVIEW

This chapter will review and discuss previous studies and techniques relevant for developing an integrated nonlinear model for simulating responses of floating wind turbine to extreme waves. Prior to this, a brief review is provided on advancement in the offshore wind industry and the chosen floating wind turbine concept for the present study.

2.1 Offshore wind energy

Offshore wind energy is the energy generated through wind farms constructed in the ocean on the continental shelf. Higher wind speeds are available offshore as compared to on-land, so energy generation is higher per amount of capacity installed (Madsen & Krogsgaard, 2010) where NIMBY opposition to construction is usually much weaker. Europe is the world leader in offshore wind power, with the first offshore wind farm (Vindeby) being installed in Denmark in 1991. Since then a rapid development has been witnessed by the industry with the total worldwide power capacity of 18,814 MW installed by the end of 2017 (GWEC, 2017). All the large offshore wind farms are currently installed in northern Europe, especially in the United Kingdom and Germany, which combined account for over two-thirds of the total offshore wind power installed worldwide. As of September 2018, the 659 MW Walney extension in the United Kingdom is the largest offshore wind farm in the world. The Hornsea wind farm under construction in the United Kingdom will become the largest when completed, at 1,200 MW. Other projects are in the planning stage, including Dogger bank in the United Kingdom at 4,800 MW, and Greater Changhua in Taiwan at 2,400 MW. The cost of offshore wind power has historically been higher than that of its onshore counterpart but have been decreasing rapidly in recent years which motivates future developments. Projections for 2020 estimated an offshore wind farm capacity of 40 GW in European waters, which would provide 4% of the European Union's demand for electricity (Tillessen, 2010). The European Wind Energy Association has set a target of 40 GW to be installed by 2020 and 150 GW by 2030 (EESI, 2010). Offshore wind power capacity is expected to reach a total of 75 GW worldwide by 2020, with significant contributions from China and the United States (Madsen & Krogsgaard, 2010).

2.1.1 Fixed offshore wind turbine

Offshore wind farm development began in a shallow water area with fixed seabed mounted structures. Currently, all the operating offshore wind farms employ fixed foundation turbines, except for a few pilot projects. They require several types of bases for stability, which mainly depends upon the water depth. To date, several different solutions exist as shown in Figure 2.1.1.

- Gravity-based structure (GBS) – for use at exposed sites in a water depth of 20-80m.
- Jacket – steel structure as used in the oil and gas industry, in a water depth of 20-80m.
- Tripod – piled or suction caisson structure in a water depth of 20-80m.

- Monopile – for use in a water depth up to 30m.

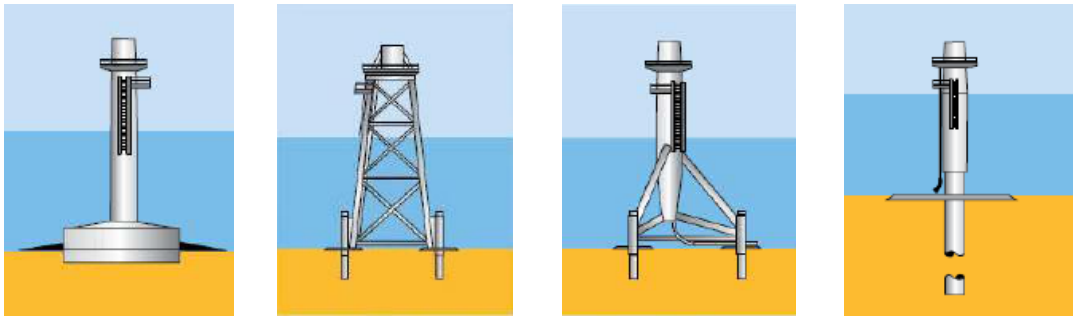

GBS Jacket Tripod Monopile

Figure 2.1.1 Fixed support structure for offshore wind turbine system (Peyard, 2015)

As water depth increases beyond 80m, these foundation types manifest several disadvantages as follows,

- Cost of fixed foundation and installation increases with water depth result-in economically infeasible option
- First natural period of the system comes close to the rotational frequency of the turbine or three times this frequency (for a three-bladed turbine). These requirements are increasingly challenging to constrain as the water depth increases, as modern wind turbines are constructed for variable rotational speed.
- Wave impact load and resulting ringing like response is expected.

These disadvantages can be overcome by choosing floating support structure to support a wind turbine in a moderately deep sea (>80m).

2.1.2 Floating offshore wind turbine

Floating support structure increases the flexibility in deploying wind turbines in water depths beyond 80m. Its foundation features are not large since mooring lines or tethers will be used instead of concrete bases. Individual floaters allow the deployment of a large and variable number of wind turbine units. There is extensive wind resource available in the deep sea (50-200m), where the floating wind turbine is potentially a highly scalable future energy source in several markets. There is significant potential and appetite for growth in Japan, the United States, and several European countries including the UK, Norway, France, Portugal, and Spain.

Table 2.1.1 Offshore floating wind potential in Europe, USA, and JAPAN
(Ian Baring-Gould, 2013; EWEA, 2013; Marine Scotland, 2014)

Country/Region	Share of offshore wind resource in deep water	Potential floating wind capacity
Europe	80%	4000 GW
USA	61%	2450 GW
JAPAN	80%	500 GW

Europe

The potential for electricity generation from floating wind turbine in Europe is vast. Over half of the North Sea is suitable for floating wind turbine deployment, with water depths between 50m to 200m as shown in Figure 2.1.2. On this basis, EWEA estimated that the energy produced from the turbines in deep water > 50m in the North Sea alone could meet the EU's electricity consumption four times over (EWEA, 2013).

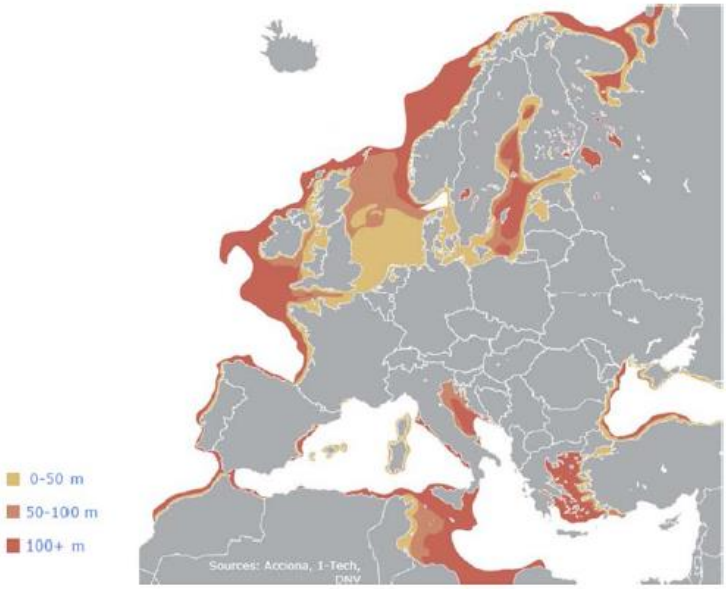

Figure 2.1.2 Water depth (50m to 200m) around Europe (DNV-GL, 2014)

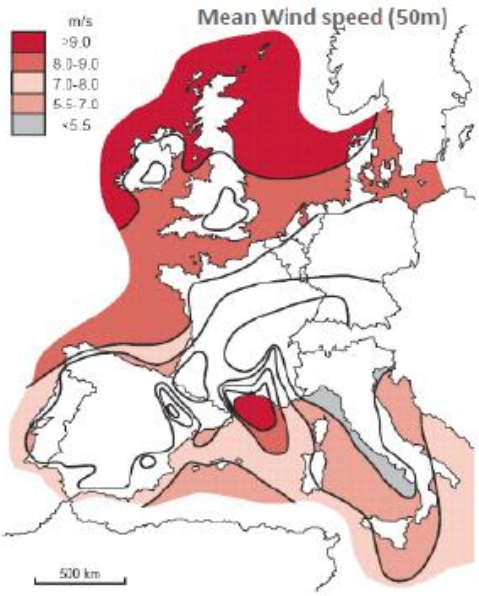

Figure 2.1.3 Mean wind speed around Europe (Maciel, 2012)

There is also significant wind resource available in the Atlantic, particularly off the coast of Scotland and England, and in the west of France and off the coasts of Portugal and Spain, where deep-sea precludes fixed-bottom offshore wind development. Deep sea is also prevalent in the Mediterranean, where the wind resource is generally less extensive than the North Sea and

Atlantic coastline; although there are pockets of strong and moderate wind which could be well suited to floating wind turbines, particularly given that the less harsh marine conditions may allow for less conservative structural designs (ORECCA, 2011).

EU targets for offshore wind power of 40 GW by 2020 and 150 GW by 2030 are expected to be achievable by predominantly using conventional fixed-bottom foundations in water depths under 50m. However, by 2050, offshore wind power capacity in Europe could reach 460 GW, which can only be achieved by accessing deep water sites > 50m using floating technology (EWEA, 2013). The 2030 target may also require a higher proportion from floating wind turbine solution if they prove to be cost competitive and the development of floating wind turbine technology is accelerated. While offshore wind turbine deployment up to 2030 is expected to be dominated by the significant growth of fixed-bottom wind turbines, from 2030, it is likely that adequate sites will become scarcer and costlier to develop with fixed-bottom structures, further from shore and in places with challenging seabed and met-ocean conditions. Floating wind turbine technology could thus be used to exploit deep water locations closer to shore, and the added flexibility of floating structures means that it has the potential to be highly scalable.

UK

The UK is blessed with excellent offshore wind resource and access to the shallow continental shelf of the North Sea. However, there is also a significant resource in deep-sea >50m, where wind speeds are often stronger and more consistent than in shallower locations. The highest mean wind speeds in the UK are in Scottish waters and off the south-west coast of the UK, where deep-sea locations are abundant. Given the importance of energy yield for wind farm economics, the Energy Technologies Institute (ETI) estimates that deploying floating wind turbine in these locations to access this stronger wind resource could result in a lower levelized cost of energy (LCOE) compared with some fixed-bottom UK Round 3 sites (ETI, 2015). Indeed, there is already evidence to suggest that a more consistent wind resource in deep sea locations can lead to higher load factors in floating turbines. The distribution of sites suitable for floating wind turbine in the UK is expected to differ to the fixed-bottom wind turbine. While the best sites for fixed-bottom offshore wind are found off the east coast of England in shallow waters (< 50m depth), the opportunities for floating wind turbines are concentrated off the coast of Scotland and Wales, where near-shore deep-water sites (> 50m depth) are located, and the geology and met-ocean conditions are suitable for floating devices. In Scotland, there are extensive deep-water locations to the east, north, and west of the country, with 123 GW of the 169 GW offshore wind potential located in water depths exceeding 60m (Scottish Enterprise, 2015).

Licensed sites for fixed-bottom offshore wind in Scotland are primarily in water depths over 40-45m and in complex seabed conditions, which suggests that the low-hanging fruit available for offshore wind may be smaller than elsewhere in the UK. On this basis, commercialised floating wind farm projects would have the potential to unlock lower cost sites in Scottish waters.

2.2 Chosen floating wind turbine concept

The vision of large-scale offshore floating wind turbines was introduced by Prof. W.E. Heronemus at university of Massachusetts in 1972, but the topic was taken up by the main research community after mid-1990 when the commercial wind industry was well established. Since then European institutions have been the leaders in this research field. Several concepts of floating platform supporting horizontal axis wind turbine were studied in the past and some of them are under research. The example includes MUFOW by Baltrop (1993), Toroidal shape by Bertacchi et al. (1994), FLOAT by Tong (1998), Tri-floater by Delft University (2002), Advanced Floating Turbine (AFT) by Nautica (2007), MIT/NREL TLP by Sclavounos et al. (2007), Hywind by Statoil (2009), WindFloat by Principle Power (2011), WindCrete by Universitat Politècnica de Catalunya (2011), Compact Semi-Sub by Mitsui Engineering & Shipbuilding (2013), Hybrid Spar by Toda Construction (2013), Advanced Spar by Japan Marine United (2013), Sway by Sway A/S (2013), TetraFloat by TetraFloat Ltd. (2014), TLPWind by Iberdrola (2014), Damping Pool by IDEOL (2015), V-Shape Semi-Sub by Mitsubishi Heavy Industries (2015), GICON-SOF by GICON (2015), Nautilus Semi-Sub by Nautilus Floating Solutions (2015), Nezzy SCD by Aerodyn Engineering (2017), SeaReed by DCNS (2018), VolturnUS by DeepCwind Consortium (2018), PelaStar by Glosten Associates (2018), Eco TLP by DBD Systems (2018). Some are even installed, e.g. Blue H Technologies TLP (2008), Hywind (2009, 2011), Windfloat (2011), Sakiyama (2016) and GICON-TLP (2017). All these floating platform concepts considered to support wind turbine are derived from the floating structures used in the offshore oil and gas industry and can be broadly classified as ballast stabilized system, i.e., spar, buoyancy stabilized system, i.e., semi-submersible and mooring line stabilized i.e., tension leg platform, as shown in Figure 2.2.1.

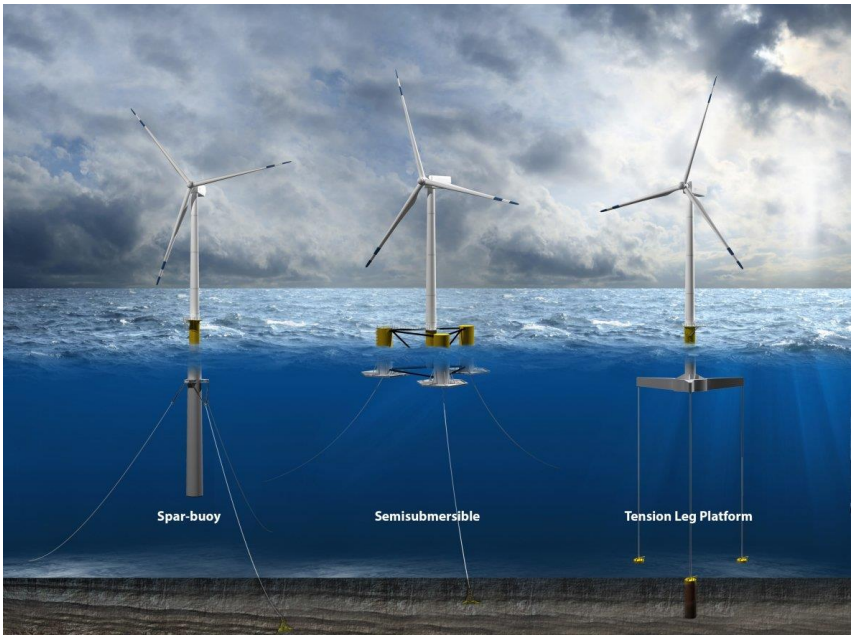

Figure 2.2.1 Floating platform concepts for offshore wind turbine (www.energy.gov)

The prime requisite for such floating system is their capability of standing stable in the water, albeit with some degree of oscillation which may vary depending on the type of floating system considered. The main movement under the action of wind and wave turns out to be strongest one for ballast and buoyancy stabilised floating structures, i.e., translation and tilting whilst the floating structure stabilised by mooring lines shift horizontally. If the floating platform allows the system to tilt appreciably, the behaviour of a wind turbine would be affected even to such an extent that possible operating limitations and/or energy output reductions would have to be considered for estimating LCOE. Therefore, the best promising concept for a floating wind turbine is deemed to be a mooring line stabilised tension leg platform which experiences minimal tilting movement. Moreover, it is lightweight and has less mooring footprints as compared to its counterpart's spar and semi-submersible. Favourable indications for the adoption of the TLP system have also been given by technical and economic results obtained from a separate study carried out by Musial et al. (2003) and Italian Electrical System (Casale, et al., 2010) and hence adopted for the present study.

A design chosen for the present study is mono-column tension leg platform as shown in Figure 2.2.1, which is nothing, but a vertical spar buoy stiffened in heave, roll and pitch mode by using a combination of pontoons and the mooring lines under tension. The tensioned mooring lines virtually eliminate the vertical heave and rotational roll and pitch motion while the lateral surge and sway motions and the rotational yaw motion are compliantly restrained. An excess of buoyancy greater than the platform weight keeps the mooring line in tension under all the loading condition. The height of a vertical spar buoy is kept enough to maintain a minimum air gap between the bottom tip of the rotor blade and wave crest elevation for all tide and extreme wave situation.

2.3 Mathematical models

Development of an integrated nonlinear model for simulating responses of a chosen tension-leg-platform wind turbine requires a definition of equations of motions and the evaluation of external forces acting on it. A set of nonlinear equations of motions are required to be defined for the concerned floating wind turbine as it may subject to high environmental loadings which may cause large motions, and the linearized equations may not give acceptable results. However, it is only practicable if the exciting forces can be calculated with the computationally efficient approach.

As chosen floating wind turbine is intended to be installed in intermediate to deep water area, they will be exposed to various loads as illustrated in Figure 2.3.1.

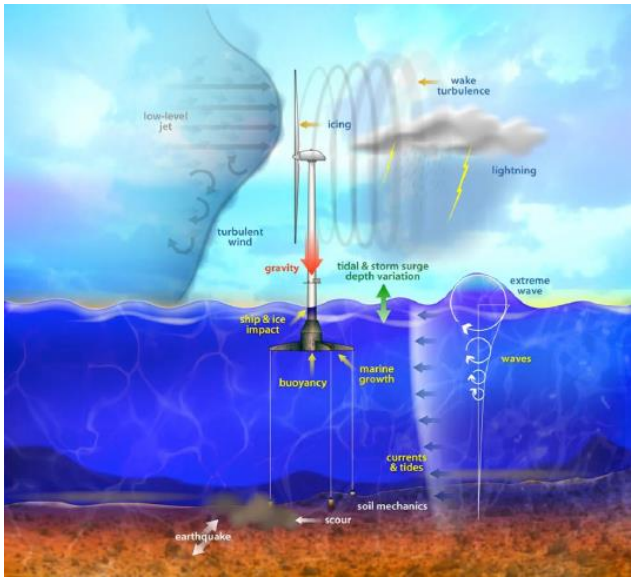

- Gravity
- Buoyancy
- Wind
- Waves & Current
- Ice
- Marine growth
- Scour
- Earthquake
- Tidal and storm surge variation

Figure 2.3.1 Loads acting on floating wind turbine (Jonkman, 2007)

The environmental loads acting on the floating wind turbine are predominantly due to wind, waves and current. Additional loads due to ice, marine growth, scour, and sea level fluctuation, is small in comparison to wind, waves and current and must be considered during the real design process. Loads due to the earthquake are outside scope of this research and therefore in this thesis, investigation of floating wind turbine response analysis is limited to environmental loads due to wind, waves and current. Hence, the forces acting on the floating wind turbine system constitutes aerodynamic forces due to the wind, hydrodynamic forces due to wave and current and the restoring forces due to mooring lines. Methods currently available for evaluating hydrodynamic forces due to wave and current and the restoring forces due to the mooring system are well established and have been successfully used in the past for designing offshore oil and gas structures. However, methods available for evaluating wind force acting on the turbine rely on several assumptions that may not hold for highly dynamic ocean environment in which floating wind turbines may be expected to operate. The control strategy of the wind turbine, and the translational (surge, sway, and heave) and rotational (roll, pitch and yaw) motions of its supporting platform will all introduce an additional effective wind contribution which may result out increase/decrease in wind force acting on the turbine. This change in wind force may resist/increase the wave-induced motions of the platform and thereby act as a damping mechanism. This damping mechanism due to the interaction between the wind turbine and its support system need to be considered while evaluating various afore-mentioned forces acting on the floating wind turbine system. Researchers have used either frequency or time domain approach for the development of numerical simulation codes. A brief review of both the approaches is provided under below sub-section.

2.3.1 Frequency domain approach

In this approach, equations of motions are solved using methods of harmonic analysis or methods of Laplace and Fourier transformations. This approach has a very strong appeal to the researchers due to its simplicity and efficiency. This approach requires that the formulation of a problem, i.e., wave kinematics, forces and motions to be completely linearized. The solution leads to a set of a linear transfer function which represents a mathematical expression of the dynamic characteristics for that platform. These transfer functions, often called as RAO's can be used directly with the wave spectra, thus resulting out response spectra from which various statistical information can be derived, e.g. fatigue life prediction. This approach has been widely used due to its simplicity and less computing time. The theory and techniques of the linearization with respect to motion, wave excitation forces, and mooring line restoring forces can be found in Mei (1989), Faltinsen (1990), and low (2009) respectively.

Several studies have been performed in the past to assess the floating wind turbine dynamic using this approach. For example, tri-floater concept by Bulder et al. (2002), a tension leg platform by Lee (2005) and Sclavounos et al. (2007), barge by Vijfhuizen (2006) etc. However, these models are useful for demonstrating initial technical feasibility. They cannot capture nonlinear dynamic characteristics and cannot model transient loading events, both of which are important for floating wind turbines because the nonlinear dynamics introduced through transient events are significant for the loading analysis. Matha (2009) performed a comparison study for frequency versus time domain analysis of a floating wind turbine and showed that some coupling between the platform motion and the tower and blades were not captured which led to natural frequencies being wrongly predicted and critical system resonances not being identified. This result underlines the importance of performing calculations for floating wind turbines in the time domain and the same approach is adopted in this thesis.

2.3.2 Time domain approach

In this approach, equations of motions are solved using numerical integration methods. This approach has the flexibility to accommodate very complicated nature of the dynamic system, where a frequency domain approach would break down. This approach lends themselves very well for determining responses of the platforms to extreme waves where non-linear effects are important. They permit inclusion of all the non-linearity's associated with floating wind turbine dynamics. This approach requires wind and wave spectra to be transferred to time series for simulating turbulent wind condition and stochastic wave surface elevations. The motion responses are obtained by solving the equations of motions using an efficient numerical time integration method. The analysis needs to be performed for sufficiently long time to get adequate steady state data for statistical analysis and to verify consistency of the simulation. This approach for analysing floating wind turbine dynamics is not used as often as it should be because of its

computing cost. However, it can become effective if the forces can be evaluated using an appropriate method which requires less computational effort.

Several numerical tools are developed to study floating wind turbine dynamics using this approach, for e.g. Bladed by Garrad Hassan (2003); Flex5 by Knauer & Hagen (2007); SIMO/RIFLEX by Fylling (2009); 3D float by UMB (2009); FAST with AeroDyn and HydroDyn by NREL (2007); FAST with charm 3D by Shim (2007); FAST with Timefloat by Roddier et al., (2009); HAWC2 with SIMO/RIFLEX by Skaare et al., (2007) and Larson and Hanson (2015).

2.4 Existing coupling scheme for wind turbine and floating platform

There are several existing numerical tools (as mentioned in the previous sub-section) capable of modelling floating wind turbine dynamic using a time domain approach. They are developed by extending either the existing design codes for a wind turbine or moored floating platform or by coupling both. Wind turbine design codes (i.e., Bladed by GL Garrad Hassan, FAST by NREL, Flex5 and HAWC2 by RNL) are used to model and simulate wind turbine behaviour whereas floating platform design codes (i.e., FAST by NREL, Charm 3D by Texas A&M University, Timefloat by Principle Power Inc, and SIMO/RIFLEX by MARINTEK) are used to analyse wave structure interaction and to simulate structure responses. Based on the code development, they are categorised as extended or coupled codes.

2.4.1 Extended codes

This category of codes includes Bladed by GL Garrad Hassan (2003), Flex5 by RNL (2007), SIMO/RIFLEX by MARINTEK (2009), and 3D float by UMB (2009). The wind turbine design code such as Bladed and Flex5 are extended by incorporating hydrodynamic subroutine which follows Morison's equation with Airy's linear wave theory. The floating platform design codes, i.e., 3D float and SIMO/RIFLEX are extended by incorporating aerodynamic subroutine which follows classical blade element and momentum theory. In these codes, forces due to wind, waves and current, and mooring lines are evaluated at each time step considering the coupling effect between wind turbine, floating support structure and mooring system. However, they all use either linear (Bladed, Flex5, and 3Dfloat) or second order wave theory (SIMO/RIFLEX) which may not be sufficient to analyse extreme waves.

2.4.2 Coupled codes

This category of codes includes FAST coupled with SWIM or WAMIT by NREL (2007), FAST coupled with Charm3D by Shim (2007), FAST coupled with TimeFloat by Roddier et al. (2009), HAWC2 coupled with SIMO/RIFLEX by Skaare et al. (2007) and Larsen and Hanson (2015). These codes make use of state-of-the-art wind turbine and moored floating platform design codes by using numerical coupling scheme among them to exchange the information during simulation. In these codes, wind turbine design codes (i.e., FAST and HAWC2) are used

to calculate the dynamic responses of turbine components, tower, and floating platform, while floating platform design codes (i.e., CHARM 3D, TimeFloat, and SIMO/RIFLEX) are employed to determine the hydrodynamic wave forces (first-order wave frequency and second order sum/difference frequency forces), viscous forces on Morison members, radiation damping forces in the form of convolution integral, and mooring restoring forces. These forces are lumped at the hull-tower interface as part of the input to solve the equations of motions for the dynamics of the turbine, tower and floating support structure. The resultant displacements, velocities, and accelerations of the hull structure are passed on to floating platform design codes for the next step calculation of the hull-tower interface forces. The computational speed of these coupled codes depends on numerous factors. These include the discretisation chosen by the user, the code features enabled, and the precise details of the coupling scheme.

The strength of above-mentioned extended and coupled codes are their state of the art aerodynamic and hydrodynamic models. However, the fact that these models are state of the art separately that does not guarantee they are state of the art when combined, especially if the application is a novel concept such as floating wind turbine where its components, i.e., wind turbine, tower, floating platform and mooring system dynamically interact with each other under the combined action of wind, waves and current. The reasons include,

I. Both models are based on different assumptions, which may be conflicting.
II. Coupling of both models may lead to unexpected results due to interface issues.
III. The models were developed for a specific purpose which may not be applicable for new applications. For example, all the afore-mentioned hydrodynamic tools follow a classical approach of Morison's equation or wave diffraction analysis using linear or second order wave theory which may be insufficient for extreme waves as pointed out by many researchers, covered under section 1.2.

Moreover, IEC 61400-3 international design standard for offshore wind turbines requires that an integrated load and response analysis be performed for a wind turbine to be certified. This type of analysis is also essential from the point of view of the designer as it enables the wind turbine performance to be optimised as well as the structural integrity verified. Full design optimisation is not possible without considering the fully coupled response of the system. Therefore, to efficiently design optimised floating wind turbines, reliable tools are needed which can model the load and response of floating wind turbines in a comprehensive and fully integrated manner and the same approach is followed in this thesis.

2.5 Existing methods for calculating forces and moments

As explained in section 2.3, loads considered in this research study are aerodynamic loads due to wind acting on the turbine rotor, hydrodynamic loads due to wave and current acting on the floating platform and restoring loads due to mooring lines. A brief review of existing methods for evaluating these loads is given in this section.

2.5.1 Wind loads

A wind turbine is a device, which extracts kinetic energy from the wind and converts it to the torque at the shaft and generates power. Hence the performance of a wind turbine includes thrust, torque and power. Modelling of wind turbine performance has been attempted in the past using various methods which solves the global and local flow fields based on various levels of approximations, i.e., Navier-Stokes solution, potential flow models, and blade element and momentum theory. A brief review on each method is given in this section.

2.5.1.1 Navier-Stokes solution

The global and local flow field of a wind turbine can be studied in detail by several existing methods based on the solution of the Navier-Stokes equations. The full set of N-S equations are non-linear and, therefore, analytical solutions are restricted. The approach computationally most demanding but physically most accurate is to solve N-S equations with a CFD solver. The flow over a wind turbine encompasses a Reynolds number range of 10^4 for the global flow to 25×10^6 at the blade local flow for megawatt sized turbines. In CFD, four basic approaches, i.e., direct numerical simulation (DNS), Large eddy simulation (LES), Reynolds Averaged Navier-Stokes (RANS) method, and Detached eddy simulation (DES) are employed for modelling the turbulent flow with their large range of Reynolds number. In DNS, the Navier–Stokes equations are numerically solved without any turbulence model. The whole range of spatial and temporal scales of the turbulence must be resolved in the computational mesh. The storage memory requirement grows very fast with the Reynolds numbers, and hence with currently available computational power, this method does not apply to the floating wind turbines with large Reynolds number range. In the LES approach, this computational cost is reduced by ignoring the smallest length scales, which are the most computationally expensive to resolve, via low-pass filtering of the Navier–Stokes equations. Such low-pass filtering, which can be viewed as a time- and spatial-averaging, effectively removes small-scale information from the numerical solution. The examples of applying this approach to the CFD modelling of wind turbine can be found in Benard et al. (2018) and Sedaghatizadeh et al. (2018). RANS model provides approximate time-averaged solution to the Navier-Stokes equations. The model can be categorised into two groups, i.e. one equation and two equation. One equation RANS turbulence models are based on one time-averaged equation appropriate for modelling wake and complex flow. The two equation RANS turbulence models, k-ε and k-ω are widely used in the CFD for

modelling wind turbines. The k-ε model calculates turbulence kinetic energy (k) and dissipation rate (ε) whereas k-ω model involves the solution of equations for the turbulence kinetic energy (k) and the specific rate of dissipation (ω). The most popular among this is the k-ω SST turbulence model, of which results match well with the experimental results (Wu, 2017; Rocha, et al., 2014). These models can have a significant effect on the CFD solution and must be selected carefully. A combination of RANS and LES, where RANS used for flow around the blades, and LES for the wake, using DES approach, is another good solution for floating wind turbine CFD modelling. The state of the art of CFD techniques for studying the aerodynamics of wind turbine blades can be found in Shourangiz-Haghighi et al. (2019).

2.5.1.2 Potential Flow Method

A potential flow method has been used by some of the earliest aerofoil design methods such as the Eppler code (1990). In this method, the fluid is assumed as inviscid, incompressible, and irrotational, and the effect of surface tensions are ignored. The flow field around the aerofoil is described through the distribution of discrete sources and vortices, with several implementations, e.g., Lifting line, panel and vortex methods. A detailed review on these methods is provided by Hansen et al. (2006). This method is based on the measured aerofoil data where aerodynamic lift, drag and pitching moment characteristics of the blades are assumed to be known and corrected for the effect of blade rotation. A more accurate predictions are expected in conditions, where local aerodynamic characteristics strongly vary with time (yawed flow) and dynamic wake effect play a significant role. Both the effects are increasingly important for floating wind turbines as addressed by Sebastian and Lackner (2011).

2.5.1.3 Blade Element and Momentum Theory

Modelling of the global flow field around wind turbines is originated from marine and aeroplane propeller theory. The first published work on lifting propellers was by Rankine (1865), who applied a one-dimensional momentum theory to analyse the global flow behaviour on a propeller disc. Later, Froude (1889) incorporated the local flow of the rotor as a disc at which there is a sudden change in pressure without any discontinuity of velocity, which is generally known as one-dimensional actuator disc theory. One-dimensional or axial momentum theory for the global flow was extended to a two-dimensional level for concentric annuli by Glauert (1935). He added the angular momentum balance which incorporates the tangential velocity of the rotating blade; which is known as general momentum theory. For the local flow, Glauert applied blade element theory where it is assumed that the aerodynamic forces at independent elements of the blade are equal to the forces on the same aerodynamic profile taken from two-dimensional wind tunnel aerofoil tests. This approach is based on Prandtl's slender wing, lifting line approximation where the forces on a wing element are taken equal to the two-dimensional forces for an equivalent angle of attack, which is formed by the mean flow plus the velocities induced

by the three-dimensional trailing system. On a wind turbine blade, the induction is due to the helical trailing vortex in the rotor wake. This induction is assumed equal to the axial and tangential induction velocity factors of momentum theory. Blade element theory is usually employed to analyse the local flow at blade whereas the momentum theory is used for the global flow region. Together, they form what is commonly known as Blade Element and Momentum theory, (BEM). Most of the contemporary predictive and design codes for wind turbine rotor blade aerodynamics are based on the analytical work of Wilson and Lissaman (1974) using the BEM method. Simple BEM theory is very rarely used in isolation, as it does not deal with the unsteady nature of the aerodynamics experienced by a turbine rotor. Therefore, several corrections (see section 3.2.3) are commonly applied in conjunction with this BEM model to account for this. The validity and limitations of the BEM theory are still under discussion. Sorensen and Mikkelsen (2001) analysed some of the basic assumptions behind this theory. Comparison of BEM results with an unsteady model of the axisymmetric inviscid form of the Navier-Stokes equations, showed the worst case to produce a maximum error of up to 3% in the axial induced velocity on the rotor. They demonstrated that inherent inconsistencies of the BEM model result in negligible errors.

The main advantage of this method is its simplicity and consequently its speed. It has also been extensively validated against measured data and shown to be accurate and reliable. This method was developed from helicopter aerodynamics and due to its convenience and reliability has remained the most widely used method for calculating the aerodynamic forces on wind turbines. Floating wind turbine design codes are no exception and BEM theory is used in all the codes currently available and hence adopted in this research study.

2.5.2 Wave loads

The evaluation of hydrodynamic forces acting on the floating structures is of immense importance to engineers involved in offshore engineering. It is a challenging task because the ocean waves are very complex in nature and its interaction with the floating platform needs to be accounted for while evaluating forces. There are a wide variety of floating platforms being considered to support the wind turbine, and they are mainly composed of slender members. Based on the type and size of the members in a structure, in comparison with the wave length, different calculation methods are available for estimating hydrodynamic forces. The hydrodynamic force evaluation methods can be broadly classified into three categories, i.e., fully nonlinear wave-structure interaction, diffraction analysis, and slender body approach.

2.5.2.1 Fully nonlinear wave structure interaction

The most accurate way for wave force evaluation is to perform a numerical analysis of the fully nonlinear interaction between the floating platform and the surrounding fluid. This approach requires fully nonlinear wave theories, which include general flow theory and fully nonlinear

potential theory (FNPT). The former is usually solved in Eulerian view and has been widely adopted by Computational Fluid Dynamics (CFD) software, e.g. OpenFOAM, StarCCM+ and ANSYS CFX. It is widely accepted that solving the equations for the Navier-Stokes models based on general flow theory is always a time-consuming task and is much more difficult, mainly when floating bodies with motions of six degrees of freedom (DoFs) are included. Therefore, many researchers have been contributing to the development of FNPT model for analysing fully nonlinear interaction between the steep waves and offshore structures, e.g. Kashiwagi (2000), Tanizawa (2001), Wu and Eatock Taylor (2003), Koo and Kim (2004), Yan and Ma (2007), Ma and Yan (2009). A detailed review of the FNPT models for wave-structure interactions can be found in Ma and Yan (2009).

In this approach, the fluid domain is governed by a fully nonlinear potential theory in which velocity potential satisfies the Laplace equation and fully nonlinear boundary conditions are imposed on both water and body surface. The problem is solved by using a time step marching procedure. At each time step, the boundary value problem for the velocity potential is solved by using FEM. Bernoulli's equation is used to find the forces acting on bodies. The time derivative of velocity potential in the Bernoulli's equation is also evaluated by solving a similar boundary value problem. Although this is not impossible, this task requires a very powerful computer resource and is therefore not feasible in practice.

2.5.2.2 Diffraction analysis using second order potential theory

An alternative approach to fully nonlinear wave structure interaction method is to carry out diffraction analysis based on the second order potential theory. This approach is generally used when the structural member in question is larger in diameter and experience significant movement, as is often the case for floating wind turbine. This approach requires diffraction and radiation effects to be considered. To incorporate these effects, an additional boundary condition of zero flow velocity perpendicular to the surface of the structure is followed. For most practical cases the resulting problem cannot be solved analytically, so numerical methods based on the assumptions of linear wave theory are used. If the hydrodynamics of the sea state is linear, the sources of loading can be sub-divided into three separate problems: radiation, diffraction and hydrostatic restoring. Wave radiation loading describes the loads which result from the influence of a moving body on the surrounding fluid when incident waves are not present. Wave diffraction loading describes the loads which result from the influence of the surrounding fluid on a stationary body when incident waves are present. Hydrostatic loading describes the static loads on the body arising from the pressure in the surrounding fluid. These three problems are then solved individually, and the resulting loads are summed together. This approach is well explained by Jonkman (2007) who incorporated this into HydroDyn subroutine of existing tool FAST developed by NREL. This approach is also followed by several existing floating wind turbine design tools such as Charm3D, TimeFloat, ADAMS, and SIMO/RIFLEX by MARINTEK. In

these codes, the hydrodynamic coefficients of the floating platform are calculated in the frequency domain using a panel-based 3D diffraction and radiation program WAMIT (developed by MIT) whereas the non-linear viscous drag contribution is included from Morison's equation.

The advantage of this method for calculating hydrodynamic loads is that it takes proper account of the influence of the body on the fluid which is particularly important for floating platforms which often have large diameters and experience significant motion. It is also possible that there may be additional dynamic effects which are only accounted for when diffraction and radiation are included in the analysis: for instance, it has been shown that the presence of wave radiation damping can in some cases reduce instabilities in platform surge motion arising from the controller actions (Jonkman et al., 2010). It illustrates the importance of including these effects in the hydrodynamic loading calculations for floating wind turbines. The computational cost of this approach is also quite high, and this method usually generates results in the frequency domain, and after that, a transformation is needed to obtain the forces in the time domain.

2.5.2.3 Slender body theory

Another approach often used in offshore engineering for wave force evaluation is based on slender body theory that requires much less computational effort and can be directly implemented in the time domain analysis. In this approach, the body is assumed as 'thin' and the forces (and/or moments) are obtained by integrating the forces on each short segment of the slender body. There are two different equations generally used for computing wave loading using this approach, i.e., Morison's and Rainey's equation.

Morison's equation

Morison's equation is a semi-empirical equation developed by Morison, O'Brien, Johnson and Schaaf (1950), for the inline force acting on a body in oscillatory flow. They proposed that the forces exerted by unbroken surface waves on a cylinder is composed of two components, an inertia force in phase with the local flow acceleration and a drag force proportional to the square of the instantaneous flow velocity. Although equation is derived for the fixed vertical cylinder, it accounts for the relative motion between the platform members and the fluid and includes added mass effect from the movement of the water. Several floating wind turbine design codes are using this equation for calculating wave loads. For example, Bladed by GL Garrad Hassan, 3Dfloat by UMB, and SIMO/RIFLEX by MARINTEK (also includes diffraction method).

A major advantage of Morison's equation is that the hydrodynamic loads are calculated in terms of wave-particle velocities and accelerations rather than velocity potential which enables it to be used not only with linear but also with nonlinear wave kinematic models. This is the reason that Morison's equation is used in most of the codes used to model fixed-bottom offshore wind turbines in relatively shallow water. However, when it comes to modelling of floating support structures, Morison's equation also has several disadvantages.

Morison's equation assumes that viscous drag dominates the drag loading, and that wave radiation damping can, therefore, be ignored. This assumption is only valid if the motions of the support structure are very small, which is usually the case for the fixed-bottom support structure. However, for floating platforms with low-frequency rigid modes, the support structure may experience significant movement, which means that wave radiation forces should be accounted for. The equation also neglects hydrostatic restoring forces; however, this can be dealt with by including additional terms to account for this.

Rainey's equation

Lighthill (1979; 1986b) showed that the inertia term of Morison's equation corresponds to the potential flow load in uniform cross flow only. It does not apply to the non-uniform flow conditions of waves. He showed (Lighthill, 1979) that the velocity gradients resulting from the flow non-uniformities produce a contribution to the potential flow load on a fixed vertical circular cylinder which does not decrease with the reduction in cylinder diameter. In terms of stokes expansion, this potential flow load from velocity gradients are of second order in wave height (Morison's inertia term being first order in wave height), like the Morison's drag term. Instead of using this term to describe them empirically, Lighthill proposed to replace Morrison's inertia term by the potential flow load calculated accurately to second order in wave height.

Rainey (1989) presented a derivation of an equation for the potential flow loading on a lattice-type structure moving partially immersed in waves. This new equation replaces the Morison's inertia term by allowing the drag term to describe the effects of vorticity exclusively. The equation calculates the potential flow wave load accurately to second order in wave height, which is an excellent improvement on Morison equation. Very complicated and computationally intensive methods can only seek such results. Moreover, the third order error is localised at the free surface intersection. Hence the equation remains attractive for fully nonlinear problems involving intermittent immersion of lattice members, which are currently beyond the most sophisticated computationally intensive methods. The primary reason for this large contrast in computational efficiency is the loads are derived from energy considerations rather than direct integration of surface pressures, which requires a lower level of flow detail for a given level of load calculation accuracy.

Rainey modified the inertia term of Morison's equation by including axial divergence and centrifugal force terms acting on the member cross-section and by introducing additional point loads at both the ends of the immersed member (see section 3.3.3). All these force components are nonlinear and do not appear in the conventional Morison equation. Several computational studies have been reported using this equation (Chitrapu, et al., 1998; Mekha, et al., 1996; Ma & Patel, 2001; Jagdale & Ma, 2012). All the results published by these authors demonstrated that the slowly varying surge and/or pitch motion might be much higher than the responses at the

incident wave frequency. It implied that the non-linear effect plays a vital role in motion analysis and the non-linear forces and moments need to be considered with great care.

One question that does arise in considering this equation is its accuracy when applied to the slender body. According to the derivation of Manners and Rainey (1992) and the discussion by Rainey (1989), the error in using this equation is of the order of $(D/L_0)^3$, where L_0 is wavelength and D is the member diameter. Thus, if the ratio (D/L_0) is small enough, the theory can be sufficiently accurate. Kim and Chen (1994) compared the results from this slender body equation with those from the diffraction analysis for the second order forces acting on a fixed articulated platform and showed that the slender body approximation could give very similar results to those of diffraction theory when a diameter of the structural member is small (less than 20%) relative to the wavelength. For the fully immersed slender body, this slender body equation is thought to be a correct potential flow solution to any order of fluid velocity and hence called as Non-Diffracting Potential Theory (NDPT) in this thesis and adopted for the wave force evaluation.

2.5.3 Mooring system loads

Mooring system is required to restrain the global movement of the platform under the action of wind, waves and currents. The mooring system dynamic is non-linear in nature and often include hysteresis effect. An accurate modelling of mooring line dynamic is, therefore, a complex problem and can be dealt with fully only by dedicated codes. The interaction of mooring lines with the floating platform can be approximated using force-displacement or quasi-static representation or by full dynamic modelling. A brief review of these methods is presented in this section.

2.5.3.1 Force-displacement representation

This is a common method for modelling foundations for fixed bottom offshore wind turbine where P-Y curves are used in the translational and rotational degrees of freedom to represent the force-displacement relationship in the soil. The method can also be used for floating wind turbines by applying non-linear spring stiffnesses in all six degrees of freedom at the fairlead position. Similarly, a damping matrix can also be included. In this method, the relevant force-displacement characteristics of the mooring system are calculated separately and added as input into the model. This method can also be extended to include a force-velocity relationship to account for mooring line drag.

The method enables the non-linear geometric restoring properties of the mooring system to be described in a single stiffness matrix, which has the advantage of simplicity and ease of implementation. However, in most cases, this method is limited since the loads are generally not specified as a function of displacement in all six degrees of freedom. Often restoring forces are specified as an independent function of each platform displacement, in which case important couplings can be missed. This can be avoided by modelling spring at each fairlead with load-

displacement data given in the discrete form and an intermittent data can be interpolated. Several existing floating wind turbine design tools follow this approach. For example, Bladed by Garrad Hassan, 3Dfloat by UMB and SIMO/RIFLEX by MARINTEK.

2.5.3.2 Quasi-static representation

In this approach, tension in each mooring line is evaluated using equations of static equilibrium, for a given platform displacement at an instantaneous time, without accounting drag and inertia of the mooring lines. This approach enables the properties of the mooring lines (i.e. length and extensional stiffness) to be provided as direct input to the system. This approach can also account for the non-linear geometric restoration of the complete mooring system, but with a full representation of the restoring forces as a function of the displacements in all degrees of freedom. This is because the restoring forces acting on the platform are calculated at each time step considering the contribution from the tension in each mooring line. Neglecting mooring line stiffness is rarely of any significance and ignoring mooring line inertia is justified by Jonkman (2009). Several existing floating wind turbine design tools follow this approach. For example, FAST by NREL, TimeFloat by Principle Power and ADAMS by MSC.

2.5.3.3 Full dynamic modelling

In this approach, an advanced numerical technique is required to solve the governing equations of motions for mooring line dynamics which are rather complicated and cannot be solved analytically. One approach is to discretise the line into point masses connected by weightless inextensible elements and solve the resulting ordinary differential equations using the finite difference method. A more general solution can also be found using the finite element method. Several discrete finite elements can be used to approximate a continuum, each with physical properties, and the differential equations for each element can be solved numerically to find the dynamics of the line. Both the methods are extremely computer intensive. There are several codes, mainly developed for the offshore oil and gas industries, which provide full models of the dynamics of the mooring lines for floating offshore structures. For example, Charm3D by Texas A&M University, SIMO/RIFLEX by MARINTEK and 3Dfloat by UMB.

The full dynamic modelling approach gives an accurate representation of the drag and inertia of mooring lines and their effect on the floating platform. These effects can be significant, especially in deep water where the mooring line is much less likely to take up its equilibrium shape instantly, and a quasi-static analysis is unable to predict the line tensions accurately. Therefore, for floating wind turbines with high drag mooring system in deep water, a full dynamic analysis of the mooring lines should be undertaken. Azcona et al. (2016) studied the influence of mooring line dynamics on the response of a floating wind turbine with three different platform concept such as semi-submersible, spar and tension leg platform. The fatigue and ultimate loads obtained for each platform design using a quasi-static and full dynamic modelling

were compared. The comparison revealed that the difference in blade and shaft loads predicted by both the methods for all the platforms were insignificant, for the tower, the difference in loads depends on platform geometry, and for mooring lines, the difference in line tensions were significant for all the platforms. For tension leg platform, a reduction in tower base loads and mooring line tensions were observed by full dynamic modelling as compared to quasi-static approach.

One limitation of this method is that it requires much more processing time than the alternatives, due to its complexity. This is a problem for offshore wind turbine design calculations, for instance as specified in IEC 61400-3, many simulations are required to fulfil the design criteria. The main objective of this thesis is to investigate the effect of nonlinear wave kinematic and force model on the global response of floating wind turbine, where quasi-static method is sufficient and hence adopted in the numerical model.

2.6 Existing wave models for predicting wave kinematics

Accurate prediction of wave kinematics (i.e., wave surface elevation and underlying water particle velocities and accelerations) are crucial in estimating the wave loads while using slender body equation in which the principal force components are drag and inertia forces. First is approximately proportional to flow speed square and the second to local fluid acceleration. The drag force is thus especially sensitive to errors in speed estimates in regions of high flow speeds, such as those near and above the mean water level. On the other hand, the calculated inertia forces are relatively sensitive to the high frequency (short) waves, and the flow due to these waves attenuates quickly with depth. Therefore, the wave surface and flow field underneath are particularly crucial while estimating wave force. Hence an appropriate wave theory shall be considered for wave modelling.

Based on the physical characteristics, waves can be divided into two main categories: steady and unsteady waves. The former denotes waves with permanent profiles over a spatial and temporal scale, and the latter represents waves with deformations such as dispersion, resonant interaction, modulation instability, overturning and breaking etc. Both the categories could be studied by using potential theories except for breaking, which is beyond the theoretical limits of the potential theories. Therefore, other approaches such as Navier-Stokes (NS) equation should be introduced. However, breaking waves is outside the scope of this research study and hence not discussed further. Next, a review on the potential wave models will be given in the below subsections.

2.6.1 Steady wave models

The steady wave model is often used to study the wave pattern, which is stationary to a moving frame. The steady wave model study began with an analytical solution based on some perturbation methods, where wave steepness is assumed to be small. Numerical techniques were

introduced later to improve accuracy since computer programming became popular within the research community. In this section, well known steady wave theories such as Airy's linear wave and Stokes nonlinear wave model will be briefly reviewed. The wave described by both the wave models is vertically symmetrical. As floating wind turbines will be installed in intermediate to deep water, a review on shallow water wave theories (i.e., cnoidal and solitary) is not relevant and hence excluded from the review.

2.6.1.1 Airy's linear wave model

A study on steady wave problem began in the 19th century, and since then linear theories are dominating. Some notable contributions were made by several British mathematicians, such as Airy (1845), Rayleigh (1876), Kelvin (1887), and Lamb (1916) etc., who systematically investigated the behaviour of linear waves. They had provided an approach to describe the motion of the free surface, which formed the basis for the potential theory. By assuming the fluid flow is inviscid, incompressible and irrotational, the Laplace equation is suggested to govern the body of fluid. Two surface boundary conditions, i.e., kinematic and dynamic were imposed to provide constraints to the problem. Since then the system has become popular and thereafter widely used as a theoretical framework to study the wave dynamics. The linear theories assumed that the wave amplitude is small so that the nonlinear terms existing in both the surface boundary conditions become insignificant and hence can be neglected. The linearized system can be easily solved, and the solution is straightforward which is discussed under section 3.3.2.1 thus details are omitted here for simplicity. The theory can be used to model regular as well as irregular waves.

The main advantage of linear theory over nonlinear ones is the potential to superimpose an infinite sum of wave harmonics, each with its amplitude, frequency, phase and direction, to simulate random sea. The wave kinematics at any given time and position can be found easily if one follows the work of Reid (1958). All wave components are then considered independent of one another, which implies that the vertical surface coordinate of a high-frequency component superimposed upon a lower one is the sum of both the components. An increased vertical displacement exaggerates the contribution of the high-frequency component to the velocity field. Velocities reach a maximum near the surface under the crests, so the application of linear superposition in this area leads to considerable overestimation. On the other hand, away from the surface, beneath the mean water level, the theory has been compared favourably with both laboratory and field data (Dean & Perlin, 1986). Reasonable agreement occurs at depth because the contribution of the high-frequency components decays rapidly with depth. This direct linear method is indeed inadequate near the surface under the crests. To overcome this difficulty several empirical stretching techniques have been proposed. Among all, the most popular ones are by Wheeler (1969) and delta stretching by Rodenbusch and Forristall (1986). Wheeler's approach implies that the surface velocities in a stretched system are equivalent to those at the mean water

level of an unstretched system. Thus, the velocity exaggeration near the surface is avoided. However, both laboratory and field data (Forristall, 1985) show that the method tends to underpredict velocities above the mean water level. In delta stretching approach, the partial derivative of the kinematic property at the surface applies up to the free surface. The error associated with this method is proportional to the height z. This method typically found to overpredict the velocity.

The background and history of linear wave theories, as well as the applications, can be found in books by Johnson (1997), Mei (1983) and Stoker (2011). Due to its simplicity and efficiency, linear wave theories have been successfully employed for modelling steady and unsteady waves of small amplitudes.

2.6.1.2 Stokes nonlinear wave model

The linear or small amplitude theory described in the preceding section provides a first approximation to the wave motion. To approach the complete solution, one may consider a perturbation procedure in which successive approximations are included. Such a method was used by Stokes (1847) and more recent contributions to the description of these stokes wave include those of De (1955), Borgman and Chappelear (1958), Bretschneider (1960), Skjelbreia and Hendrickson (1960), Tsuchiya and Yamaguchi (1972), Schwartz (1974), Cokelet (1977b), Schwartz & Vanden-Broeck (1979) and Rienecker & Fenton (1981).

Stokes (1847) came up with the remarkable nonlinear wave theory and unveiled the reason of asymmetric wave profile that exhibits a sharper peak and flatter trough in deep and finite water depth. However, stokes fifth order solution is limited in a situation where the wave steepness is large. To apply the Stokes wave theory for large steepness waves, Chappelear (1961) developed a numerical technique which could be applied to the desired order and was later improved by Dean (1965). Accurate numerical solutions for Stokes wave were also obtained by Schwartz (1974), Cokelet (1977b), Schwartz & Vanden-Broeck (1979), Rienecker & Fenton (1981), and Fenton (1985). Subsequently, Fenton (1988) came up with a fully nonlinear numerical solver and improved the accuracy of Stokes wave theory to the breaking limit, which could be applied for waves in general situations both in deep and finite water depth.

2.6.1.3 Suitability of steady wave models

Based on the previous works, Dean (1974) and Le Méhauté (1976) had discussed the applicability of the various theoretical models, i.e., the linear wave model and first to fifth order Stokes wave model for steady wave problems and suggested the boundaries between each models in terms of the wave steepness and water depth. Additionally, the fifth order Stokes wave (Fenton, 1985) and the fifth order cnoidal wave (Fenton, 1979) were compared, and their suitability was discussed by Fenton (1990). By using this guidance, researchers can determine which model should be employed according to the wave steepness and water depth for steady wave problems.

This guidance restricts each wave model in specific circumstances, beyond which they become inaccurate.

As pointed out by Stoker (2011), the basic nonlinear steady wave theories are not uniformly valid in the complete range of water depth. Also, the spike waves discovered in the deep water by Lukomsky et al. (2002a; 2002b), which have sharper crests in comparison with Stokes waves, cannot be explained by the aforementioned steady wave models. To develop a universal theory which is accurate for arbitrary depth and able to model spike waves, Clamond (2003) suggested a renormalized cnoidal wave theory, by introducing Fourier-Padé approximation. According to Clamond (2003), all the types of waves, i.e., the Stokes waves, cnoidal waves, solitary wave, as well as the newly discovered spike waves, can be represented by the renormalized cnoidal wave theory accurately.

Although these models are improved by introducing new techniques either theoretically or numerically, they are only applicable for solving steady wave problems. However, a wave is a stochastic process, and the random sea is unsteady without a permanent profile. It consists of a spectrum of wave components with different amplitudes, frequencies, and phase. The evolution of random sea involves very complicated physics such as linear dispersion of various components and the nonlinear wave-wave interaction that generates extreme wave surface significantly higher than predicted by linear wave theory as evidenced by field observations, (Kjeldsen, 1990; Sand, et al., 1990; Skourup, et al., 1996; Yasuda, et al., 1998), laboratory observations (Phillips, 1981; Stansberg, 1993; 1998a; Onorato, et al., 2006; Xia, et al., 2015), and the numerical simulations (Gibson & Swan, 2007; Goullet & Choi, 2011). These non-stationary features are very important for extreme wave analysis and cannot be modelled by using afore-mentioned steady wave models.

2.6.2 Unsteady wave models

Benjamin & Feir (1967) first found that the waves of finite amplitude were not able to remain stable in a permanent profile when generated in the wave tank. This phenomenon cannot be explained by using the Stokes wave theory alone. Soon after, they carried out the analysis to third order and realised that this phenomenon was due to the energy exchange between the carrier wave and its side-bands. Their discovery of the side-band instability emphasised the importance of studying the unsteady wave problems, in which the nonlinear effects are of utmost importance. Since the nonlinearities are very important for studying extreme wave in random seas, the higher order wave models are required. In this section, some well-known unsteady wave models are reviewed.

2.6.2.1 Second order wave models

The second order wave theories consider the nonlinear wave-wave interaction one order higher than the linear wave models and are often applied in a theoretical study of nonlinear

unsteady waves. It was Longuet-Higgins (1963) who came up with the second order statistical model to investigate the probability distribution of free surface elevation in a deep sea. An explicit expression of free surface considering additional second order corrections are given by Sharma & Dean (1979), Forristall (2000) and Toffoli, et al. (2006). The kinematics beneath an irregular wave surface can be determined using this theory which includes contributions of sum and difference frequencies added to the first order solution from the linear wave theory. Although the second order wave models consider the interaction between every two wave components, they are only accurate for small and moderate steepness waves. An extreme random sea always consists of large steepness wave with a narrow band spectrum of frequencies. In that case, the results given by second-order theory will be inaccurate as nonlinear effects higher than the second order cannot be neglected. The inadequacy of second-order theory for modelling nonlinear irregular wave is also confirmed by many researchers, e.g. Phillips (1981), Onorato et al. (2006), Gibson & Swan (2007), Ning et al. (2009). Hu and Zhao (1993) have numerically verified that the use of second-order random wave theory is appropriate only when the significant wave slope is less than about 0.02.

2.6.2.2 Nonlinear Schrödinger equations

Benjamin & Feir (1967) developed a third order wave model to investigate the modulation instability, which unveiled the importance to study the nonlinear wave-wave interaction. To examine the modulation instability of gravity waves in finite water depth, Whitham (1967) came up with the third order formulations for arbitrary depth and concluded that the wave train would remain unstable unless the characteristic water depth $k_0 d \leq 1.363$. Subsequently, Benjamin & Hasselmann (1967) validated this conclusion by using a very similar method as Benjamin & Feir (1967). Both of their studies are further confirmed by Phillips's investigations (Phillips, 1960; 1981) on resonant interaction. A recent and detailed review of the modulation instability and the related studies can be found in the annual review by Dias & Kharif (1999). More recently, the near-resonant interaction described by Benjamin & Feir (1967) was also considered in the statistical models for random waves, such as the investigation on the statistics of the crest (Gibson, et al., 2007) and kurtosis of deep water waves (Fedele, 2015). Such third order wave theories are fundamental as they contributed to the understanding of unsteady waves.

The nonlinear Schrödinger equation (NLSE) is a useful tool to study the dynamics of the gravity water waves in deep and finite water depth. There are several versions of NLSE have been developed. For example, third order weakly nonlinear equation derived by Zakharov (1968) referred as cubic NLSE, fourth order Dysthe equation by Dysthe (1979) which is one order higher than cubic NLSE and fourth order enhanced NLSE by Trulsen et al. (1999). Although versatile versions of NLSE have been suggested in the past, they are only accurate when both wave steepness and local bandwidth are small. Henderson et al. (1999) simulated travelling waves

based on the cubic NLSE and fully nonlinear Higher-Order BEM and concluded that there was an excellent agreement between the results of these two models only for waves with small initial steepness ($\varepsilon < 0.056$). Clamond, et al. (2006) investigated the evolution of the envelope soliton of initial steepness $\varepsilon = 0.091$ using the Enhanced NLSE-4 and their fully nonlinear approach separately. Through comparing the free surface profiles, they concluded that the former was only valid for a limited period at the beginning of the simulation before rogue waves are formed, which indicated that the Enhanced NLSE-4 is inaccurate when wave steepness becomes large, i.e., $\varepsilon \geq 0.21$. Toffoli et al. (2010) have simulated random directional wave field based on the modified Dysthe equation by Trulsen & Dysthe (1996) and the HOS method. By comparing the results obtained from these two models, they found discrepancies between them within the first 20 peak periods when the initial experimental steepness reached $\varepsilon = 0.16$. Slunyaev et al. (2013) have compared the analytical solution of the CNLSE with the numerical results of the Dysthe equation and the fully nonlinear Euler equations. They concluded that the CNLSE is not accurate for simulating waves evolving into its breaking limit, i.e., $\varepsilon \geq 0.42$. Hu et al. (2015) compared the breather solution to the CNLSE with numerical results based on the NS solver, in which it is found that the analytical solution for $\varepsilon = 0.22$ provides good agreement only within the first 20 peak periods.

2.6.2.3 Fully nonlinear wave model

Considering the significant nonlinearity associated with the extreme random sea and its effect on wave kinematics, it is necessary to consider fully nonlinear theories, which include general flow theory and fully nonlinear potential theory. The general flow theory is based on the Navier-Stokes (NS) and continuity equation, which includes the viscous and turbulent effects with or without considering compressibility of fluids. Both mesh based, and meshless methods have been attempted to solve such models. However, these models are computationally costly hence not considered in the present study. In the fully nonlinear potential theory (FNPT), the flow is assumed to be inviscid and irrotational. The equations are usually solved by the boundary element or desingularized boundary integral methods (BEM) and the finite element method (FEM). Many researchers have been contributing to the development of FNPT model for modelling steep extreme waves, e.g. Kashiwagi (2000), Tanizawa (2001), Wu and Eatock Taylor (2003), Koo and Kim (2004), Yan and Ma (2007), Ma and Yan (2009). A detailed review of the FNPT models for modelling nonlinear waves can be found in Ma and Yan (2009). Compared to the NS model, the computational efficiency of the FNPT models is relatively high as evidenced in Yan et al. (2015) who examined the computational robustness of the FNPT based method, the Quasi Arbitrary Lagrangian Eulerian Finite Element Method (QALE-FEM), with the general flow theory-based solver, OpenFOAM. Also, the comparisons between the FNPT results and the experimental data (Yan & Ma, 2007; Ma & Yan, 2009) has shown that model is sufficiently

accurate in many cases where viscosity plays an insignificant role (for steep non-breaking waves). However, the reliability of these numerical models based on FNPT relies on the accuracy of wave generation.

There are three ways to generate waves in the fully nonlinear wave simulation practices. The first one is to specify an inlet boundary condition, where the wave elevation, velocity (or velocity potential) and the pressure (or the time derivative of velocity potential) are specified by either analytical solutions based on linear or 2nd order wave theories or results from other FNPT model. This method is usually adopted by CFD software, hybrid models combining the FNPT and CFD software, e.g. Yan and Ma (2010), Sriram, Ma and Schlurmann (2014), Hildebrandt and Sriram (2014), who uses the FNPT model to provide the inlet conditions to the general flow solver. The second one is to specify the initial wave surface together with a periodic state on the lateral boundaries, e.g. Adcock et al. (2011) and has been applied by FNPT models. Another popular way is to generate the waves using a wavemaker, the same as in the laboratory experiments, e.g. Kashiwagi (2000), Tanizawa and Minami (2001), Yan and Ma (2007), Ma and Yan (2009), and the meshless methods in Lagrangian view, e.g. Ma (2007) and Zhou and Ma (2010). The FNPT has been proved to be reliable to generate non-breaking incident waves using the wavemaker. Its results agree well with the experimental data if the same wave paddle signals as in the corresponding experiments are adopted (Sriram, et al., 2013; Hildebrandt & Sriram, 2014; Yan, et al., 2015).

2.6.3 Generation of Extreme Wave

In the laboratory or numerical simulation, an extreme wave is being simulated using a realistic wave spectrum (e.g., JONSWAP spectrum) with a random phase approach. This rare event would happen only once in approximately 3000 waves according to a Rayleigh wave height distribution. Therefore, this method is not often adopted for generating an extreme wave in a wave tank. Alternatively, spatial-temporal focusing of a wave group has been widely used to generate an extreme or breaking wave in the laboratory (Ning, et al., 2009; Sun, et al., 2009; Li , et al., 2008; Liu & Hong, 2004; Baldock, et al., 1996; Rapp & Melville, 1990). However, based on the Longuet-Higgins (1952) wave model, Kriebel (2000) proposed an efficient procedure for the generation of an extreme wave by embedding it within a random sea; Pei (2007) discussed the relationship between H_{max}/H_s and the energy percentage within the combined wave model (Kriebel , 2000). Zhao et al. (2009) summarised four-wave focusing model for the generation of an extreme wave by combining extreme wave model with regular and random wave model. The wave focusing models mentioned above can generate the extreme waves in finite space and time successfully. Nevertheless, the previous studies on the formation of extreme waves based on Longuet-Higgins (1952) wave model have raised some questions. First, while the combined wave model is an efficient procedure for the generation of extreme waves (Kriebel , 2000), how much

energy must go into each portion of the sea state to produce an extreme wave having a height greater than two times the significant wave height. If nearly all the spectral energy is required to produce a highly nonlinear extreme wave, then combined superposition would be an unlikely mechanism for the generation of such waves at sea, because the simulation results will be unrealistic; and this shortcoming also applies to phase modulation focusing model by Zhao et al. (2009). Second, because of the randomness of initial phases, the efficiency of the combined wave model for the generation of extreme waves is not so high. Finally, the methodologies taken by focusing models of phase modulation are out of accord with the initial random phases distributed in $(0, 2\pi)$ according to the Longuet-Higgins (1952) wave model theory. This thesis considered these issues while generating extreme waves in a numerical wave tank. Wave are generated without altering components derived from spectra, on large space and time scale, allowing nonlinear self-focusing of wave groups through amplitude dispersion effect. This procedure will not only keep the statistical properties of the wave train and the structure of the target wave spectrum but also make the initial random phases distribute in $(0, 2\pi)$ and generate extreme waves at certain time and space.

2.7 Main contribution and objectives of the study

After reviewing advancements in the offshore wind industry, it is found that the floating wind turbine is potentially a highly scalable future energy source for countries having moderately deep sea (50m to 200m), where the wind resource is abundant, and the NIMBY opposition is nil. Tension leg platform is found to be the most promising concept to deploy wind turbines in such water depths. Although natural periods of such floating system are far away from the predominant wave period range, the non-linear effect can give rise to force components at their natural frequencies, and even if these components are small their effect on the dynamic response can be significant. The wave-induced responses of a tension leg platform usually consist of four categories of responses, i.e., first order motions at wave frequency, low-frequency surge, sway and yaw motion, high-frequency heave, roll and pitch motion, and steady drift. After reviewing and comparing existing wave kinematic modelling and force evaluation techniques, it is found that the fully nonlinear potential theory (FNPT) for wave kinematic modelling and non-diffracting potential theory (NDPT) for wave force evaluation are suitable to study these responses to extreme waves.

The main contribution of this thesis is to formulate an integrated numerical model to simulate responses of floating wind turbine to extreme waves, in which the wave kinematics are calculated using fully nonlinear potential theory (FNPT), wave forces are computed using non-diffracting potential theory (NDPT), and the wind turbine and motions of the floating platform are fully coupled. The results predicted using this model are used to demonstrate the effect of FNPT wave kinematic model and NDPT wave force model on the prediction of the afore-mentioned wave

induced responses of a chosen tension-leg-platform wind turbine. An effect of FNPT wave kinematic model is investigated by comparing these responses with the most commonly used analytical wave kinematic models, i.e. Airy's linear wave theory with wheeler's stretching approximation and Fenton's nonlinear steady wave theory. Similarly, an effect of the NDPT wave force model is investigated by comparing these responses with the conventional Morison's force equation.

Like the hydrodynamic model, after reviewing and comparing existing wind and mooring force evaluation methods, it is found that the blade element and momentum theory for wind force evaluation and quasi-static representation for mooring load estimation are suitable for the present study. All are evaluated considering the interaction between the wind turbine, tower, floating platform and the mooring system. In the numerical model, the whole floating wind turbine system is considered as a rigid body system. The wind turbine rotor, tower, and floating platform are considered as a rigid part of the whole rigid body system. An effect of rotating blades and its operating controls are considered, but blade and tower's flexibility are not included.

As the main aim of the present study is to develop an integrated model to study the global responses of a TLPWT to extreme waves, it includes the following tasks:

- To develop a theoretical basis for modelling floating wind turbine dynamics which includes the definition of equations of motions and the various external forces acting on it.
- To develop a numerical procedure for solving the equations of motions.
- To validate the numerical model using published experimental results.
- To assess the effect of the nonlinear wave kinematic model (FNPT) on the global response of a chosen tension-leg-platform wind turbine in an extreme regular, bichromatic and random wave group.
- To assess the effect of the nonlinear wave force model (NDPT) on the global response of a chosen tension-leg-platform wind turbine which includes, first order motions at wave frequency, low-frequency or slowly varying motions, and high-frequency ringing and springing motions.

2.8 Outline of the thesis

Chapter-1 presented the research background with motivation and the problems identified with the existing numerical tools for simulating responses of floating wind turbine to extreme waves. Chapter-2 provides the review of literature which began with recent advancement in the offshore wind industry with future market potential for floating wind turbine technologies and identifies the most promising floating wind turbine concept for the present study. The review continues with the existing mathematical models, force evaluation and wave kinematic modelling techniques relevant to the development of an integrated numerical model. The mathematical

model developed for simulating responses of a chosen tension-leg-platform wind turbine, which consists of formulation for equations of motions and the various forces acting on it are presented in the Chapter-3 whereas numerical procedure developed for solving the equations of motions is presented in Chapter-4. Chapter-5 presents the validation of the numerical model with the published experimental results followed by the discussion on convergence tests performed for the numerical model. Chapter-6, -7 and -8 presents the effect of nonlinear wave kinematic model (FNPT) on the global response of a chosen tension-leg-platform wind turbine subjected to extreme regular, bichromatic and random waves respectively. Similarly, Chapter-9 presents the effect of nonlinear wave force model (NDPT) on the global response of a chosen tension-leg-platform wind turbine. Chapter-10 presents the conclusions drawn from the study and recommendations for the future work.

3 INTEGRATED NONLINEAR MODELLING OF FLOATING WIND TURBINE

This chapter describes the mathematical model developed for simulating global responses of a floating wind turbine. Emphasis is given to the moored structure since the chosen floating wind turbine belongs to this group of offshore structure. The equations of motions and the formulation developed for modelling various loads considered under this research study are presented in this chapter. The combined wind turbine and its floating support, i.e., tension leg platform, have been referred as TLPWT (Tension Leg Platform Wind Turbine) system throughout this thesis.

3.1 Mathematical model

3.1.1 Definition of motions and reference axis system

The structural model of the TLPWT system is represented by a rigid body with six degrees of freedom in three-dimensional (right handed) X-Y-Z plane, with its origin at its centre of gravity. The motions are defined by,

Three translations of the structure's centre of gravity in X-, Y- and Z-axis:

- surge in the longitudinal X-direction,
- sway in the lateral Y-direction
- heave in the vertical Z-direction

Three rotations about these axes:

- roll about X-axis
- pitch about Y-axis
- yaw about Z-axis

Both, translational and rotational motions are positive in the direction of the axis system. These definitions of motions and the corresponding reference axis system for the chosen TLPWT system is illustrated in Figure 3.1.1.

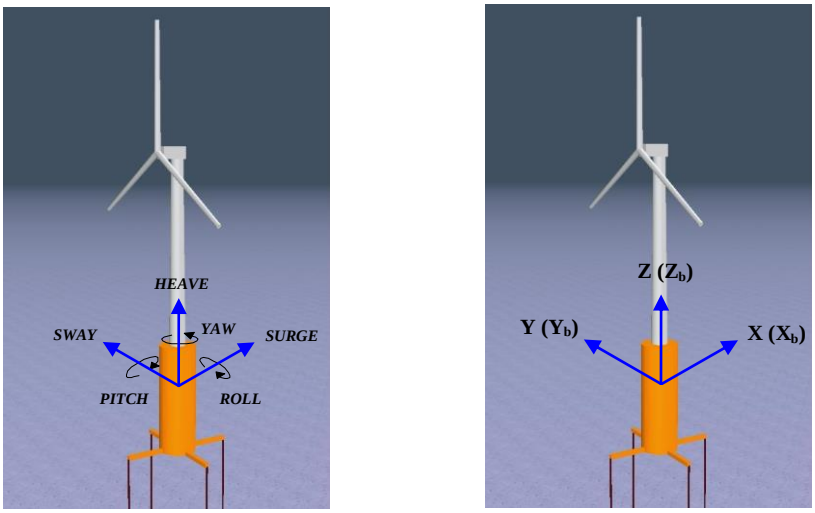

Figure 3.1.1 Modes of motions and reference axis system

The following reference axis system is followed for defining forces and resulting motion responses of TLPWT system.

- Space-fixed axis system (g-system) – This is an inertial axis system located at the centre of gravity of structure. The origin of this axis system coincides with the structure's centre of gravity when it is at rest.
- Body-fixed axis system (b-system) – This axis system has its origin always at the structure's centre of gravity and hence moves with the structure with respect to an above-mentioned inertial axis system.
- Member-bound axis system (m-system) – This axis system is fixed for each member with its x-axis along its length. This axis system is used for calculating local member forces.
- Wind and Wave reference axis system (w-system) – This axis system is like a space-fixed axis system but located on the still water level with its x-axis along the direction of the wind and/or wave propagation. Wind velocities and wave kinematics are computed in this axis system.

Details of the transformation between these axes system are given in APPENDIX A.

3.1.2 Equations of motions

A floating wind turbine is considered as a rigid body and the equations expressing their translational ($\vec{X}$) and rotational $(\vec{\theta})$ motions are formulated using Newton and Euler's law of motions respectively. The translational and rotational motion equations given in Eq. (3.1.1) and Eq. (3.1.2) are obtained by equating total external force and moment acting on the structure to the rate of change of linear and angular momentum respectively.

$$\frac{d\vec{P}}{dt} = \vec{F} \tag{3.1.1}$$

$$\frac{d\vec{L}}{dt} = \vec{N} \tag{3.1.2}$$

where,

$\vec{P}$ = linear momentum of the body at its centre of gravity

$\vec{F}$ = total external force acting on the body at its centre of gravity

$\vec{L}$ = angular momentum of the body about its centre of gravity

$\vec{N}$ = total external moment acting on the body about its centre of gravity

Linear momentum $\vec{P}$ of the body is given by,

$$\vec{P} = M\overrightarrow{U_c} \tag{3.1.3}$$

where, M is total mass of the body and $\overrightarrow{U_c}$ is velocity of the body at its centre of gravity.

The total velocity $\vec{U}$ at any point on the body can be written as:

$$\vec{U} = \overrightarrow{U_c} + \vec{\Omega} \times \overrightarrow{r_b} \tag{3.1.4}$$

where $\overrightarrow{r_b}$ is a vector from the centre of gravity to the point of consideration and $\vec{\Omega}$ is angular velocity around the centre of gravity.

For practical use, Eq. (3.1.1) needs to be expressed in matrix form with elements composed of projected components of vectors. Hence it can be re-written as,

$$[M]\begin{Bmatrix}\frac{dU_{c,x}}{dt}\\ \frac{dU_{c,y}}{dt}\\ \frac{dU_{c,z}}{dt}\end{Bmatrix}=\begin{Bmatrix}F_x\\ F_y\\ F_z\end{Bmatrix} \tag{3.1.5}$$

where, $U_{c,x}$, $U_{c,y}$ and $U_{c,z}$ are the components of $\overrightarrow{U_c}$ in x, y and z direction respectively and $[M]$ is a diagonal matrix, whose diagonal entries are all equal to the total body mass M.

The derivatives of the velocities with respect to time can be related to the translational displacement of the centre of gravity of structure in the space-fixed axis system by:

$$\left[\frac{dU_{c.x}}{dt},\frac{dU_{c.y}}{dt},\frac{dU_{c.z}}{dt}\right]=\left[\frac{d^2x_c}{dt^2},\frac{d^2y_c}{dt^2},\frac{d^2z_c}{dt^2}\right] \tag{3.1.6}$$

$$\overrightarrow{U_c}=\frac{d\vec{X}}{dt} \tag{3.1.7}$$

Angular momentum $\vec{L}$ in Eq. (3.1.2) is defined as,

$$\begin{aligned}\vec{L} &= \iiint_{\Xi}\overrightarrow{r_b}\times\left(\overrightarrow{U_c}+\vec{\Omega}\times\overrightarrow{r_b}\right)dm\\ &= \iiint_{\Xi}\overrightarrow{r_b}\times\overrightarrow{U_c}\,dm+\iiint_{[I]}\overrightarrow{r_b}\times\vec{\Omega}\times\overrightarrow{r_b}\,dm\\ &= \iiint_{\Xi}\left[|\overrightarrow{r_b}|^2\,\vec{\Omega}\;-\overrightarrow{r_b}\cdot\left(\vec{\Omega}\cdot\overrightarrow{r_b}\right)\right]dm\end{aligned} \tag{3.1.8}$$

where Ξ, is the space occupied by the mass of body,

The components of $\vec{L}$ in the moving system can be derived from equation (3.1.8) as,

$$L_i=\sum_{j=1}^{3}I_{ij}\,\Omega_j \qquad (i=1,2,3) \tag{3.1.9}$$

where 1, 2 and 3 correspond to x_b, y_b and z_b axis respectively; and I_{ij} are the moment of inertia defined as,

$$I_{ij}=\iiint_{\Xi}\left[\delta_{ij}\sum_{k=1}^{3}{x_{bk}}^2-x_{bi}x_{bj}\right]dm \qquad (i,j=1,2,3) \tag{3.1.10}$$

where $\delta_{ij} = \begin{cases} 1 & i = j \\ 0 & i \neq j \end{cases}$ and $r_b = x_b i_b + x_b j_b + x_b k_b$ has been used, with (i_b, j_b, k_b) representing the unit vectors in the x_b, y_b and z_b direction respectively.

It is noted that I_{ij} is independent of time and therefore need only to be evaluated once. This is the main advantage for expressing equation (3.1.2) in terms of moving body- fixed axis system. However, one should bear in mind that the time derivative in equation (3.1.2) has a more complicated form in the body-fixed axis system. This time derivative is determined using the following relationship (Marion, 1965).

$$\frac{d\vec{L}}{dt} = \frac{d\vec{L}}{d_b t} + \vec{\Omega} \times \vec{L} \tag{3.1.11}$$

where $\frac{d\vec{L}}{d_b t}$ represents the time derivative in the moving body-fixed axis system.

This equation is valid for any vector, hence similarly for the angular velocity, we have:

$$\frac{d\vec{\Omega}}{dt} = \frac{d\vec{\Omega}}{d_b t} + \vec{\Omega} \times \vec{\Omega} = \frac{d\vec{\Omega}}{d_b t} \tag{3.1.12}$$

This means that the time derivative of the angular velocity is the same in both space and body fixed axis system. Substituting equation (3.1.9) into equation (3.1.11) gives:

$$\frac{dL_i}{dt} = \sum_{j=1}^{3} I_{ij} \frac{d\Omega_j}{dt} + \sum_{j,k,l=1}^{3} \mathcal{E}_{ijk}\, \Omega_j I_{kl} \Omega_l \qquad (i = 1,2,3) \tag{3.1.13}$$

where,

$$\mathcal{E}_{ijk} = \begin{cases} 0, & for\ any\ equal\ indices \\ +1, & if\ i,j,k\ form\ an\ even\ permutation\ of\ 1,2,3 \\ -1, & if\ i,j,k\ form\ an\ odd\ permutation\ of\ 1,2,3 \end{cases} \tag{3.1.14}$$

Equation (3.1.2) can now be rewritten in matrix form as,

$$\begin{Bmatrix} \sum_{j=1}^{3} I_{1,j} \frac{d\Omega_j}{dt} + \sum_{j,k,l=1}^{3} \mathcal{E}_{1jk} \Omega_j I_{kl} \Omega_l \\ \sum_{j=1}^{3} I_{2,j} \frac{d\Omega_j}{dt} + \sum_{j,k,l=1}^{3} \mathcal{E}_{2jk} \Omega_j I_{kl} \Omega_l \\ \sum_{j=1}^{3} I_{3,j} \frac{d\Omega_j}{dt} + \sum_{j,k,l=1}^{3} \mathcal{E}_{3jk} \Omega_j I_{kl} \Omega_l \end{Bmatrix} = \begin{Bmatrix} N_1 \\ N_2 \\ N_3 \end{Bmatrix} \tag{3.1.15}$$

where, the N_i represent the moment components relative to the moving system.

The governing equations (3.1.5) and (3.1.15) have been written in two different axis system, and therefore the transformation linking these two systems is required. It has the following form (Refer APPENDIX A.1).

$$\begin{Bmatrix} x_g \\ y_g \\ z_g \end{Bmatrix} = \begin{Bmatrix} x_c \\ y_c \\ z_c \end{Bmatrix} + [T_{bg}] \begin{Bmatrix} x_b \\ y_b \\ z_b \end{Bmatrix} \tag{3.1.16}$$

Here $[T_{bg}]$ is the transform matrix defined as:

$$[T_{bg}] = \tag{3.1.17}$$

$$\begin{bmatrix} cos\,\beta\,cos\,\gamma & -cos\,\beta\,sin\,\gamma & sin\,\beta \\ sin\,\alpha\,sin\,\beta\,cos\,\gamma + cos\,\alpha\,sin\,\gamma & -sin\,\alpha\,sin\,\beta\,sin\,\gamma + cos\,\alpha\,cos\,\gamma & -sin\,\alpha\,cos\,\beta \\ -cos\,\alpha\,sin\,\beta\,cos\,\gamma + sin\,\alpha\,sin\,\gamma & cos\,\alpha\,sin\,\beta\,sin\,\gamma + sin\,\alpha\,cos\,\gamma & cos\,\alpha\,cos\,\beta \end{bmatrix}$$

where $(\alpha\ \beta\ \gamma)$ are Euler angles. The angular velocity can be expressed in terms of the Euler angles as (see A.3 in APPENDIX A):

$$\vec{\Omega} = \begin{Bmatrix} \Omega_1 \\ \Omega_2 \\ \Omega_3 \end{Bmatrix} = \begin{Bmatrix} \dot{\alpha}\cos\beta\cos\gamma + \dot{\beta}\sin\gamma \\ \dot{\beta}\cos\gamma - \dot{\alpha}\cos\beta\sin\gamma \\ \dot{\gamma} + \dot{\alpha}\sin\beta \end{Bmatrix} \tag{3.1.18}$$

It is noted that the translational velocity $\overrightarrow{U_c}$ and the angular velocity $\vec{\Omega}$ can be evaluated from equations (3.1.5) and (3.1.15) once the forces and moments are known. The coordinate (x_c, y_c, z_c) and the Euler angles (α, β, γ) can then be found from equations (3.1.7) and (3.1.18) respectively, thus enabling the position and orientation of the body to be determined.

These equations can be summarized as follows,

$$[M]\frac{d\overrightarrow{U_c}}{dt} = \vec{F} \tag{3.1.19}$$

$$[I]\frac{d\vec{\Omega}}{dt} + \vec{\Omega} \times [I]\vec{\Omega} = \vec{N} \tag{3.1.20}$$

$$\frac{d\vec{X}}{dt} = \overrightarrow{U_c} \tag{3.1.21}$$

$$[B]\frac{d\vec{\theta}}{dt} = \vec{\Omega} \tag{3.1.22}$$

where, $\vec{F}$ is the total external force, $\vec{N}$ is the moment of $\vec{F}$ about the centre of gravity, $[M]$ and $[I]$ are the mass and inertia matrix, respectively and $[B]$ is a transformation matrix relating angular velocities to time derivatives of Euler angles (α, β, γ) defined in Eq. (3.1.18).

$$[B] = \begin{bmatrix} \cos\beta\cos\gamma & \sin\gamma & 0 \\ -\cos\beta\sin\gamma & \cos\gamma & 0 \\ \sin\beta & 0 & 1 \end{bmatrix} \tag{3.1.23}$$

For convenience, the translational motions in Eqs. (3.1.19) and (3.1.21) have been written in terms of components of vectors in the space-fixed axis system while the rotational motions in Eqs. (3.1.20) and (3.1.22) have been written in terms of components in the body fixed axis system. Therefore, all the non-diagonal entries in matrices $[M]$ and $[I]$ are zero and $I_{11} = I_{22}$ if the distribution of the mass is axis-symmetric. Furthermore, the floating wind turbine may have an initial translational and angular displacement due to the wind forces acting on the turbine rotor and its supporting tower. That means nonlinear term appearing in Eq. (3.1.20) $\vec{\Omega} \neq 0$, hence, $\vec{\Omega} \times [I]\,\vec{\Omega} \neq 0$ and the motions may be of six degrees of freedom.

3.1.3 Loads acting on floating wind turbine

The total external forces and moments acting on the floating wind turbine system considered under this study are due to gravity, buoyancy, wind (aerodynamic), waves and current (hydrodynamic) and mooring lines (restoring) as illustrated in Figure 3.1.2.

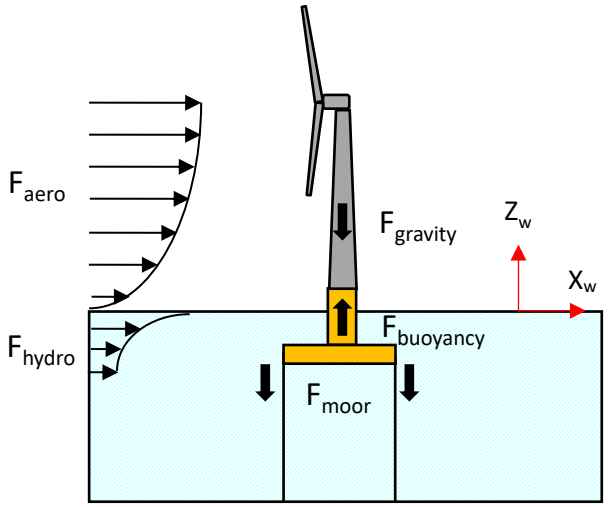

Figure 3.1.2 Loads considered in the current study

The total external force $\vec{F}$, and moment $\vec{N}$, appearing on the right-hand side of Eq. (3.1.19) and (3.1.20) can be written as,

$$\vec{F} = \overrightarrow{F_{gravity}} + \overrightarrow{F_{aero}} + \overrightarrow{F_{hydro}} + \overrightarrow{F_{moor}} \tag{3.1.24}$$

$$\vec{N} = \overrightarrow{N_{gravity}} + \overrightarrow{N_{aero}} + \overrightarrow{N_{hydro}} + \overrightarrow{N_{moor}} \tag{3.1.25}$$

where, $\overrightarrow{F_{gravity}}$ and $\overrightarrow{N_{gravity}}$ are forces and moments due to gravity; $\overrightarrow{F_{aero}}$ and $\overrightarrow{N_{aero}}$ are excitation forces and moments due to wind acting on the turbine rotor and its supporting tower; $\overrightarrow{F_{hydro}}$ and $\overrightarrow{N_{hydro}}$ are excitation forces and moments due to waves and current acting on the floating platform that also includes buoyancy effect. $\overrightarrow{F_{moor}}$ and $\overrightarrow{N_{moor}}$ are restoring forces and moments due to mooring lines.

For floating wind turbine system, wind forces acting on the turbine rotor and its supporting tower may affect the motions of its floating support system, and subsequently mooring line tension. In return, the motions of the floating support system due to waves and current may affect the wind forces acting on the turbine rotor and tower. This interaction effect needs to be considered while evaluating forces and moments in Eq. (3.1.24) and Eq. (3.1.25). The following section presents the formulation developed for evaluating forces and moments due to wind, wave, current and mooring system considering interaction effect among wind turbine, tower, platform and mooring system.

3.2 Aerodynamic model

The loads due to wind primarily acts upon turbine rotor, T and its supporting tower dT_{drag} as illustrated in Figure 3.2.1.

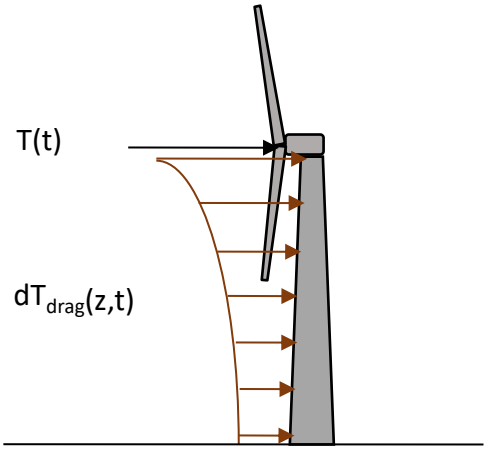

Figure 3.2.1 Aerodynamic Loads

The load acting on the turbine rotor, T is determined using classical blade element and momentum theory whereas load acting on the tower, dT_{drag} is determined using the quadratic drag force equation. Although the method used for determining these loads are relatively simple, it has opted to couple this to the platform motions. To do such coupling, the load determination process is altered to accommodate the influence of platform motions. The wind loading mainly depends upon incoming wind velocity, and therefore the effect of platform motions on this velocity is captured in terms of relative wind velocity seen by the turbine and its supporting tower. The procedure to calculate wind loading can be divided into the following stages,

- Defining wind regime
- Selecting appropriate wind spectra, and
- Applying an appropriate wind load calculation method

3.2.1 Wind regime

Wind is the primary source of external load affecting the structural integrity of the turbine and its supporting tower. Therefore, it is imperative for the designer to describe the wind regime accurately. Various parameters concerning wind need to be known are mean wind speed, variation about the mean in short-term (gust), daily, seasonal and annual, and variation with height and direction. These parameters are highly site-specific and can only be determined with enough accuracy by measurements at a site for a sufficiently long period.

3.2.1.1 Wind Shear Profile

The variation of mean wind speed with respect to height is termed as wind shear. The surface roughness of sea resists the air flow close to its surface where wind speed tends to be zero. To describe this shear effect on the mean wind speed at a certain elevation, two main models are

commonly employed: logarithmic and power law. The logarithmic model is considered to be more reliable than power law in the lowest 10m to 20m of the planetary boundary layer. For 20m to 100m, both the models can produce a reasonable prediction of wind speed in neutral atmospheric condition. For 100m to near the top of the atmospheric boundary layer, the power law produces a more accurate prediction of wind speed. Both the wind speed profile models are described in Eq. (3.2.1) and (3.2.2).

Logarithmic
$$\overline{V_w}(z) = \overline{V_w}(z_r)\frac{ln\left(\frac{z}{z_0}\right)}{ln\left(\frac{z_r}{z_0}\right)} \tag{3.2.1}$$

or

Power law
$$\overline{V_w}(z) = \overline{V_w}(z_r)\left(\frac{z}{z_r}\right)^{\propto_{shear}} \tag{3.2.2}$$

where,

$\overline{V_w}(z)$	=	mean wind speed at height 'z'
$\overline{V_w}(z_r)$	=	mean wind speed at reference height 'z_r'
z_r	=	reference height
z_0	=	surface roughness length
$\propto_{shear}$	=	power law coefficient

DNVGL-RP-C205 (2017) recommends a typical value of z_0 as 0.0001-0.01 and $\propto_{shear}$ as 0.12 for open sea with waves.

3.2.1.2 Wind Turbulence

Wind speed varies in space as well as time due to gust or turbulence which is an inherent feature of the atmospheric mixing process and the surface friction to which wind flow is subjected to. A typical wind speed distribution is shown in Figure 3.2.2. This unsteady nature of the wind can be described either by gust factor or by power spectrum and turbulence intensity.

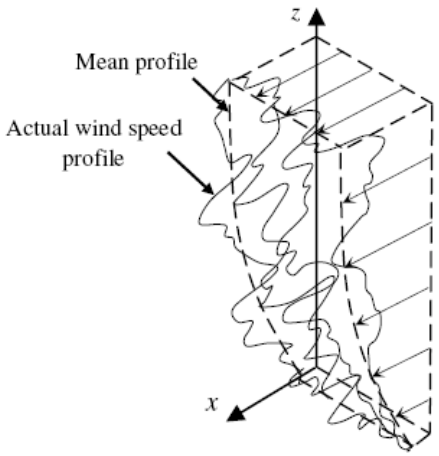

Figure 3.2.2 Wind Speed Profile (Kühn, et al., 2017)

To capture the effect of turbulence, wind speed is described as a superposition of a steady (mean) wind speed $\overline{V_w}(z)$ and a varying turbulent wind speed which can be described by a

turbulence intensity I_{turb}, and a power spectral density $S(f)$. The turbulence intensity I_{turb} is a characterization of the overall level of turbulence and is defined as,

$$I_{turb} = \frac{\sigma_{V_w}}{\overline{V_w}(z)} \tag{3.2.3}$$

where, σ_{V_w} is the standard deviation of the variation of wind speed about its mean $\overline{V_w}(z)$, which is generally taken as 10-minute average. This intensity only captures non-temporal information (height, roughness at the surface, etc.) and could be interpreted to form the boundary condition for the temporal fluctuation. The temporal information of the turbulence (e.g. the frequency of wind speed fluctuation) is captured in the turbulence power spectral density function $S(f)$, from which a wind speed time series can be constructed.

In literature, several turbulence spectra are available, e.g. Kaimal, et al. (1972). From this spectrum, a wind speed time series can be constructed to determine the aerodynamic loading over time. One of the mathematical procedure to determine this time series is a harmonic series method. This method involves the summation of a series of cosine waves at various angular frequencies (ω_i) with weighted amplitude in line with the spectrum definition, covered in Eq. (3.2.4). By doing so, a time series of wind speed can be developed.

$$V_w(z,t) = \overline{V_w}(z) + \sum_{n=1}^{N_c} \sqrt{2\, S(f_i)\, \Delta f_i}\, \cos(\omega_i t - \emptyset_i) \tag{3.2.4}$$

where ω_i is the angular frequency corresponding to frequency f_i, $\emptyset_i$ is the phase angle at frequency f_i, modelled as a random number between 0 to 2π and $S(f_i)$ is the power spectral density. However, in this thesis our aim is to study the effect of nonlinearity associated with the hydrodynamic model, hence the mean wind speed profile is considered.

3.2.2 Effect of platform motions on wind load

The wind loading depends mainly on the incoming wind speed $V_w(z,t)$ and therefore the effect of platform motions on the wind speed is captured in terms of relative wind speed $V_{w,rel}(z)$ seen by the turbine and tower at each instant of time t.

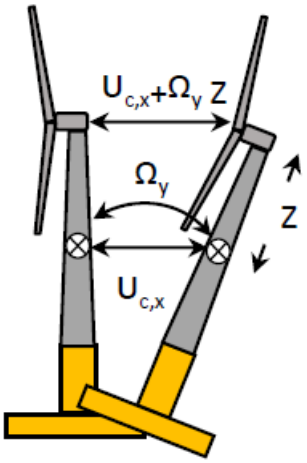

Figure 3.2.3 Effect of platform motions on relative wind speed

Looking at the schematic representation illustrated in Figure 3.2.3, the motions of interest here are the translational surge/sway and rotational roll/pitch, since they both contribute to the horizontal movement along the tower length. The relative wind speed for which the wind loads are to be determined at each instant of time, t is given by,

$$V_{w,rel}(z) = V_w(z) - U(z) \tag{3.2.5}$$

where,

$V_w(z)$ = variation of wind speed over height, Eq. (3.2.1) or (3.2.2)

$U(z)$ = velocity of platform at point of interest which is further defined as, $\overrightarrow{U_c} + \vec{\Omega} \times \vec{z}$

Hence, the total velocity of platform at 'z' in the matrix form can be written as,

$$\begin{Bmatrix} U_x \\ U_y \\ U_z \end{Bmatrix} = \begin{Bmatrix} U_{c,x} + z\,\Omega_y \\ U_{c,y} - z\,\Omega_x \\ U_{c,z} + 0 \end{Bmatrix} \tag{3.2.6}$$

where, $\overrightarrow{U_c}$ is velocity of structure at its centre of gravity, $\vec{\Omega}$ rotational velocity of platform and $\vec{z}$ is point of interest (for example, hub height for wind turbine and element location for tower).

This relative velocity is used while evaluating wind loading acting on the turbine and its supporting tower and detailed in the subsequent sections.

3.2.3 Loads on turbine

Wind flowing through the rotor blades produces lift and drag force on its cross-sectional element which combined results in a torque on the rotor and thrust along the rotor axis. The torque determines power extracted by the wind turbine whereas thrust determines the loads acting on the turbine rotor. The aerodynamic thrust acting on the turbine rotor induces two types of loads on the floating wind turbine: a point load, T at top of the tower and its moment around the centre of gravity of the structure.

The classical Blade Element Momentum (BEM) theory by Glauert (1935), who combined blade element theory and momentum theory, is used for determining the aerodynamic thrust acting on the wind turbine rotor. Blade element theory assumes that the blades can be divided spanwise into small elements that act independently of adjacent elements and operate aerodynamically as two-dimensional aerofoils whose aerodynamic forces can be calculated based on the local flow condition. These elemental forces are summed up along the span of the blade to calculate the total force and moment exerted on the turbine. The other half of BEM, the momentum theory, assumes that the loss of pressure or momentum in the rotor plane is caused by the work done by the airflow passing through the rotor plane on the blade elements. Using the momentum theory, one can calculate the induced velocities from the momentum lost in the flow in axial and tangential directions. These induced velocities affect the inflow in the rotor plane and, therefore, also affect the forces calculated by the blade element theory. The coupling of these

two theories sets up an iterative process to determine the induced velocities near the rotor and subsequently aerodynamic forces.

The aerodynamic forces acting on the turbine rotor mainly depends upon wind speed and the turbine's control strategy, (i.e., by controlling rotor speed and blade pitch angle). However, its dependence on wind speed is a dependence on the relative wind speed at the hub as it moves along with the supporting floating platform under the action of ocean waves and current. A formulation developed based on BEM theory to model the aerodynamic force acting on the wind turbine rotor accounting relative wind speed at the hub are presented in this section. With this method, it is possible to calculate the loads from wind turbine for the given wind speed and the corresponding settings of rotor's rotational speed and blade pitch angle.

Blade Element and Momentum Theory

The BEM theory is implemented by dividing the blade of a wind turbine into a finite number of elements along its length. As these elements rotate in the rotor plane, they trace out an annular region, shown in Figure 3.2.4, across which the momentum balance takes place.

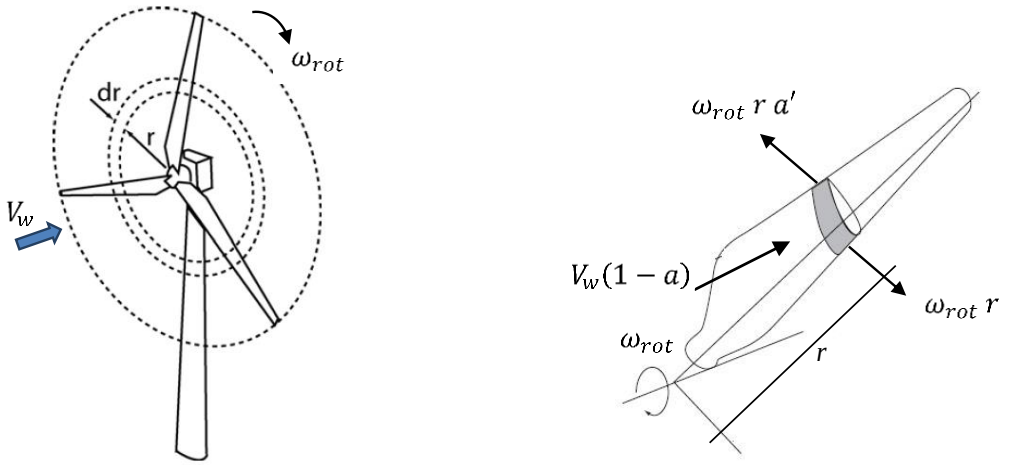

Figure 3.2.4 Annular plane used in BEM theory

Each turbine blades are identical and equally spaced around its centre. The blades are rotating with an angular velocity ω_{rot} rad/sec and are subjected to a steady wind speed, V_w ($z = rotor\ hub$) over the rotor plane. r is a radius of blade element having length dr. a and a' are axial and tangential induction factor representing axial and tangential velocities in the wake. The resultant wind velocity vector and forces relative to the blade elements chord line are illustrated in Figure 3.2.5 a) and b) respectively.

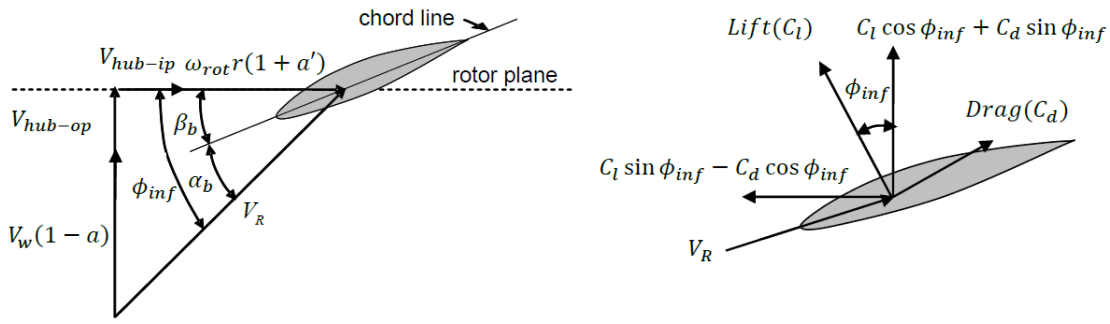

a) Velocity vector b) Forces

Figure 3.2.5 Velocities and Forces acting on blade element

The resultant wind speed V_R, and an inflow angle ϕ_{inf} can be calculated using Eq. (3.2.7) and (3.2.8) following velocity vector presented in Figure 3.2.5 a).

$$V_R = \frac{(V_w - V_{hub-op}).(1-a)}{\sin(\phi_{inf})} \tag{3.2.7}$$

$$\phi_{inf} = tan^{-1}\left(\frac{(V_w - V_{hub-op}).(1-a)}{\omega_{rot}.r.(1+a') - V_{hub-ip}}\right) \tag{3.2.8}$$

where, V_{hub-ip} and V_{hub-op} are velocity of the hub in and out of rotor plane calculated using Eq. (3.2.6), where z is used as hub height from the centre of gravity of the structure.

Many upwind turbines have a pre-cone angle ψ to prevent tower impact. An effect of this pre-cone angle is incorporated by multiplying incident wind speed with $\cos\psi$. Hence the above equations can be re-written as,

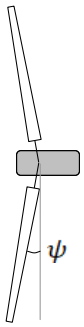

$$V_R = \frac{(V_w - V_{hub-op}).(1-a).\cos(\psi)}{\sin(\phi_{inf})} \tag{3.2.9}$$

$$\phi_{inf} = tan^{-1}\left(\frac{(V_w - V_{hub-op}).(1-a).\cos(\psi)}{\omega_{rot}.r.(1+a') - V_{hub-ip}}\right) \tag{3.2.10}$$

The thrust from each blade element is determined by calculating the aerodynamic forces acting on it and resolving them perpendicular to the rotor plane as shown in Figure 3.2.5 b). The aerodynamic forces are calculated by means of its 2D aerofoil characteristics (i.e., drag and lift coefficient, C_d and C_l respectively) using an angle of attack, α_b determined from the resultant velocity vector presented in Figure 3.2.5 a) where β_b is blade pitch angle.

For turbine with B number of identical blades, thrust and torque acting on each blade element is obtained by using Eq. (3.2.11) and Eq. (3.2.12) respectively.

$$dT = \frac{1}{2}.\rho_{air}.{V_R}^2.\left(C_l.cos(\phi_{inf}) + C_d.sin(\phi_{inf})\right).B.c.dr \tag{3.2.11}$$

$$dQ = \frac{1}{2}.\rho_{air}.{V_R}^2.\left(C_l.sin(\phi_{inf}) - C_d.cos(\phi_{inf})\right).B.c.dr.r \tag{3.2.12}$$

where, ρ_{air} is air density, and c is chord length. The coefficient of thrust C_T for the annulus is defined as,

$$C_T = \frac{T}{0.5.\rho_{air}.\left(V_w - V_{hub-op}\right)^2.A} \tag{3.2.13}$$

where A is area of annulus $(2\pi r dr)$.

C_T is, therefore, given by equation,

$$C_T = \sigma_r \frac{(1-a)^2.\cos^2(\psi)}{\sin^2(\phi_{inf})}.\left(C_l.cos\left(\phi_{inf}\right) + C_d.sin\left(\phi_{inf}\right)\right) \tag{3.2.14}$$

where,

$\sigma_r = \frac{B.c}{2.\pi.r}$, solidity ratio

The axial and tangential induction factor present in Eq. (3.2.11) and Eq. (3.2.12) for dT and dQ can be determined iteratively by comparing the thrust and torque given above with those predicted using annulus momentum theory.

An annulus momentum theory is based on an actuator disc theory first proposed by Rankine (1865) and Froude (1889). The theory considered one-dimensional flow past a rotor which is replaced by an actuator disc enclosed in a stream tube. As wind flows through the rotor, some kinetic energy is extracted from the wind thus reducing its velocity. As the mass flow rate through the rotor must remain constant, it implies an increase in area in the wake. Figure 3.2.6 illustrates the stream tube around the rotor disc and gives relationship for wind speeds at each stage of flow.

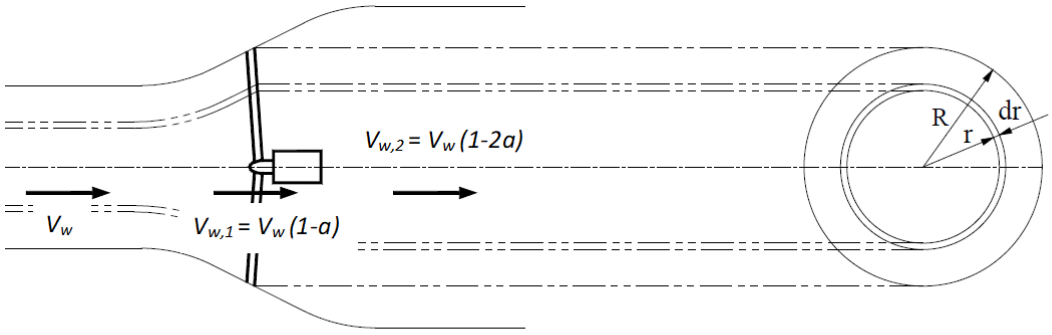

Figure 3.2.6 Annular stream tube

Stoddard (1987) derived this using axial momentum theory and Bernoulli's equation. The analysis applies conservation of mass, linear momentum theory and energy equation to determine the thrust T on the actuator disc and the work done by this force: i.e. the power P_o extracted from the wind. This one-dimensional momentum theory does not account for either the geometry or the rotations of the blades. To address this deficiency, Glauert (1935) proposed two-dimensional momentum theory where stream tube is discretised into N_e annular elements of length dr and assumed having no radial dependency.

By applying axial momentum equation to annular ring at radius r with length dr, local thrust dT and dQ is given by,

$$\mathrm{dT} = 4\,\pi\,\mathrm{r}\,\rho_{air}\left(V_w - V_{hub-op}\right)^2 (1-a)\,a\,dr \tag{3.2.15}$$

$$\mathrm{dQ} = 4\,\pi\,\mathrm{r}^3\,\rho_{air}\left(V_w - V_{hub-op}\right)\omega_{rot}\,(1-a)\,a'dr \tag{3.2.16}$$

Now, we have two sets of equations for thrust, dT and torque, dQ that can be solved iteratively for the induced velocities a and a' (refer Appendix B) and the forces on each blade element. However, before we solve these systems of equations, we would like to consider several corrections to BEM theory. These corrections include tip and hub losses to account for vortices shed at these locations, Glauert and Buhl's empirical correction to account for large induced velocities ($a > 0.4$), skewed wake correction to model the effect of incoming flow that is not perpendicular to rotor plane and 3-D rotational correction.

Corrections for BEM method

Tip and Hub losses

The correction for losses at tip and hub considers the influence of vortices shed at these locations. They play a key role in the induced velocity distribution at the rotor. This correction is incorporated using Prandtl's correction factor, F_c which can be expressed by the following formulae,

$$\mathrm{F}_{tip} = \frac{2}{\pi}\cos^{-1}\exp\left(-\frac{\mathrm{B}(\mathrm{R_{tip}}-\mathrm{r})}{2\,\mathrm{r}\sin(\phi_{inf})}\right) \tag{3.2.17}$$

$$\mathrm{F}_{hub} = \frac{2}{\pi}\cos^{-1}\exp\left(-\frac{\mathrm{B}(\mathrm{r}-\mathrm{R_{hub}})}{2\,\mathrm{r}\sin(\phi_{inf})}\right) \tag{3.2.18}$$

where, B is number of blades, r is local radius, ϕ_{inf} is flow angle, $\mathrm{R_{tip}}$ and $\mathrm{R_{hub}}$ are radius of blade tip and hub respectively.

Total correction factor can be calculated using below formulae,

$$\mathrm{F}_c = \mathrm{F_{tip}}\,\mathrm{F_{hub}} \tag{3.2.19}$$

This correction factor is used to modify the thrust and torque given in Eq. (3.2.15) and Eq. (3.2.16) derived from the momentum theory.

$$\mathrm{dT} = 4\,\pi\,\mathrm{r}\,\rho_{air}\left(V_w - V_{hub-op}\right)^2 (1-a)\,a\,F_c\,dr \tag{3.2.20}$$

$$\mathrm{dQ} = 4\,\pi\,\mathrm{r}^3\,\rho_{air}\left(V_w - V_{hub-op}\right)\omega_{rot}\,(1-a)\,a'F_c\,dr \tag{3.2.21}$$

Glauert and Buhl's empirical corrections

As the induction factor, a is greater than 0.4, wind turbines will be under a turbulence wake state. This puts an upper limit for the validity of the basic theory. Glauert (1926) developed a correction to the rotor thrust coefficient based on experimental measurements of helicopter rotors with large induced velocities. Buhl (2004) later developed a new relation between rotor thrust coefficient and induction factor which solved the instability caused by applying Glauert (1926) correction as illustrated below:

For $C_T \geq 0.96$ $$a = \frac{18F_c - 20 - 3\sqrt{C_T\,(50 - 36F_c) + 12F_c(3F_c - 4)}}{36F_c - 50} \quad (3.2.22)$$

Skewed wake correction

Although BEM method was originally proposed to solve for the axisymmetric flow, wind turbines are often running at yaw angles. This again invalidates the basic theory unless a correction is used accounting for the skewed effect. Snel and Schepers (Snel & Schepers, 1995) derived the following correction formulation:

$$a_{skew} = a\left(1 + \frac{15\pi}{32}\frac{r}{R}\tan\frac{\chi}{2}\cos\Upsilon\right) \quad (3.2.23)$$

where, χ is wake skew angle, and Υ is azimuth angle.

Rotational Effect

The effect of rotation was first investigated intensively for helicopter rotor. Later, the fact that aerodynamic power tends to exceed the design value for wind turbine starts attracting more attention and translated to different mechanism. These include centrifugal pumping effect, stall delay, rotational augmentation, etc. Despite of these developments, a census approach is still lacking, particularly for the effect on the drag. Nevertheless, the 3D correction of Snel et al. (1993) received amble attention and is incorporated in the present work. It provides an increase of the aerodynamic lift coefficient for the effects of rotation, which is described below:

$$C_{l,rot} = C_{l,non-rot} + 3.1\left(\frac{\omega_{rot}\,r}{V_R}\right)^2\left(\frac{c}{r}\right)^2(C_{l,pot} - C_{l,non-rot}) \quad (3.2.24)$$

where, the 'potential lift coefficient' $C_{l,pot}$ is defined as $2\pi\sin(\alpha_b - \alpha_{b,0})$, $\alpha_{b,0}$ is angle of attack when lift coefficient is zero.

Combined Blade Element and Momentum Theory

Thus, we have a set of equations that can be iteratively solved for the axial and tangential induction factors accounting corrections for losses described in the previous section.

From blade element theory, the thrust from each blade element of length dr is equivalent to,

$$dT = \frac{1}{2}.\rho_{air}.{V_R}^2.\left(C_l.cos(\phi_{inf}) + C_d.sin(\phi_{inf})\right).B.c.dr \quad (3.2.25)$$

and the torque produced by each blade element is equivalent to,

$$dQ = \frac{1}{2}.\rho_{air}.{V_R}^2.\left(C_l.sin(\phi_{inf}) - C_d.cos(\phi_{inf})\right).B.c.r.dr \quad (3.2.26)$$

From axial momentum

$$dT = 4\,\pi\,r\,\rho_{air}\left(V_w - V_{hub-op}\right)^2(1-a)\,a\,F_c\,dr \quad (3.2.27)$$

From angular momentum

$$dQ = 4\,\pi\,r^3\,\rho_{air}\left(V_w - V_{hub-op}\right)\omega_{rot}\,(1-a)\,a'F_c\,dr \quad (3.2.28)$$

By equating Eq (3.2.25) with Eq (3.2.27) and Eq (3.2.26) with Eq (3.2.28) and re-arranging an axial and tangential induction factor yields the following formulae,

Axial induction factor a,

$$a = \frac{1}{\frac{4F_c\ sin^2(\phi_{inf})}{\sigma_r\left(C_l\cos(\phi_{inf}) + C_d\sin(\phi_{inf})\right)} + 1} \tag{3.2.29}$$

Tangential induction factor a',

$$a' = \frac{1}{\frac{4F_c\ \sin(\phi_{inf})\cos(\phi_{inf})}{\sigma_r\left(C_l\sin(\phi_{inf}) - C_d\cos(\phi_{inf})\right)} - 1} \tag{3.2.30}$$

APPENDIX B illustrates the iteration procedure for computing axial and tangential induction factors for each blade element. Once the axial and tangential induction factors are found, axial thrust, torque and power can be found for each element using equation given by either blade element theory or momentum theory. The thrust, torque and power on each element then can be summed up along the blade to get total thrust, T and torque, Q acting on the wind turbine and corresponding generated power, P_o.

$$\mathrm{T} = \frac{1}{2}.\rho_{air}.\mathrm{B}.\sum_{\mathrm{i}=1}^{N_e} {\mathrm{V_R}_i}^2.\left(C_{l_i}.\cos\left(\phi_{inf_i}\right) + C_{d_i}.\sin\left(\phi_{inf_i}\right)\right).\mathrm{c_i}.\mathrm{dr}_i \tag{3.2.31}$$

$$\mathrm{Q} = \frac{1}{2}.\rho_{air}.\mathrm{B}.\sum_{\mathrm{i}=1}^{N_e} {\mathrm{V_R}_i}^2.\left(C_{l_i}.\sin\left(\phi_{inf_i}\right) - C_{d_i}.\cos\left(\phi_{inf_i}\right)\right).\mathrm{c_i}.\mathrm{r_i}.\mathrm{dr}_i \tag{3.2.32}$$

$$\mathrm{P_o} = \frac{1}{2}.\rho_{air}.\mathrm{B}.\sum_{\mathrm{i}=1}^{N_e} {\mathrm{V_R}_i}^2.\left(C_{l_i}.\sin\left(\phi_{inf_i}\right) - C_{d_i}.\cos\left(\phi_{inf_i}\right)\right).\mathrm{c_i}.\mathrm{r_i}.\omega_{rot}.\mathrm{dr}_i \tag{3.2.33}$$

where, N_e is number of elements along the blade

3.2.4 Loads on tower

The wind load acting on the tower is determined using drag equation with wind velocity at height 'z' above sea surface. The vertical variation of the wind velocity is estimated using either logarithmic or power law expression given in Eq. (3.2.1) and (3.2.2). The wind force per unit tower length is expressed by,

$$dT_{drag}(z) = C_d\ \frac{1}{2}\ \rho_{air}\ D(z)\big(V_w(z) - U(z)\big)\big|\big(V_w(z) - U(z)\big)\big| \tag{3.2.34}$$

where, C_d is drag coefficient, ρ_{air} is air density, $D(z)$ is tower diameter at elevation 'z' and $\big(V_w(z) - U(z)\big)$ is component of relative wind velocity normal to the tower axis at elevation 'z'.

The wind load acting on the tower may be important in extreme wind condition as wind load acting on the turbine rotor in parked (or idling) condition is less dominant as compared to operating condition.

3.2.5 Total wind load

Total forces and moments due to wind acting on the floating wind turbine system can be written as,

$$\overrightarrow{F_{aero}} = T + \int_{l_d} dT_{drag}\, dl_t \tag{3.2.35}$$

$$\overrightarrow{N_{aero}} = \overrightarrow{r_{hub}} \times T + \int_{l_d} \vec{r} \times dT_{drag}\, dl_t \tag{3.2.36}$$

where, l_d is tower length exposed to wind and, $\overrightarrow{r_{hub}}$ is position vector of wind turbine hub and $\vec{r}$ is position vector along the tower to the center of gravity of TLPWT system.

For simulation purpose, Eq. (3.2.35) and (3.2.36) need to be expressed in matrix form with elements composed of projected components of vectors. Therefore, forces and moments are derived in matrix form and included under APPENDIX C-1.

3.3 Hydrodynamic model

The estimation of wave loads acting on the offshore structures is a complex task involving various wave models, load calculation methods, and probability analysis. However, it is of vital importance when a cost-effective and durable structure is to be designed. Floating wind turbines will be deployed in a moderately deep sea, a region of the sea where until now very few floating platforms have been built. The offshore oil and gas industry have considerable experience building floating platforms for deeper water depths, however, in their case cost had a low priority compared with aspects such as time scale, safety, and reliability. For the offshore wind industry, the cost is an additional factor, and hence the existing wave load estimation procedure needs to be modified to optimise loading without compromising structures reliability.

The procedure necessary to estimate wave loading can be divided into the following stages,

- Determining design wave or wave climate
- Selecting an appropriate wave kinematic model
- Selecting an appropriate wave load calculation method.

3.3.1 Wave climate

Wave is a primary source of external load affecting motions of the platform and consequently, the structural integrity of the wind turbine and its supporting tower. Therefore, it is imperative for the designer to describe the wave condition accurately. The waves in the ocean environment can be viewed at three levels, i) individual waves, ranging in size from the smallest ripple to the extreme wave. These individual waves combine to make a ii) sea state, which is generally assumed to be stationary over three hours. Sea states are usually defined in terms of stochastic spectra parameterised by the significant wave height, H_s and peak period, T_p. The whole collection of sea states is defined as, iii) wave climate, typically represented as a sea-state scatter

probability table. This table also shows the probability of occurrence of sea states for each combination of significant wave height and peak period. For load and response analysis of floating wind turbines, there are two approaches to translate sea state condition into hydrodynamic loading, one is deterministic design wave approach, and other is a stochastic spectral approach.

A design wave approach is concerned with the survival against the largest wave which structure is likely to encounter during its design life. In this approach, the structure must survive the forces exerted by a train of regular waves. The height and period of this regular wave train is derived statistically as the most probable largest wave at design location for a given return period. The design wave approach is straightforward to apply and usually makes no exceptional computational demand. This approach can be applied in both frequency and time domain analysis. However, since in extreme conditions nonlinearities manifest themselves, time domain analysis which can simulate or mimic these nonlinearities are generally required. However, as offshore wind industry is moving into the deeper water with an increase in turbine size, its floating support structures will be larger and (relatively) more compliant, and hence extreme and fatigue response will become increasingly important in its design. In such circumstances, the design process must consider the entire range of sea conditions which will be encountered during the structures design life, rather than a single severe wave. For this reason, an alternative stochastic spectral approach to design is more widely adopted.

In stochastic spectral approach, time series of a random wave is obtained from the energy spectra for the design sea state. A brief description of these methods is given by Sarpkaya and Isaacson (1981). A more rigorous mathematical description of these concepts can be found in the book by Price and Bishop (1974). The spectral approach is in terms of its frequency content, clearly demonstrates the effect of natural frequency response. The probabilistic approach is concerned with the number of times given loads or response levels are exceeded and is thus relevant to fatigue life.

The description of all the wave models associated with afore-mentioned approaches is beyond the scope of this thesis. However, a brief description of wave models adopted under this research study based on the literature review presented under section 2.6 is given in the following sub-section.

3.3.2 Wave kinematic model

Three different wave kinematic models are considered for the present study, i.e., Airy's (1845) linear wave theory using wheeler stretching (LWT), Fenton's (1985) nonlinear steady wave theory based on 5^{th} order stokes theory (NLSWT) and QALE-FEM numerical scheme (Ma & Yan, 2006) based on fully nonlinear potential theory (FNPT). Details of these wave kinematic models are given below.

3.3.2.1 Airy's linear wave theory (LWT)

This theory gives a linearized description of the propagation of gravity wave on the surface of a homogeneous fluid layer. The theory assumes that the fluid layer has a uniform mean depth, and the fluid flow is inviscid, incompressible and irrotational. The theory is often used to get a quick estimate of wave characteristics and their effects. This approximation is accurate for small ratios of the wave height to water depth (H/d) for waves in shallow water, and wave height to wave length (H/L_0) for waves in deep water.

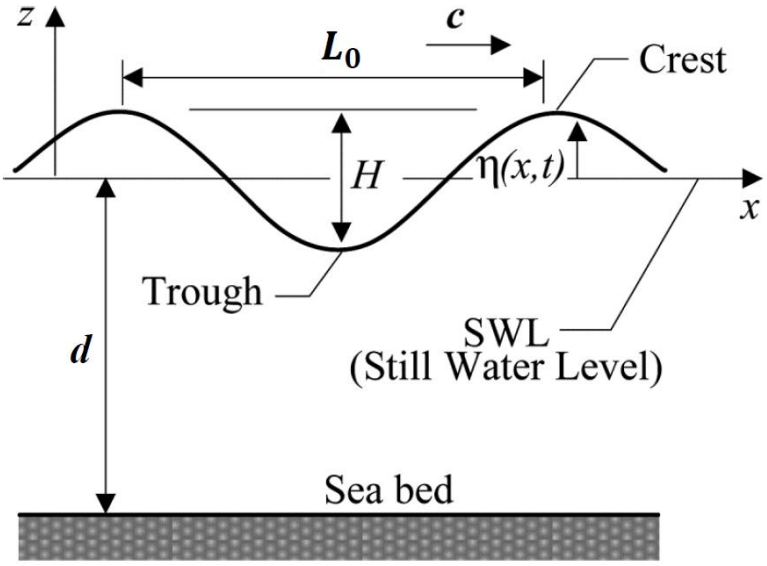

Figure 3.3.1 Sketch for progressive wave train

As shown in Figure 3.3.1, the wave propagates in the horizontal direction with coordinate x, and a fluid domain bound above by a free surface at $z = \eta(x,t)$, with z the vertical coordinate (positive in the upward direction) and t being time. The free surface elevation $\eta(x,t)$ of one wave component is sinusoidal and is given by,

$$\eta(x,t) = \frac{H}{2}\cos(kx - \omega t) \tag{3.3.1}$$

where, ω and k are angular frequency and wave number respectively.

The associated velocity potential $\phi(x,t)$ is given by,

$$\phi(x,t) = \frac{H}{2}\frac{g}{\omega}\frac{cosh\, k(z+d)}{\cosh kd}\sin(kx - \omega t) \tag{3.3.2}$$

Wheeler (1969) proposed a co-ordinate stretching for the evaluation of water particle velocities and accelerations above mean water level. The term $(z+d)$ appearing in the numerator of Eq. (3.3.2) need to be replaced by $(z+d)\, d/(d+\eta)$. The wave induced water particle kinematic parameters such as horizontal and vertical water particle velocity and accelerations can be derived from the velocity potential given in Eq. (3.3.2) by applying wheelers co-ordinate stretching. This procedure of evaluating water particle kinematics is programmed using FORTRAN 90 and verified by students from hydrodynamic research group of City, University of London.

3.3.2.2 Fenton's Nonlinear Steady Wave Theory (NLSWT)

This theory is based on 5th order stokes theory giving a nonlinear description of the periodic surface wave propagating on an inviscid fluid layer of constant mean depth. The theory uses a perturbation series approach where the expansion parameter is wave steepness, $kH/2$ itself. The perturbation solution developed as a power series in terms of $\varepsilon = kH/2$ is expected to converge as more and more terms are considered in the expansion. Convergence does not occur for steep waves unless a different perturbation parameter from that of Stokes is chosen. Fenton (1985), developed the formulation for 5th order Stokes wave theory with good convergence properties which is computationally efficient and includes closed-form asymptotic expressions for both deep and shallow water waves. The theory is often used to determine the wave kinematics (i.e., free surface elevation and flow acceleration and velocities) for a steep regular wave.

The theory assumes a periodic wave propagating without change of form over a layer of fluid on a horizontal impermeable bed as shown in Figure 3.3.2. The origin is on the bed with horizontal and vertical co-ordinate x and z respectively. This reference system moves with the same velocity as waves so that in this frame all motion is steady.

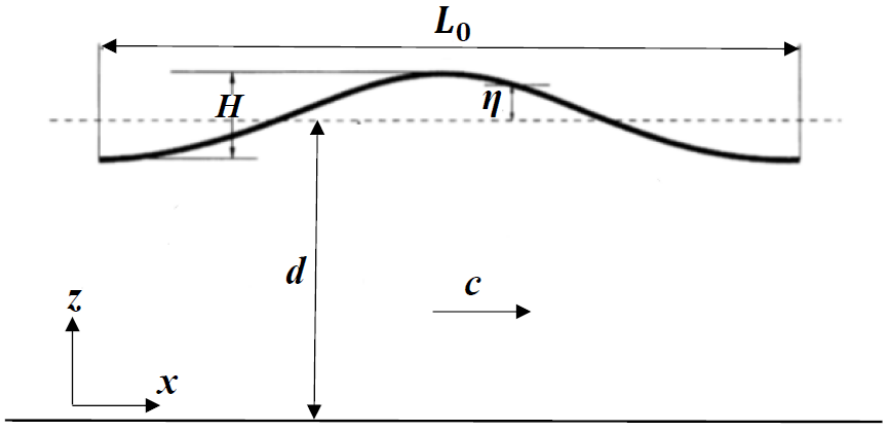

Figure 3.3.2 One wave of steady periodic wave train

The free surface elevation $\eta(x,t)$ is given by,

$$\eta(x,t) = \frac{1}{k}\sum_{n=1}^{5} \varepsilon^n \, b_n \cos n\,(kx - \omega t) \tag{3.3.3}$$

The associated velocity potential $\phi(x,t)$ is given by,

$$\phi(x,t) = C_0 \left(\frac{g}{k^3}\right)^{1/2} \sum_{n=1}^{5} \varepsilon^n \, a_n \, cosh(nkz) \, sin\, n\,(kx - \omega t) \tag{3.3.4}$$

where, coefficients C_0, a_n and b_n are dimensionless function of water depth d and wave length L_0 and given in Fenton (1985). The wave induced water particle kinematic parameters such as horizontal and vertical water particle velocity and accelerations can be derived from the velocity potential given in Eq. (3.3.4). This procedure of evaluating water particle kinematics is

programmed using FORTRAN 90 and verified by students from hydrodynamic research group of City, University of London.

3.3.2.3 FNPT based QALE-FEM

The QALE-FEM (Quasi Arbitrary Lagrangian Eulerian Finite Element Method) numerical tool is developed based on the fully nonlinear potential theory (FNPT) by Ma and Yan (2006) to simulate steep nonlinear wave and predict associated wave kinematics. The computational domain for the numerical simulation is chosen as a 2-D rectangular tank as shown in Figure 3.3.3 where waves are generated using wave maker mounted at the left end while the absorbing boundary conditions are applied at the right end of the tank. For the absorbing boundary conditions, a damping zone with a Sommerfeld condition is chosen. A Cartesian coordinate system is used with $O_w X_w Y_w Z_w$ plane on the mean free surface.

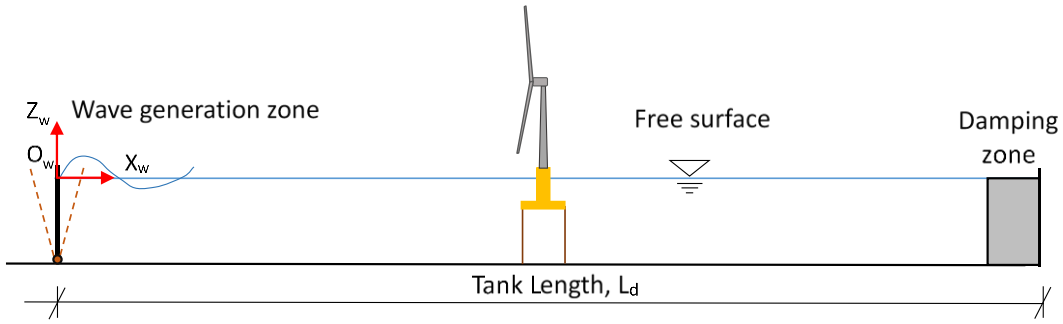

Figure 3.3.3 Numerical wave tank

The flow in the tank is governed by FNPT (fully non-linear potential theory) in which the velocity potential ϕ satisfies the Laplace's equation in the fluid domain.

$$\nabla^2 \phi = 0 \tag{3.3.5}$$

On the free surface, $z = \eta(x, y, t)$ the velocity potential satisfies both kinematic and dynamic conditions in the following Lagrangian form,

$$\frac{Dx}{Dt} = \frac{\partial \phi}{\partial x}, \frac{Dy}{Dt} = \frac{\partial \phi}{\partial y}, \frac{Dz}{Dt} = \frac{\partial \phi}{\partial z} \tag{3.3.6}$$

$$\frac{D\phi}{Dt} = -gz + \frac{1}{2}|\nabla \phi|^2 + p \tag{3.3.7}$$

where D/Dt is the substantial (or total time) derivative following fluid particles and g is the gravitational acceleration. In equation (3.3.7) the atmospheric pressure is taken as zero. On all rigid boundaries such as wavemaker, velocity potential satisfies,

$$\frac{\partial \phi}{\partial n} = \vec{n} \cdot \vec{U}(t) \tag{3.3.8}$$

where $\vec{U}(t)$ and $\vec{n}$ are the velocity and the unit normal vector of the rigid boundaries respectively. The positive direction of the normal vector points outside of the fluid domain. Here the flow is assumed as inviscid and irrotational and the equations are solved using QALE-FEM numerical scheme. In this numerical scheme, the complex unstructured mesh is generated only

once at the beginning of the calculation and is moved to conform to the motion of the boundaries at other time steps, avoiding the necessity of high-cost remeshing that makes this numerical scheme more efficient as compared to conventional FEM. A comparison of results produced using this numerical scheme and the experimental data (Yan & Ma, 2007; Ma & Yan, 2009) has shown that the model is sufficiently accurate in cases where viscosity plays an insignificant role (for steep non-breaking waves). During simulation at each time step, the wave surface and associated water particle kinematics are obtained at a given location on the structural members through the dynamically linked library to perform the force calculation and subsequent response analysis.

There are two types of wave makers considered for generating waves, i.e., flap or piston type as depicted in Figure 3.3.4. The former is generally being used to generate deep water waves and the latter for the generation of shallow water waves. The transfer function S_0 for these wave makers are given below. The detailed derivations can be found from Dean and Dalrymple (1991).

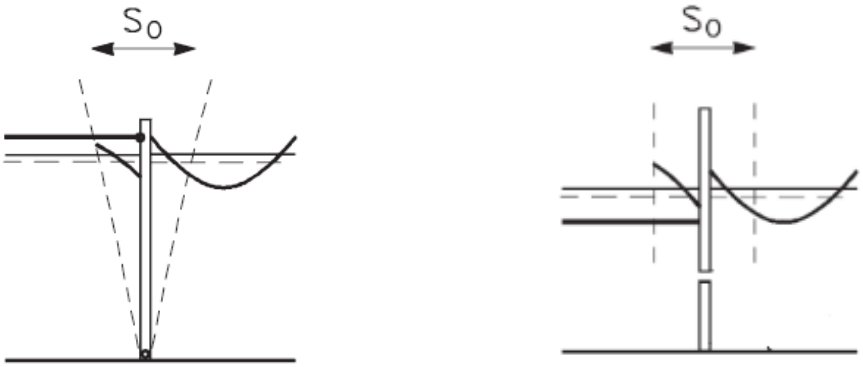

a) Flap type wave maker b) Piston type wave maker

Figure 3.3.4 Wave maker

For Flap,
$$TF = \frac{H}{S_0} = \frac{2\sinh(kd)\,(1-\cosh(kd)+kd\sinh(kd))}{kd\,(\sinh(kd)\cosh(kd)+kd)} \tag{3.3.9}$$

For Piston,
$$TF = \frac{H}{S_0} = \frac{2\sinh^2(kd)}{\sinh(kd)\cosh(kd)+kd} \tag{3.3.10}$$

where, H = wave height

k = wave number

d = water depth

Based on the above transfer function, following expressions can be used to calculate the wave maker motions $x_p(t)$ for generating regular wave, bichromatic wave, and random wave.

For regular wave,
$$x_p(t) = -\frac{amp}{TF}\cos(\omega t) \tag{3.3.11}$$

For bichromatic wave,
$$x_p(t) = \sum_{i=1}^{2} -\frac{amp_i}{TF_i}\cos(\omega_i\, t) \tag{3.3.12}$$

For random wave, $$x_p(t) = \sum_{i=1}^{N_c} -\frac{amp_i}{TF_i}\cos(\omega_i\, t + \emptyset_i) \tag{3.3.13}$$

where ω_i is angular frequency of ith component; $\emptyset_i$ is phase angle of ith component which is random variable uniformly distributed between (0 to 2π); amp_i is amplitude of ith wave component obtained from $\sqrt{2\,S(\omega_i)\,\Delta\omega_i}$, where $S(\omega_i)$ is power spectral density which can be obtained from any standard or measured spectrum. N_c is number of frequency component.

As random phase angle method is used to generate a random wave in this thesis, the number of wave components, N_c is taken as 1000 to simulate true gaussian process which gives the right wave groupiness (Tucker, et al., 1984). To avoid unphysical high-frequency first order wave excitation, the spectrum is set to zero beyond cut-off frequency ω_c which is determined by limiting its amplitude to 0.5% of amplitude at peak wave frequency.

3.3.3 Wave and current loads on platform

The wave load acting on the members of the floating wind turbine is evaluated using a slender body approach. In this approach, the body is assumed as thin and the forces (and/moments) are obtained by integrating the forces (and/moments) on each short segment 'dl_w' of the slender body. The force on each short segment is decomposed into two parts – an in-viscid inertia force '$F_{inertia}$' and a viscous drag force 'F_{drag}'. The inertia force due to in-viscid flow given by Rainey (1995) is used, and the drag force from the Morison's equation is employed to account for the viscous effect. Rainey (1995) modified inertia force term of Morison's equation by including axial divergence and centrifugal force terms acting on the member cross section '$d\vec{f}_1$' and by introducing point loads '$\overrightarrow{F_2}$' and '$\overrightarrow{F_3}$' at the member ends, as shown in Figure 3.3.5 and expressed in Eq. (3.3.14). All these additional force components are nonlinear, and they do not appear in the conventional Morison's equation.

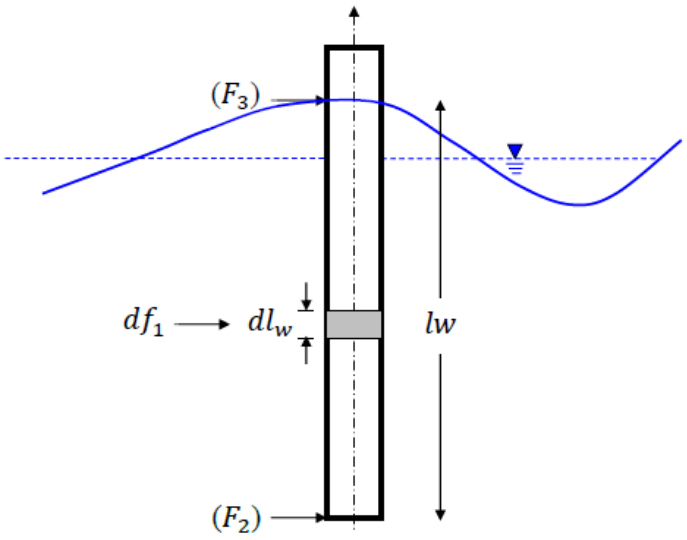

Figure 3.3.5 Inertia force acting on member

$$\overrightarrow{F_{hydro}} = \underbrace{\int_{l_w} d\vec{f_1} + \overrightarrow{F_2} + \overrightarrow{F_3}}_{F_{inertia}} + \underbrace{\int_{l_w} d\overrightarrow{f_{drag}}}_{F_{drag}} \tag{3.3.14}$$

where, l_w is wetted length of member.

This force equation is applied here for the chosen tension leg platform which consists of vertical spar buoy and equi-spaced horizontal prismatic members, i.e., pontoons. Force per unit immersed length $d\vec{f_1}$ and point loads, $\overrightarrow{F_2}$ acts on both vertical spar buoy and pontoons whereas point load $\overrightarrow{F_3}$ acts at the intersection of surface piercing vertical spar buoy and wave surface. Hence, the total wave force and its moment acting on the floating wind turbine system is given by,

$$\begin{aligned}\overrightarrow{F_{hydro}} = &\int_{l_w} d\overrightarrow{f_{1-spar}} + \sum_{i=1}^{N_p}\int_{l_w} d\overrightarrow{f_{1-pontoon_i}} + \overrightarrow{F_{2-spar}} + \sum_{i=1}^{N_p}\overrightarrow{F_{2-pontoon_i}} \\ &+\overrightarrow{F_{3-spar}} + \int_{l_w} d\overrightarrow{f_{\text{drag}-spar}} + \sum_{i=1}^{N_p}\int_{l_w} d\overrightarrow{f_{\text{drag}-pontoon_i}}\end{aligned} \tag{3.3.15}$$

$$\begin{aligned}N_{hydro} = &\int_{l_w} \vec{r} \times d\overrightarrow{f_{1-spar}} + \sum_{i=1}^{N_p}\int_{l_w} \vec{r} \times d\overrightarrow{f_{1-pontoon_i}} + \overrightarrow{r_e} \times \overrightarrow{F_{2-spar}} + \sum_{i=1}^{N_p}\overrightarrow{r_e} \\ &\times \overrightarrow{F_{2-pontoon_i}} + \overrightarrow{r_f} \times \overrightarrow{F_{3-spar}} + \int_{l_w} \vec{r} \times d\overrightarrow{f_{\text{drag}-spar}} \\ &+\sum_{i=1}^{N_p}\int_{l_w} \vec{r} \times d\overrightarrow{f_{\text{drag}-pontoon_i}}\end{aligned} \tag{3.3.16}$$

where, N_p is number of pontoons and $\vec{r}$, $\overrightarrow{r_e}$, and $\overrightarrow{r_f}$ are position vector of element length, immersed end and intersection point respectively. The description of each force component from Eq. (3.3.14) is given below,

3.3.3.1 Force per unit immersed length, $d\overrightarrow{f_1}$

The force per unit immersed length of a structural member having cross sectional area, S is given by,

$$\begin{aligned}d\vec{f_1} = {} & \rho_w S\{\overrightarrow{a_w} - \vec{g}\}_n && \text{Froude krylov + Static buoyancy force} \\ & + [M_a]\{\overrightarrow{a_w} + (\vec{l} \cdot [V]\vec{l})\overrightarrow{u_r}\} && \text{Diffraction + Axial divergence force} \\ & - [M_a]\dot{U} && \text{Added mass force} \\ & - 2[M_a]\tilde{\Omega}\{\overrightarrow{u_r}\}_a && \text{Negative centrifugal force} \\ & + \{([V] + \tilde{\Omega})[M_a]\overrightarrow{u_r}\}_n && \text{Non-cylindrical force term 1} \\ & - [M_a]([V] + \tilde{\Omega})\{\overrightarrow{u_r}\}_n && \text{Non-cylindrical force term 2}\end{aligned} \tag{3.3.17}$$

where,

ρ_w = sea water density

S = cross section area of member

$\{\overrightarrow{a_w}\}_n$ = water particle acceleration (temporal plus convective) vector

$$\begin{bmatrix} 0 \\ \frac{\partial v}{\partial t} + u\frac{\partial v}{\partial x} + v\frac{\partial v}{\partial y} + w\frac{\partial v}{\partial z} \\ \frac{\partial w}{\partial t} + u\frac{\partial w}{\partial x} + v\frac{\partial w}{\partial y} + w\frac{\partial w}{\partial z} \end{bmatrix}$$

$\{\vec{g}\}_n$ = gravitational acceleration vector, pointing downward, i.e., $g = -ge_z$

$[M_a]$ = added mass matrix transverse to member

$\vec{l}$ = upward unit vector along the member centreline

$[V]$ = velocity gradient matrix,

$$\begin{bmatrix} \frac{\partial u}{\partial x} & \frac{\partial v}{\partial x} & \frac{\partial w}{\partial x} \\ \frac{\partial u}{\partial y} & \frac{\partial v}{\partial y} & \frac{\partial w}{\partial y} \\ \frac{\partial u}{\partial z} & \frac{\partial v}{\partial z} & \frac{\partial w}{\partial z} \end{bmatrix}$$

$\overrightarrow{u_r}$ = relative velocity vector,

$$\begin{Bmatrix} u - U_x \\ v - U_y \\ w - U_z \end{Bmatrix} \text{ where, } \begin{Bmatrix} u \\ v \\ w \end{Bmatrix} = \begin{Bmatrix} u_w + u_c \\ v_w + v_c \\ w_w \end{Bmatrix}$$

Here, u_w,v_w, and w_w are wave induced water particle velocities in x, y, and z direction whereas u_c and v_c are current velocities in x and y direction.

$\vec{U}$ = velocity of the body at the corresponding point, i.e. $\overrightarrow{U_0} + \vec{\Omega} \times \vec{r}$ ($\vec{r}$ is a position vector from the centre of gravity to the relevant point)

$\widetilde{\Omega}$ = matrix composed of the components of angular velocity and defined by $\widetilde{\Omega}x = \Omega \times x$ for any axial vector x.

$$\begin{bmatrix} 0 & -\Omega_z & \Omega_y \\ \Omega_z & 0 & \Omega_x \\ -\Omega_y & \Omega_x & 0 \end{bmatrix}$$

$\{\ \}_n$ = transverse component normal to the member axis

$\{\ \}_a$ = axial component along the member axis

It can be seen from Eq. (3.3.17) that the force per unit immersed length has six parts. Fifth and sixth force terms are non-cylindrical terms which cancels for any shape where the principal added mass values are equal. For the chosen floating platform, pontoons are prismatic members having equal added mass, and hence contribution of these force terms is zero and hence not considered hereafter.

Re-arranging Eq. (3.3.17) as,

$$d\vec{f}_1 = \underbrace{(1+C_a)\rho_w S\{\overrightarrow{a_w}\}_n}_{\substack{Froude-krylov \\ F_{fk}}} + \underbrace{\rho_w S\{-\vec{g}\}_n}_{\substack{static\ buoyancy \\ F_{sb}}} + \underbrace{[M_a]\{(\vec{l}\cdot[V]\vec{l})\overrightarrow{u_r}\}}_{\substack{axial\ divergence \\ F_{div}}} - \underbrace{[M_a]\dot{U}}_{\substack{added\ mass \\ F_{adm}}} - \underbrace{2[M_a]\widetilde{\Omega}\{\overrightarrow{u_r}\}_a}_{\substack{centrifugal \\ F_{cf}}} \quad (3.3.18)$$

where, C_a is added mass coefficient

Each force component from Eq. (3.3.18) is briefly explained below.

Froude-Krylov force, F_{fk}

This force component is introduced by the unsteady pressure field generated by undisturbed waves. This force together with the diffraction force makes up the total non-viscous force acting on the members of the floating platform. This force is part of the Morison's equation but is more precisely defined here because the wave-induced particle acceleration includes both temporal and convective terms.

Static buoyancy force, F_{sb}

This force component is due to hydrostatic pressure acting on the member having a non-zero angle from vertical.

Axial divergence force, F_{div}

According to Manner and Rainey (1992), this term is interpreted as the force caused by a decrease in the added mass per unit length due to a divergence of the axial incident flow. If the incident flow in the direction of the member centreline is constant along the member, this term is zero. This term is important when there is convective acceleration.

Added mass force, F_{adm}

This is an additional force term caused by submerged member disturbing a flow accelerating relative and normal to its axis. This is also part of inertia term of Morison's equation but is more precisely defined to include fluid temporal and convective accelerations, including total acceleration of the body. It also includes centripetal and coriolis values in its derivation. The force F_{adm} per unit immersed length is given as,

$$F_{adm} = -[M_a]\,\dot{U} \quad (3.3.19)$$

By taking time derivative of velocity of member segment 'dl_w', Eq. (3.3.19) can be re-written as,

$$F_{adm} = -[M_a]\left(\frac{d\overrightarrow{U_c}}{dt} + \frac{d\vec{\Omega}}{dt}\times\vec{r} + \overrightarrow{\Omega}\times\left(\vec{\Omega}\times\vec{r}\right)\right) \quad (3.3.20)$$

It can be seen from Eq. (3.3.20) that the first and second term of added mass force is linear and depends upon translational and rotational acceleration of the body respectively, whereas last term is nonlinear and depends upon product of angular velocity. The linear added mass force is separated out from Eq. (3.3.20) so that they can be combined with body mass $[M]$ and inertia $[I]$

matrix in the motion equations (3.1.19) and (3.1.20) respectively. The detailed explanation on doing so is given under next chapter, section 4.3.1. Hence the Eq. (3.3.20) can be re-written as,

$$F_{adm\_l} = -[M_a]\left(\frac{d\overrightarrow{U_c}}{dt} + \frac{d\vec{\Omega}}{dt} \times \vec{r}\right) \tag{3.3.21}$$

$$F_{adm\_nl} = -[M_a]\left(\vec{\Omega} \times \left(\vec{\Omega} \times \vec{r}\right)\right) \tag{3.3.22}$$

Centrifugal force, F_{cf}

This is an additional transverse force when there is a combination of axial flow and member rotation about a transverse axis. The combination occurs when a member is moving in a circle with the member's velocity along its axis. The force is proportional to the cross product of angular velocity and the relative velocity in the axial direction. This is similar in some sense to the well-known Coriolis force acting on a particle moving in an inertial coordinate system. In some simple cases, such as a thin body moving in a circle, this term is also interpreted as 'negative centrifugal force'. In this thesis, this term is called as centrifugal force following Rainey (1995).

3.3.3.2 Point force at an immersed end, $\overrightarrow{F_2}$

The point force at an immersed end of the member $\overrightarrow{F_2}$, which will be referred as bottom point force $\overrightarrow{F_{bp}}$ hereafter in this thesis is given by,

$$\overrightarrow{F_{bp}} = pS\vec{l} - \left(\frac{1}{2}\overrightarrow{u_r} \cdot [M_a]\overrightarrow{u_r}\right)\vec{l} + \left(\vec{l} \cdot \overrightarrow{u_r}\right)[M_a]\overrightarrow{u_r} \tag{3.3.23}$$

This force acts at the end of vertical spar buoy and horizontal pontoons. First part of equation is axial Froude Krylov force where, $p = p_h + p_s$ is sum of hydrodynamic and static water pressures- the second of which provides the axial buoyancy and hydrostatic restoring force together with the term of $\{-g\}_n$ in Eq. (3.3.18). $\vec{l}$ is unit vector along the member axis and out of the member at the end. The pressure p is given by,

$$p = -\rho_w\left(gz + \frac{\partial\phi}{\partial t} + \frac{1}{2}(u^2 + v^2 + w^2)\right) \tag{3.3.24}$$

where, u, v, and w are the fluid velocity due to incident wave and current

The second part of equation (3.3.23) is axial end force which is possibly important for the shallow draft structure, as for deep draft structure, it is small in comparison with the 'microseism' second-order diffracted pressure. The third part is a normal force causing munk moment. These forces tend to rotate the member, about a normal to its axis, until the member's axis is normal to the flow velocity. The velocity squared term in the expression for pressure together with the second and third term in equation (3.3.23) provides a force that is of the second order of wave amplitude. First, two force components act in the axial direction of the member whereas the third force component acts normal to it.

3.3.3.3 Point force at wave surface intersection, $\overrightarrow{F_3}$

The point force at an intersection of sea surface and surface piercing member of structure $\overrightarrow{F_3}$, which will be termed as intersection force $\overrightarrow{F_{int}}$ hereafter in this thesis is given by,

$$\overrightarrow{F_{int}} = \frac{1}{2}\, tan\, \alpha_{ac} \left[(\overrightarrow{t_u} \cdot \overrightarrow{u_r})[M_a]\overrightarrow{u_r} - \left(\overrightarrow{t_u} \cdot \left(\vec{l} \times [M_a]\overrightarrow{u_r}\right)\right)\left(\vec{l} \times \overrightarrow{u_r}\right) \right] \tag{3.3.25}$$

where α_{ac} is the acute angle between the member centreline and the surface normal of the undisturbed wave, and $\overrightarrow{t_u}$ is a unit vector in their joint plane, normal to the member axis and pointing out of the fluid. If the structure has no initial inclination, $tan\, \alpha_{ac}$ is determined by the motion of structure and the wave, and such a point load is of third order with respect to the wave amplitude. This intersection force and its moment component act on vertical spar buoy.

3.3.3.4 Drag force, F_{drag}

The drag force per unit immersed length of structural member having diameter D, is given by,

$$df_{drag} = C_d \frac{1}{2}\, \rho_w\, D\, \overrightarrow{u_r}\, |\overrightarrow{u_r}|\, dl_w \tag{3.3.26}$$

where, C_d is a drag coefficient and $\overrightarrow{u_r}$ is component of relative velocity normal to the member axis.

3.3.3.5 Total wave load

Total wave load acting on the members of floating wind turbine is given by,

$$\begin{aligned} F_{hydro} = & \int_{l_w} \overrightarrow{F_{fk-spar}} + \sum_{i=1}^{Np} \int_{l_{wi}} \overrightarrow{F_{fk-pontoon_\iota}} + \int_{l_w} \overrightarrow{F_{sb-spar}} + \sum_{i=1}^{Np} \int_{l_{wi}} \overrightarrow{F_{sb-pontoon_\iota}} \\ & + \int_{l_w} \overrightarrow{F_{div-spar}} + \sum_{i=1}^{Np} \int_{l_{wi}} \overrightarrow{F_{div-pontoon_\iota}} + \int_{l_w} \overrightarrow{F_{adm\_l-spar}} \\ & + \sum_{i=1}^{Np} \int_{l_{wi}} \overrightarrow{F_{adm\_l-pontoon_\iota}} + \int_{l_w} \overrightarrow{F_{adm\_nl-spar}} \\ & + \sum_{i=1}^{Np} \int_{l_{wi}} \overrightarrow{F_{adm\_nl-pontoon_\iota}} + \int_{l_w} \overrightarrow{F_{cf-spar}} + \sum_{i=1}^{Np} \int_{l_{wi}} \overrightarrow{F_{cf-pontoon_\iota}} \\ & + \overrightarrow{F_{bp-spar}} + \sum_{i=1}^{Np} \overrightarrow{F_{bp-pontoon_\iota}} + \overrightarrow{F_{int-spar}} + \int_{l_w} \overrightarrow{F_{drag-spar}} \\ & + \sum_{i=1}^{Np} \int_{l_{wi}} \overrightarrow{F_{drag-pontoon_\iota}} \end{aligned} \tag{3.3.27}$$

$$
\begin{aligned}
N_{hydro} = & \int_{l_w} \overrightarrow{N_{fk-spar}} + \sum_{i=1}^{Np} \int_{l_{wi}} \overrightarrow{N_{fk-pontoon_\iota}} + \int_{l_w} \overrightarrow{N_{sb-spar}} + \sum_{i=1}^{Np} \int_{l_{wi}} \overrightarrow{N_{sb-pontoon_\iota}} \\
& + \int_{l_w} \overrightarrow{N_{div-spar}} + \sum_{i=1}^{Np} \int_{l_{wi}} \overrightarrow{N_{div-pontoon_\iota}} + \int_{l_w} \overrightarrow{N_{adm\_l-spar}} \\
& + \sum_{i=1}^{Np} \int_{l_{wi}} \overrightarrow{N_{adm\_l-pontoon_\iota}} + \int_{l_w} \overrightarrow{N_{adm\_nl-spar}} \\
& + \sum_{i=1}^{Np} \int_{l_{wi}} \overrightarrow{N_{adm\_nl-pontoon_\iota}} + \int_{l_w} \overrightarrow{N_{cf-spar}} + \sum_{i=1}^{Np} \int_{l_{wi}} \overrightarrow{N_{cf-pontoon_\iota}} \\
& + \overrightarrow{N_{bp-spar}} + \sum_{i=1}^{Np} \overrightarrow{N_{bp-pontoon_\iota}} + \overrightarrow{N_{int-spar}} + \int_{l_w} \overrightarrow{N_{drag-spar}} \\
& + \sum_{i=1}^{Np} \int_{l_{wi}} \overrightarrow{N_{drag-pontoon_\iota}}
\end{aligned}
\tag{3.3.28}
$$

To determine the wave loading incorporating rigid body motions of structure, the loading on each individual member is estimated in terms of relative velocities and accelerations of the structure in its translational and rotational modes. The total loading is obtained by summing these forces and moments along the principal axis of the structure in space and body fixed axis system respectively. The velocities and accelerations of the structure are determined from the solution of the motion equations which is discussed under the next chapter.

The following procedure has been employed to derive the wave loading calculations in three-dimensional matrix form for numerical simulation purpose.

- The wave kinematics, i.e. water particle acceleration, velocity and dynamic pressure which are defined in the wave reference axis system (w-system) are first transferred into body fixed axis system (b-system) and then to member fixed axis system (m-system).
- The force and moment calculations are carried out in the member fixed axis system for each element of the member and then integrated over its length.
- The forces and moments obtained in member fixed axis system are then transferred into space and body fixed axis system respectively and then summed up to obtain the total surge, sway, and heave force as well as roll, pitch, and yaw moment.

If $d\vec{f}$ is a force per unit submerged length acting on arbitrarily oriented cylinder having elemental length dl_w. Force in space fixed axis system can be written as,

$$
\begin{Bmatrix} F_x \\ F_y \\ F_z \end{Bmatrix}_g = [T_{bg}][T_{mb}] \int_{l_w} [T_{mb}]^{-1}[T_{bg}]^{-1} \begin{Bmatrix} df_x(\eta, u, \dot{u}, ..) \\ df_y(\eta, u, \dot{u}, ..) \\ df_z(\eta, u, \dot{u}, ..) \end{Bmatrix}_m dl_w \tag{3.3.29}
$$

where inverse of matrix $[T_{mb}], [T_{bg}]$ are multiplied within integral to transfer wave kinematics into member fixed axis system along the member length and after evaluating and integrating the forces, they are re-multiplied to get the forces in space fixed axis system. Similarly, moments are obtained using the following relationships,

$$\begin{Bmatrix} N_x \\ N_y \\ N_z \end{Bmatrix}_b = [T_{mb}] \int_{l_w} [T_{mb}]^{-1} [T_{bg}]^{-1} \vec{r} \begin{Bmatrix} df_x(\eta, u, \dot{u}, ..) \\ df_y(\eta, u, \dot{u}, ..) \\ df_z(\eta, u, \dot{u}, ..) \end{Bmatrix}_m dl_w \tag{3.3.30}$$

where $\vec{r}$ is position vector of element dl_w from the centre of gravity of whole body.

For simulation purpose, each force and moment component from Eq. (3.3.27) and Eq. (3.3.28) are derived in matrix form and included under APPENDIX C-2.

3.4 Mooring system model

Floating wind turbine systems are held in position by means of the mooring system. For the chosen tension leg platform wind turbine, it provides stability in addition to station keeping. The mooring system is the main contributor to such system's stability that means a failure in this component would likely to cause a destruction of the complete system. When the platform is displaced from its equilibrium position, the tethered mooring lines will exert forces on the platform to restore it to its original equilibrium position. These restoring forces and their moments are non-linear functions of platform displacement and in this thesis, they are modelled using a quasi-static approach. The formulation developed for evaluating forces and moments due to mooring lines are included under APPENDIX C-3.

4 NUMERICAL PROCEDURE FOR SOLVING EQUATIONS OF MOTIONS

The motion equations defined for the chosen floating wind turbine described in the previous chapter are highly nonlinear not only because of nonlinear wave kinematic and nonlinear force models adopted but also due to the product of variables appearing in the motion equations. The nonlinearity further manifests while evaluating forces and moments as they are dependent on the instantaneous position, velocity, and acceleration of the structure which are not known before solving the equations. To solve these equations, the following numerical procedure is employed.

1. Start from an initial state in which the displacement and velocity of the structure are zero and the environmental parameters such as water depth, wind, wave and current are given.
2. Compute the instantaneous length of structural members exposed to wind and waves.
3. Compute the forces and moments by performing numerical integration.
4. Solve the equations of motions to give new position and velocity of the structure.
5. Go to step 2 and repeat for the next time step.

This chapter presents the above numerical procedure in detail including the description of FORTRAN programme developed under this research study.

4.1 Instantaneous length of TLPWT members exposed to wind and waves

To compute the instantaneous length of the chosen TLPWT members exposed to wind and waves, one needs to find the common point between a three-dimensional curved wave surface and a straight line in the space representing a central line of the surface piercing structural member of the TLPWT system. Since the surface changes with time and the attitude of the TLPWT being determined during the process of the solution, this point must be found at each time step during the simulation. Below procedure is followed to obtain this common point for the wave surface and surface piercing member of the TLPWT system.

The wave surface and the centreline of the surface piercing member of the TLPWT as illustrated in the Figure 4.1.1 is expressed by the following two equations respectively.

For wave, $$z = \eta(x, y, t) \tag{4.1.1}$$

For TLPWT members, $$z = A_1(t)x + B_1(t)y + C_1(t)$$
$$z = A_2(t)x + B_2(t)y + C_2(t) \tag{4.1.2}$$

The co-ordinate of the common point (x_s, y_s, z_s) must satisfy the below equation,

$$\{\eta(x_s, y_s, t) - [A_1(t)\, x_s + B_1(t)\, y_s + C_1(t)]\}^2 + \{\eta(x_s, y_s, t) - [A_2(t)\, x_s + B_2(t)\, y_s + C_2(t)]\}^2 = 0 \tag{4.1.3}$$

This is equivalent to minimising the following function,

$$G(x_s, y_s, t) = \begin{Bmatrix} \{\eta(x_s, y_s, t) - [A_1(t)x_s + B_1(t)y_s + C_1(t)]\}^2 \\ + \\ \{\eta(x_s, y_s, t) - [A_2(t)x_s + B_2(t)y_s + C_2(t)]\}^2 \end{Bmatrix} \tag{4.1.4}$$

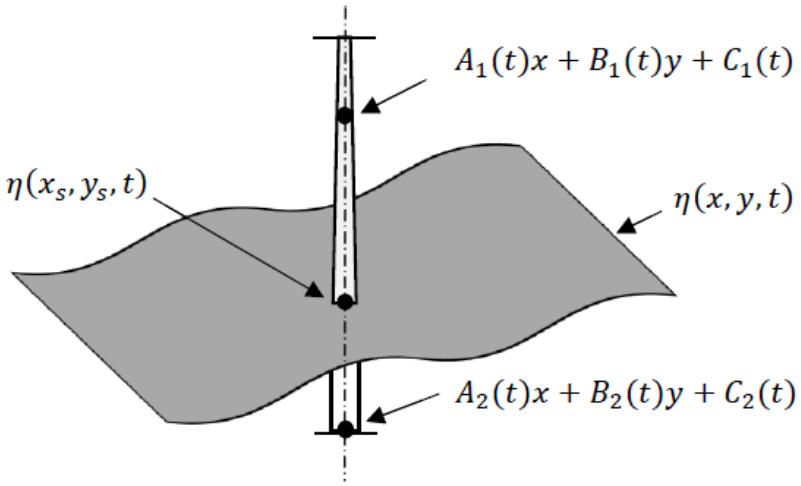

Figure 4.1.1 Surface piercing member of TLPWT

The downhill simplex method developed by Nelder and Mead (1965) is used to minimize the function $G(x_s, y_s, t)$ with the tolerable error, ε_s being taken as 1e-06. This method requires solely evaluation of function instead of derivatives of functions that are computationally expensive. This method is fast if a good initial estimate of the minimum can be specified for the problem. In this model, the coordinates of the intersection point between the centreline of the vertical member of the TLPWT system and the mean free surface is taken as an initial estimate.

Once the common point is found, length of the TLPWT members exposed to wind and waves can be determined and that defines the limits for integrating forces due to wind, waves and current. This procedure is programmed using FORTRAN 90 and validated with the MATLAB code for spar developed by Ma and Patel (2001).

4.2 Computation of forces and moments

After the instantaneous length of TLPWT members exposed to wind and waves are found, the forces and moments due to the wind, waves, current, and mooring system can be calculated using the numerical integration method. An iterative blade element and momentum theory is used to calculate the wind loads acting on the turbine rotor whereas quadratic drag force equation is used to calculate the wind loads acting on the tower and floating platform members exposed to wind. The wave and current loads acting on the tower and floating platform members exposed to waves are calculated using Rainey's slender body approach whereas mooring loads are calculated using a quasi-static approach. The formulation for calculating these external forces and its moment components are presented in the previous chapter. The integration procedure adopted for its implementation in the numerical model is described under the following subsection.

4.2.1 Iterative blade element and momentum theory

In the numerical model, the BEM theory is employed to calculate the wind forces acting on the turbine rotor. The theory is altered to account for the effect of wave-induced platform motions as described under section 3.2.3, i.e. including relative velocities and directions. The theory is

applied by dividing blade of a wind turbine spanwise into small elements that act independently of surrounding elements and operate aerodynamically as 2-D aerofoil whose forces can be calculated based on the local flow conditions, i.e., induced wind velocities in an axial and tangential direction, and corresponding drag and lift coefficients. These induced velocities affect the inflow in the rotor plane and hence affect the forces. An iterative procedure attached in APPENDIX B is employed to calculate the induced velocities in an axial and tangential direction so that the forces on that element can be computed using aerofoils drag and lift coefficients. The forces on each element of the blade for all the blades of the turbine are then summed up to calculate the total thrust acting on the wind turbine rotor at each time step during the simulation.

4.2.2 Numerical integration using Simpson's rule

In the numerical model, wind, waves, and current loads acting on the respective exposed length of the tower and platform members are evaluated using an adaptive recursive Simpson's rule. A well-known feature of this method is that the number of divisions along the member will be doubled if the error tolerance is exceeded. This feature can reduce the computational cost in the sense that no more than the necessary computations are needed to achieve the desired accuracy. Its disadvantage is that the segments are halved uniformly according to a global error estimate, and so when the integrand changes rapidly in some areas and distributes quite uniformly in others, the segment in the latter part of the domain may become too small. In this case, wind speed profile is assumed to follow either logarithmic or power law whereas the wave kinematics decays exponentially with the water depth. If wind speed profile follows a logarithmic or power law, the property of integrand will be very different at the tower base and for rest of the top segment of the tower where such wind speed profiles become nearly uniform. If the adaptive recursive Simpson's rule is simply used over the whole tower length, it can be expected that the segments become unnecessarily small and the computational cost will be higher. To avoid this, the tower length is first divided into ten parts and then the recursive Simpson's rule is applied. Although the chosen floating platform has a shallow draft, the property of integrand may vary significantly over its member lengths. Due to high water particle velocities and accelerations associated with extreme waves, integrand will be highly exponential and hence will need a higher number of segments for recursive Simpson's rule to start with. In the simulation, twenty segments are used for the chosen floating platform members. The relative error tolerance (ε1) needed in this rule to control the process is chosen such that the further reduction of (ε1) leads to a negligible difference.

4.3 Solving equations of motions

The equations of motions for floating wind turbine have already been described in chapter 3, section 3.1. These are given by twelve first order nonlinear ordinary differential equations with $\vec{X}, \vec{\theta}, \overrightarrow{U_c}, and\ \vec{\Omega}$ being the unknown variables. The forces and moments appearing on the right

side of equations depends upon the displacement, velocity and acceleration of the platform. Such system of equations can be written in the following form,

$$\dot{x}_i = f(x_j, \dot{x}_j, t), \text{ where i, j = 1, 2…12} \tag{4.3.1}$$

There are several methods available for solving a system of first order ordinary differential equations if they are written in the following form,

$$\dot{x}_i = f(x_j, t), \text{ where i, j = 1, 2…12} \tag{4.3.2}$$

If the initial condition of all the state variables is known, the system of equations given by Eq. (4.3.2) can be solved by any standard numerical time integration method. Depending on the method used for numerical integration, the general procedure involves the evaluation of the right-hand side of Eq. (4.3.2) once or multiple times at each time step. The procedure becomes computationally intensive if the right-hand side is complicated function of the state variables and if more than one evaluation is needed at each time step. Therefore, it is decided to re-formulate the equations of motion such that the right-hand side of the equations does not contain the acceleration terms. This is discussed in the following section. The general procedure followed here is like that described by Pauling and Webster (1986).

4.3.1 Formulation of equations of motions

The total external force and moment appearing on the right-hand side of equations of motions at time t is given by,

$$\vec{F}(t) = \overrightarrow{F_{gravity}}(t) + \overrightarrow{F_{aero}}(t) + \overrightarrow{F_{hydro}}(t) + \overrightarrow{F_{moor}}(t) \tag{4.3.3}$$

$$\vec{N}(t) = \overrightarrow{N_{gravity}}(t) + \overrightarrow{N_{aero}}(t) + \overrightarrow{N_{hydro}}(t) + \overrightarrow{N_{moor}}(t) \tag{4.3.4}$$

By expanding hydrodynamic force and moment terms, above equations can be written as,

$$\begin{aligned}\vec{F}(t) = \overrightarrow{F_{gravity}}(t) + \overrightarrow{F_{aero}}(t) + \overrightarrow{F_{fk}}(t) + \overrightarrow{F_{sb}}(t) + \overrightarrow{F_{div}}(t) + \overrightarrow{F_{adm}}(t) \\ + \overrightarrow{F_{cf}}(t) + \overrightarrow{F_{bp}}(t) + \overrightarrow{F_{int}}(t) + \overrightarrow{F_{moor}(t)}\end{aligned} \tag{4.3.5}$$

$$\begin{aligned}\vec{N}(t) = \overrightarrow{N_{gravity}}(t) + \overrightarrow{N_{aero}}(t) + \overrightarrow{N_{fk}}(t) + \overrightarrow{N_{sb}}(t) + \overrightarrow{N_{div}}(t) + \overrightarrow{N_{adm}}(t) \\ + \overrightarrow{N_{cf}}(t) + \overrightarrow{N_{bp}}(t) + \overrightarrow{N_{int}}(t) + \overrightarrow{N_{moor}(t)}\end{aligned} \tag{4.3.6}$$

Here, the force $\overrightarrow{F_{adm}}$ and moment $\overrightarrow{N_{adm}}$ consists of both linear and nonlinear added mass force and moment terms. The force $\overrightarrow{F_{adm\_l}}$ and moment $\overrightarrow{N_{adm\_l}}$ are linearly dependant on the acceleration and velocity of the body whereas nonlinear force $\overrightarrow{F_{adm\_nl}}$ and moment $\overrightarrow{N_{adm\_nl}}$ terms are dependent on the product of acceleration and velocity of the body. Eqs. (4.3.5) and (4.3.6) can be re-written by separating linear force and moment terms as follows,

$$\vec{F}(t) = \overrightarrow{F_o}(t) + \overrightarrow{F_{adm\_l}}(t) \tag{4.3.7}$$

$$\vec{N}(t) = \overrightarrow{N_o}(t) + \overrightarrow{N_{adm\_l}}(t) \tag{4.3.8}$$

where, $\overrightarrow{F_o}(t)$ and $\overrightarrow{N_o}(t)$ are total nonlinear force and moment terms acting on the floating wind turbine system. $\overrightarrow{F_{adm\_l}}(t)$ and $\overrightarrow{N_{adm\_l}}(t)$ are force and moment components of transverse

added mass force, which is linearly dependant on translational and rotational acceleration of the body and is given by,

$$\overrightarrow{F_{adm\_l}}(t) = [a_{11}(t)]\frac{d\overrightarrow{U_c}}{dt} + [a_{12}(t)]\frac{d\vec{\Omega}}{dt} \tag{4.3.9}$$

$$\overrightarrow{N_{adm\_l}}(t) = [a_{21}(t)]\frac{d\overrightarrow{U_c}}{dt} + [a_{22}(t)]\frac{d\vec{\Omega}}{dt} \tag{4.3.10}$$

The total external forces and moments given in Eq. (4.3.7) and Eq. (4.3.8) can be re-written as follows,

$$\vec{F}(t) = \overrightarrow{F_o}(t) + [a_{11}(t)]\frac{d\overrightarrow{U_c}}{dt} + [a_{12}(t)]\frac{d\vec{\Omega}}{dt} \tag{4.3.11}$$

$$\vec{N}(t) = \overrightarrow{N_o}(t) + [a_{21}(t)]\frac{d\overrightarrow{U_c}}{dt} + [a_{22}(t)]\frac{d\vec{\Omega}}{dt} \tag{4.3.12}$$

where, the added mass and inertia matrices $[a_{11}(t)]$, $[a_{12}(t)]$, $[a_{21}(t)]$, and $[a_{22}(t)]$ are time dependant due to integration of elemental forces and moments over instantaneous wetted length of the TLPWT members. Hence, the equations of motions can be re-written as,

$$[M]\frac{d\overrightarrow{U_c}}{dt} = \vec{F}(t) \tag{4.3.13}$$

$$[I]\frac{d\vec{\Omega}}{dt} = \vec{N}(t) - \left(\vec{\Omega} \times [I]\vec{\Omega}\right) \tag{4.3.14}$$

$$\frac{d\vec{X}}{dt} = \overrightarrow{U_c} \tag{4.3.15}$$

$$\frac{d\vec{\theta}}{dt} = [B]^{-1}\,\vec{\Omega} \tag{4.3.16}$$

Following Eq. (4.3.11) and (4.3.12), Eq. (4.3.13) and (4.3.14) can be written as follows,

$$[M]\frac{d\overrightarrow{U_c}}{dt} = \overrightarrow{F_o}(t) + [a_{11}(t)]\frac{d\overrightarrow{U_c}}{dt} + [a_{12}(t)]\frac{d\vec{\Omega}}{dt} \tag{4.3.17}$$

$$[I]\frac{d\vec{\Omega}}{dt} = \overrightarrow{N_o}(t) + [a_{21}(t)]\frac{d\overrightarrow{U_c}}{dt} + [a_{22}(t)]\frac{d\vec{\Omega}}{dt} - \left(\vec{\Omega} \times [I]\vec{\Omega}\right) \tag{4.3.18}$$

By re-arranging, above equations can be re-written as,

$$([M] - [a_{11}(t)])\frac{d\overrightarrow{U_c}}{dt} - [a_{12}(t)]\frac{d\vec{\Omega}}{dt} = \overrightarrow{F_o}(t) \tag{4.3.19}$$

$$-[a_{21}(t)]\frac{d\overrightarrow{U_c}}{dt} + ([I] - [a_{22}(t)])\frac{d\vec{\Omega}}{dt} = \overrightarrow{N_o}(t) - \left(\vec{\Omega} \times [I]\vec{\Omega}\right) \tag{4.3.20}$$

The above equations can be re-written in the matrix form as,

$$\begin{bmatrix} [M] - [a_{11}(t)] & -[a_{12}(t)] \\ -[a_{21}(t)] & ([I] - [a_{22}(t)]) \end{bmatrix} \begin{Bmatrix} \frac{d\overrightarrow{U_c}}{dt} \\ \frac{d\vec{\Omega}}{dt} \end{Bmatrix} = \begin{Bmatrix} \overrightarrow{F_o}(t) \\ \overrightarrow{N_o}(t) - \left(\vec{\Omega} \times [I]\vec{\Omega}\right) \end{Bmatrix} \tag{4.3.21}$$

Re-arranging above equations as,

$$\begin{Bmatrix} \frac{d\overrightarrow{U_c}}{dt} \\ \frac{d\vec{\Omega}}{dt} \end{Bmatrix} = \begin{bmatrix} [M] - [a_{11}(t)] & -[a_{12}(t)] \\ -[a_{21}(t)] & ([I] - [a_{22}(t)]) \end{bmatrix}^{-1} \begin{Bmatrix} \overrightarrow{F_o}(t) \\ \overrightarrow{N_o}(t) - (\vec{\Omega} \times [I]\vec{\Omega}) \end{Bmatrix} \tag{4.3.22}$$

$$\begin{Bmatrix} \frac{d\overrightarrow{U_c}}{dt} \\ \frac{d\vec{\Omega}}{dt} \end{Bmatrix} = \begin{bmatrix} [m_{11}(t)] & [m_{12}(t)] \\ [m_{21}(t)] & [m_{22}(t)] \end{bmatrix} \begin{Bmatrix} \overrightarrow{F_o}(t) \\ \overrightarrow{N_o}(t) - (\vec{\Omega} \times [I]\vec{\Omega}) \end{Bmatrix} \tag{4.3.23}$$

where,
$$\begin{bmatrix} [m_{11}(t)] & [m_{12}(t)] \\ [m_{21}(t)] & [m_{22}(t)] \end{bmatrix} = \begin{bmatrix} [M] - [a_{11}(t)] & -[a_{12}(t)] \\ -[a_{21}(t)] & ([I] - [a_{22}(t)]) \end{bmatrix}^{-1} \tag{4.3.24}$$

Based on Eq. (4.3.22) and Eq. (4.3.23), the equation of motions can be re-written as,

$$\frac{d\overrightarrow{U_c}}{dt} = [m_{11}(t)]\,\overrightarrow{F_o}(t) + [m_{12}(t)]\,(\overrightarrow{N_o}(t) - \vec{\Omega} \times [I]\vec{\Omega}) \tag{4.3.25}$$

$$\frac{d\vec{\Omega}}{dt} = [m_{21}(t)]\,\overrightarrow{F_o}(t) + [m_{22}(t)]\,(\overrightarrow{N_o}(t) - \vec{\Omega} \times [I]\vec{\Omega}) \tag{4.3.26}$$

$$\frac{d\vec{X}}{dt} = \overrightarrow{U_c} \tag{4.3.27}$$

$$\frac{d\vec{\theta}}{dt} = [B]^{-1}\,\vec{\Omega} \tag{4.3.28}$$

The right side of Eq. (4.3.25) and (4.3.26) does not have any terms which are dependent on accelerations and hence can be integrated using any of standard numerical time integration method.

In the simulation, a cosine taper function is used to multiply the total force and moment terms appearing on the right side of Eq. (4.3.25) and (4.3.26) to reduce the effect of transient response. This will enable the exciting forces and moments to build up gradually from zero to its full value over a period specified by the taper function. This function is given by,

$$Z_{taper}(t) = \begin{cases} 1 - cos\left(\frac{\pi}{2 \cdot t \cdot T_{taper}}\right), & t \le T_{taper} \\ 1, & t > T_{taper} \end{cases} \tag{4.3.29}$$

where, T_{taper} is duration of taper function which is generally taken as 10 times of peak or characteristic wave period.

4.3.2 Numerical integration of equations of motions

The equations of motions presented in preceding sub-section are a system of first order, non-linear ordinary differential equations with the translational $\vec{X}$ and rotational $\vec{\theta}$ motions and its velocities $\overrightarrow{U_c}$ and $\vec{\Omega}$ being the unknown variables. An efficient numerical method is required to accurately and quickly perform simulation by solving equations of motions. Simple methods like Euler, modified Euler, need a very small-time step, and thus a large amount of computing time, to remain stable. Therefore, a more elaborate method is required to increase accuracy and to reduce the calculation time. A runge-kutta-fehlberg (also denoted as RKF45) method is well

suited for this purpose, as it gives procedure to determine the optimum step size, h being used. At each time step, two different approximations for the solution are made and compared. If they are in close agreement, the approximation is accepted. If they do not agree to a specified accuracy, the step size is reduced. Therefore, the method is stable at large time steps and relatively fast.

In the present study, fifth order Runge-Kutta method with an adaptive step size control is used. The details of this method may be found in Shampine (1994). The method adapts the number and position of the grid points during the iteration to keep the local error within the specified bound. It can be used for any initial value problem (I.V.P.) of the following type.

$$\frac{dy}{dt} = f(t,y) \quad t_0 \le t \le t_{max} \; where, t_{max} \; is \; simulation \; time \; T_{sim}$$
$$y(t_0) = y_0 \tag{4.3.30}$$

If we denote the solution of variable y_i at any time t_i and the time step as h, then an approximation to the solution of above equation can be made using a Runge-Kutta method of order 4 as,

$$y_{i+1} = y_i + \frac{25}{216}K_1 + \frac{1408}{2565}K_3 + \frac{2197}{4104}K_4 - \frac{1}{5}K_5 \tag{4.3.31}$$

A better approximation for the solution of above equation can be made using Runge-Kutta method of order 5 as,

$$z_{i+1} = z_i + \frac{16}{135}K_1 + \frac{6656}{12825}K_3 + \frac{28561}{56430}K_4 - \frac{9}{50}K_5 + \frac{2}{55}K_6 \tag{4.3.32}$$

where, the constants K_1 to K_6 used in the above equations are,

$$K_1 = h\, f(t_i, y_i) \tag{4.3.33}$$
$$K_2 = h\, f\left(t_i + \frac{1}{4}h, y_i + \frac{1}{4}K_1\right)$$
$$K_3 = h\, f\left(t_i + \frac{3}{8}h, y_i + \frac{3}{32}K_1 + \frac{9}{32}K_2\right)$$
$$K_4 = h\, f\left(t_i + \frac{12}{13}h, y_i + \frac{1932}{2197}K_1 - \frac{7200}{2197}K_2 + \frac{7296}{2197}K_3\right)$$
$$K_5 = h\, f\left(t_i + h, y_i + \frac{439}{216}K_1 - 8K_2 + \frac{3680}{513}K_3 - \frac{845}{4104}K_4\right)$$
$$K_6 = h\, f\left(t_i + \frac{1}{2}h, y_i - \frac{8}{27}K_1 + 2K_2 - \frac{3544}{2565}K_3 + \frac{1859}{4104}K_4 - \frac{11}{40}K_5\right)$$

The optimal step size sh can be determined by multiplying the scalar s time the current step size h. The scalar s is,

$$s = \left(\frac{\varepsilon_{tol}}{2|z_{i+1} - y_{i+1}|}\right)^{1/4} \approx s = 0.84\left(\frac{\varepsilon_{tol}}{|z_{i+1} - y_{i+1}|}\right)^{1/4} \tag{4.3.34}$$

Runge-Kutta-Fehlberg method uses fourth order Runge-Kutta method given by Eq. (4.3.31) and approximates the value of the local truncation error (at a specific node) along with the fifth order method given by Eq. (4.3.32). Since each of the above method makes use of the same

values of K_1,…., K_6 one of the big advantages of coupling these two methods is that only six function evaluations are required at each time step to obtain both 4th and 5th order approximations.

It can be seen from Eq. (4.3.31) and Eq. (4.3.32), that it is necessary to evaluate the right hand side of the system of equations six times for each time step. The computational procedure followed can be outlined as follows,

1. Begin with a known position and attitude of structure, specified as initial condition with a prescribed error tolerance ε_{tol}, and user specified step size h.
2. The instantaneous wetted length of TLPWT members and forces and moments due to wind, waves, and mooring system are calculated using numerical procedure described under section 4.1 and 4.2 respectively. Thus, the coefficient of matrices $m_{11}(t)$, $m_{12}(t)$, $m_{21}(t), m_{22}(t)$ and total forces $\overrightarrow{F_o}(t)$ and moments $\overrightarrow{N_o}(t)$ present in motion equations are now determined.
3. The constants K_1 to K_6 from Eq. (4.3.33) can be evaluated to find the approximation to the solution y_{i+1} and z_{i+1} using Eq. (4.3.31) and (4.3.32) respectively.
4. The numerical approximation of the global discretization error at the point t_{i+1} is estimated based on the difference between the solution of the fifth order runge-kutta method and the embedded fourth order formula.

$$\varepsilon_1 = |z_{i+1} - y_{i+1}| \tag{4.3.35}$$

5. If $\varepsilon_1 \geq \varepsilon_{tol}$ then decrease the step size to half and return to step 2 where new value of z_{i+1} and y_{i+1} are computed for this reduced step size. To calculate step size, scaling factor of s decribed in Eq. (4.3.35) is used.
6. Repeat the procedure until $t \leq T_{sim}$, where T_{sim} is final simulation time.

In the above-mentioned procedure, ε_1 is determined using the maximum error of the displacement components at the furthest point from the centre of gravity (here wind turbine hub height is used). The displacement at this point is calculated by the angular and translational displacement of the structure. ε_{tol} is the desired accuracy that is specified as $\varepsilon_{tol} = \varepsilon_2 \max(\overline{X_{hub}}, 1e-06)$, where ε_2 is the relative error tolerance and $\overline{X_{hub}}$ is the maximum of three displacement components of the above point at previous time step. ε_2 is determined through the numerical test.

Following the above procedure, the motion responses and the corresponding force and moment components are computed at each time step and stored in a separate output file. It enables to investigate the influence of any specific force component on the response of the structure. It will be particularly useful when a nonlinear response of the structure is being studied in which case one is interested in finding out the sensitivity of the response to changes in any specific force component. It may be noted that the numerical model developed under this research is suitable to study the nonlinear large amplitude responses of a chosen tension-leg-platform wind turbine.

A resonant motion such as low-frequency surge, sway, and yaw, and high-frequency ringing and springing heave, roll and pitch motions are good examples of studies where this numerical model can be effectively used.

4.3.3 Global performance analysis

Global performance analysis is generally carried out to determine the effect of environmental loads on the response parameters associated with overall floating wind turbine and its components, such as wind turbine, tall supporting tower, platform hull and mooring lines. The primary results expected from this analysis provide the input required for their structural design. The parameters chosen for the wind turbine are blade airgap, turbine fore-aft displacement, and thrust acting on the rotor. For the tower, the bending moment acting on it is chosen which is resultant of excitation loads due to wind and wave and restoring loads from the mooring lines and platform buoyancy. For platform hull, global motions such as offset, and heel angle and associated wave loads are considered whereas, for station keeping system, tension in each mooring line is considered. All these parameters depend upon individual components of the floating wind turbine and interaction among them. During the simulation, each component of the floating wind turbine, i.e., wind turbine, tower, platform and mooring lines dynamically interact with each other at each time step to produce the resultant time histories of their respective response parameters. As explained under previous section 4.3.2, along with the motions and the various forces and moments, the response parameters such as blade airgap and turbine fore-aft displacements are also calculated at each time step and stored under separate files during the simulation. The formulation used to calculate each parameter in the simulation are presented in the equations below,

A. Wind turbine response parameter

Blade airgap, AG

$$AG = \left(Z_{heave} + \theta_{pitch} \times Z_{blade-tip}\right) - \eta \tag{4.3.36}$$

Turbine fore-aft displacement, $X_{turbine}$

$$\overrightarrow{\Delta_{turbine}} = \begin{Bmatrix} X_{turbine} \\ Y_{turbine} \\ Z_{turbine} \end{Bmatrix} = \left(\vec{X} + \vec{\theta} \times \overrightarrow{Z_{hub}}\right) \tag{4.3.37}$$

Thrust, T

$$\mathrm{T} = \frac{1}{2}.\rho_{air}.\mathrm{B}.\sum_{\mathrm{i}=1}^{N_e} {\mathrm{V_R}_i}^2.\left(C_{l_i}.\cos\left(\phi_{inf_i}\right) + C_{d_i}.\sin\left(\phi_{inf_i}\right)\right).\mathrm{c_i}.\mathrm{dr}_i \tag{4.3.38}$$

B. Tower response parameter

Bending moment in tower at COG of TLPWT, T_{BM}

$$T_{BM} = \overrightarrow{r_{hub}} \times T + \int_{l_d} \vec{r} \times dT_{drag}\ dl_d + \int_{l_w} \vec{r} \times df_{wave}\ dl_w + \sum_{i=1}^{N_{moor}} \overrightarrow{r_{moor,i}} \times T_{moor,i} \tag{4.3.39}$$

C. Platform hull

Wave force, F_{hydro}

$$\overrightarrow{F_{hydro}} = [T_{bg}][T_{mb}] \int_{l_w} d\overrightarrow{f_{wave}}\ dl_w \tag{4.3.40}$$

D. Mooring line response

Tension in mooring line, T_{moor}

$$Tmoor_j = \begin{cases} Tmoor_{in} + \dfrac{EA}{Li_j}\left(Lt_j - Li_j\right)\ if\ \left(Lt_j > Li_j\right) \\ 0 \qquad\qquad otherwise \end{cases} \tag{4.3.41}$$

The description of each parameter from the above equations are given in the previous chapter under respective sections. These response parameters are chosen to investigate their predictions using hybrid hydrodynamic model suggested in this thesis.

4.4 FORTRAN programming

The above numerical procedure is programmed using FORTRAN 90. In the code, $\varepsilon_1 = \varepsilon_2$ is used, leaving the choice of only one parameter associated with accuracy control, although the two error tolerances are not necessarily relevant. This choice makes the investigation of convergence simpler. If the error is small enough, the results should not be different from those obtained by using two different error tolerance values. However, this error tolerance is relevant when simulations are performed using analytical wave kinematic modelling such as Airy's linear wave theory and Fenton's nonlinear steady wave theory. For FNPT based QALE-FEM, in addition to afore-mentioned error tolerances, mesh size is an additional parameter which play significant role in the convergence. An optimized mesh size needs to be obtained through convergence study before commencing any simulation. Based on the convergence study, it is found that 40 divisions per wave length and 100-time steps per wave period are required to achieve enough accuracy for extreme regular wave. For extreme random wave group, 100 divisions per peak wave length and 200-time steps per peak wave period are enough to achieve the desired accuracy.

5 NUMERICAL MODEL VALIDATION AND CONVERGENCE TESTS

The numerical model presented in chapter 3 and 4 is validated using published experimental results by DeepCwind consortium (Prowell, et al., 2013). DeepCwind consortium has conducted a 1/50th scale model test program where several floating wind turbine platforms were tested under a variety of wind and wave loading conditions at the Maritime Research Institute Netherlands (MARIN) wave basin. A range of cases are chosen from these experimental results for the validation purpose. The investigation using these chosen validation cases should shed significant light on whether the numerical model is reliable and accurate. Also, the results of convergence tests performed by controlling error tolerance parameters associated with the integration of force and motion equations described under section 4.4 are discussed.

5.1 Comparison with experimental results

The numerical model is validated by comparing its results with 1/50th scale model test data obtained from Prowell et al. (2013) for a tension-leg-platform wind turbine system shown in Figure 5.1.1. The wind turbine used in the test was based on NREL 5MW horizontal axis wind turbine with a rotor diameter of 126m. The turbine was mounted on to the DeepCwind tension leg platform which is basically a shallow draft spar buoy stiffened in roll and pitch mode by using a combination of horizontal pontoons and the mooring lines under tension.

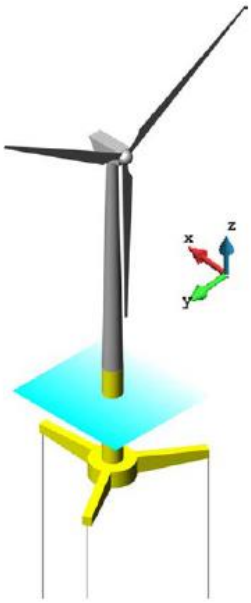

Figure 5.1.1 Tension-leg-platform wind turbine test model

This section first outlines the details of floating wind turbine components, i.e., wind turbine, tower, platform and mooring lines. Using these details, comparison of numerical model's

prediction with the test data are presented that focuses on global response of concerned floating wind turbine resulting from the aerodynamic and hydrodynamic loads.

5.1.1 Details of floating wind turbine test model

A DeepCwind tension-leg-platform wind turbine consists of a 5MW horizontal axis wind turbine, supported by hollow conical frustum shape tower and tension leg floating platform which is anchored to the seabed via tethered mooring lines in a water depth of 200m. Table 5.1.1 gives the pertinent system properties for the wind turbine, tower, floating platform, and mooring system.

Table 5.1.1 Details of tension-leg-platform wind turbine test model

A. Wind Turbine	
Power Output	5 MW
Rotor Orientation, Configuration	Upwind, 3blades
Rotor / Hub Diameter	126m / 3m
Hub height above SWL	90m
Overhang/Shaft Tilt/Precone	$10.58m/0^0/0^0$
Turbine Mass	397 160kg
B. Tower	
Tower height	77.6m
Tower base elevation above SWL	10m
Tower top elevation above SWL	87.6m
Tower base diameter	6m
Tower top elevation above SWL	3.87m
Tower Mass	302 240 kg
C. Floating Platform and Tether	
Legs Configuration 3 radially at	120^0
Radius to fairlead	30m
Draft of fairlead	28.5m
Mass	661 600kg
Displacement	2 8400 000kg
Platform draft	30m
Radius to anchor	30m

In the test model, turbine blades and tower were designed to be rigid to eliminate the aero-elastic complexities resulting from its flexibility. The blade's distributed aerodynamic properties along with the lift and drag coefficients of respective aerofoils are given in the attached APPENDIX D. A floating platform hull consists of vertical spar buoy and three equi-spaced horizontal pontoons. The principal dimensions of platform hull and pontoon arrangement is shown in Figure 5.1.2.

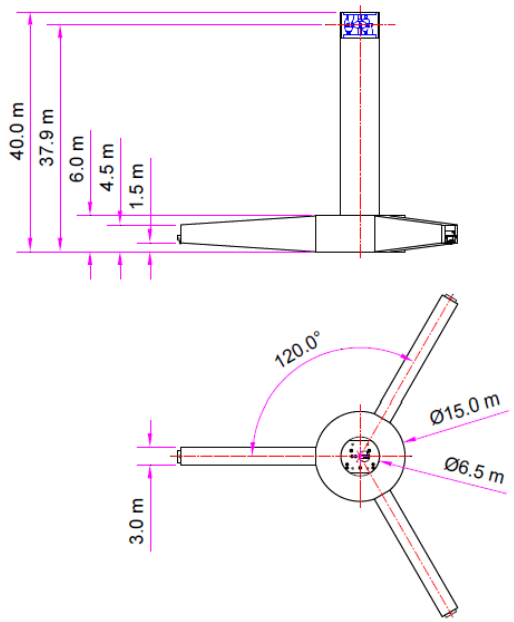

Figure 5.1.2 Principal dimensions of platform hull

5.1.2 Natural period of test model

Natural period of the concerned floating wind turbine test model is obtained from the calm water free decay test. The test is conducted by introducing a displacement to the platform in its all individual degrees of freedom and then allowing the system to come to rest. By performing FFT on time series of platform displacement in each degree of freedom, natural periods of the concerned structure are obtained. Figure 5.1.3 shows the time series of platform surge displacement and corresponding amplitude spectra where peak response appears at a frequency which is surge natural frequency of the platform. Here the platform was displaced to the full-scale equivalent of 4m in surge direction.

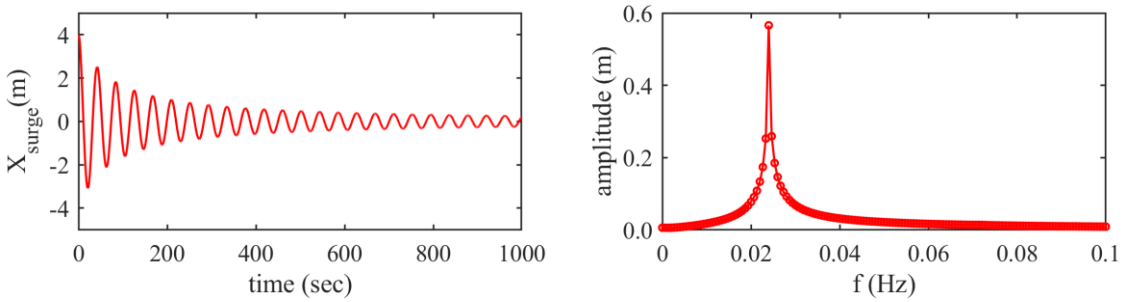

Figure 5.1.3 Time series and amplitude spectra of platform surge motion

Following the above procedure, all six DOF natural periods of the concerned floating wind turbine test model are calculated. Table 5.1.2 presents the comparison of natural periods for the concerned floating wind turbine measured by experiment and predicted by FAST software by NREL and the numerical model developed under this research study.

Table 5.1.2 Comparison of natural periods from numerical model and test data

Degree of freedom	Natural period (sec.)		
	Measured	Predicted	
	Experiment	FAST (NREL)	Numerical model
Surge	39.3	40.2	41.6
Sway	39.3	40.2	41.6
Heave	1.25	1.05	0.96
Roll	3.7	3.11/2.03*	2.05
Pitch	3.7	3.08/2.03*	2.05
Yaw	18.2	16.8	16.5

* without tower flexible mode (Koo, et al., 2012)

It can be seen from Table 5.1.2 that the overall simulated natural periods agree well with the model test results and the results predicted by NREL developed software FAST. However, some differences do exist which are mainly seen due to an assumption of a rigid tower in the numerical simulation model, as roll and pitch natural period calculated by Koo et al. (2012) by including rigid tower matched well with the predictions by the present numerical model.

5.1.3 Wind turbine performance

An aerodynamic model adopted in the present numerical model is validated by comparing its prediction of wind turbine performance parameter such as the thrust acting on the rotor with the test results. During the test, the wind was generated using a suspended rectangular rack with 35 fans, a series of screens, and an elliptically shaped nozzle which was 200m wide and 150m tall (full scale), this is being larger than the rotor swept area. Various wind environment generated, and the corresponding operating conditions of the turbine chosen for the validation are presented in the Table 5.1.3.

Table 5.1.3 Wind turbine operating parameter

Mean Steady Wind Speed (m/s)	Reference Height (m)	Rotor Speed (RPM)	Blade Pitch Angle (deg.)
7.0	90	4.95	6.4
9.0	90	5.66	6.4
11.4	90	7.78	6.4
16.0	90	9.19	6.4
21.0	90	12.73	6.4
30.5	90	0.0	85.0

The air density was taken as 1.225kg/m^3. To best represent the wind profile, the measured hub height wind speed was multiplied by a factor of 0.952 and a vertical power law wind shear exponent of 0.0912 was employed. These parameters yielded the best comparison between the

measured hub height wind speed and the information gleaned from the spatial survey of the wind generation machine output used for testing. Table 5.1.4 show the comparison of thrust values predicted by the numerical model as compared to the test results and predictions by FAST software developed by NREL, for steady wind cases described in the Table 5.1.3.

Table 5.1.4 Comparison of wind turbine thrust

Mean Steady Wind Speed (m/s)	Thrust (kN)		
	Experiment	FAST	Numerical Model
7.0	126.1	102.6	102.4
9.0	156.9	143.4	143.3
11.4	202.7	247.2	245.6
16.0	381.7	413.0	408.1
21.0	749.8	779.3	771.7
30.5	156.8	153.2	147.0

It can be seen from Table 5.1.4 that the wind turbine thrust which is critical for simulating the global response of the floating wind turbine is captured well by the numerical model. The maximum percentage difference of 19% and 21% with respect to test results are seen for the wind speed of 7m/s and 11.4m/s respectively. For the rest of the wind speeds, the percentage difference in predictions were within 10%. These differences could be resulting from the measurement error during the test as thrust comparisons with the established wind turbine design code FAST developed by NREL are seen matching well with the percentage differences less than 5% for all the tested wind speeds. The maximum thrust values predicted are very similar to the NREL 5MW reference wind turbine thrust value of 800kN.

Next, the global response of the concerned floating wind turbine is compared under the steady wind, regular wave, and combined irregular wave + steady wind. This systematic approach allows for easier identification of root causes for discrepancies between the test data and the numerical model. These noted results highlight many merits of numerical model's predictive capabilities in addition to potential shortcomings in the test data, as well as possible areas of improvement for the numerical model. Lastly, it should be noted that all the relevant global motion results presented in the subsequent sections are given with respect to the centre of gravity of the total system.

5.1.4 Global response under steady wind only

Numerical simulations for the concerned floating wind turbine's responses subjected to six steady wind environments detailed in Table 5.1.3 were conducted and compared with the experimental test data. Figure 5.1.4 presents the comparison of mean surge motion of the platform and the corresponding mean bending moment in tower at its base, for various steady wind speeds.

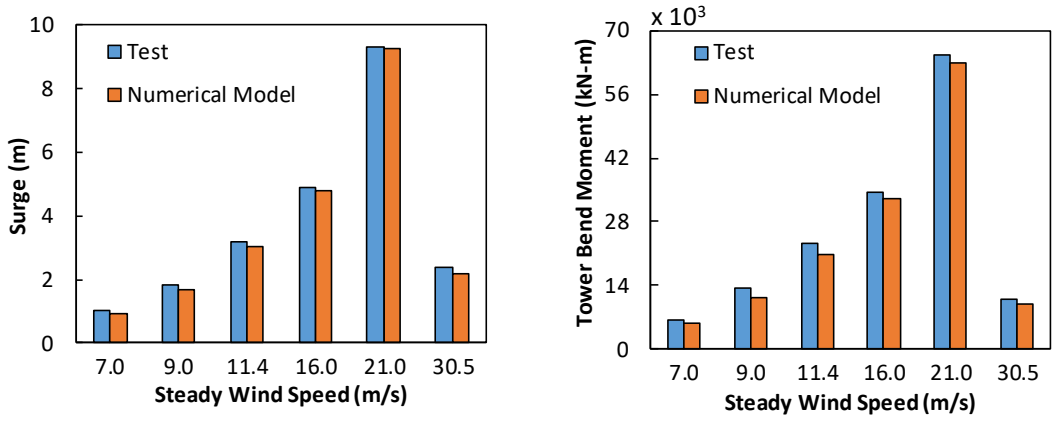

Figure 5.1.4 Comparison of global response parameters a) mean surge, and b) mean tower base bending moment

It can be seen from Figure 5.1.4 that the comparison between the numerical model and the test data is quite favourable. One noticeable trend shown in the figure is that the numerical model appears to underpredict the mean surge offset with the largest discrepancy, from percentage difference point of view, occurring at low operational wind speed and for extreme wind speed where the blades are feathered, and the rotor is parked. For these afore-mentioned conditions, thrust load acting on the rotor is low and the aerodynamic drag loads acting on the nacelle and instrumentation cable bundle, which are not included in the numerical model, may be contributing a substantial portion of the total overall system surge force. Unlike the total system surge loading, the system overturning moment leading to tower bending response is dominated by the rotor, because it is higher above the sea water level than the centre of pressure for the tower, cable bundle, or platform. The rotor thrust by the numerical model is well predicted as shown in Table 5.1.4, so it stands to reason that the simulation and test data bending moment responses are very similar in Figure 5.1.4.

5.1.5 Global response under regular wave only

To validate the numerical model to test data due to wave excitation, the response of the DeepCwind tension leg platform to regular waves in the absence of wind is investigated. Since there was no wind, the blades were feathered, and the rotor was parked. Seven different regular waves with period of 7.5, 12.1, 14.3, and 20sec were considered. Two distinct amplitudes were investigated for periods of 12.1, 14.3, and 20sec for assessing any nonlinearity in the system response. All waves propagated in the positive surge direction. The DeepCwind tension leg platforms performance in the presence of regular waves is characterised by statistics of platform surge motion and pitch accelerations. For numerical model, simulation is run for 50 wave periods to achieve the desired steady-state results. The statistics for surge motion and pitch accelerations of the platform (i.e., mean, standard deviation, and range) are presented in Figure 5.1.5.

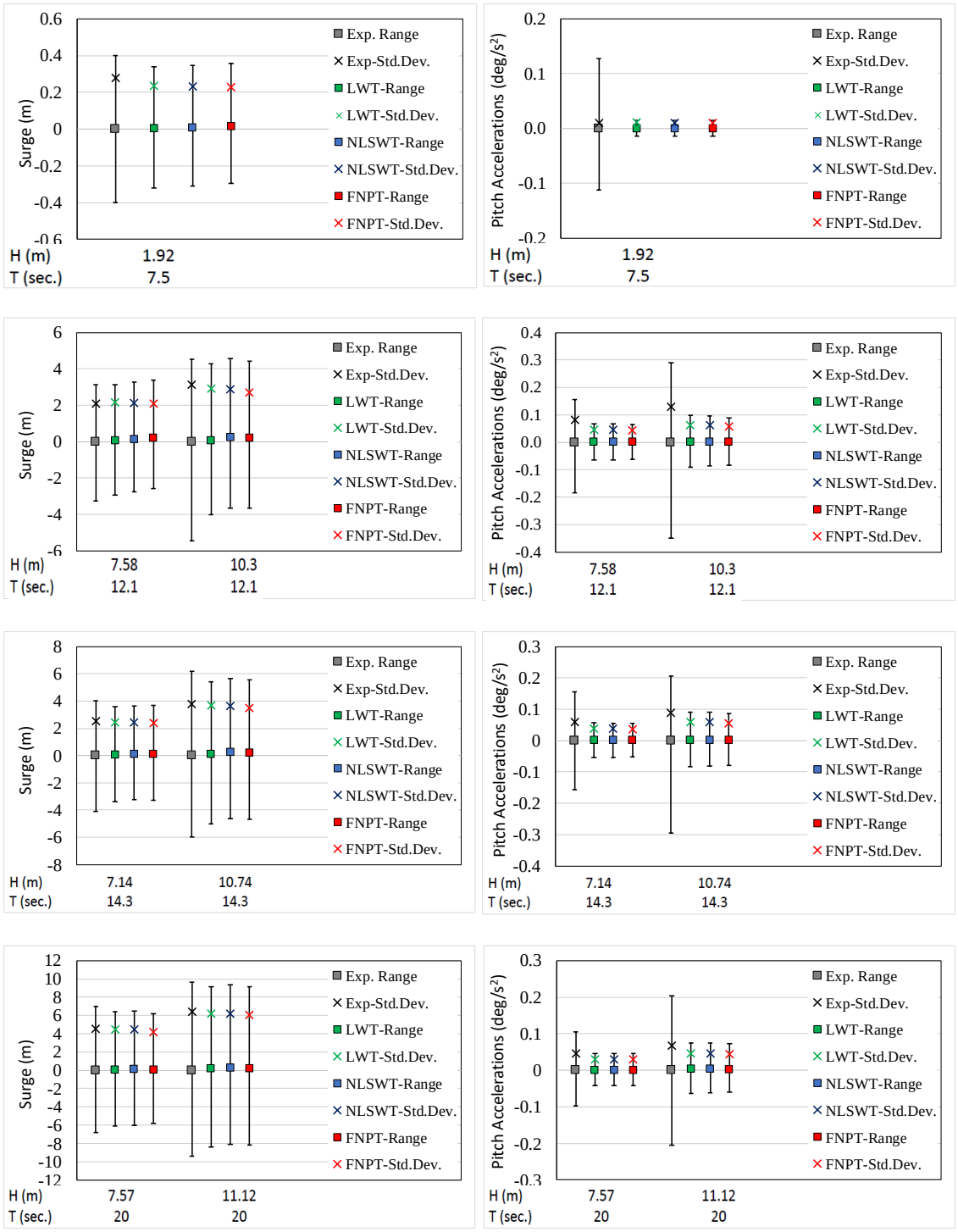

Figure 5.1.5 Comparison of statistics from numerical model and test data for a) surge motion, and b) pitch acceleration

The comparison of platform surge motion statistics presented in Figure 5.1.5 are quite good, as evidenced by numerical model's capability to capture the increase in surge motion response for a given wave period with increasing wave amplitude. However, there are some notable discrepancies between predictions by numerical models and the test data. The numerical model modestly underpredicts the pitch accelerations for the wave period of 7.5s, 12.1s and 14.3s which

is also observed by Prowell et al. (2013) while validating FAST model with the same test data. The higher order components associated with these waves are in close proximity of the concerned structure's pitch natural period causing resonance. In the numerical model, the tower was modelled as rigid, and hence pitch natural period of the structure is well away from the higher order hydrodynamic components. This underprediction of platform pitch and its effect on surge motion is attributed to lack of excitation due to higher order hydrodynamic components. Past investigations have shown this phenomenon to be important in understanding the pitch response of a TLP (Kim, 1991; Naess & Ness, 1992). It is particularly true because typical pitch and roll frequencies of TLPs reside outside the range of significant wave energy and are not directly excited. These simple load cases suggest that the floating wind turbine dynamics are reasonably recreated across many different independent wind and wave conditions but appear to systematically underestimate extremes for investigated response quantities.

5.1.6 Global response under combined steady wind and irregular wave

To complete the validation study, a combined steady wind and irregular wave cases are studied. Test data obtained from various combined wind and wave loading scenarios as identified in Table 5.1.5 are used for the comparison. A structure was excited with a JONSWAP spectrum while simultaneously being subjected to steady wind. Numerical simulations were conducted for 43 minutes with the 10-minute portion of time history containing maximum response is selected for reporting statistical results. A comparison of statistical results for wave surface elevation, pitch accelerations and tendon tensions are presented in Figure 5.1.6 and Figure 5.1.7 for normal and extreme wave conditions respectively. Tension statistics are presented for tendon 1 (downwind tendon) which exhibits maximum variation among all the tendons.

Table 5.1.5 Combined wind and wave tests for operating and extreme condition

Condition	Wind Speed	Blade Pitch	Rotor Speed	H_s	T_p	γ
Operating	7	6.4	4.95	2.0	7.5	2.0
	9		5.66	2.0	7.5	2.0
	11.4		7.78	2.0	7.5	2.0
	11.4		7.78	7.1	12.1	2.2
	16.0		9.19	7.1	12.1	2.2
	21.0		12.73	7.1	12.1	2.2
Extreme	21.0		12.73	10.5	14.3	3.0
	30.5	85.0	0.0	10.5	14.3	3.0

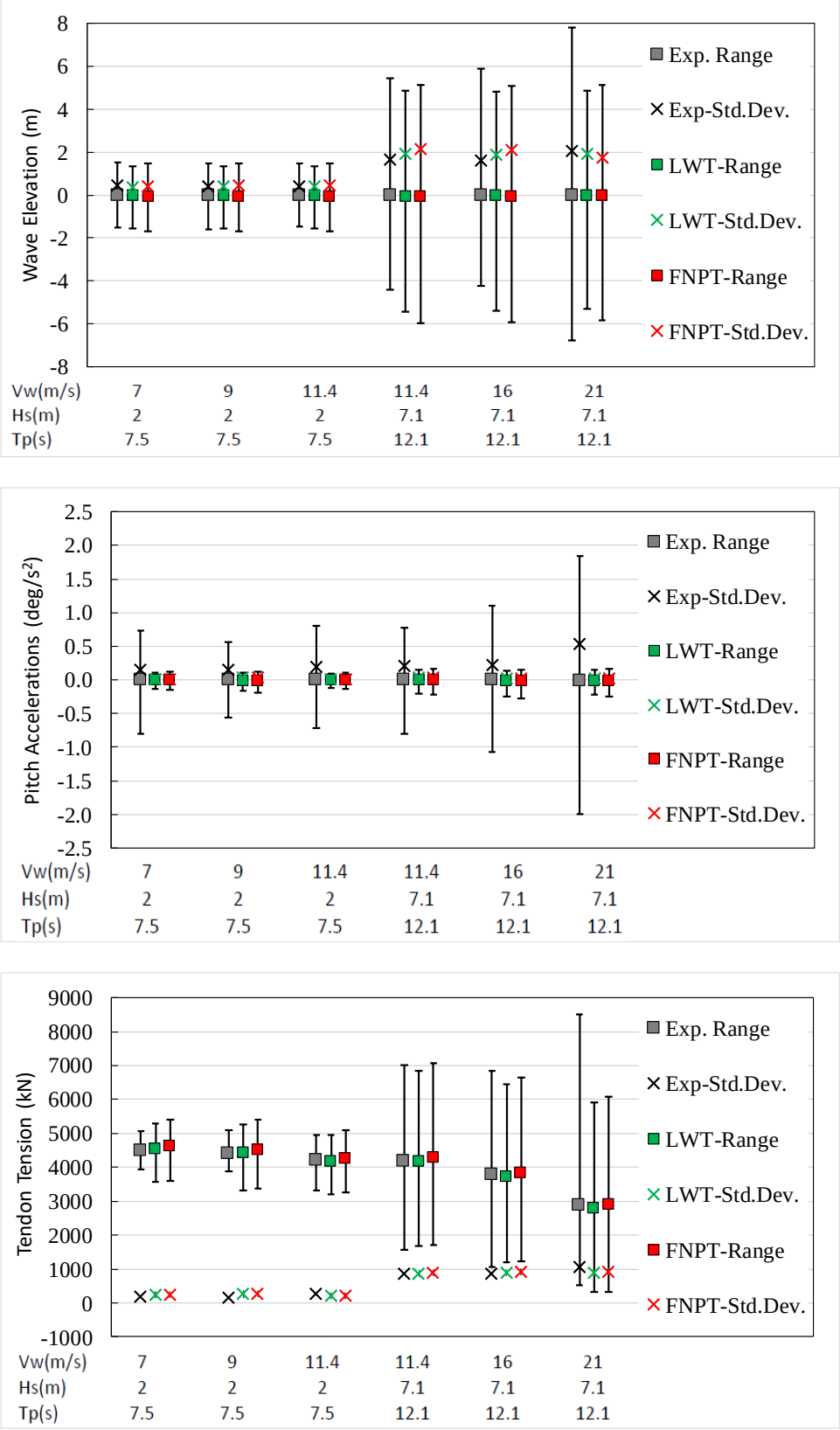

Figure 5.1.6 Comparison of statistics from numerical model and test data for a) wave elevation, b) pitch accelerations, and c) tendon tensions for operating condition

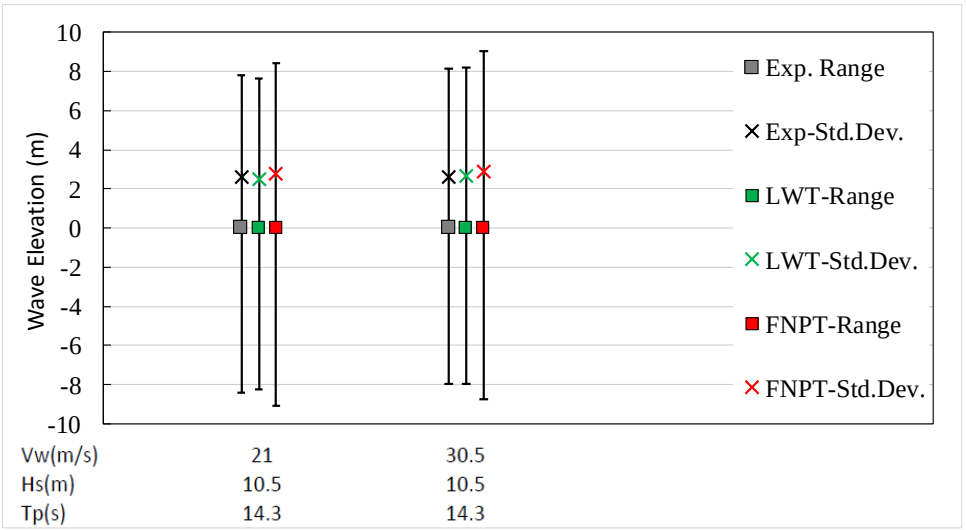

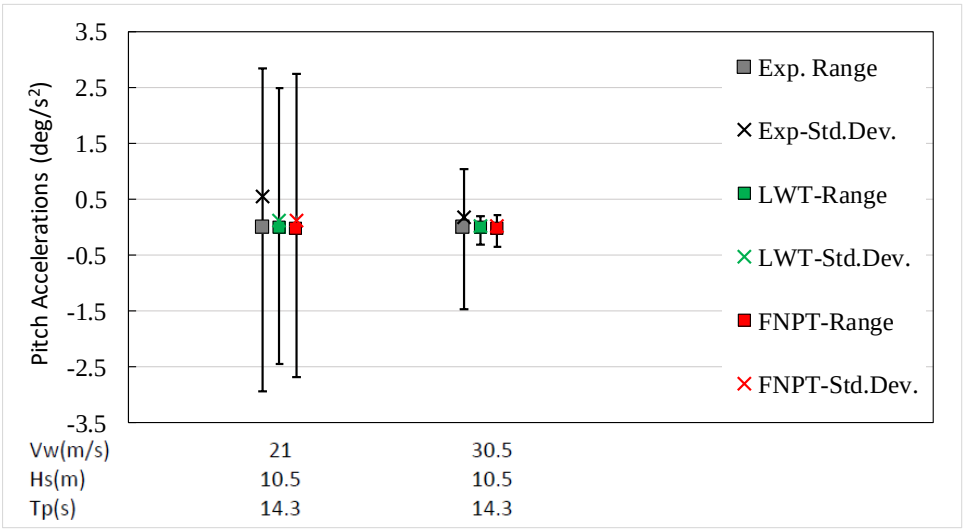

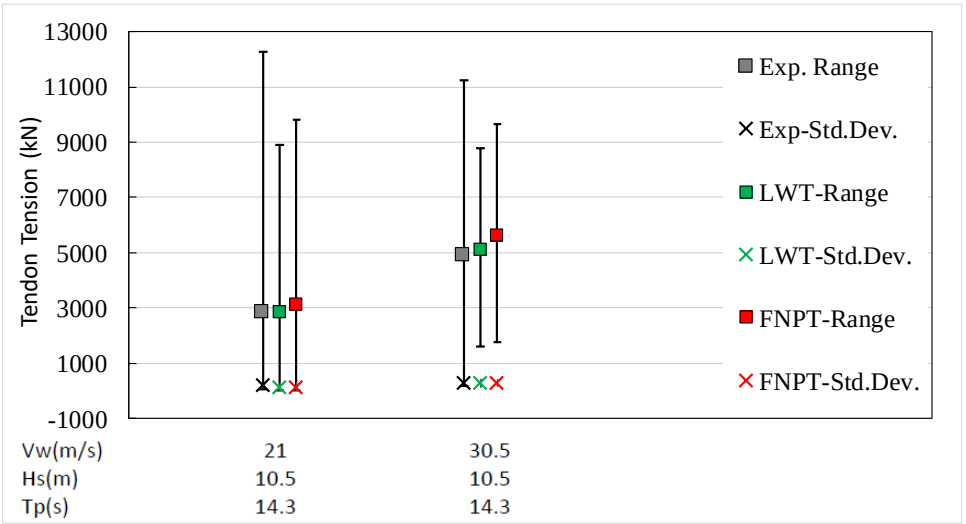

Figure 5.1.7 Comparison of statistics from numerical model and test data for a) wave elevation, b) pitch accelerations, and c) tendon tensions for extreme condition

A summary of quantitative statistics of wave surface elevation presented in Figure 5.1.6 and Figure 5.1.7 for normal and extreme wave conditions show reasonable agreement. The results for presented cases should be viewed with the consideration that the differences in wave surface statistics will likely propagate to the structures response parameters. Again, the platform pitch accelerations are significantly underestimated which is also observed by Prowell et al. (2013) while validating FAST model with the same test data. The extent of underestimation is more significant than that for the regular wave tests. It suggests that the numerical model was not capturing some excitation mechanism. Based on past findings (Naess and Ness 1992; Kim 1991) showing that second-order sum-frequency wave loads contribute significantly to the pitch response of a TLP, it was hypothesized that this was at least partially attributable to their absence in the simulation. Tendon tensions showed better agreement, however some differences do exist which are mainly due to quasi-static modelling of mooring lines, where drag and inertia loading is not considered.

Despite underprediction of platform pitch accelerations in all the test cases, the numerical model did a decent job predicting the character of the floating wind turbine's dynamic response for many of the investigated parameters. In addition to this, one more trend was observed during experimental validation for regular and irregular wave cases. For example, numerical model with FNPT wave model predicted structures dynamic response lower as compared to linear wave model in regular wave cases whilst higher for irregular wave cases. However, the wave steepness used in the test were relatively low and hence the differences in responses predicted by all the three models were not significant. This trend is further investigated in subsequent chapters in detail.

5.2 Convergence tests

In the previous section, numerical model described in this thesis has been validated using experimental results by specifying two convergence parameters, i.e. a time step, h and error tolerance ε_{tol}. Reasonable agreement with the experimental data has been achieved. However, one may wonder what would happen if other values of time step and error tolerances are used. In this section, the convergence parameters are discussed to shed some light on whether the time step and error tolerances used are appropriate and on the choice of these parameters in the calculations. Although similar investigations have been carried out for all the cases presented in this thesis, only those corresponding to steepest regular wave from Figure 5.1.5, whose wave height, H is $10.3m$ and period, T_o is $12.1sec$, are presented here.

For investigating the effect of time step and error tolerance, chosen case is run with various time steps and error tolerances. Figure 5.2.1 and Figure 5.2.2 presents the time histories of surge, and pitch response obtained by using different step size h, and error tolerance ε_{tol}.

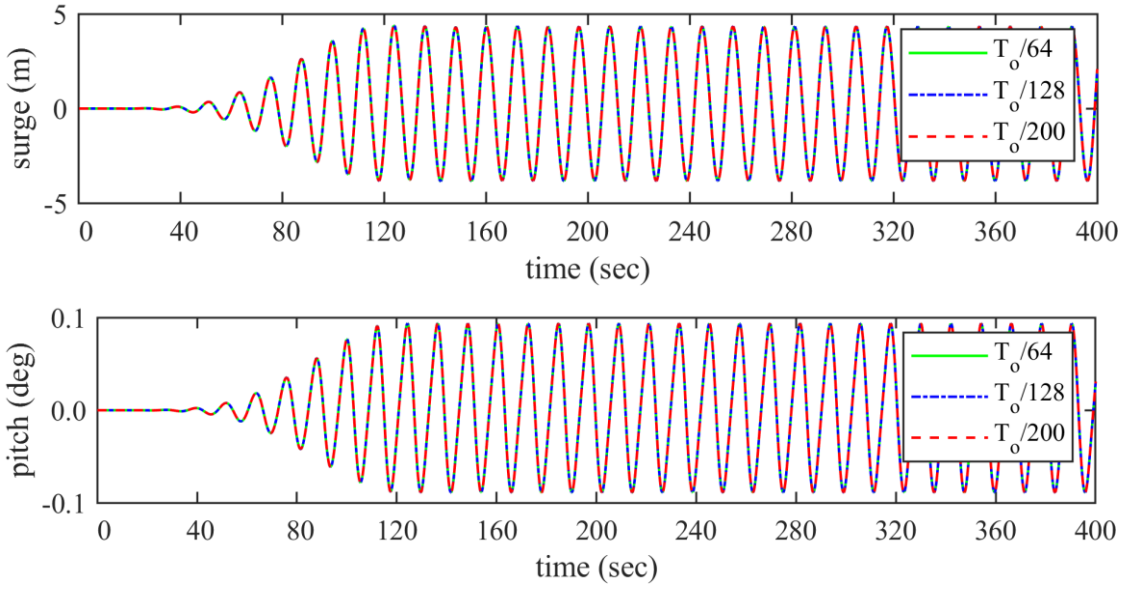

Figure 5.2.1 Surge and Pitch motion for various time step with error tolerance 1E-06

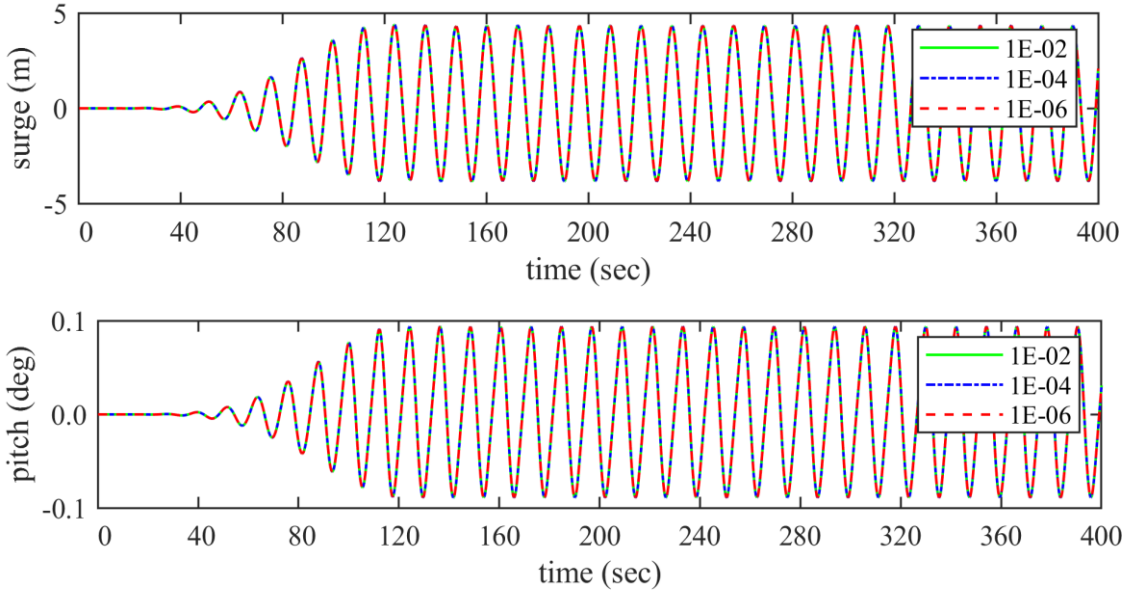

Figure 5.2.2 Surge and Pitch motion for various error tolerances with time step *T_0/128*

It can be seen from the Figure 5.2.1 and Figure 5.2.2 that it is difficult to differentiate surge and pitch motion obtained by using different time step and error tolerances, therefore an error analysis is performed by calculating error in both surge and pitch motions for various time steps and error tolerances with respect to their high values. In this case high values of time step size $h_{max} = T_o/200$ and $\varepsilon_{tol-max} = 1E-07$ is used. The percentage error calculated using below Eq. (5.2.1) for surge and pitch motion is presented in Figure 5.2.3 and Figure 5.2.4.

$$\%\ error = \frac{1}{N_t}\sum_{t=0}^{T_{sim}}\left|\frac{y(t)-Y(t)}{y(t)}\right| \tag{5.2.1}$$

where,

$Y(t)$ = surge or pitch motion obtained using high time step, $h_{max} = T_o/200$ and error tolerance $\varepsilon_{tol-max} = 1e-07$

$y(t)$ = surge or pitch motion obtained using distinct time step, h and error tolerance ε_{tol}

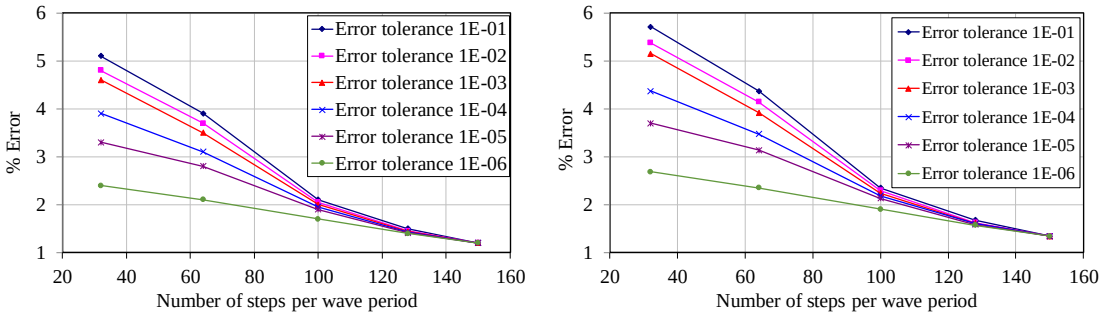

Figure 5.2.3 % error for surge and pitch motion for various time steps

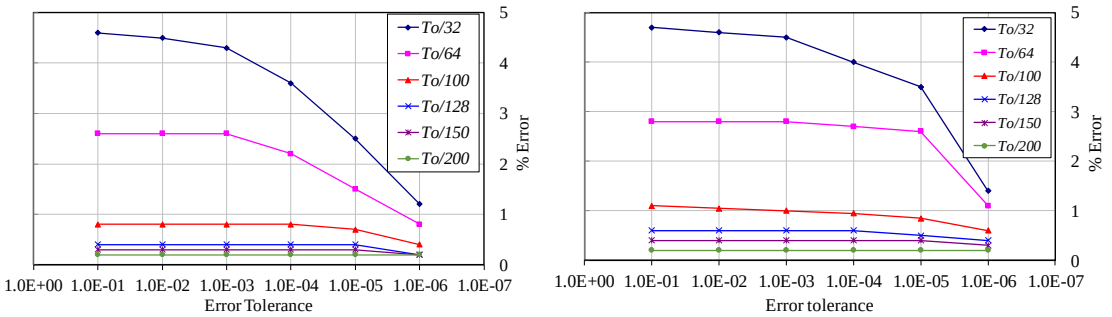

Figure 5.2.4 % error for surge and pitch motion for various error tolerances

It can be seen from the error analysis that % error obtained in surge and pitch varies significantly with respect to time step for all the analysed error tolerances. A time step $T_o/128$ is enough to achieve % error less than 2% for all the error tolerances. A similar analysis is carried out by comparing % error with respect to error tolerances for all the analysed time steps and the results are presented in Figure 5.2.4. It can be seen from the results that % error does not change for time step $T_o/128$ greater than 1E-06 for all the analyzed error tolerances.

These investigations seem to suggest that the number of time step $T_o/128$, and error tolerance 1E-06 selected for the above validation cases are appropriate. Nevertheless, it should be noted that the investigations on how numerical results are related only to error tolerances without considering step size may not be considered as complete because the results depend on both. Considering these uncertainties, the conclusions about the selection of the time steps and error tolerances may not hold for general cases, though it would be considered as a good indication. On this basis, the results for all the cases presented in this thesis have been analysed by using different time steps and error tolerances; though the results obtained by only using $T_o/128$-time step and 1E-06 error tolerance are presented.

6 RESPONSE OF TLPWT TO EXTREME REGULAR WAVE

The term **Regular Wave** often refers to a unidirectional train of waves with constant height and period, and hence its length. They are not expected to be found in a real ocean environment, however, have a crucial role in modelling of sea conditions for engineering investigations and often form the basis of design, especially in conjunction with the spectral method of analysis. They are commonly used to determine the response amplitude operator of a floating platform by numerical computation or laboratory experiment. They are also used for extreme wave analysis where a wave is derived statistically as the most probable largest wave at the design location for a given return period.

If the ratio of height to length (also known as steepness) of a regular wave is sufficiently small, they are considered to be linear. The surface profile of such waves can then be well approximated by a sinusoidal function, and theoretical description of complete wave motion including its water particle kinematics are readily available. When the steepness of wave is higher, they are known as finite amplitude or nonlinear. The surface profile then becomes sharper at the crest and flatter in the trough. The theoretical description of such waves requires non-linear terms to be included as they involve additional harmonics, which travel at the overall wave celerity and increases in order with steepness. Traditionally, such waves are modelled using various nonlinear steady wave theories (e.g. stokes second through fifth order, cnoidal and stream function theory) including Airy's linear wave theory. However, the problem of selecting, from many available wave theories, the most suitable one for a design environment is difficult. Most of the available studies comparing different wave theories are mainly concerned with examining the ability of the different theories to fit the boundary conditions, and they recommend one theory or another to be used in a specific situation (e.g., deep, intermediate or shallow water). This, however, will not guarantee that the chosen wave theory will predict the actual forces and the moments on the structure more accurately. The prime reason behind this is, all the afore-mentioned analytical wave models assume that the wave propagates without changing its form and thus the dispersive properties of the wave field are neglected. This shortcoming is of significance when considering extreme waves since it is now widely recognised that such waves are both nonlinear and unsteady. The FNPT base wave model included in the numerical model developed and presented in chapter 3, consists of both complete nonlinearity and unsteadiness for extreme waves with its steepness limit up to breaking.

This chapter presents the effect of a fully nonlinear wave model (FNPT) on the response of a tension-leg-platform wind turbine to extreme regular wave. The ability of FNPT based QALE-FEM in predicting nonlinear wave surface and underlying water particle kinematics, and their effect on the responses of a chosen floating wind turbine are investigated. The wave kinematics and corresponding responses of TLPWT are further compared with the two most widely used

design oriented analytical waves models such as Airy's linear wave theory (LWT) with wheeler stretching and Fenton's nonlinear steady wave theory (NLSWT) based on 5th order stokes theory. First section of the chapter compares wave surface profile and underlying water particle kinematics predicted by all the three wave models, i.e., Airy's LWT, Fenton's NLSWT, and FNPT based QALE-FEM. The subsequent sections of the chapter compare the motion response and global performance of TLPWT under various extreme regular wave conditions including resonance.

6.1 Effect of nonlinear wave model (FNPT) on wave kinematic prediction

6.1.1 Comparison of wave kinematics using experimental results

To verify the accuracy with which aforementioned wave models can model the nonlinear wave events, comparisons of its numerical results with the laboratory data are made using measurements of both wave surface elevation and underlying water particle kinematics. Figure 6.1.1 shows the wave surface comparison using numerical results with the measurements for a laboratory generated regular wave event corresponding to high frequency ($T_0 = 0.6s, H = 2.7cm$) and low frequency ($T_0 = 1.78s, H = 7.8cm$) wave in a water depth of 0.91m, obtained from OTC 6522, Zhang et al. (1991).

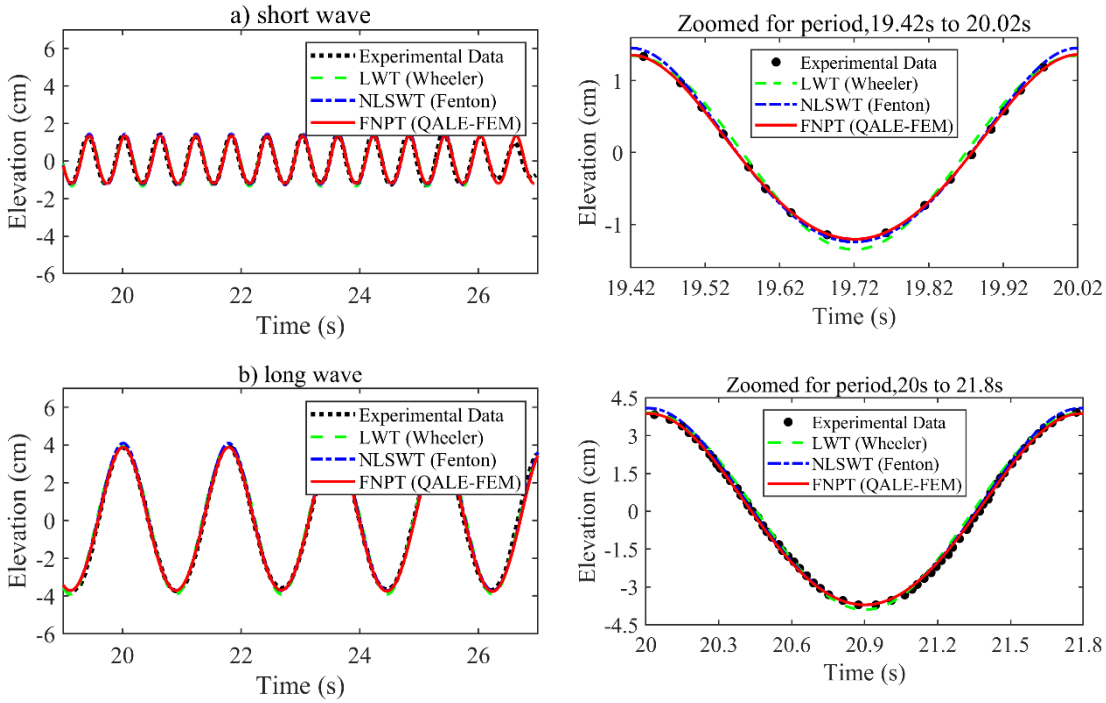

Figure 6.1.1 Comparison of wave surface elevation for a) short wave ($T_0 = 0.6s$, $H = 2.7cm$) and b) long wave ($T_0 = 1.78s$, $H = 7.8cm$)

The agreement between the FNPT based numerical tool QALE-FEM and experimental data is excellent, demonstrating that the nonlinear behaviour of a wave is correctly modelled including redistribution of energy into the high and low frequency components. The crest predicted is narrower while adjacent troughs predicted are broader and less deep as compared to Airy's LWT

wave model. Fenton's NLSWT wave model, predicted trough surface and period well but overpredicted crest height. However, the differences seen in this case are not significant because the wave steepness used in the experiment were low. To see the maximum differences in the prediction of wave surface elevations using all the three wave models, steepness of both the waves is increased and wave surface profile are regenerated and compared in Figure 6.1.2.

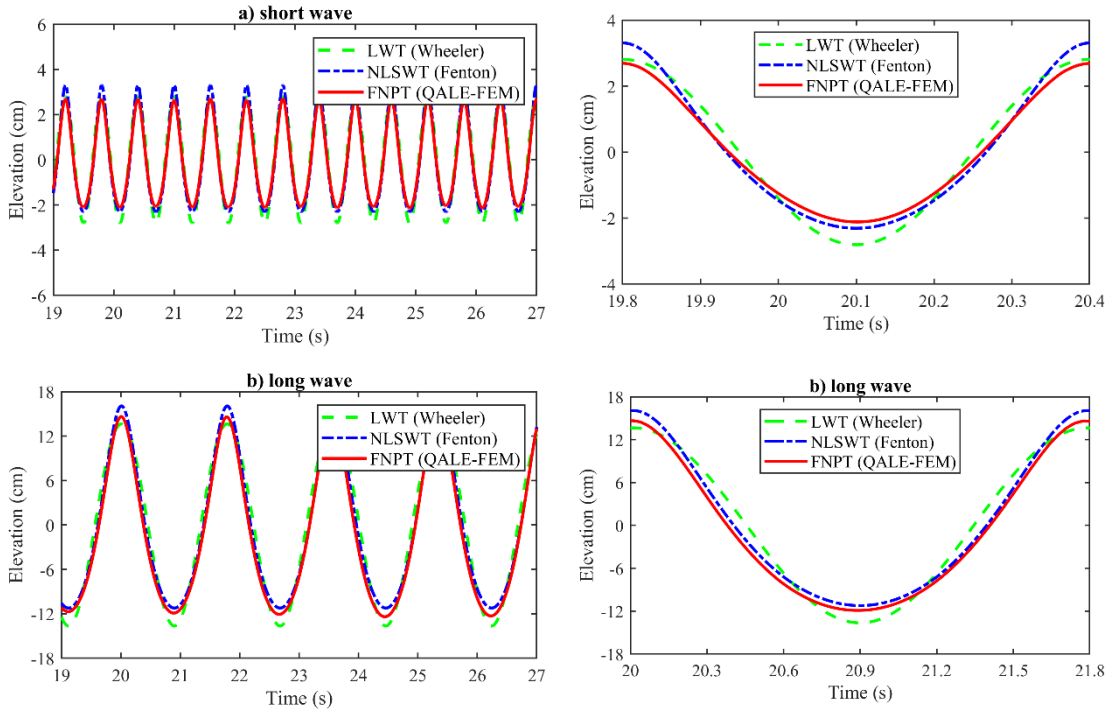

Figure 6.1.2 Comparison of wave surface elevation for a) steep short wave ($T_0 = 0.6s$, $H = 5.6cm$) and b) steep long wave ($T_0 = 1.78s$, $H = 27cm$)

Figure 6.1.2 shows distinct wave surface elevations predicted by all the three wave models. For short wave, crest height predicted by QALE-FEM is lower as compared to other two wave models whereas for long wave, crest height is predicted higher as compared to Airy's LWT wave model and lower as compared to Fenton's NLSWT wave model. The total wave height predicted by QALE-FEM is lower for both short and long wave as compared to predictions by both, Airy's LWT and Fenton's NLSWT wave model. This is mainly noticed due to an inherent assumption of uniform waveform on which both the models are based upon. In Fenton's NLSWT wave model, the solution incorporates nonlinearity of the wave motion but neglects the unsteadiness or the transient nature of a wave. Here, a large wave is characterised by representative wave height, H and period, T_0 and it is assumed that the wave forms part of a regular wave train that propagates without change of form and thus the dispersive properties of the wave field are neglected. This shortcoming is of significance when considering extreme waves as they are both, nonlinear and unsteady. Airy's LWT wave model incorporates, unsteadiness but ignores the nonlinearity. Here, a wave is assumed as uniform and freely propagating satisfying linear dispersion equation.

Next, water particle kinematics underlying wave surface are compared with the laboratory measurements obtained from the same source Zhang et al. (1991) in Figure 6.1.3. It shows depth variation of horizontal water particle velocity arising beneath the regular wave's crest and trough.

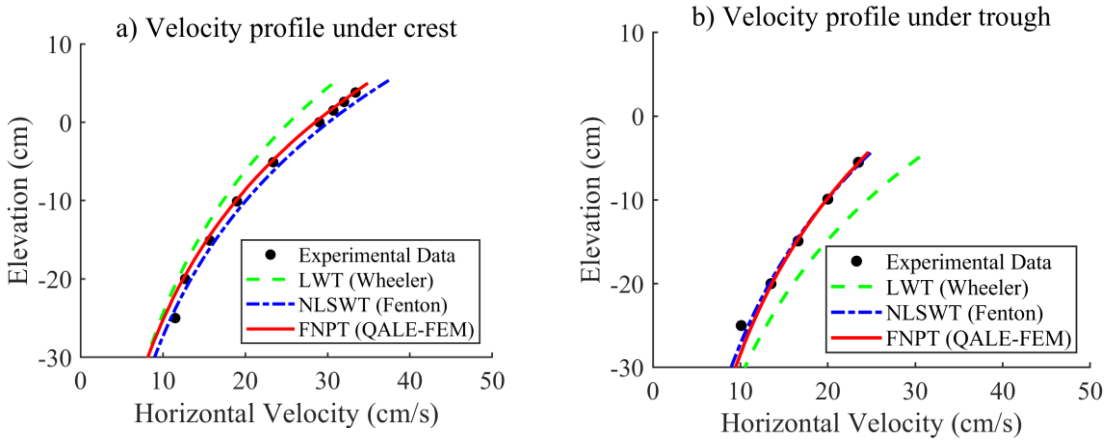

Figure 6.1.3 Comparison of horizontal water particle velocity (T_0 = *1s*, H = *9.7cm*) under a) crest and b) trough

The FNPT based QALE-FEM accurately predicts both, the significant increase in near-surface water particle velocity as well as a reduction in it arising below the mean sea level. Airy's LWT wave model with wheeler stretching underpredicts water particle velocity at the crest and overpredicts it at a trough, whereas Fenton's NLSWT wave model slightly overpredicts velocity at crest but predicts it well at a trough. To see the maximum difference in prediction of horizontal velocities by all the three wave models, steepness of wave (H/L_0) is further increased to 0.1 and horizontal water particle velocity variation up to seabed are regenerated and presented in Figure 6.1.4.

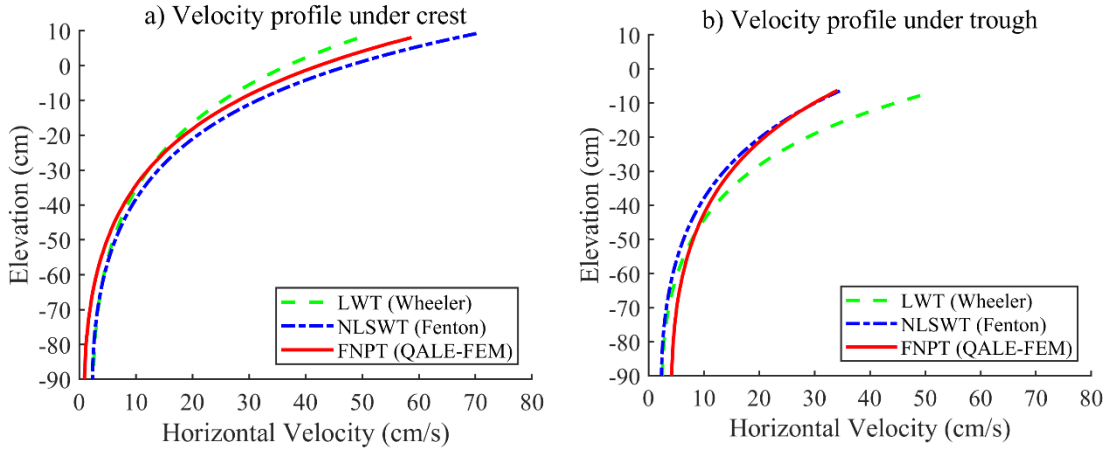

Figure 6.1.4 Comparison of horizontal water particle velocity (T_0 = *1s*, H = *15.6cm*) under a) crest and b) trough

Figure 6.1.4 shows a significant difference in prediction of horizontal velocity at crest and trough by Airy's LWT wave model as compared to the other two nonlinear wave models (NLSWT and FNPT). This is mainly noticed due to reduced accuracy of empirical wheeler's

stretching technique employed while evaluating water particle velocities. Fenton's wave model overpredicts horizontal velocity under crest throughout the wave field as compared to predictions by FNPT based QALE-FEM. At trough, it matched horizontal velocities well at a surface but underpredicted it in the lower layers of the wave field. This difference is noticed due to its inherent assumption of a uniform waveform and ignorance of dispersive properties of the wave field.

The results presented in Figure 6.1.1 to Figure 6.1.4 confirms the accuracy of the FNPT based QALE-FEM numerical tool, in predicting both the wave surface and underlying water particle kinematics. The QALE-FEM enables the water particle kinematics to be determined at, and immediately beneath an instantaneous steep wave surface. This region may contain asymmetric wave surface and large water particle velocities that are very important from a design perspective. This is also a region where approximate design-oriented wave modelling solution such as Airy's LWT using wheeler stretching and Fenton's NLSWT are less accurate. Also, the measurement errors associated with laboratory studies in this region lead to significant uncertainty.

Having established this comparison between reliable FNPT based QALE-FEM numerical tool with traditional design-oriented analytical models (i.e., LWT and NLSWT), QALE-FEM is further used for comparing wave surface profiles and underlying water particle kinematics in the practical range of water depths, where chosen tension-leg-platform wind turbines are intended to be built.

6.1.2 Comparison of wave kinematics using numerical results

Tension leg platforms are considered to be the most favourable floating platform to deploy wind turbines in water depths between 80m (the approximate upper limit for bottom fixed structure) to 200m (where spar is likely to be cheaper). As wave kinematics are extreme in shallow water, the performance of three wave models in predicting wave surface and underlying water particle kinematics are examined in a water depth of 100m for eight wave periods ranging from 6 to 20 sec. The wave heights are chosen by limiting steepness (H/L_0) of a wave to 0.1 or 30m whichever is minimum. The particulars of wave characteristics are given in Table 6.1.1.

For the water depth of 100m, first, three wave periods represent the case of deep water ($d/L_0 > 1/2$) while rest of the cases represent intermediate water depths ($1/20 < d/L_0 < 1/2$). The wave steepness (H/L_0) varies between 1/17 (for the longest wave, $L_0 = 521$m) to a maximum of 1/10 for waves with periods ≤ 14sec. The wave surface elevation calculated by Airy's linear wave theory (LWT), Fenton's nonlinear steady wave theory (NLSWT) and QALE-FEM based on FNPT are presented in Figure 6.1.5 where wave surface $\eta(t)$ is normalised by input wave amplitude, amp and time increment, t by wave period, T_0.

Table 6.1.1 Particulars of extreme regular wave

Wave parameters			H/L_0	d/L_0	Condition
Period (T_0) (sec)	Height (H) (m)	Length (L_0) (m)	-	-	
6	5.6	56	0.100	1.780	deep water
8	10.0	100	0.100	1.001	deep water
10	15.6	156	0.100	0.641	deep water
12	22.3	223	0.100	0.448	Intermediate
14	29.7	297	0.100	0.337	Intermediate
16	30.0	373	0.080	0.268	Intermediate
18	30.0	448	0.067	0.223	Intermediate
20	30.0	521	0.058	0.192	Intermediate

Figure 6.1.5 clearly shows an effect of nonlinearity in prediction of wave surface elevation using fully nonlinear wave model QALE-FEM, for all the waves considered here. The prediction is distinct for waves in deep and intermediate water depth. For deep water waves (i.e., T_0-6sec, T_0-8sec and T_0-10sec), reduction in both crest and total height is seen with maximum effect on a shortest wave (i.e., T_0-6sec). For intermediate water depth waves (i.e., T_0-12sec, T_0-14sec, T_0-16sec, T_0-18sec and T_0-20sec), an increase in crest height and reduction in total height is seen consistently. This reduction or increase in crest height and reduction in total wave height (from crest to trough) is mainly seen due to nonlinear behaviour of a wave such as transfer of energy from low to high frequency components and vice versa for deep and intermediate water depth waves respectively. To see this effect of nonlinearity in the prediction of wave surface elevation as compared to the other two wave models, the predicted crest and wave height are normalised by input wave and presented in Figure 6.1.6.

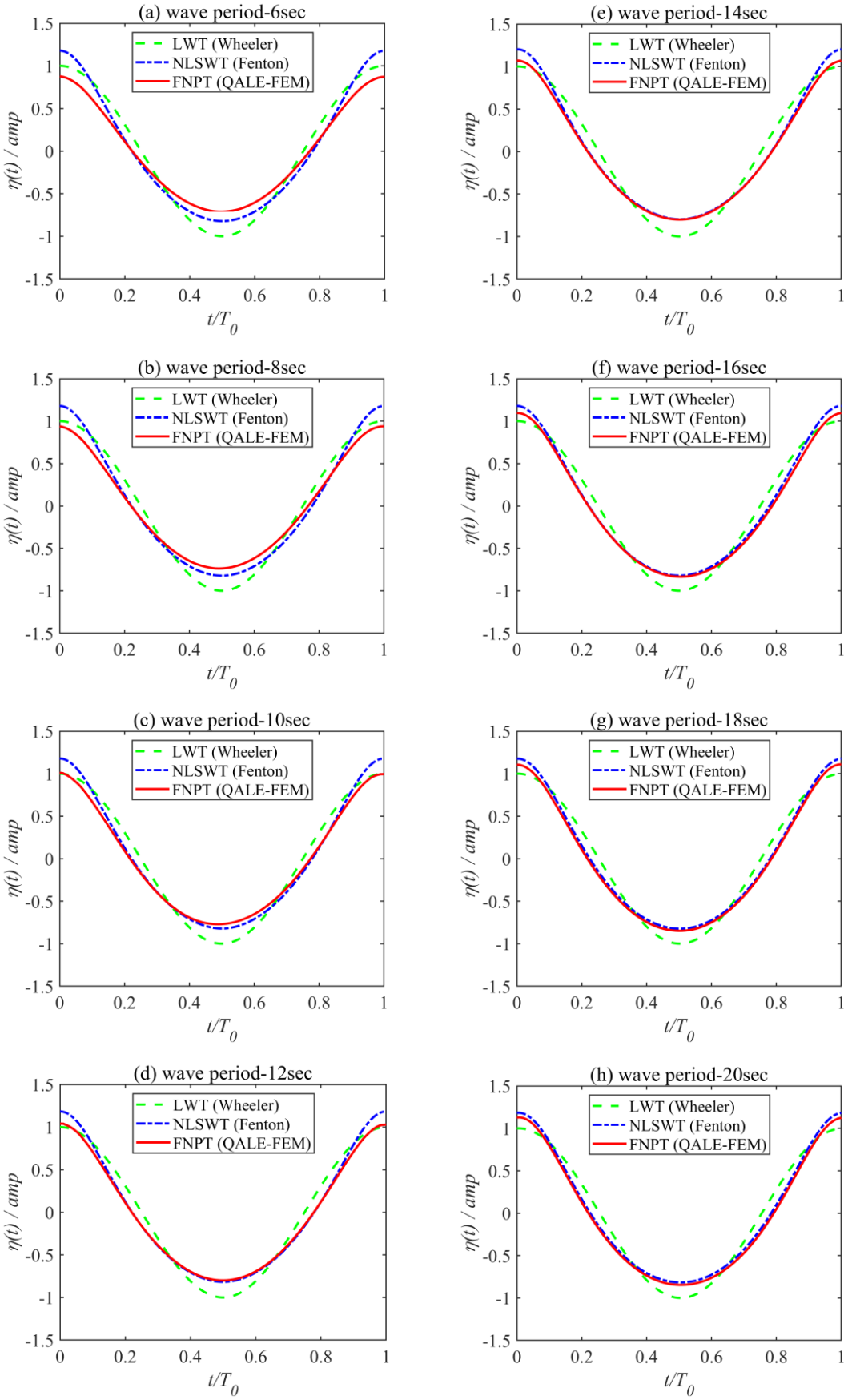

Figure 6.1.5 Comparison of wave surface elevation for wave period a) 6sec, b) 8sec, c) 10sec, d) 12sec, e) 14 sec) f) 16sec, g) 18 sec, h) 20sec

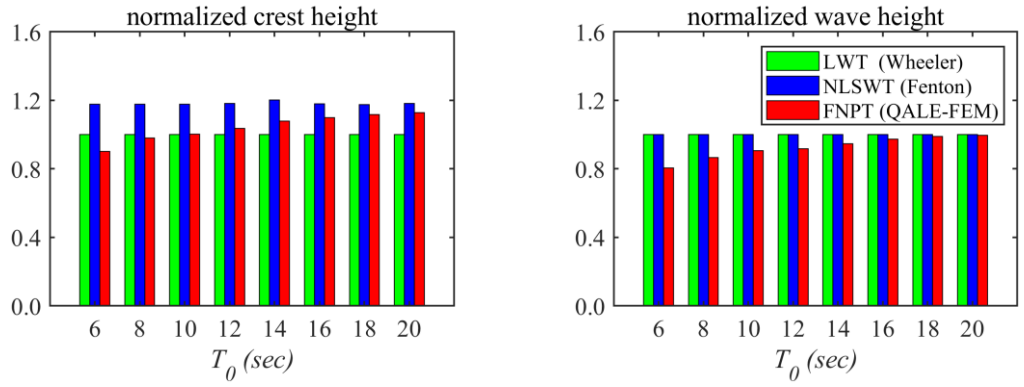

Figure 6.1.6 Normalised crest and wave height for various wave periods

Figure 6.1.6 shows that the QALE-FEM predicts crest height lower for deep water waves and higher for intermediate water waves as compared to input wave crest. The difference ranged from -10% for short wave period (T_0-6 sec) to 13% for long wave period (T_0-20sec). Fenton's wave model predicts crest 18% higher as compared to input wave crest for the entire range of periods whereas compared to QALE-FEM, its over prediction ranges from 30% for short wave (T_0-6sec) to 5% for long wave (T_0-20sec). Total wave height predicted by QALE-FEM is lower than predicted by both, Airy's linear and Fenton's nonlinear wave model for all the wave periods with difference ranging from -19% for short wave (T_0-6 sec) to -1% (negligible) for long wave (T_0-20sec).

We can further study an effect of nonlinearity on wave surface elevation by studying its statistical parameters. The statistical parameters such as mean and skewness for waves considered in Figure 6.1.5 are presented in Table 6.1.2.

Table 6.1.2 Sea-surface elevation statistics for various wave periods

Wave period (sec)	Sea-surface elevation statistics					
	mean			skewness		
	Airy (LWT)	Fenton (NLSWT)	QALE (FNPT)	Airy (LWT)	Fenton (NLSWT)	QALE (FNPT)
6	0.0	0.0	0.0394	0.0	0.3917	0.2657
8	0.0	0.0	0.0856	0.0	0.3922	0.2892
10	0.0	0.0	0.1720	0.0	0.3932	0.3131
12	0.0	0.0	0.3326	0.0	0.4043	0.3337
14	0.0	0.0	0.5922	0.0	0.4492	0.3913
16	0.0	0.0	0.5977	0.0	0.3909	0.3970
18	0.0	0.0	0.6260	0.0	0.3820	0.3995
20	0.0	0.0	0.6285	0.0	0.3751	0.4080

The trend shown in Table 6.1.2 is consistent with what is observed in Figure 6.1.5. Larger the wave period, more noticeable the change in mean and skewness of wave surface elevation

predicted by QALE-FEM. Largest mean and skewness is achieved for the longest wave period (T_0-20 sec) by QALE-FEM. Airy's and Fenton's wave model showed zero mean value due to its inherent assumption of uniform waveform. However, the largest skewness achieved by Fenton's wave model is seen for a wave period of 14sec which is largest wave period having highest wave steepness among all the analysed waves listed in Table 6.1.1. The difference in predicting wave surface profile and its associated statistical parameters using three different wave models is seen considerable, hence the difference in predicting water particle kinematics is studied next.

The profiles of horizontal and vertical velocities and accelerations with respect depth predicted using three different wave models are presented in Figure 6.1.7 through Figure 6.1.10 for the extreme regular wave conditions detailed in Table 6.1.1. Here the velocity and acceleration profiles are normalised with respect to maximum values predicted by QALE-FEM numerical scheme. This shows under and over prediction of wave kinematics using other two design-oriented wave models LWT and NLSWT as compared to QALE-FEM. The vertical co-ordinate specifying wave surface elevations are normalised by water depth.

The plots showing variation of maximum velocities and accelerations with respect to depth, as depicted in Figure 6.1.7 through Figure 6.1.10 also show some nonlinear features as detailed below,

a. The horizontal water particle velocity profiles presented in Figure 6.1.7 clearly shows the effect of nonlinearity in its prediction using fully nonlinear wave model QALE-FEM. The estimated velocities are higher at the crest and lower near seabed as compare to predictions by linear wave model. Although this effect is observed for deep water waves, it is far more significant for waves in intermediate water depths where the transfer of energy to the low frequency component is larger.
b. The vertical water particle velocity and horizontal water particle acceleration profiles presented in Figure 6.1.8 and Figure 6.1.9 shows noticeable difference in their predictions by all the three wave models for short wave (T_0-6sec), however the differences reduce with increase in period with minimal differences are noticed for longest wave (T_0-20sec).
c. The vertical water particle acceleration profiles presented in Figure 6.1.10 shows significant difference in its prediction by Airy's linear wave model as compare to nonlinear wave models by Fenton and QALE-FEM. This is mainly noticed due to significant difference in wave surface prediction at trough and empirical technique of wheeler stretching employed to evaluate accelerations.

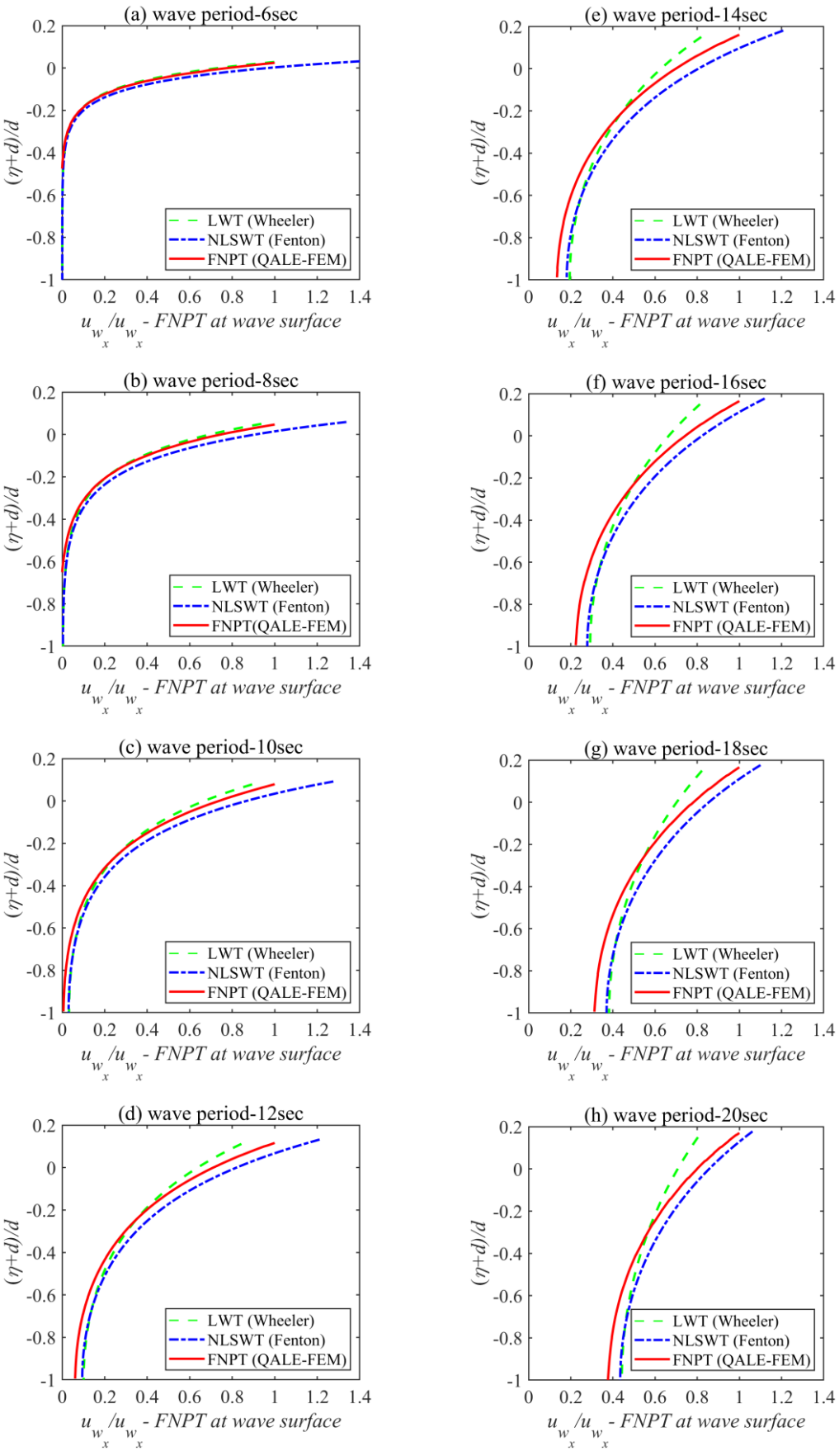

Figure 6.1.7 Comparison of horizontal water particle velocity for wave period a) 6sec, b) 8sec, c) 10sec, d) 12sec, e) 14 sec) f) 16sec, g) 18 sec, h) 20sec

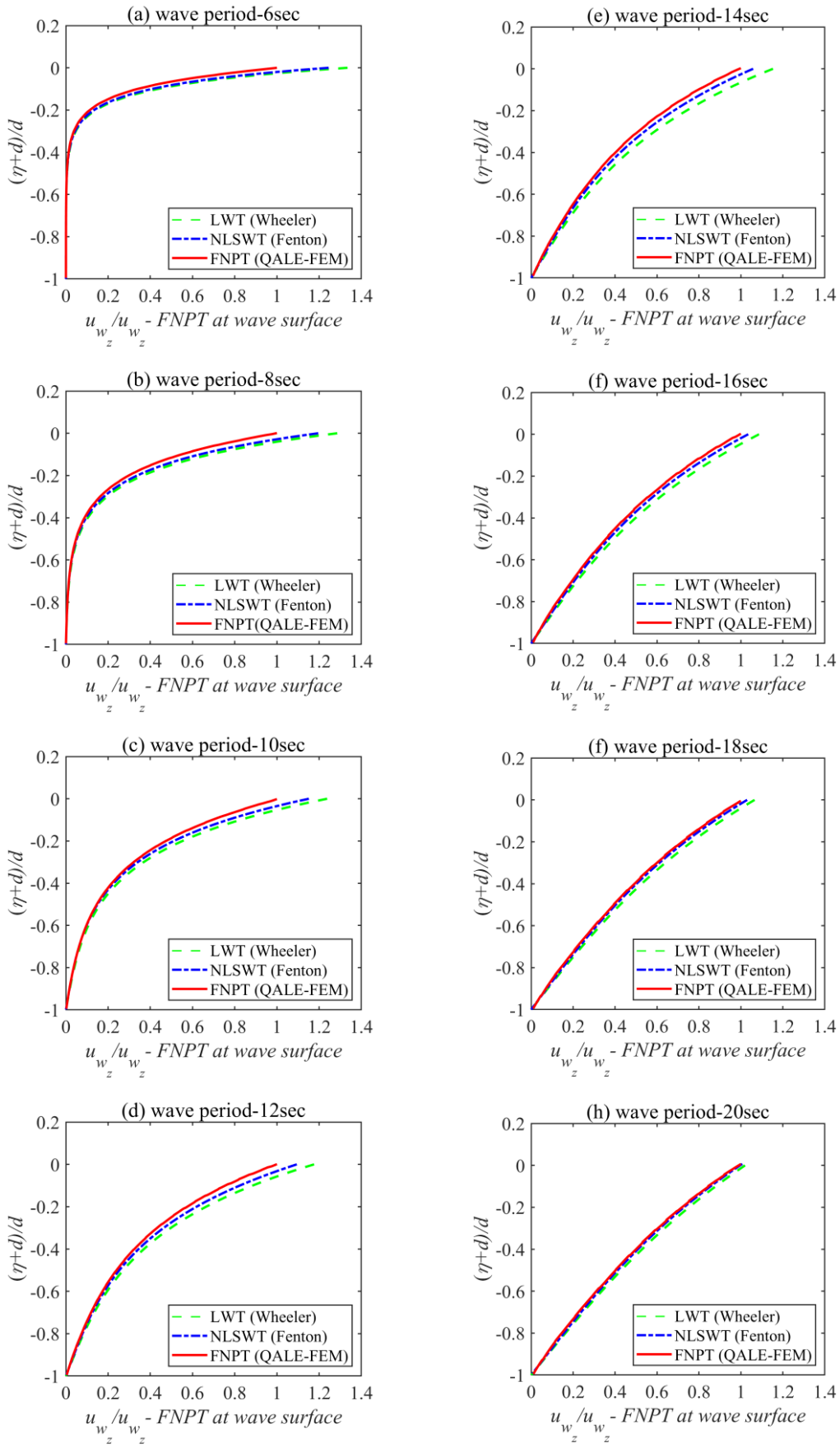

Figure 6.1.8 Comparison of vertical water particle velocity for wave period a) 6sec, b) 8sec, c) 10sec, d) 12sec, e) 14 sec) f) 16sec, g) 18 sec, h) 20sec

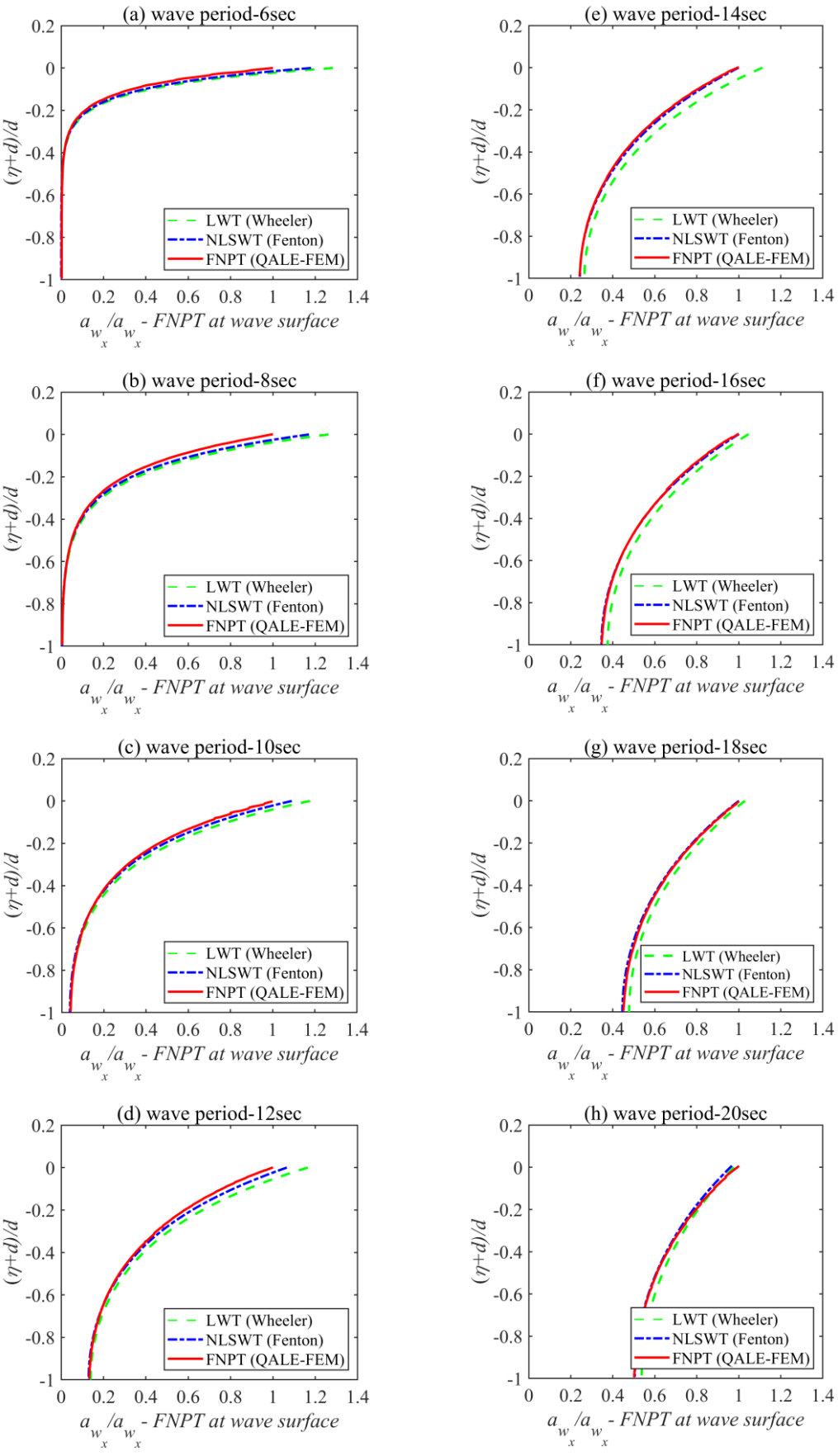

Figure 6.1.9 Comparison of horizontal water particle acceleration for wave period a) 6sec, b) 8sec, c) 10sec, d) 12sec, e) 14 sec) f) 16sec, g) 18 sec, h) 20sec

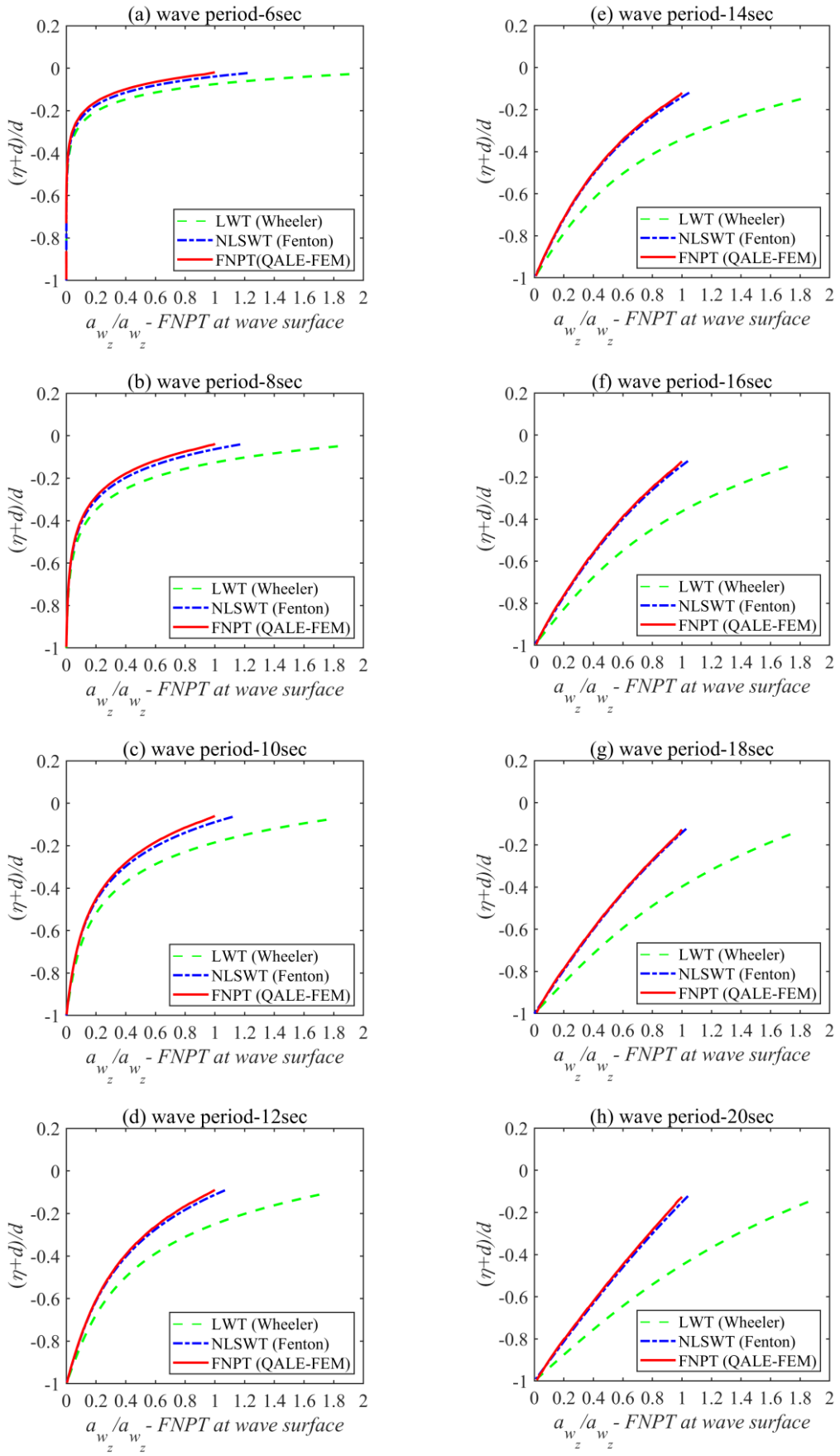

Figure 6.1.10 Comparison of vertical water particle acceleration for wave period a) 6sec, b) 8sec, c) 10sec, d) 12sec, e) 14 sec) f) 16sec, g) 18 sec, h) 20sec

To study the quantitative difference, the maximum velocities and accelerations are calculated using different wave models at crest and elevation -30m from mean sea level (as the TLPWT used for the response analysis has a draft of 30m) and compared in Figure 6.1.11 through Figure 6.1.14 for various wave periods.

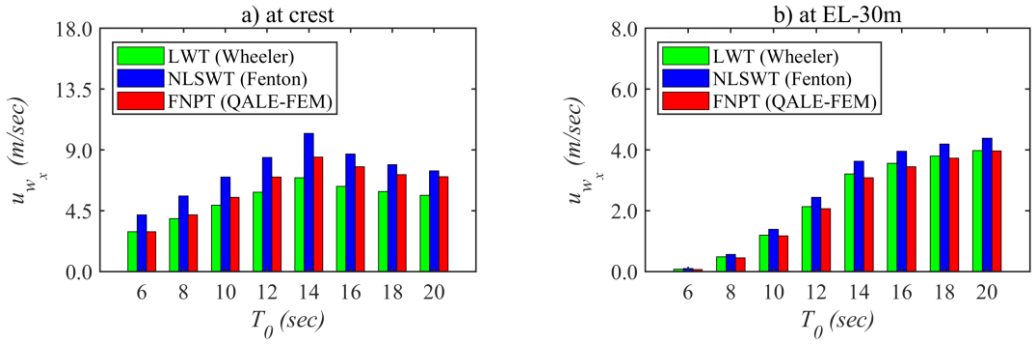

Figure 6.1.11 Comparison of horizontal water particle velocity by different wave theories

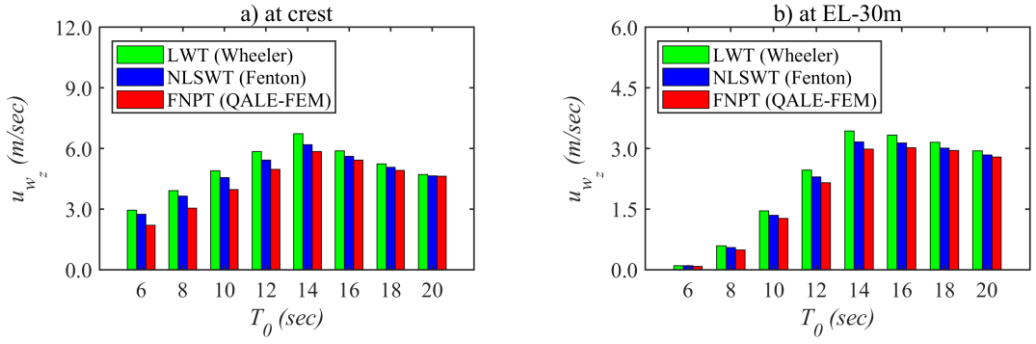

Figure 6.1.12 Comparison of vertical water particle velocity by different wave theories

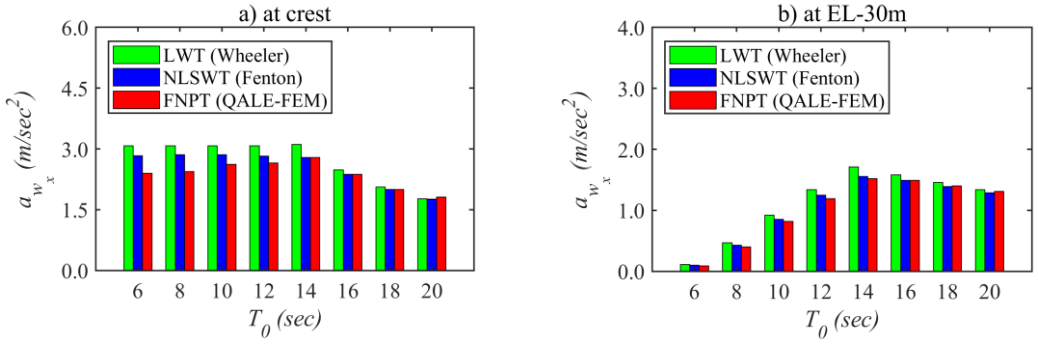

Figure 6.1.13 Comparison of horizontal water particle acceleration by different wave theories

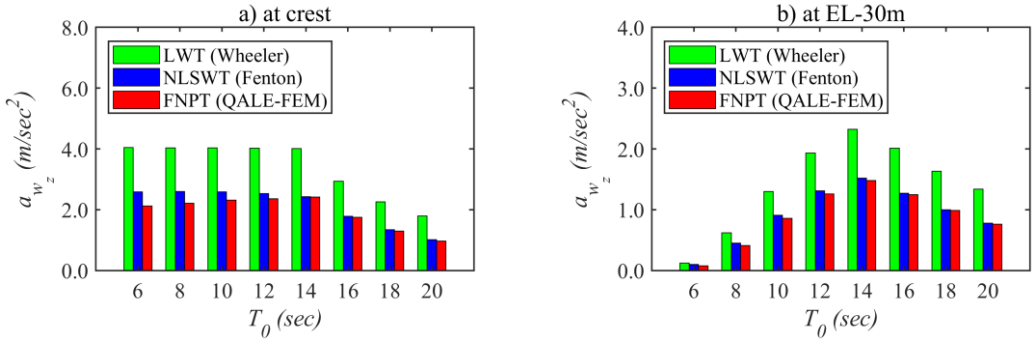

Figure 6.1.14 Comparison of vertical water particle acceleration by different wave theories

From the results presented in Figure 6.1.11 through Figure 6.1.14, following was noted.

a. Horizontal water particle velocity

   Linear wave model consistently under predicted horizontal velocity at free surface and over predicted it at EL -30m as compared to predictions by QALE-FEM, for all the analysed wave periods. The differences at free surface ranged from -0.2% for short wave (T_0-6sec) to -19.6% for long wave (T_0-20sec). At elevation -30m, these differences ranged from 12.8% to 0.1%. Fenton's wave model over predicted velocity at both crest and elevation -30m. The maximum differences at crest ranged from 42.4% for short wave (T_0-6sec) to 6.3% for long wave (T_0-20sec).

b. Vertical water particle velocity

   Airy's linear and Fenton's nonlinear wave model over predicted vertical water particle velocity for all the wave periods as compared to QALE-FEM. The differences at free surface ranged from 33.5% for short wave (T_0-6sec) to 2% for long wave (T_0-20sec) for linear wave model whereas for Fenton's nonlinear wave model differences ranged from maximum of 24.5% for short wave period (T_0-6sec) to 0.7% for long wave period (T_0-20sec). At elevation -30m, these differences ranged from 23.9% to 5.2% for linear wave model and from 15.9% to 1.6% for Fenton's nonlinear wave model.

c. Horizontal water particle accelerations

   The horizontal accelerations showed similar prediction trend as shown by vertical velocity. The differences at free surface ranged from 28.4% for short wave period (T_0-6sec) to -2.3% for long wave period (T_0-20sec) for linear wave model, whereas for Fenton's nonlinear wave model, differences ranged from maximum of 18% for short wave period (T_0-6sec) to -3.3% for long wave period (T_0-20sec). At elevation -30m, these differences ranged from 16.5% to 2.5% for linear wave model and from 9% to -1.1% for Fenton's nonlinear wave model.

d. Vertical water particle accelerations

   The vertical accelerations showed relatively large difference in prediction of accelerations by linear wave model. The differences at free surface ranged from 90% for short wave period (T_0-6sec) to 86% for long wave period (T_0-20sec) for linear wave model, whereas for Fenton's nonlinear wave model, differences ranged from maximum of 22% for short wave period (T_0-6sec) to 4% for long wave period (T_0-20sec). At elevation -30m, these differences ranged from 62.1% to 77.1% for linear wave model and 20.3% to 2.6% for Fenton's nonlinear wave model.

Based on the results presented in this section, the non-linear behaviour of wave may be subdivided into two categories. First corresponds to the transfer of wave energy into high frequency component which can be interpreted as local nonlinearity. In contrast, the second category corresponds to the transfer of wave energy into low frequency component which can be

interpreted as global nonlinearity. This redistribution of energy produces wave crest that is lower for deep water waves and higher for intermediate water waves as compared to linear wave solution. However, in both the cases crest produced is narrower while trough is broader and less deep. Considering the profile of horizontal velocity arising beneath the wave crest, these higher harmonics are producing large increase in vertical gradient of velocity close to the instantaneous water surface and reduction in near bed horizontal velocity as compared to linear wave solution. Although this effect is observed in deep water, it is far more significant in intermediate water depth where transfer of energy to the low frequency component is larger.

The maximum difference in horizontal water particle velocity predicted by Airy's linear wave model as compared to QALE-FEM is seen for longest wave (T_0-20sec) whereas difference in vertical velocity and accelerations in horizontal and vertical direction are seen for shortest wave (T_0-6sec). The maximum difference in all the horizontal and vertical velocity and accelerations predicted by Fenton's wave model as compared to QALE-FEM are seen for deep water waves. This difference for short wave is mainly seen due to the effect of nonlinearity on wave height prediction which is seen stronger for deep water waves where Fenton's wave model predicts wave height almost 30% higher than QALE-FEM.

The nonlinearity of a wave is generally measured by its height, H and length, L_0 (or period,T_0) in a particular water depth, d. Wave steepness H/L_0, and water depth to wave length ratio d/L_0, which is linked to wave height, wave length, and water depth is normally employed to describe the nonlinearity of a wave input. The range of validity of various wave theories available for computing water particle kinematics is also based on these two parameters (Le Méhauté, 1976). Therefore, the effect of these two parameters, H/L_0 and d/L_0 on prediction of wave surface and underlying water particle kinematics is studied next.

6.1.2.1 Effect of wave steepness (H/L_0) and water depth (d/L_0)

To study the influence of wave steepness (H/L_0) and water depth to wave length ratio (d/L_0), the profile of wave surface elevation and underlying water particle kinematics are generated for three sets of H/L_0 - 0.02, 0.06 and 0.10, and d/L_0 - 0.327, 0.490, and 0.654. Here effect of wave steepness is studied for a wave period of 14sec in a water depth of 100m. The d/L_0 ratios are corresponding to wave with a period of 14sec in a water depth of 100m, 150m and 200m. Steepness of wave (H/L_0) is maintained as 0.1. The normalised crest and wave height is presented in Figure 6.1.15 and Figure 6.1.16 for various wave steepness and water depths respectively. The statistical parameters such as mean, and skewness are presented in Table 6.1.3 and Table 6.1.4 respectively.

It can be seen from Figure 6.1.15 and Figure 6.1.16 that the effect of wave steepness variation is more on difference in crest height prediction whereas effect of water depth variation is more on difference in both, crest and total wave height prediction using three different wave models.

The normalised crest height for wave steepness of 0.02, 0.06 and 0.1 is 1.04, 1.11, and 1.20 by Fenton's wave model and 1.01, 1.06, and 1.09 by QALE-FEM. The normalised total wave height predicted by QALE-FEM for water depth of 100m, 150m, and 200m is 0.947, 0.917, and 0.902.

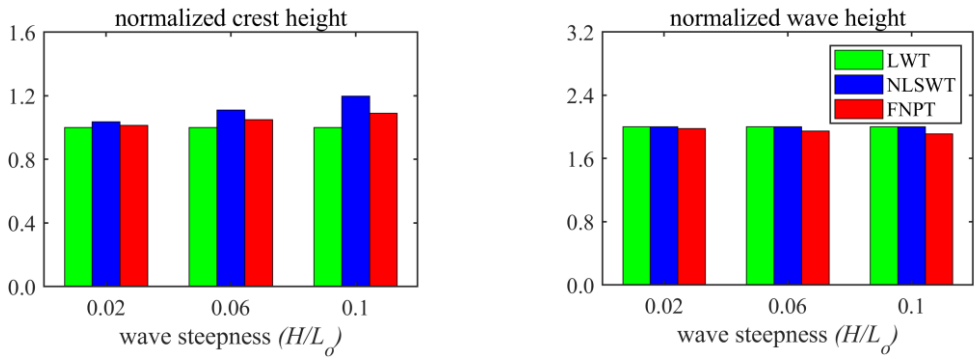

Figure 6.1.15 Normalised crest and wave height for various wave steepness

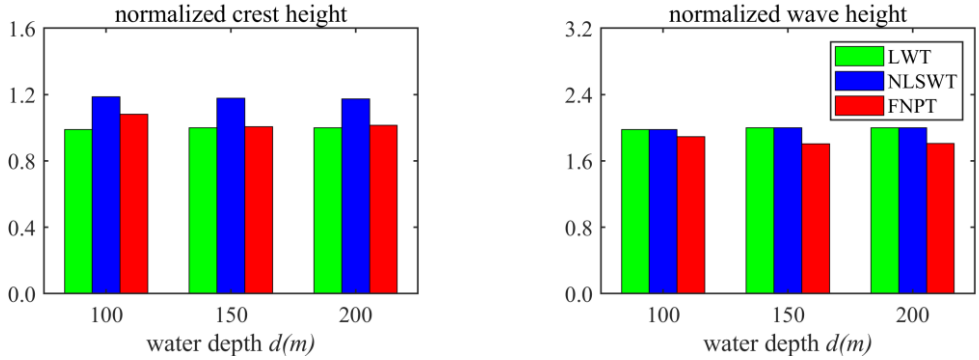

Figure 6.1.16 Normalised crest and wave height for various water depths

Table 6.1.3 Sea-surface elevation statistics for various wave steepness

Wave steepness (H/L_0)	Sea-surface elevation statistics					
	mean			skewness		
	Linear	Fenton	FNPT	Linear	Fenton	FNPT
0.020	0.0	0.0	0.0235	0.0	0.0754	0.0750
0.060	0.0	0.0	0.2067	0.0	0.2375	0.2249
0.100	0.0	0.0	0.5922	0.0	0.4492	0.3913

Table 6.1.4 Sea-surface elevation statistics for various water depths

Water depth (m)	Sea-surface elevation statistics					
	mean			skewness		
	Linear	Fenton	FNPT	Linear	Fenton	FNPT
100	0.0	0.0	0.5922	0.0	0.4492	0.3913
150	0.0	0.0	0.4202	0.0	0.3908	0.3125
200	0.0	0.0	0.3286	0.0	0.3831	0.3076

The trend of statistical parameters presented in Table 6.1.3 and Table 6.1.4 is consistent with what is observed in Figure 6.1.15 and Figure 6.1.16. The larger the wave steepness and the lower

the water depth, the higher the mean value of the wave surface profile. Skewness, which is a measure of nonlinearity, also follows a similar trend.

Figure 6.1.17 through Figure 6.1.18 summarizes the maximum velocities and accelerations calculated by different wave models at crest for various wave steepness and water depths respectively.

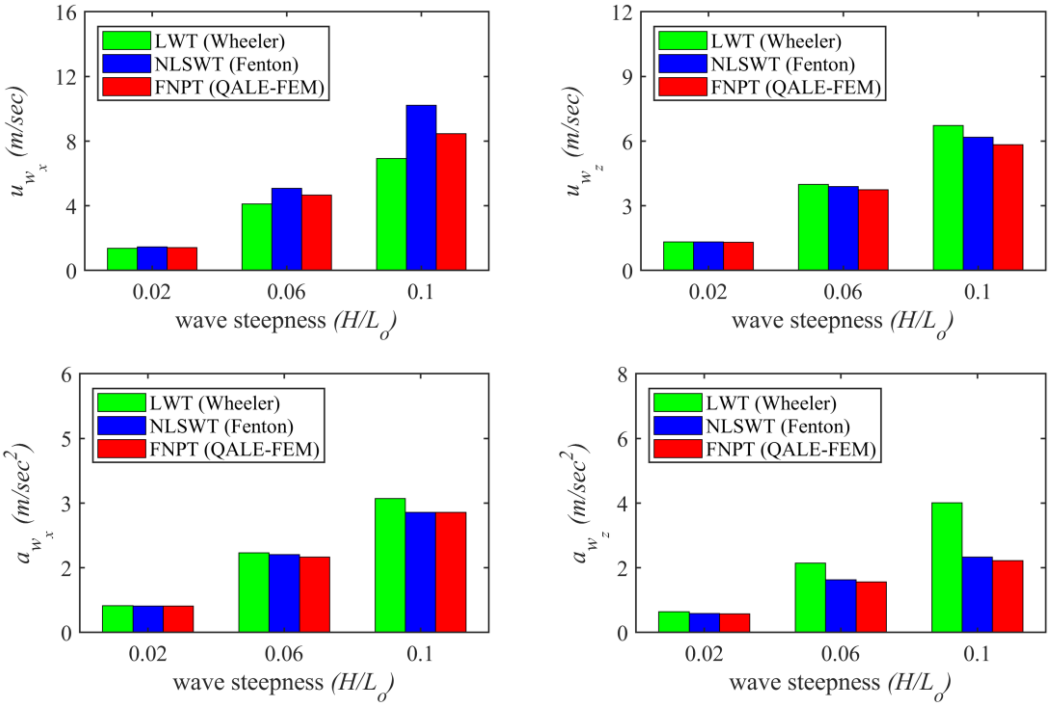

Figure 6.1.17 Comparison of maximum wave kinematics for various wave steepness, H/L_0

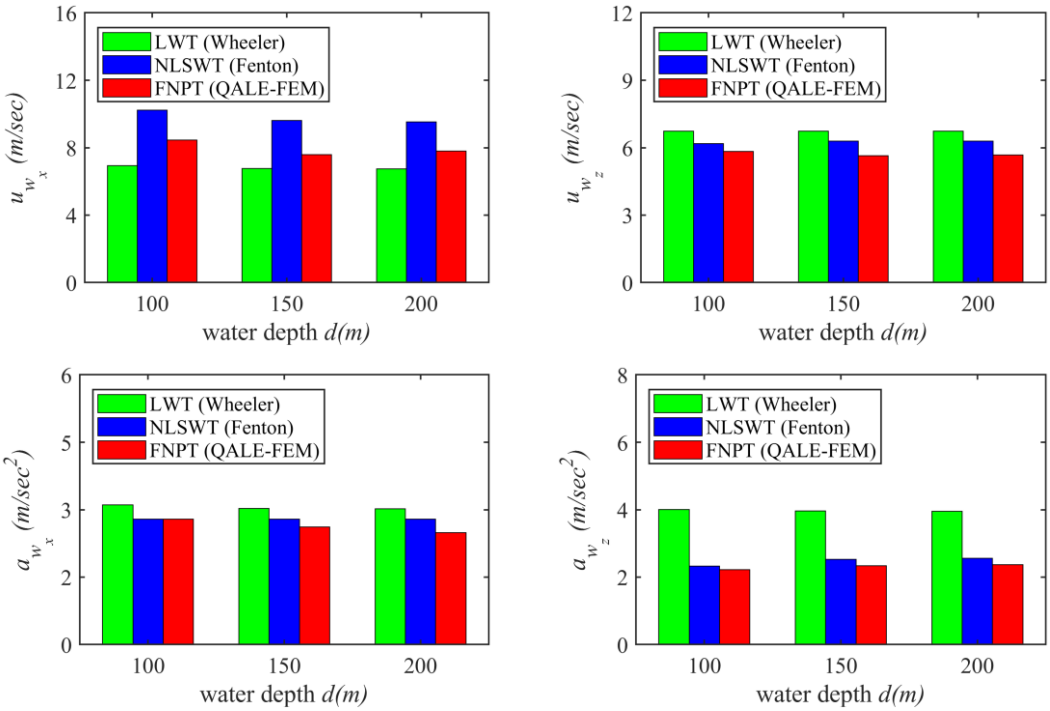

Figure 6.1.18 Comparison of maximum wave kinematics for various water depths, d

It can be seen from Figure 6.1.17 that the differences in prediction of wave kinematics by different wave models are increasing with the increase in wave steepness showing differences are insignificant for lower wave steepness of 0.02, considerable for 0.06, and significant for 0.1. Figure 6.1.18 shows the reduction in difference in water particle velocities and accelerations predicted by different wave models with the increase in water depth, however, considerable differences do exist for maximum water depth of 200m.

6.1.2.2 Comparison for Predicted Vs Target wave surface

The comparison of wave kinematics presented in previous section is based on predicted wave surface. In this section wave kinematics are compared for target wave surface where steepness of wave (H/L_0) is kept same in all the three wave models. To achieve this, wave height predicted by QALE-FEM is fed into both Airy's linear wave model and Fenton's nonlinear wave model and wave kinematics are compared. For comparison three wave parameters from Table 6.1.1 are chosen, i.e., T_0 -6sec, T_0 -14sec and T_0 -20sec. The comparison of maximum velocity and acceleration at crest and EL -30m estimated by different wave models are presented in Figure 6.1.19 through Figure 6.1.22. Here legend LWT-P, NLSWT-P and FNPT denotes water particle kinematics predicted by LWT, NLSWT and FNPT wave models for predicted wave surface based on given input wave. The legend LWT-T and NLSWT-T denotes water particle kinematics predicted by LWT and NLSWT wave model for target wave which is equal to wave height predicted by FNPT based QALE-FEM.

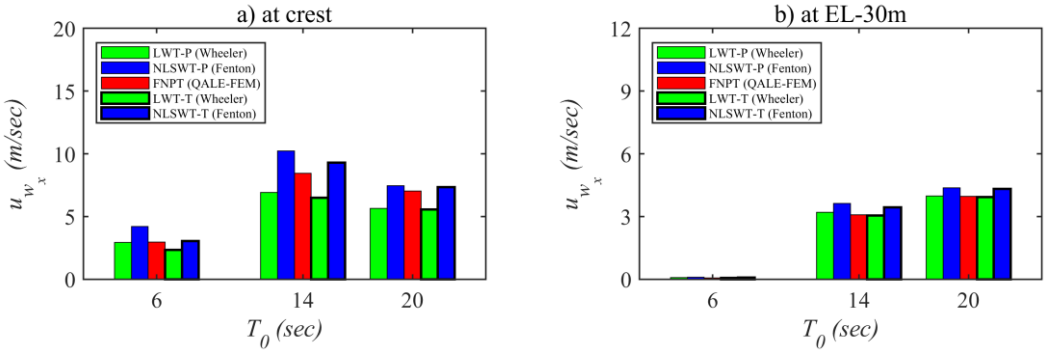

Figure 6.1.19 Comparison of horizontal water particle velocity by different wave theories

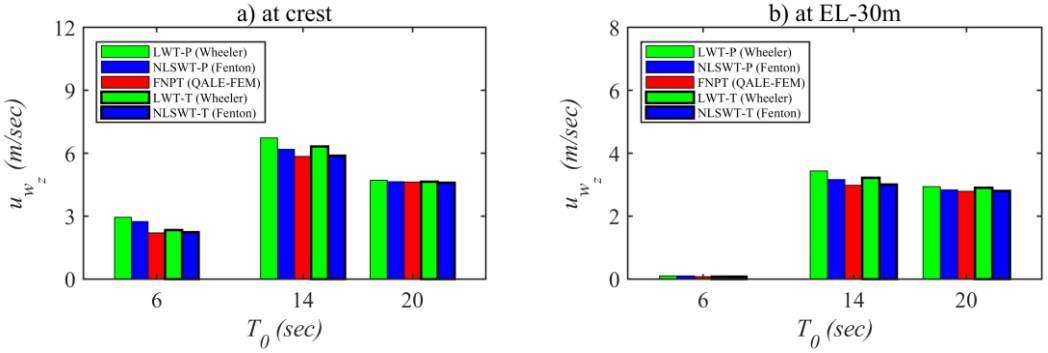

Figure 6.1.20 Comparison of vertical water particle velocity by different wave theories

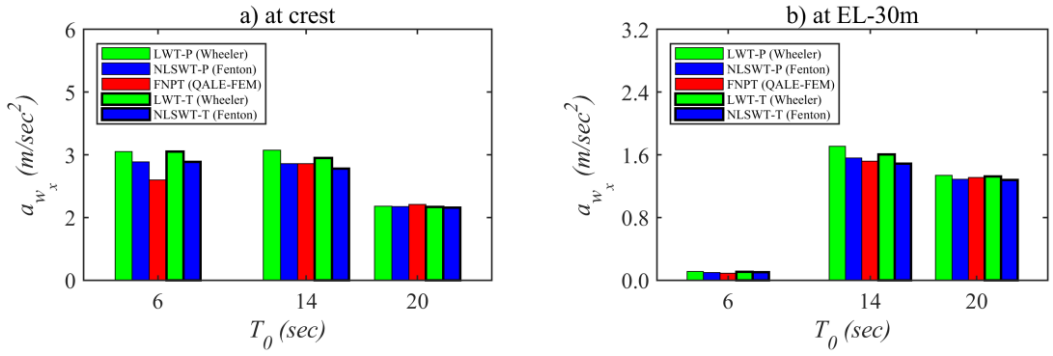

Figure 6.1.21 Comparison of horizontal water particle acceleration by different wave theories

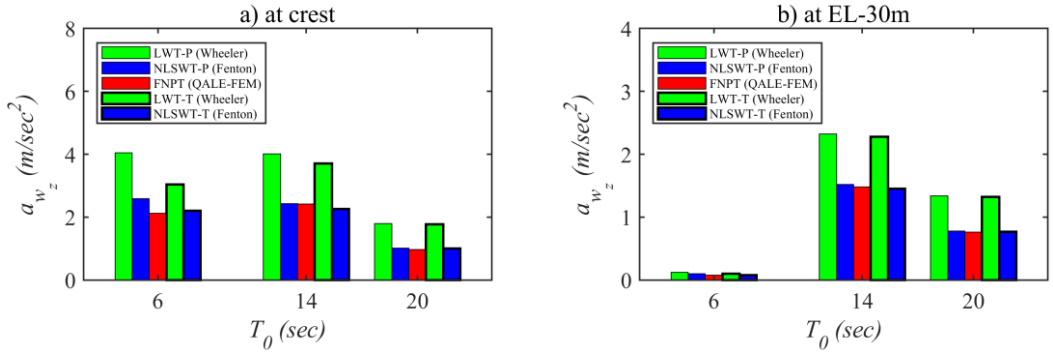

Figure 6.1.22 Comparison of vertical water particle acceleration by different wave theories

It can be seen from Figure 6.1.19 that the difference between horizontal water particle velocity predicted at crest by LWT and FNPT is high for target wave as compared to predicted wave whereas the difference in prediction by NLSWT and FNPT are seen significantly less. The reduction in difference is seen more for short wave with T_0-6 sec as for this wave maximum difference in prediction of wave surface elevations were noted. A similar trend is noticed for horizontal water particle velocity at EL -30m. The difference in vertical water particle velocity and accelerations at crest and EL-30m, predicted by both LWT and NLSWT wave model as compared to FNPT wave model is more for target wave as compared to predicted wave as shown in Figure 6.1.20 and Figure 6.1.22. Here also the maximum difference is noted for short wave T_0-6sec, where maximum difference in wave surface prediction by all three models were noticed. A similar trend is also noticed for horizontal water particle accelerations as shown in Figure 6.1.21, but the maximum differences were noticed for steep wave T_0-14sec. This comparison demonstrates that the difference in wave kinematics predicted by Airy's LWT and QALE-FEM is high for target wave as compared to predicted wave whereas differences in predictions by Fenton's wave model and QALE-FEM are seen low. This shows that the Fenton's nonlinear wave model predicts water particle kinematics with sufficient accuracy for a known regular wave surface, i.e. target or measured wave.

From the results presented in section 6.1, it is seen that how different wave model affects the prediction of wave surface and its underlying water particle kinematics. To see the effect of these different wave models in predicting motion response, the response analysis is performed for a

chosen tension-leg-platform wind turbine which is like the one used for model validation in Chapter 5. However, the platform configuration used for model validation was designed for the water depth of 200m, and the response analysis needs to be performed in water depths ranging from 100m to 200m. Therefore, a parametric study is undertaken to optimised platform configuration. The platform configuration derived based on the parametric study is detailed under the following section.

6.2 Parametric Study

The offshore environment in which the wind turbine must operate is a prime design consideration for designing its floating support system. To perform a parametric study to obtain realistic design, some basic design criteria must be defined. While selecting design criteria, one must keep in mind a prime goal that is to minimise the cost of electricity by controlling CAPEX and OPEX. A complete LCOE analysis of floating wind turbine is not realistic here, but consideration has been given to some design and performance characteristics of it that may affect the cost. For example, to minimise the CAPEX (i.e., material and construction cost), the steel mass, tendon pretension, and displacements are minimised; whereas to limit the OPEX (i.e. operating expenditure) the tendon, tower, blade and nacelle loads, and their variations are minimised. Considering the above goals, the following design criteria are set for optimising platform configuration,

- The surge and sway natural periods should be longer than 25s to avoid first order wave excitation.
- The heave, roll and pitch natural periods should be shorter than 3.5s to avoid first order wave excitation.
- To limit the angle at tendon connection, the mean of platform offset shall not exceed 5% of water depth. Here, a mean of platform offset is result of excitation and restoring forces acting on the platform. The excitation forces considered are due to wind and waves, and restoring forces are due to buoyancy and mooring lines. In the preliminary design, wind speed is set at rated turbine speed which results in maximum turbine thrust and surge force due to waves is considered applying regular wave with a period of 14 sec having steepness (H/L_0) of 0.1 as these parameters yield maximum wave kinematics.

Also, further constraint on the natural period shall be considered as 1P and 3P excitation. During operation, the maximum $f1p$ is approximately 0.2Hz while the minimum $f3p$ is approximately 0.37Hz. To avoid both first-order wave excitation and 3P excitation; the first coupled pitch and tower bending mode shall then fall between 2.7s and 3.5s. Though platform's pitch natural period falls between these periods it will still be susceptible to second, third or higher order wave loads.

The baseline design given in chapter 5, section 5.1.1 is modified by performing parametric study adhering to above-set criteria. The number of pontoons and their cross section and length are the parameters considered for the modification to meet the above-set criteria.

The modified platform configuration based on the parametric study are presented in Table 6.2.1 and the natural periods of a complete floating wind turbine with a modified platform configuration are presented in Figure 6.2.1 for the water depth of 100m, 150m, and 200m.

Table 6.2.1 Details of parameterized platform configuration

Parameters	Baseline design	Modified design
Number of pontoons	3	4
Length	22.5m	25m
Cross section at free end	3m x 3m	3m x 5m
Cross section at fixed end	3m x 6m	3m x 6m
Legs Configuration radially at	120^0	90^0
Radius to fairlead and anchor	30m	32.5m
Draft of fairlead	28.5m	28.5m
Platform draft	30m	30m
Mass	661 600kg	793 927kg
Displacement	2 840 000kg	3 579 000kg
Mooring stiffness, AE	7430kN	7000kN

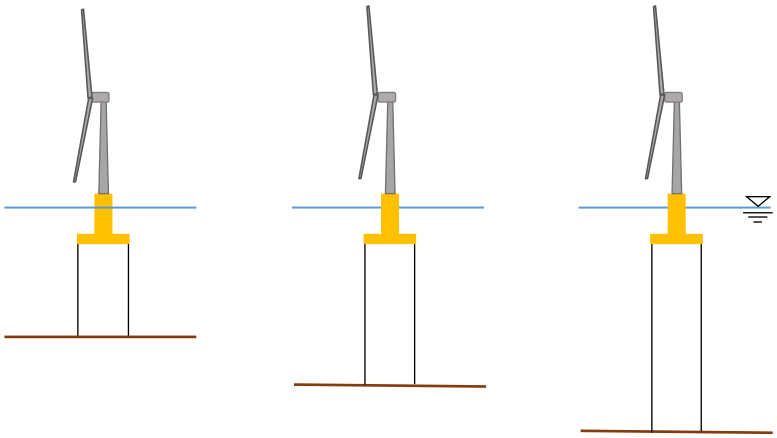

Water depth	100m	150m	200m
Natural period			
Surge	25.2 sec	31.2 sec	37.5 sec
Heave	0.6 sec	0.7 sec	0.9 sec
Pitch	1.2 sec	1.5 sec	1.8 sec

Figure 6.2.1 Natural period of parameterized platform configuration

This parameterised TLPWT is further used for the dynamic analysis to study its responses under various wave conditions including resonance.

6.3 Effect of nonlinear wave kinematic on motion response of TLPWT

Global motion analysis of a parameterised TLPWT is performed to study its motion responses under various environmental conditions comprising regular wave. The environmental conditions considered here uses monochromatic incident waves with predominant periods having extreme height. Various wind speeds and corresponding operational settings of the turbine (i.e., rotor speed and blade pitch angle) given in Table 5.1.3 are used. The current speed is considered as zero whereas hydrodynamic coefficients in the wave force calculations are set as $C_a = 1.0$ and $C_d = 1.0$ based on Reynolds and Keulegan-Carpenter number (Chakrabarti, 2005). The wind and wave headings are considered as collinear and fixed at zero degrees with respect to the x-axis. With this assumption, the structure moves only in the x-z plane; hence the motions are surge, heave and pitch. At the beginning of the simulation, a cosine taper function is imposed on the total forces and moments to reduce the transient effects produced by the impulsive loading. The motions and associated hydrodynamic loading resulting from the analysis are studied using their time history, amplitude spectra, range (minimum to maximum) and statistical parameters such as standard deviation and skewness.

Three different loading conditions as detailed in Table 6.3.1 below, are chosen to investigate the effect of nonlinear wave kinematic on motion response and associated hydrodynamic loading.

Table 6.3.1 Loading condition

Loading condition (LC)	Description
WO	TLPWT subjected to wave only
WW-O-V_w	TLPWT subjected to combined wave and wind (turbine in operating condition at wind speed of V_w)
WW-P-V_w	TLPWT subjected to combine wave and wind (turbine in parked condition exposed to extreme wind speed of V_w)

The motion responses and hydrodynamic loadings are further compared with the design-oriented analytical wave models, i.e. Airy′s LWT and Fenton′s NLSWT wave models.

6.3.1 First order response

6.3.1.1 Motion response under wave excitation

Global motion analysis of a TLPWT under loading condition wave only (WO), is performed to see the clear difference in its motion predictions using different wave models from the state where the body is at rest or in static equilibrium. The first case presented here uses a monochromatic incident wave with a period of 14sec having steepness (H/L_0) of 0.1 in a water depth of 100m. These wave parameters yield maximum water particle kinematics among all the cases listed in Table 6.1.1 as detailed in section 6.1.2. Time history and amplitude spectra of wave surface elevation predicted using three different wave models considered under this study are presented in Figure 6.3.1, and the corresponding motion responses of TLPWT are presented

in Figure 6.3.2. Here, the wave surface elevation and translational motions such as surge and heave are normalised by input wave amplitude amp, whereas pitch motion is normalised by wave steepness (H/L_0).

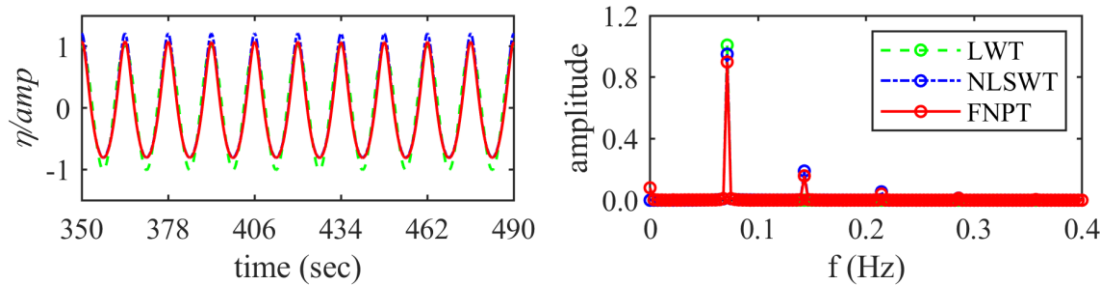

Figure 6.3.1 Time history and amplitude spectra of wave surface elevation

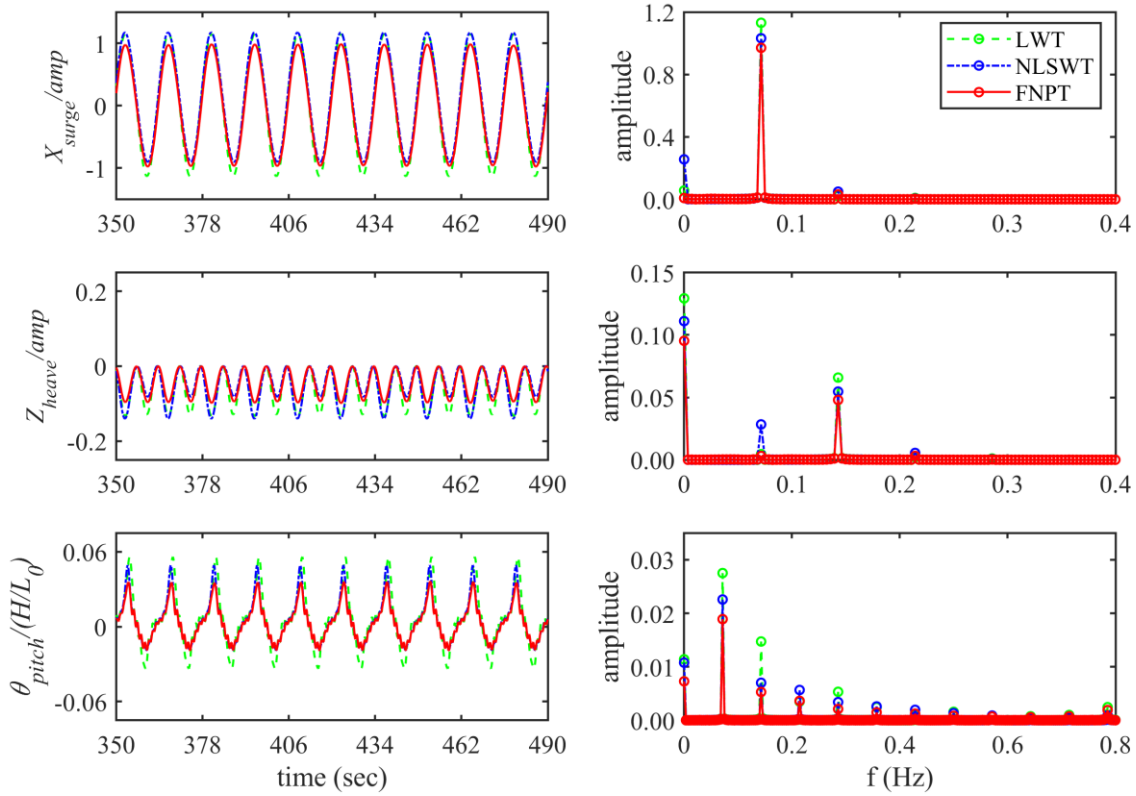

Figure 6.3.2 Time history and amplitude spectra of TLPWT motions for LC: WO

The time history plots presented for wave only condition in Figure 6.3.2 showed positive mean for surge and pitch motion whereas negative mean for heave motion. This is mainly seen because of the mean drift force resulting from nonlinearity present in the numerical model. The nonlinearity here primarily constitutes nonlinearity in wave kinematics, wave forces and the equation of motion. The negative mean for heave motion is not only the result of wave loading but also due to the set-down effect resulting from the positive surge and pitch motion of the platform. The motions in all the modes are predicted higher by Airy's linear wave model as compared to predictions using nonlinear wave models by Fenton and QALE-FEM. Comparing motions using both the nonlinear wave models (i.e., Fenton and QALE-FEM), Fenton's model predicted surge and pitch motions higher at crest but matched well at a trough, reflecting wave

surface profile predictions as depicted in Figure 6.3.1. The heave motion, which is dominated by second order response, its first order response also showed a similar trend. The maximum value of motions in each mode are predicted higher by Fenton's model and the range of motions.

The predominant peak response appeared at the input wave frequency (f_w) for surge and pitch motions whereas, for heave motion, at second harmonics ($2f_w$) of it. For surge motion, the response peaks also appeared at second harmonics ($2f_w$) of input wave frequency (f_w), but the magnitudes were seen insignificant. Airy's LWT and Fenton's NLSWT wave model predicted surge motion 16% and 6% higher as compared to QALE-FEM. For heave motion which is dominated by second order response, Airy's LWT and Fenton's NLSWT wave model predicted it 35% and 42% higher as compared to QALE-FEM. For pitch motion, responses appeared at input wave frequency and at multiple harmonics of input wave frequency. The responses beyond fourth ($4f_w$) harmonics were seen less (< 10%) as compared to responses at input wave frequency (f_w). The significant differences in motion amplitude were seen at second harmonics of input wave frequency where Airy's linear wave model predicted response 2.7 times and Fenton's wave model by 1.3 times of response predicted by QALE-FEM. Overall, Airy and Fenton's wave model predicted pitch motion 60% and 22% higher as compared to QALE-FEM.

This comparison shows that the platform motions are predicted considerably higher by Airy's linear wave model as compared to predictions by both the nonlinear wave models (Fenton and QALE-FEM). This is seen because in the case presented here, inertia part of the wave force dominates total wave force acting on the structure. This inertia force is mainly dependent on the water particle accelerations, which are predicted higher by Airy's LWT wave model as compared to both the nonlinear wave models for the entire wetted length of the structure over which forces are integrated to obtain the total force acting on the structure. This wetted length is a function of wave surface profile variation which is also predicted higher by Airy's wave model that further contributes to higher wave loading and hence the higher platform motions. The drag part of wave force is dependent upon the water particle velocity. Though Airy's wave model underpredicted it at wave crest as compared to nonlinear wave models, the difference gets reduced with depth and reverses the sign before the keel of the platform. Therefore, the effect of higher horizontal water particle velocity predicted by nonlinear wave models is not seen in this case.

In the numerical model, the elemental forces due to waves (such as inertia and drag) are computed at each time step along the instantaneous wetted length of the member of the platform and then integrated over it. The forces and moments obtained in such a manner are then summed up over all the platform members to obtain the total force and moment acting on the platform. Thus, during the simulation, this different force and moment component (i.e., inertia and drag) are available separately (in addition to the total force and moment acting on the platform). The time history and respective amplitude spectra of inertia, drag and total wave force in surge, heave and pitch modes for the above presented case are presented in Figure 6.3.3, Figure 6.3.4 and

Figure 6.3.5 respectively. Here, the forces are normalised by platform buoyancy force f_{buoy} and moments are normalised by product of platform buoyancy force and draft h_d respectively.

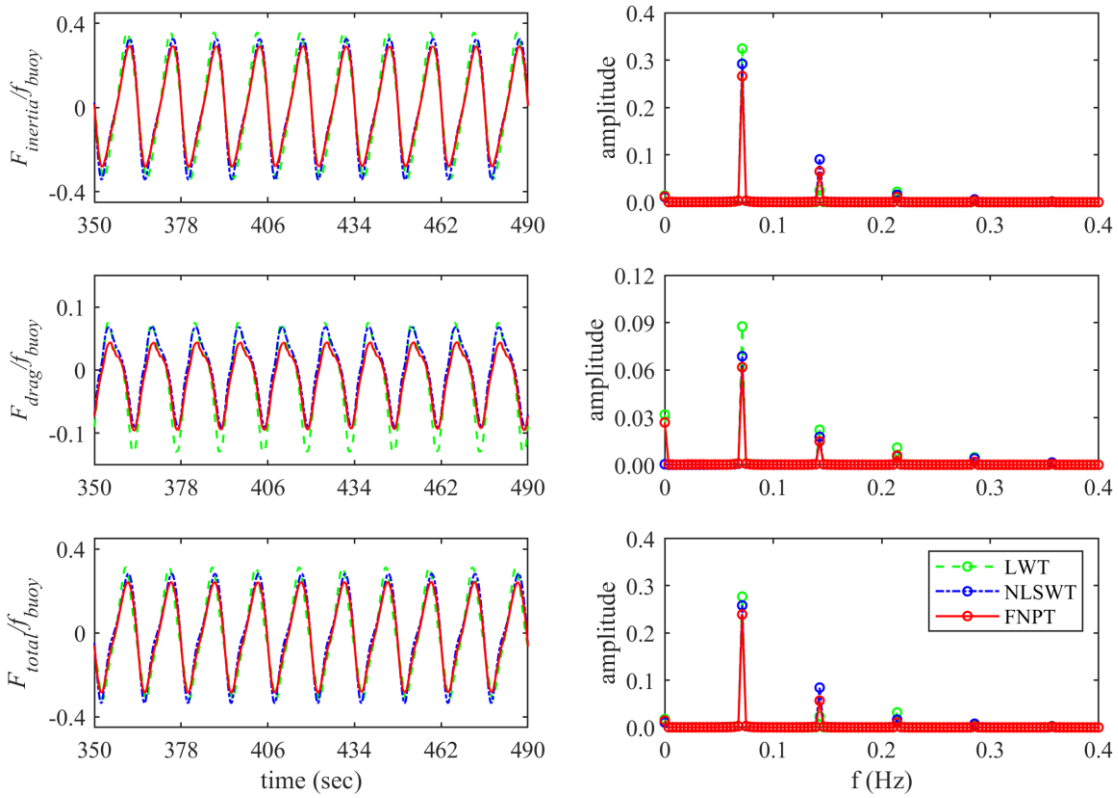

Figure 6.3.3 Time history and amplitude spectra of surge force for LC: WO

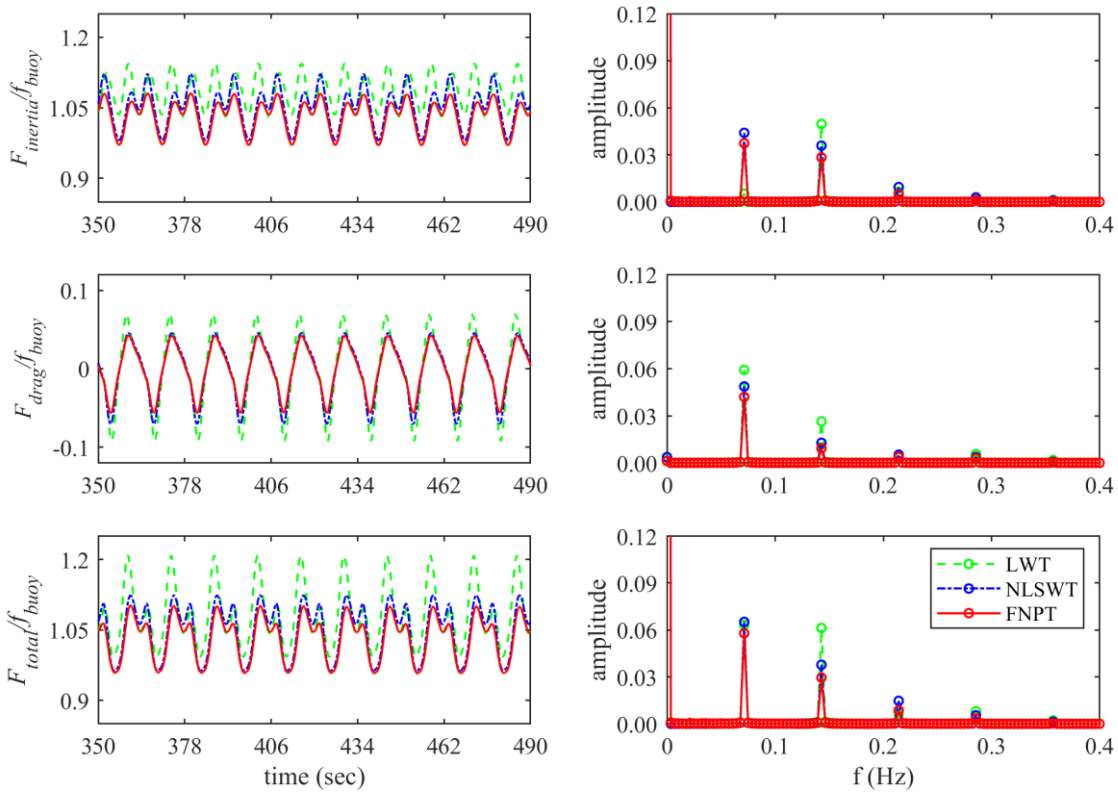

Figure 6.3.4 Time history and amplitude spectra of heave force for LC: WO

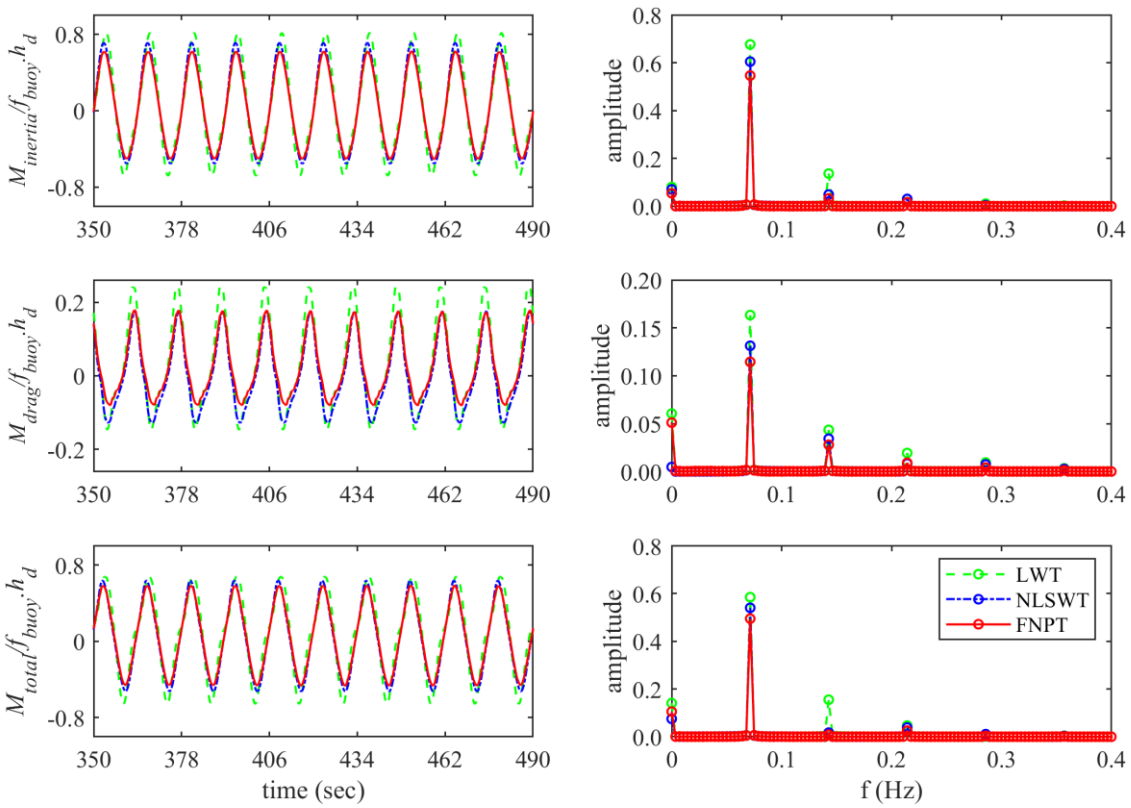

Figure 6.3.5 Time history and amplitude spectra of pitch moment for LC: WO

It can be seen from Figure 6.3.3, Figure 6.3.4 and Figure 6.3.5 that the total wave force and its component, inertia and drag in the surge, heave and pitch directions are predicted higher by Airy's LWT wave model as compared to nonlinear wave models (i.e., Fenton's NLSWT and FNPT based QALE-FEM). This overprediction of wave force by Airy's LWT wave model as compared to FNPT based QALE-FEM is seen due to approximation such as wheeler stretching used to predict the water particle kinematics up to wave surface that overestimates horizontal and vertical accelerations as shown in systematic wave kinematic comparison presented in section 6.1.2. The overprediction of wave force by Fenton's NLSWT wave model as compared to FNPT based QALE-FEM is mainly seen due to overprediction of wave surface elevation and hence underlying water particle kinematics. This overprediction of wave height by Fenton's wave model is primarily due to its inherent assumption of uniform waveform and ignoring wave dispersion.

This example demonstrates how different wave model affect predictions of wave surface and underlying water particle kinematics and its consequential effect on the wave forces and resulting motion predictions for the chosen TLPWT. However, the loading condition considered here is wave only where the structure is at rest or in static equilibrium before wave approaches. In practice floating wind turbine will always have an offset and heel angle due to wind load acting on the turbine and its supporting tower and hence the motion responses are examined next for combined wind and wave loading while the turbine is operating and in a parked condition.

6.3.1.2 Motion response under combined wind and wave excitation

Global motion analysis of a TLPWT under combined wind and wave loading condition is performed to see the difference in its motion predictions using different wave models when the structure has an offset and heel angle due to wind loads acting on the turbine and its supporting tower. An appropriate combination of wind and wave loading is necessary for the design purpose in an integrated analysis. In the IEC 61400-3 (2009), different load cases are introduced for the design of floating offshore wind turbine to assure its integrity during installation, operation and survival. The defined load cases are given below,

- Power production
- Power production plus occurrence of fault
- Start-up
- Normal shutdown
- Emergency shutdown
- Parked (standing still or idling)
- Parked and fault condition
- Transport, assembly, maintenance and repair

Among these, the turbine in power production and parked condition are considered to produce maximum offset and heel angle for the platform. During operating condition, the turbine produces maximum load while running at its rated wind speed, whereas during parked condition, drag force due to extreme wind acting on tower produces maximum surge loads. Both these sources of loads may produce maximum offset and heel angle for the platform and hence considered for the study. The rated wind speed of 21m/s is considered for turbine under the operating condition and an extreme wind speed of 30.5m/s is considered for the turbine in a parked condition. The case presented here uses monochromatic incident wave the same as used in the previous section. Time history and amplitude spectra of motion response of TLPWT for turbine under the operating, (WW-O-21) and in parked, (WW-P-30.5) condition are presented in Figure 6.3.6 and Figure 6.3.7 respectively.

The time history plots presented for co-existing wind and wave condition in Figure 6.3.6 and Figure 6.3.7 showed an increase in positive mean for surge and pitch motion of the platform as compared to wave only condition. This is expected due to the presence of wind turbine thrust and its large moment resulting due to its higher elevation from the centre of gravity of the structure. The heave time series also showed further increased in negative mean due to an additional set-down effect resulting from the increase in positive surge and pitch motion of the platform. A slight reduction in motion amplitudes were seen due to aerodynamic damping. The overall platform motions under both the loading conditions, ‘WW-O-21’ and ‘WW-P-30.5’ are seen predicted higher by Airy’s and Fenton’s wave model as compared to predictions by QALE-FEM.

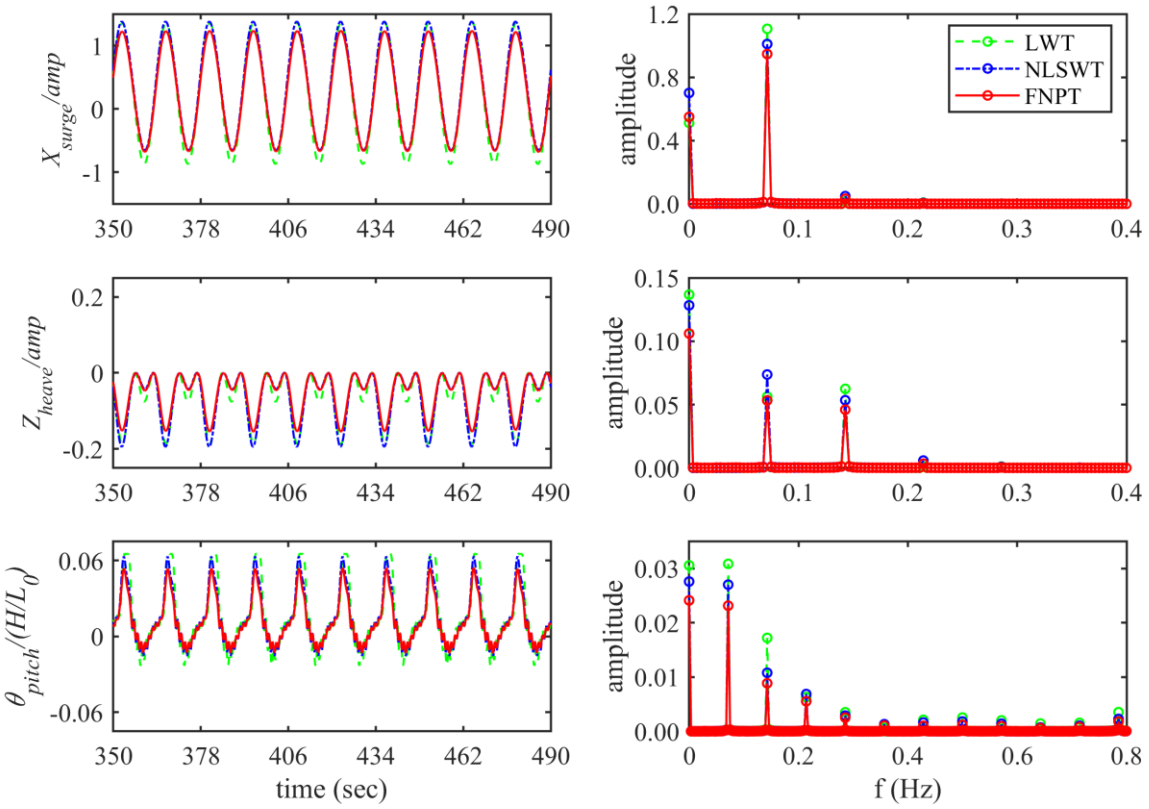

Figure 6.3.6 Time history and amplitude spectra of TLPWT motions for LC: WW-O-21

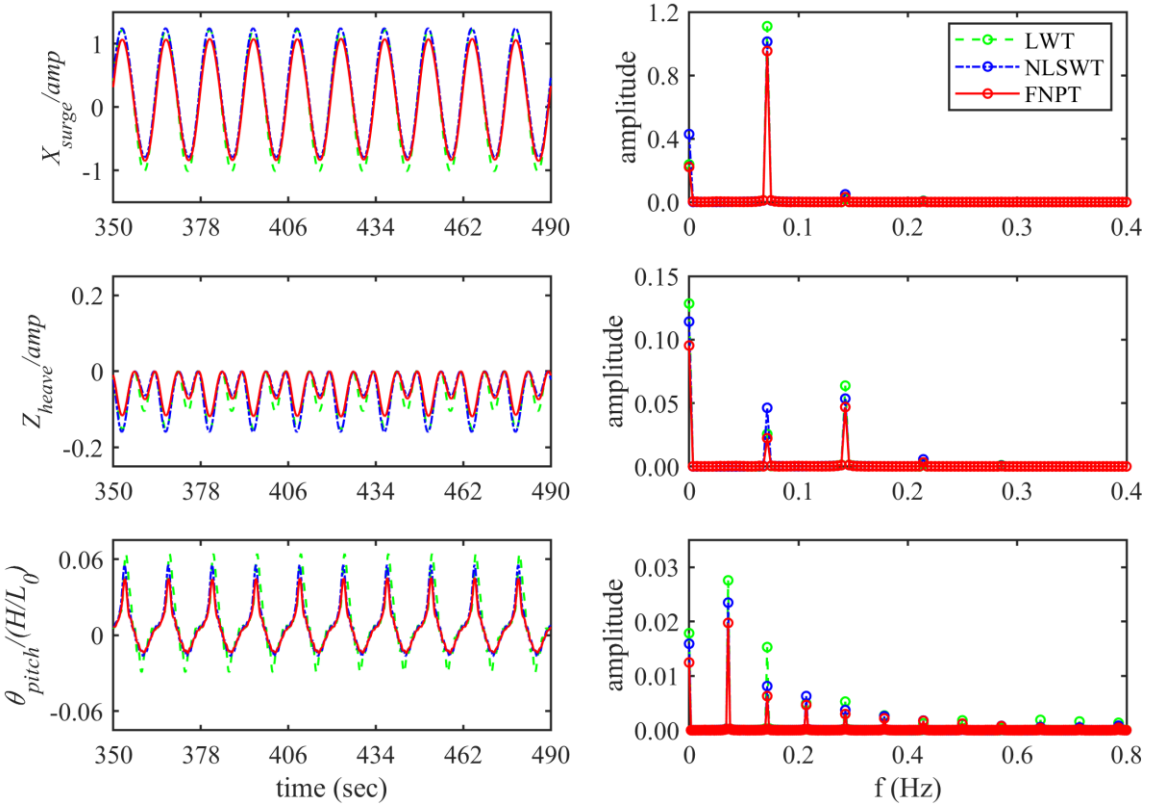

Figure 6.3.7 Time history and amplitude spectra of TLPWT motions for LC: WW-P-30.5

The maximum differences in surge motions were seen approximately same for both the loading condition where Airy's and Fenton's wave model predicted it 16% and 6% higher as compared to QALE-FEM. The heave motion was seen dominated by second order response under wave only loading condition, however this dominance is seen reducing with the increase in wind loading with maximum effect seen for turbine under operating condition at its rated speed. The first order responses under WW-O-21 loading condition are predicted higher by Fenton as compared to Airy's linear wave model but the overall heave response is predicted higher by Airy's linear wave model. Airy and Fenton's wave model predicted heave motion higher by 17% and 22% for co-existing wind and wave while turbine is operating at rated wind speed (WW-O-21) and by 28% and 33% for turbine in parked condition (WW-P-30.5). Similar observations were made for platform pitch motions. The responses appeared at input wave frequency and multiple harmonics of input wave frequency. The responses beyond fourth harmonics were seen less (< 10%) as compared to responses at input wave frequency. The significant difference in motion amplitudes were seen at second harmonics of input wave frequency for co-existing wind wave condition (WW-O-21.8) where Airy's linear wave model predicted responses 2.8 times and Fenton's wave model by 1.4 times of motions amplitude predicted by QALE-FEM. Overall, Airy's and Fenton's wave model predicted pitch motion 30% and 16% higher as compared to QALE-FEM for co-existing wind and wave (WW-O-21.8) where turbine is operating at its rated wind speed (WW-O-21.8) and by 56% and 20% for turbine in parked condition (WW-P-30.5).

This comparison shows that the platform motions under both the analysed co-existing wind and wave loading conditions (WW-O-21 and WW-P-30.5) are predicted considerably higher by Airy's linear wave model as compared to predictions by both the nonlinear wave models (NLSWT and FNPT) despite damping effect provided by wind loading. The wind loading acting on turbine rotor and its supporting tower depends mainly upon wind speed. However, its dependence upon wind speed is a dependence on the relative wind speed at hub as it moves along with the supporting platform under the action of waves. To investigate this interaction effect in more general case the calculations and comparisons have been carried out for platform responses under various wave conditions as detailed in Table 6.1.1 while the turbine is operating at its rated wind speed of 21m/s. The range of steady normalised platform motions (measured from minimum to maximum) and the corresponding hydrodynamic forces are presented in Figure 6.3.8, Figure 6.3.9 and Figure 6.3.10 in the surge, heave and pitch modes respectively.

The results presented in Figure 6.3.8 through Figure 6.3.10 shows the increase in difference in normalised platform motions predicted by three different wave models with the increase in wave periods up to period of 14sec and thereon differences are seen reducing. The maximum differences noticed at wave period of 14sec where Airy's wave model predicted surge, heave and pitch motion higher by 16%, 17% and 27% as compared to QALE-FEM whereas Fenton' wave model predicted it higher by 6%, 22% and 13% respectively.

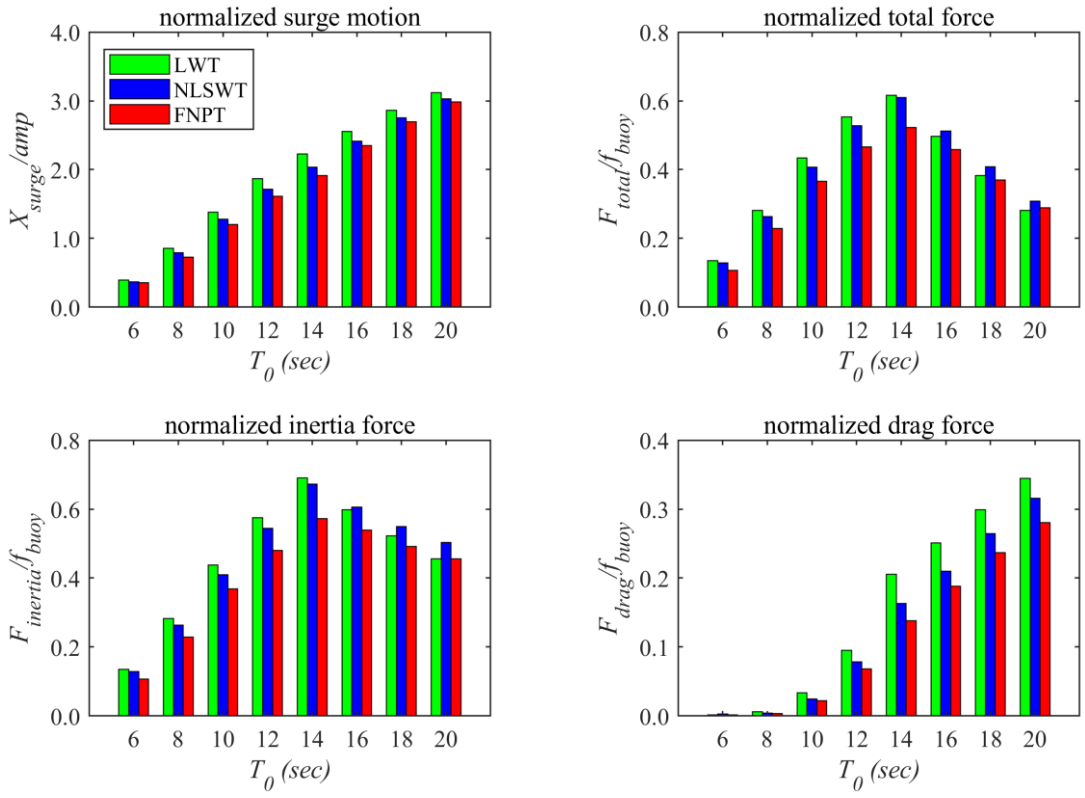

Figure 6.3.8 Range of normalised surge motion and corresponding wave forces for various wave periods

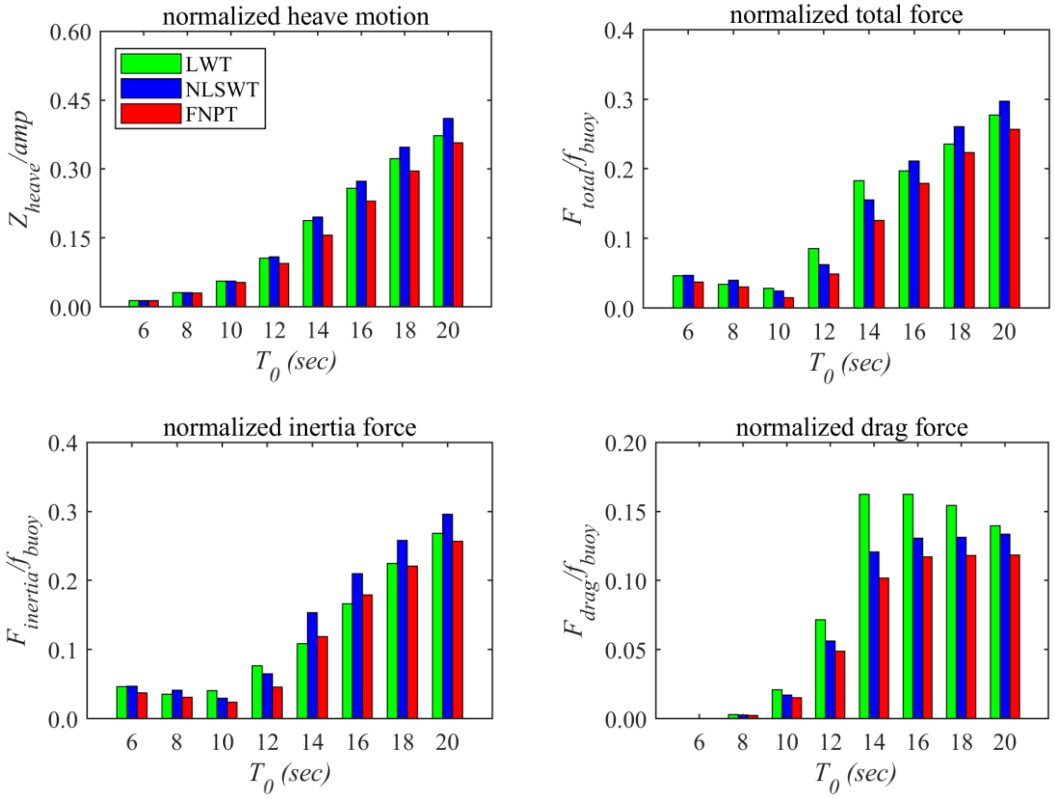

Figure 6.3.9 Range of normalised heave motion and corresponding wave forces for various wave periods

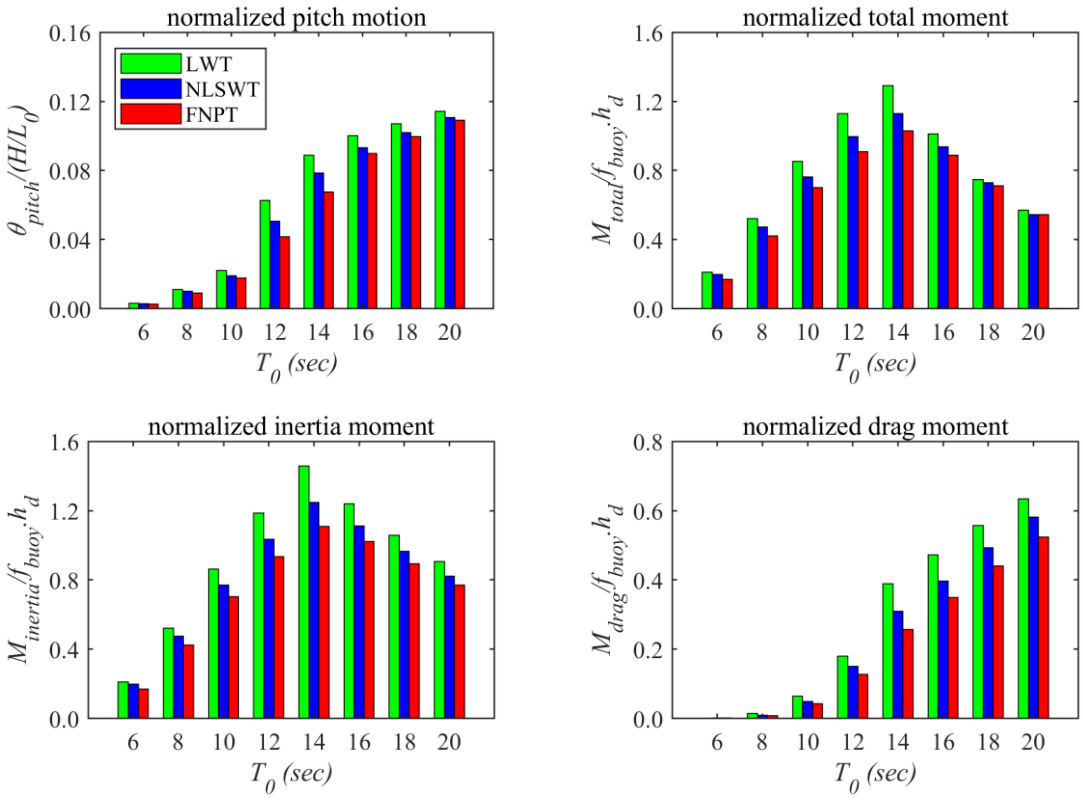

Figure 6.3.10 Range of normalised pitch motion and corresponding moments due to wave forces for various wave periods

The inertia force in surge and pitch direction increases with an increase in wave period up to a period of 14sec and reduces thereon whereas drag force increases with an increase in the wave period. However, the total wave force follows the trend of inertia force as it dominates total wave force over the drag force. Inertia force dominance reduces with increase in wave period which reflects in total wave force and the corresponding platform motions showing less difference in their predictions using different wave models.

6.3.1.3 Effect of wave steepness on motion response

The non-linearity of a wave is dependent on both its height, H and period, T_0 (or length, L_0). A steepness of wave H/L_0, which is linked to both wave height and period is normally employed to describe the nonlinearity of an input wave. To study the influence of this parameter on wave nonlinearity and consequently on predictions of TLPWT motions, three sets of H/L_0 - 0.02, 0.06 and 0.10 are generated for simulation purpose. Based on wave steepness H/L_0, these data sets are intended to simulate a mild, medium and an extreme sea state respectively. Loading condition of co-existing wave and wind with turbine in operating condition (WW-O-21) at wind speed of 21m/sec is considered. The wave period and water depth used in this case is 14 secs and 100m respectively. A range of steady normalised platform motions and the corresponding hydrodynamic forces against various wave steepness′s predicted by different wave models are

presented in Figure 6.3.11, Figure 6.3.12 and Figure 6.3.13 for the surge, heave and pitch modes respectively.

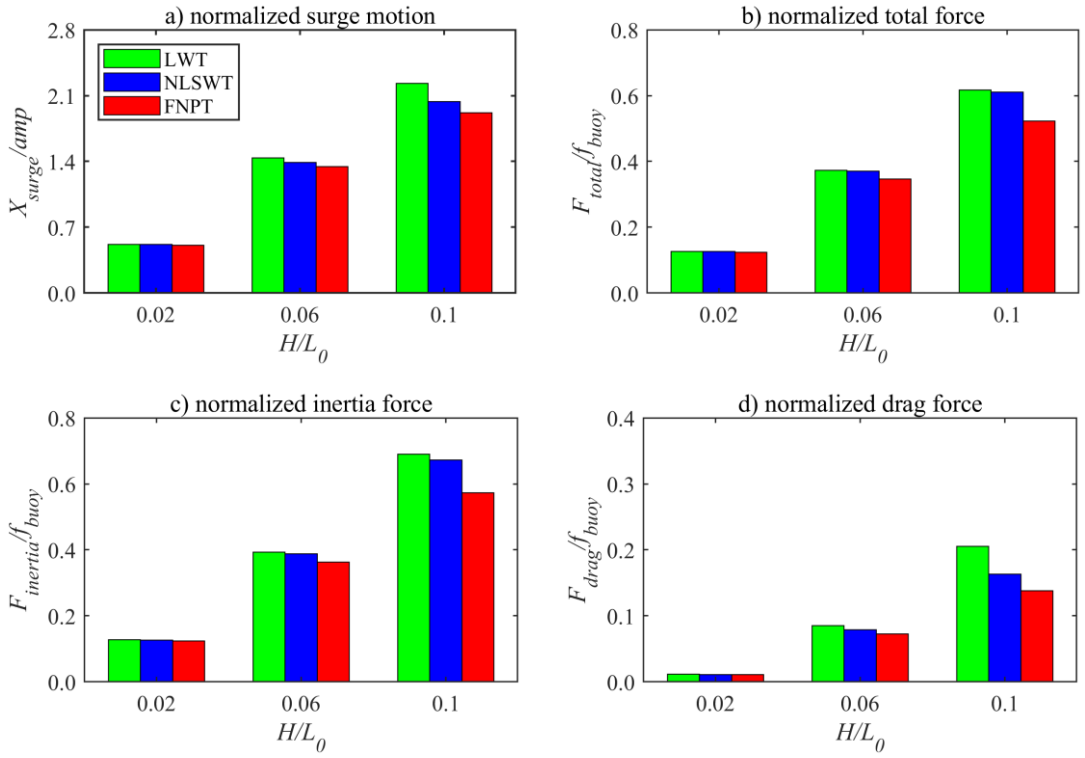

Figure 6.3.11 Range of normalised surge motion and wave forces for various wave steepness

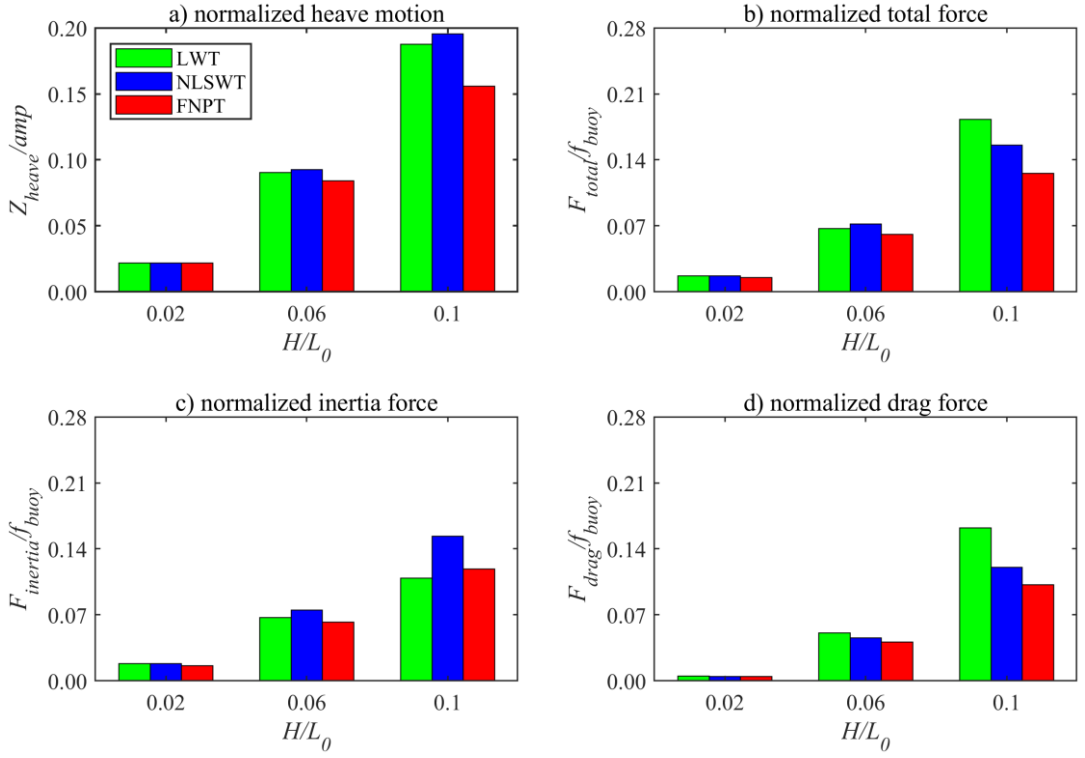

Figure 6.3.12 Range of normalised heave motion and wave forces for various wave steepness

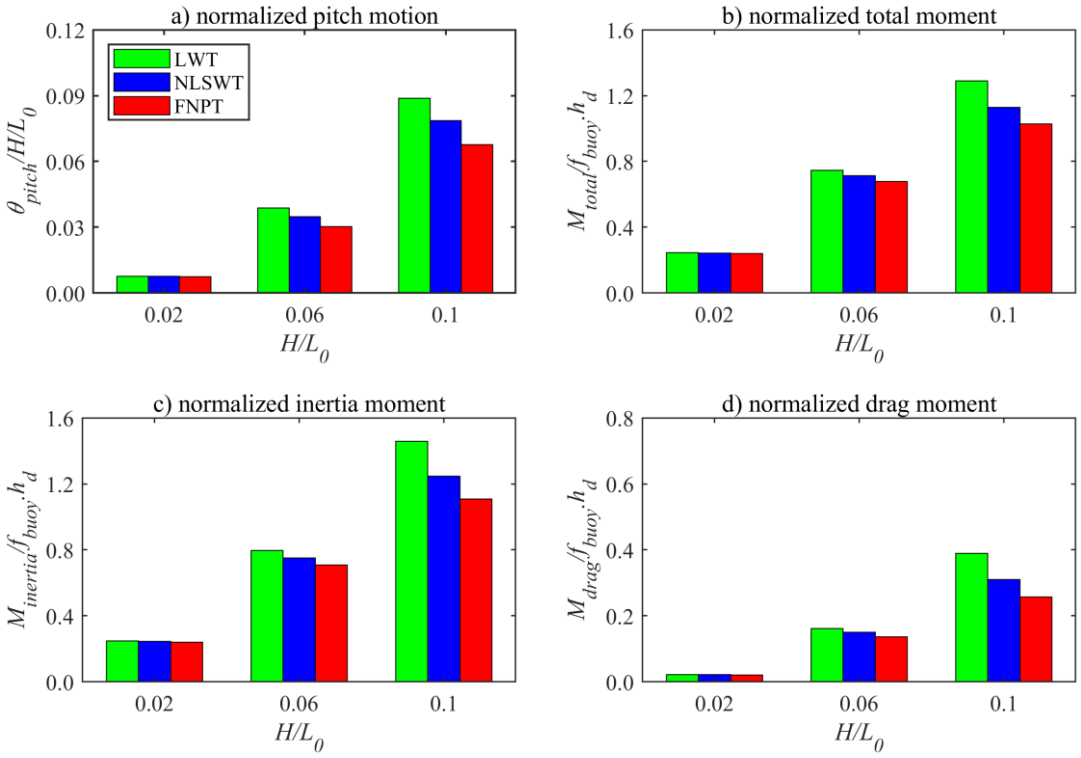

Figure 6.3.13 Range of normalised pitch motion and moments due to wave forces for various wave steepness

As expected, the difference between platform motions and the corresponding hydrodynamic forces predicted by three different wave models are smallest at a benign sea state while significant for extreme sea state reflecting the difference in prediction of wave surface and its underlying water particle kinematics as depicted in Figure 6.1.15 and Figure 6.1.17. For benign sea state with wave steepness of 0.02, difference in platform motions are insignificant. At wave steepness of 0.06, difference in platform motions are visible but not high. For extreme sea state, difference in all the motions predicted by different wave models is significant. The surge, heave and pitch motion predicted by LWT Vs FNPT are 15%, 17% and 27% whereas by NLSWT Vs FNPT are 8%, 22% and 13% respectively. Table 6.3.2 summarizes the motion statistics, such as standard deviation and skewness for varied wave steepness which showed trend consistent with what is observed in Figure 6.3.11, through Figure 6.3.13. Larger the wave steepness, more noticeable the difference in standard deviation of the platform motions and skewness which is indicator of nonlinearity.

Table 6.3.2 Normalised motion statistics for various wave steepness

Platform motions	Wave model	Statistical parameters					
		Standard deviation			Skewness		
H/L_0 →		0.02	0.06	0.10	0.02	0.06	0.10
Surge	LWT	0.182	0.506	0.782	0.350	0.209	0.137
	NLSWT	0.182	0.490	0.715	0.352	0.261	0.263
	FNPT	0.178	0.470	0.670	0.355	0.257	0.207
Heave	LWT	0.008	0.030	0.059	-0.914	-1.099	-0.964
	NLSWT	0.008	0.031	0.065	-0.913	-1.141	-1.165
	FNPT	0.008	0.028	0.050	-0.953	-1.193	-1.120
Pitch	LWT	0.003	0.010	0.026	0.216	0.686	1.121
	NLSWT	0.003	0.009	0.022	0.216	0.712	1.211
	FNPT	0.003	0.008	0.018	0.219	0.683	1.225

6.3.1.4 Effect of water depth on motion response

TLPWT are most likely to be considered for water depths between 100m to 200m. The performance of the parameterised design was examined for 100m and 200m water depth with mid-depth of 150m. No changes in platform configuration are implemented other than extending tendon lengths. However, there was a decrease in tendon stiffness due to increase in its length which affects its natural period. The natural period of the platform for each water depth considered here is presented in Figure 6.2.1. Loading condition of co-existing wave and wind with the turbine in operating condition (WW-O-21) at wind speed of 21m/sec is considered. The wave with a period of 14 sec and steepness H/L_0 of 0.1 is considered in all the water depths. A range of steady state normalised platform motions and the corresponding hydrodynamic forces acting on it in various water depths, predicted by different wave models are presented in Figure 6.3.14, Figure 6.3.15 and Figure 6.3.16 for the surge, heave and pitch modes respectively.

It can be seen from Figure 6.3.14 and Figure 6.3.15 that the difference between platform translational motions and corresponding hydrodynamic forces predicted by three different wave models are reducing with an increase in water depths. The difference between rotational pitch motion and relevant moments due to hydrodynamic forces predicted by three different wave models are increasing with an increase in water depth. It is due to a decrease in tendon stiffness with an increase in water depth. Although the difference in wave surface and associated water particle kinematics predicted by three different wave models are reducing with an increase in water depth as depicted in Figure 6.1.17 and Figure 6.1.18 their effect on platform motions and hydrodynamic forces are considerable.

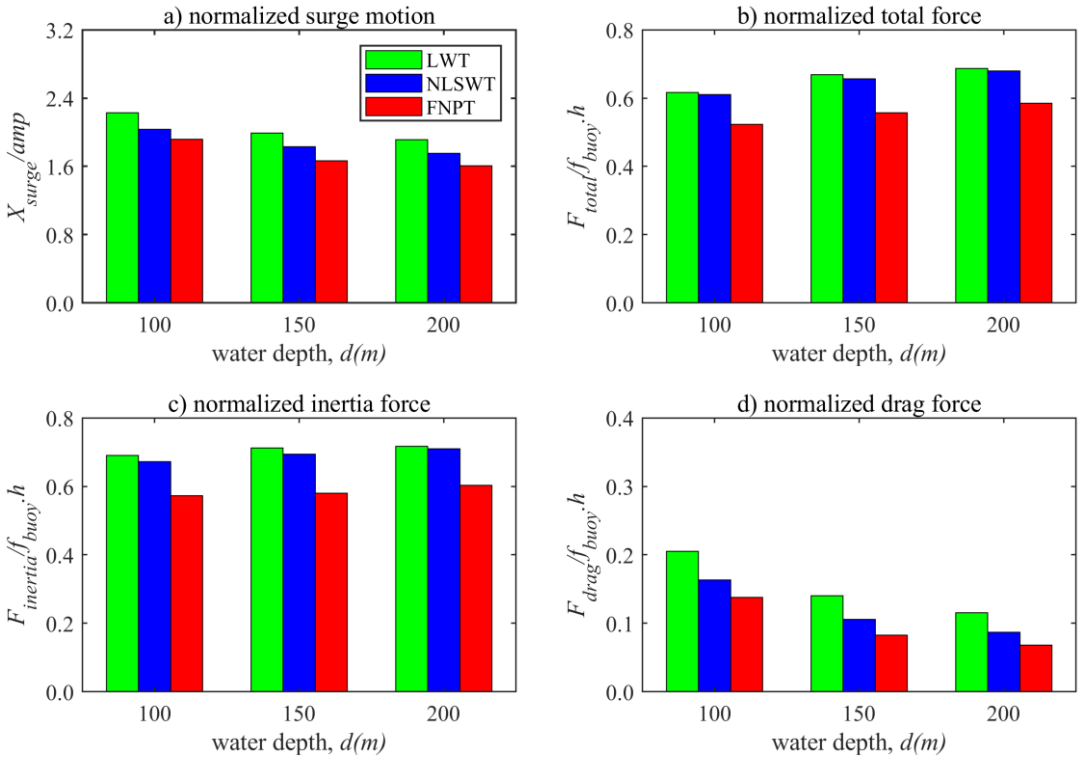

Figure 6.3.14 Range of normalised surge motion and wave forces for various water depths

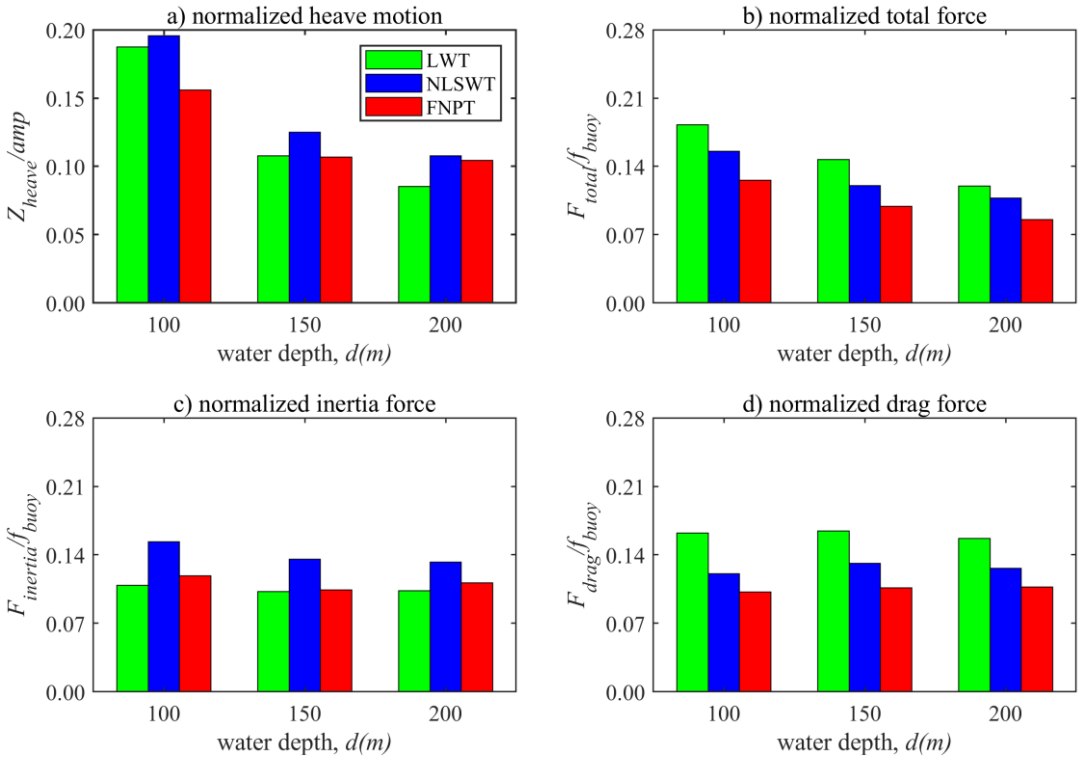

Figure 6.3.15 Range of normalised heave motion and wave forces for various water depths

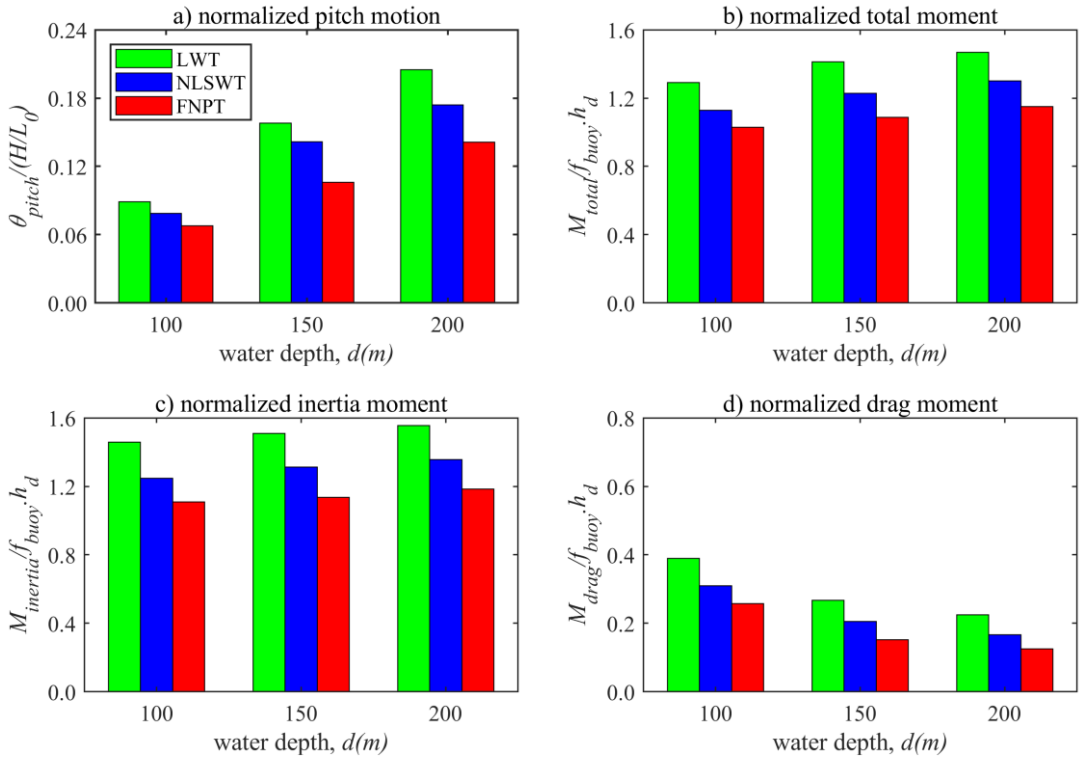

Figure 6.3.16 Range of normalised pitch motion and moments due to wave forces for various water depths

Table 6.3.3 summarizes the motion statistics, such as standard deviation and skewness for varied water depth which showed trend consistent with what is observed in Figure 6.3.14 through Figure 6.1.16. The larger the water depth more noticeable the difference in standard deviation of the platform motions and skewness which is indicator of nonlinearity.

Table 6.3.3 Normalised motion statistics for various water depths

Platform motion	Wave model	Statistical parameters					
		Standard deviation			Skewness		
Water depth, d →		100m	150m	200m	100m	150m	200m
Surge	LWT	0.782	0.704	0.674	0.137	0.022	-0.019
	NLSWT	0.715	0.646	0.619	0.263	0.029	0.020
	FNPT	0.670	0.581	0.553	0.207	0.002	-0.001
Heave	LWT	0.059	0.036	0.030	-0.964	-0.782	-0.726
	NLSWT	0.065	0.045	0.039	-1.165	-0.736	-0.595
	FNPT	0.050	0.042	0.037	-1.120	-0.701	-0.493
Pitch	LWT	0.026	0.039	0.053	1.121	0.888	0.772
	NLSWT	0.022	0.035	0.045	1.211	1.055	0.796
	FNPT	0.018	0.026	0.036	1.225	1.079	0.634

The result shows that the wave surface and underlying water particle kinematics predicted by different wave models affect TLPWT motions considerably in water depth ranging from 100m to 200m where tension leg platforms are considered to be favourite.

6.3.1.5 Motion response comparison for target wave

The motion response comparison presented in the previous section were based on predicted wave surface where it was shown that Airy's LWT and Fenton's NLSWT wave model overpredicts platform motions as compared to motions predicted by FNPT based QALE-FEM. In this section, motion responses are compared for the target wave surface where steepness of wave (H/L_0) is kept the same in all the three wave models. It is achieved by measuring wave height from steady wave surface elevation from QALE-FEM simulation and feeding back into Airy's and Fenton's wave model. By doing so, wave crest and associated wave kinematics predicted by all the three wave models will be different, but wave steepness will be identical. An effect of this difference in wave crest and wave kinematics on motion response of the chosen structure is studied for loading condition of co-existing wave and wind with the turbine in operating condition at the rated wind speed of 21m/sec. A range of steady-state crest height and normalised platform motions predicted by different wave models for all the wave conditions listed in Table 6.1.1 in a water depth of 100m are presented in Figure 6.3.17.

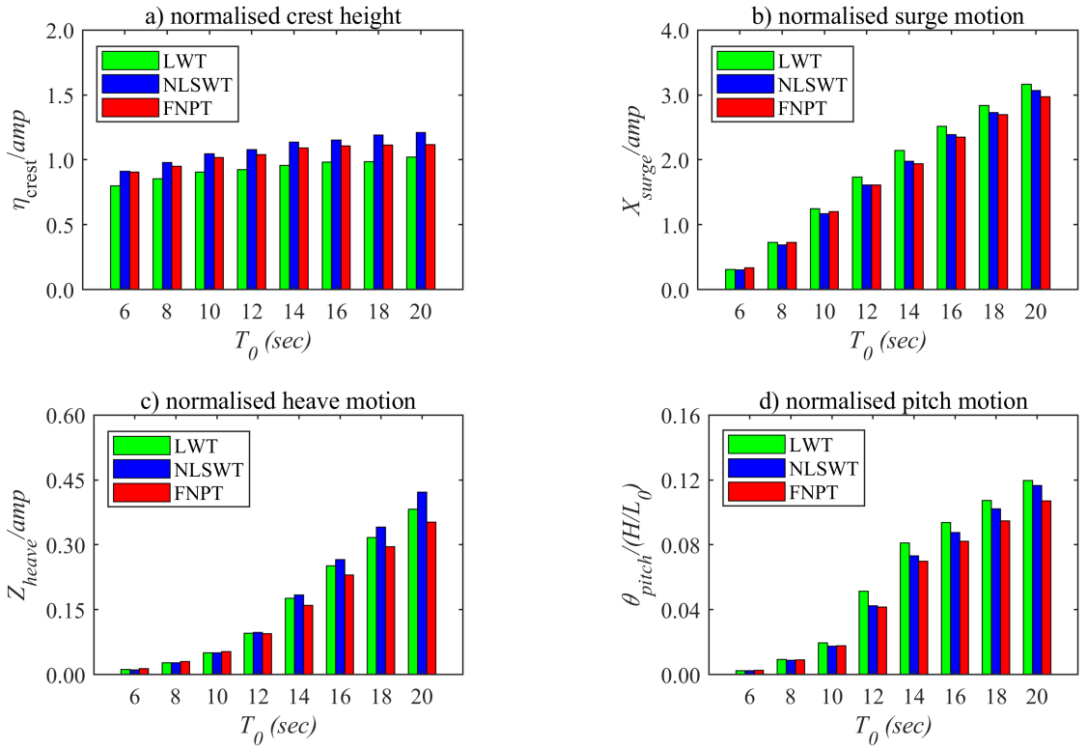

Figure 6.3.17 Range of normalised crest height and TLPWT motions for target wave

It can be seen from Figure 6.3.17 that the difference in crest height prediction by both the nonlinear wave models are increasing with increase in wave period (that means d/L_0) as compared to predictions by linear wave model. The maximum % difference in crest height

predicted by NLSWT and FNPT wave models is seen as 19% and 10% as compared to LWT wave model respectively. The difference in crest height predicted by both the nonlinear wave models, i.e., NLSWT and FNPT are seen insignificant for deep water waves (i.e., 6sec,8sec, and 10sec). For intermediate water waves, the difference in crest height predictions are seen increasing with increase in wave period. An effect of this difference in crest height and associated wave kinematics as depicted in Figure 6.1.19 through Figure 6.1.22 can be seen in predictions of motion responses of chosen TLPWT system. Airy's LWT wave model overpredicted motion responses in all the modes with maximum differences are noted for wave period of 14sec for surge and pitch mode and for wave period of 20sec for heave mode whereas Fenton's NLSWT wave model overpredicted all the motion responses for a longest wave period of 20sec. The maximum percentage difference predicted by Airy's LWT model in surge, heave and pitch mode is noted as 10%,9%, and 16% while by Fenton's NLSWT model noted as 3%, 19% and 9%.

This example demonstrates the effect of nonlinearity in predicting wave kinematic and consequently motion responses. The overprediction of wave kinematics and motion responses by Airy's LWT wave model as compared to FNPT wave model are mainly seen due to wheeler stretching approximation used. The slight overpredictions by Fenton's NLSWT wave model as compared to QALE-FEM are seen due to its assumption of a uniform waveform. However, for deep water waves its predictions are seen matching well with the predictions by QALE-FEM. For intermediate water waves, differences are seen but less than 10% for dominant surge and pitch motions which is mainly reflecting the difference in crest height prediction. Hence Fenton's NLSWT wave model is sufficient for modelling extreme regular waves with target wave surface and can be used.

The results of motion responses presented in this section showed that the Airy's LWT and Fenton's NLSWT wave model predicted motion responses higher as compared to fully nonlinear wave model for both predicted and target wave. This is observed because natural periods of structure are far away from the analysed wave periods. The surge motion of chosen platform configuration has longer natural period than predominant wave period range whereas heave motion has shorter natural period. However, pitch motion of the platform generally has a natural period closer to the lower limit of predominant wave period range and can get excited due to extreme wave. Therefore, the pitch resonance response of concerned floating wind turbine is studied next.

6.3.2 High-frequency resonance (springing) response

The high-frequency resonance response of a chosen tension-leg-platform wind turbine is studied in a water depth of 200m where it tends to have a lower pitch natural period (between 1-4sec). The mooring line stiffness is set here to 2750kN which yields a natural period of the structure as 37.5s, 1.4s, and 2.9s for the surge, heave and pitch motion respectively. These natural

periods are within design limits set under section 6.2. The case presented here uses a monochromatic incident wave with a period of 8.7sec which is three times of pitch natural period of the structure. A height of a wave used is obtained by limiting its steepness, H/L_0 to 0.1. The same wave steepness is maintained in all the wave models. This is achieved by measuring wave height from steady wave surface elevation from QALE-FEM simulation and feeding back into Airy's LWT and Fenton's NLSWT wave model as target wave.

Time history and amplitude spectra of wave surface elevation and pitch motion of the structure predicted by all the three wave models are presented in Figure 6.3.18 and Figure 6.3.19 respectively. The pitch motions are presented for loading condition wave only, and combined wave and wind while the turbine is operating at its rated wind speed of 21m/s (WW-O-21) and in the parked condition exposed to an extreme wind speed of 30.5m/s (WW-P-30.5).

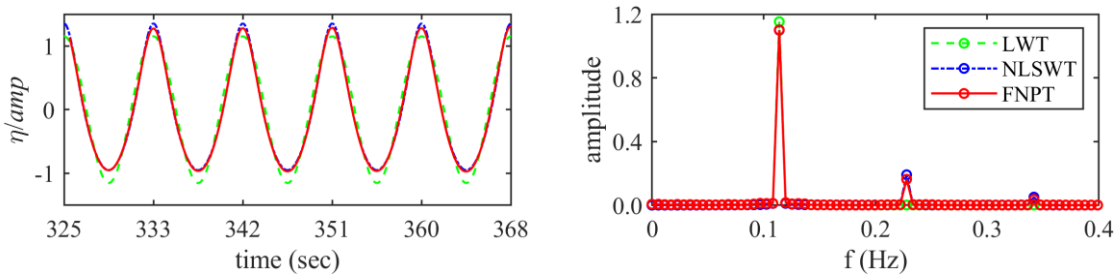

Figure 6.3.18 Time history and amplitude spectra of wave surface elevation

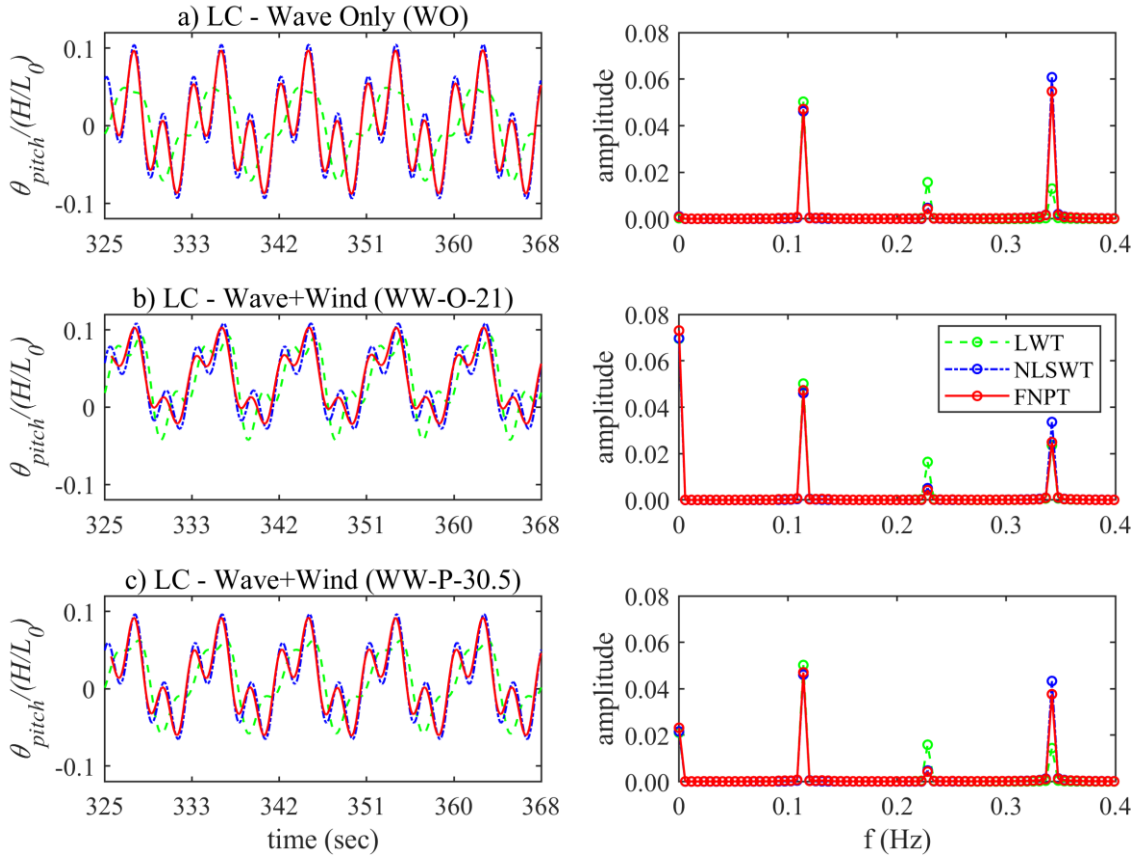

Figure 6.3.19 Time history and amplitude spectra of resonant pitch motion

It can be seen from Figure 6.3.19 a) that the pitch motion of the structure under 'WO' loading condition is predicted higher by both the nonlinear wave models by more than 50% as compared to predictions by linear wave model. Comparing pitch motions using both the nonlinear wave models, i.e., NLSWT Vs FNPT, the difference in predictions were seen insignificant (< 5%). It reinforces the fact that Fenton's NLSWT wave model predicts wave kinematic very close to fully nonlinear wave model FNPT for target/measured wave surface. The peak responses appear at input wave frequency (f_w), second harmonics of it ($2f_w$) and at third harmonics ($3f_w$) which is structures pitch natural frequency $(f_{n-pitch})$. The response amplitudes predicted by both the nonlinear wave models at pitch natural frequency are of a nearly equal magnitude to responses at input wave frequency. The responses predicted at pitch natural frequency by Fenton's NLSWT wave model and FNPT based QALE-FEM are 4.6 and 4.2 times higher than predictions by Airy's LWT wave model. The higher pitch motions predicted by both the nonlinear wave models as compared to linear wave model are mainly seen due to higher third harmonic force component predicted by them which excited the pitch response of the structure.

The time history plots of pitch motion presented for co-existing wave and wind in Figure 6.3.19 b) and c) showed an increase in its mean but the reduction in its amplitude as compared to wave only condition. The pitch motion predicted by FNPT wave model is seen 5% lower and 35% higher as compared to linear wave model while the turbine is operating at rated wind speed and in the parked condition respectively. It is mainly seen due to the damping effect produced by aerodynamic thrust acting on the turbine rotor. The turbine loads during rated wind speeds are higher as compared to the turbine loads in the parked condition; therefore, the damping effect was seen higher for rated wind speed. The responses predicted at pitch natural frequency by Fenton's NLSWT wave model and FNPT based QALE-FEM are seen reducing with an increase in the turbine loads. However, the turbine may produce less loads while operating at lower wind speed and consequently, will generate less damping. To investigate this effect of aerodynamic damping in more general case, calculations and comparisons of pitch motions are carried out for several wind speeds given in Table 5.1.3, and the range of pitch motions (measured from minimum to maximum) are presented in Figure 6.3.20.

It can be seen from the pitch motion ranges presented in Figure 6.3.20 that the increase in wind speed up to a rated wind speed of 21m/s produces higher turbine loads and hence higher damping which reduces the motion amplitudes. The maximum differences in pitch motions predicted by different wave models while turbine in operating condition are seen for lowest analysed operating wind speed of 7m/s where nonlinear wave models NLSWT and FNPT predicted pitch motions higher by 40% and 39% as compared to LWT wave model respectively. This higher pitch motion predicted by nonlinear wave models may have an impact on global response parameters of the chosen floating wind turbines components, i.e., wind turbine, tower,

platform hull and mooring system. Therefore, the effect of pitch resonance on the global response of a chosen floating wind turbine components is studied next.

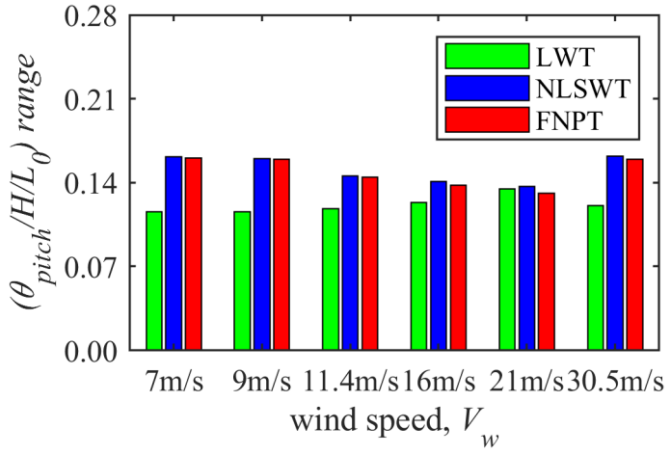

Figure 6.3.20 Range of normalised pitch motions for various wind speeds

6.4 Effect of nonlinear motions on global performance of TLPWT

Global performance of a TLPWT is assessed by investigating the effect of its nonlinear motions predicted by FNPT based QALE-FEM on the response parameters associated with its components, i.e., wind turbine, tall supporting tower, platform hull and mooring lines. The response parameters are further compared using design oriented analytical wave models, i.e. Airy's LWT and Fenton's NLSWT. Key response parameters associated with each component of a floating wind turbine are chosen to investigate their predictions using aforementioned wave models. Here global response parameters such as thrust acting on the wind turbine, the bending moment in a tower, and tension in each mooring line are chosen for the investigation.

As seen in the previous section 6.3.1 and 6.3.2, analytical wave models such as LWT and NLSWT predicted motion responses higher as compared to FNPT wave model at predominant wave frequencies. However, for pitch resonance condition, both the nonlinear wave models predicted motions higher as compared to linear wave model with the maximum differences for lower turbine loads that occurs when turbine is operating at low wind speed of 7m/s. Therefore, the resonance wave parameters and wind speed of 7m/s is chosen for investigating global response parameters. Time history of global response parameters corresponding to high-frequency pitch resonance motion is presented in Figure 6.4.1. Here wind turbine thrust is normalised by its steady state value T_{ss}, a tower bending moment is normalised by product of buoyancy force f_{buoy} and draft h_d of the platform, and mooring line tensions are normalised by their initial tension value $Tmoor_{in}$.

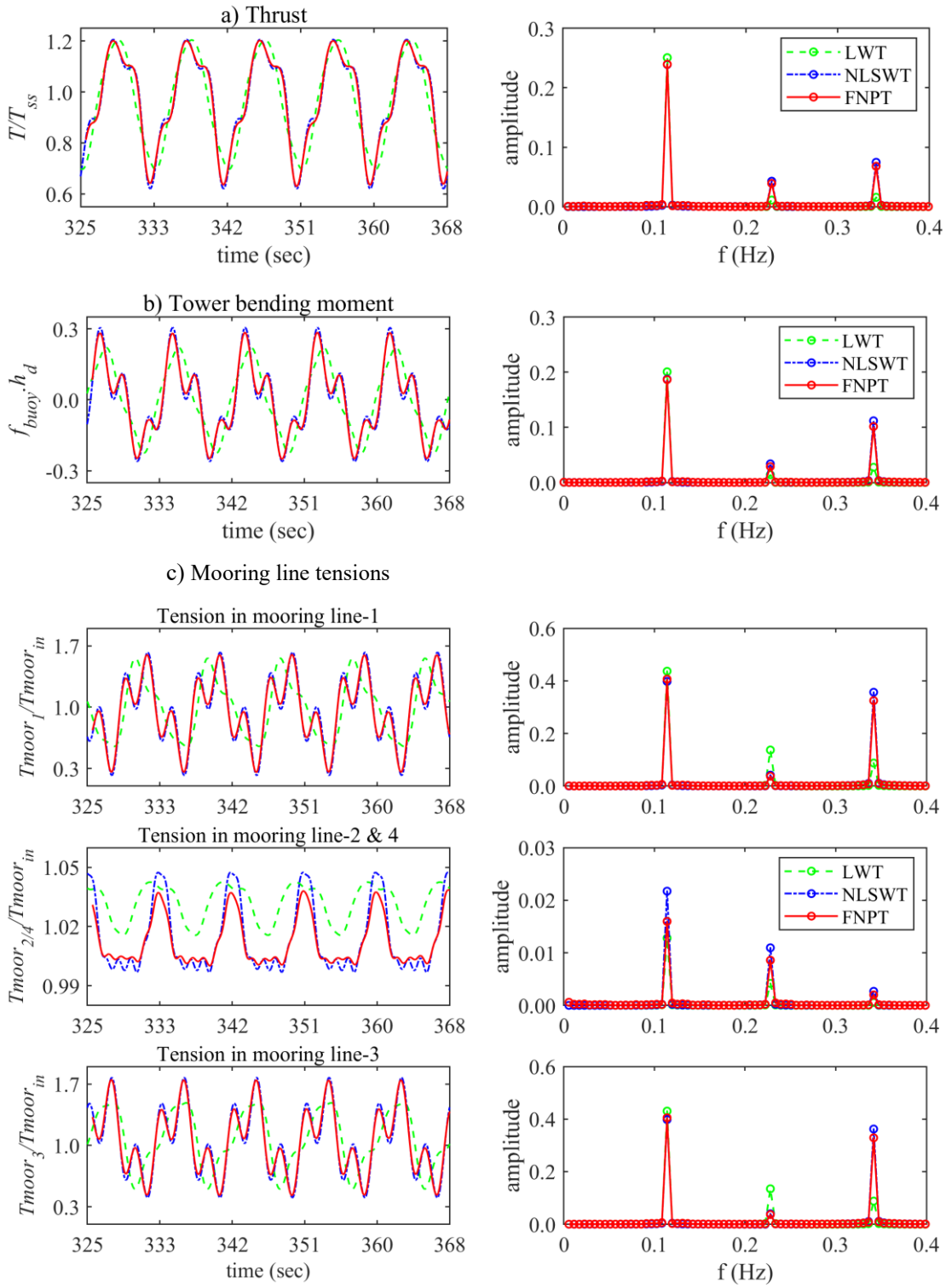

Figure 6.4.1 Time history and amplitude spectra of global response parameters corresponding to resonant pitch motion for LC: WW-O-7

The wind turbine thrust presented in Figure 6.4.1 a) showed no significant difference in its variations predicted by all the wave models considered here. The nonlinear wave models NLSWT and FNPT predicted it 16% higher as compared to LWT wave model.

The tower bending moment presented in Figure 6.4.1 b) showed a considerable difference in its variation predicted by LWT wave model as compared to nonlinear wave models NLSWT and FNPT. The nonlinear wave models NLSWT and FNPT predicted it 27% and 25% higher as compared to LWT wave model respectively.

The tension in each mooring line presented in Figure 6.4.1 c) showed a significant difference in its variation predicted by LWT wave model as compared to nonlinear wave models NLSWT and FNPT. The nonlinear wave models NLSWT and FNPT predicted it higher by 40% and 39% for mooring line-1, 88% and 57% for mooring line-2 and 4, and 40% and 39% for mooring line-3 as compared to LWT wave model respectively. Here, mooring line-3 and 1 is in upwind and downwind direction respectively, whereas mooring line-2 and 4 are in a sway direction. The predominant tension responses for mooring line-1 and 3 appeared at input wave frequency and pitch natural frequency of the structure whereas for mooring line-2 and 4 responses appeared at input wave frequency and second harmonics of it. Tension amplitude of mooring line-1 and 3 at pitch natural frequency are 75% of amplitude at incident wave frequency. These amplitudes are predicted four times higher by both the nonlinear wave models as compared to linear wave model.

To investigate the effect of platform pitch motion on these response parameters in more general cases, the calculations and comparisons are carried out for all these parameters for various wind speeds while the turbine is in operating or in the parked condition. Each parameters range (measured from minimum to maximum) for various wind speeds are presented in Figure 6.4.2.

It can be seen from Figure 6.4.2 that all the response parameters are predicted higher by nonlinear wave models as compared to linear wave model for all the wind speeds while the turbine is in operation or parked condition. However, the differences are seen reducing with an increase in the wind turbine loading due to aerodynamic damping except for tension in mooring line-2 and 4. No significant differences are seen for all the parameters except tension in mooring line-2 and 4 for a wind speed of 21m/s which is rated speed of the turbine and produces maximum thrust on the wind turbine and hence maximum damping. This is observed because tensions in mooring line-2 and 4 are mainly dependent on the surge and heave motion of the platform; therefore, an effect of resonant pitch motion and corresponding aerodynamic damping is not seen. This example demonstrates the importance of nonlinear wave model in predicting the motion responses of a floating wind turbine and associated global response parameters of its components.

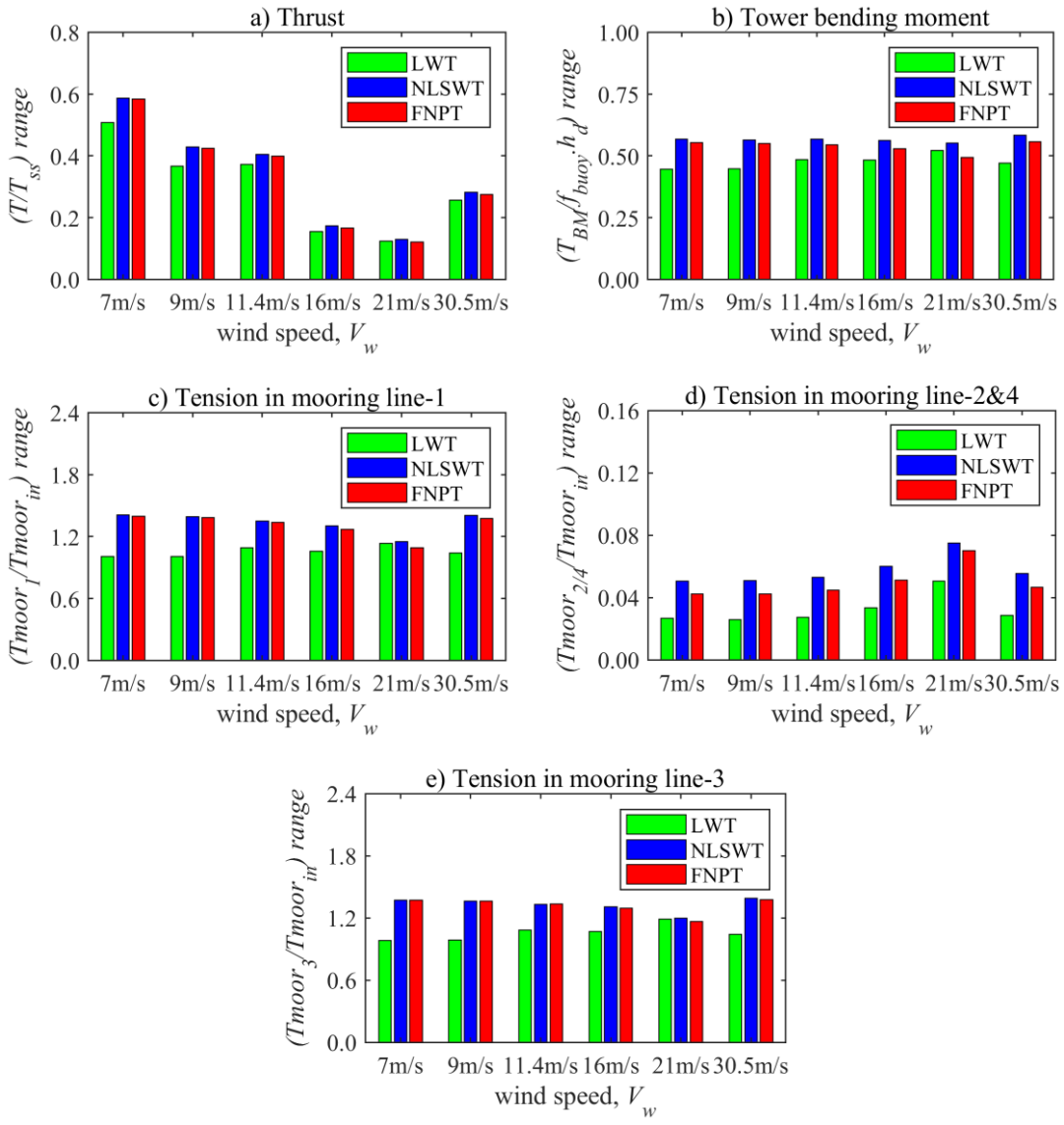

Figure 6.4.2 Range of global response parameters for various wind speeds corresponding to resonant pitch motion

The results presented in this chapter showed a significant difference in the prediction of wave kinematics, associated hydrodynamic forces and motion responses of a chosen floating wind turbine by linear wave model (LWT) as compared to nonlinear wave models (NLSWT and FNPT). Comparing response predictions by both the nonlinear wave models, i.e., NLSWT and FNPT, minimum differences in predictions are seen consistently in all the cases for target wave. For the predicted wave, the significant differences are seen only for deep water waves where Fenton's NLSWT model predicted wave surface profile significantly higher and hence the higher wave kinematics. It is mainly seen due to its assumption of a uniform waveform. Thus, for extreme regular waves with target surface, Fenton's NLSWT model is enough for modelling nonlinear wave.

Although Fenton's NLSWT model is enough for modelling nonlinear wave in moderate water depth, it is only applicable for the regular waves and waves is a stochastic process and the

random sea is unsteady without a permanent profile. It consists of a spectrum of wave components with different frequencies and amplitudes at random phases. The evolution of random sea involves very complicated physics such as dispersions of different wave components and the nonlinear wave-wave interactions which are very important and cannot be modelled by using the Fenton's theory as mentioned in the literature review. Therefore, the global response of concerned floating wind turbine is studied next under regular wave group (bi-chromatic waves) followed by random wave group where FNPT based QALE-FEM and Airy's LWT wave model with wheeler stretching approximation are used for modelling wave.

7 RESPONSE OF TLPWT TO EXTREME REGULAR WAVE GROUP

A regular wave group often called as a bi-chromatic wave is a periodic signal resulting from the linear superposition of two regular waves with frequencies, ω_1 and ω_2 and equal amplitude, $amp_1 = amp_2 = amp$. Hence, the equation for wave surface elevation can be written as,

$$\eta(x,t) = amp_1\, cos(k_1 x - \omega_1 t) + amp_2\, cos(k_2 x - \omega_2 t) \tag{7.1}$$
$$= 2\, amp\, cos\left(\frac{1}{2}(\Delta k\, x - \Delta\omega\, t)\right) \cos\left(\bar{k}x - \bar{\omega}\, t\right)$$

where, $\Delta k = k_1 - k_2$, $\Delta\omega = \omega_1 - \omega_2$, $\bar{k} = (k_1 + k_2)/2$, and $\bar{\omega} = (\omega_1 + \omega_2)/2$. Here, the wave group can be interpreted as a carrier wave $(\bar{k}, \bar{\omega})$, modulated by an envelope wave $(\Delta k, \Delta\omega)$. Although for many practical purposes, linear wave theory produces a satisfactory approximation of the underlying nonlinear process, this is not the case for the propagation of certain class of bi-chromatic waves which was demonstrated by Stansberg (1998a) through an experimental study in a wave tank. The measured wave groups that were generated using only two frequencies showed large deviations from the linear wave theory at some distance from the wave maker. The crest height of an extreme wave identified in a wave group was seen ranging between 1.5-2 times of crest height predicted by linear wave theory. These observations motivated to investigate the effect of linear (LWT) and nonlinear (FNPT) wave model considered in this thesis, in predicting responses of a chosen tension-leg-platform wind turbine (TLPWT) subjected to extreme regular wave group.

The first section of the chapter compares characteristics of an extreme wave, and its occurrences predicted by both the wave models. The subsequent sections of the chapter compare its effect on the motion response and global performance of a chosen tension-leg-platform wind turbine.

7.1 Nonlinear wave surface evolution in a freely propagating regular wave group

7.1.1 Comparison of wave surface using experimental results

To verify the accuracy with which Airy's LWT wave model and FNPT based QALE-FEM can model the extreme wave occurring in a regular (bi-chromatic) wave group, a comparison of its numerical results with the laboratory data are made using measurements of wave surface elevations. The measurements performed at high-speed wave basin in MARIN and reported by Westhuis et al. (2001) are used for the comparison. A schematic sketch showing the test facility is depicted in Figure 7.1.1. Resistance type wave probes were positioned at x = 20, 40, 60, 80, 100, 120, 140, 160 and 180[m] at the centreline of the tank, to measure the spatial evolution of travelling wave group. The steering signals for the stroke of the flap were sent directly to the wave maker and were strictly bi-chromatic; hence no second-order wavemaker theory was used to correct the signal.

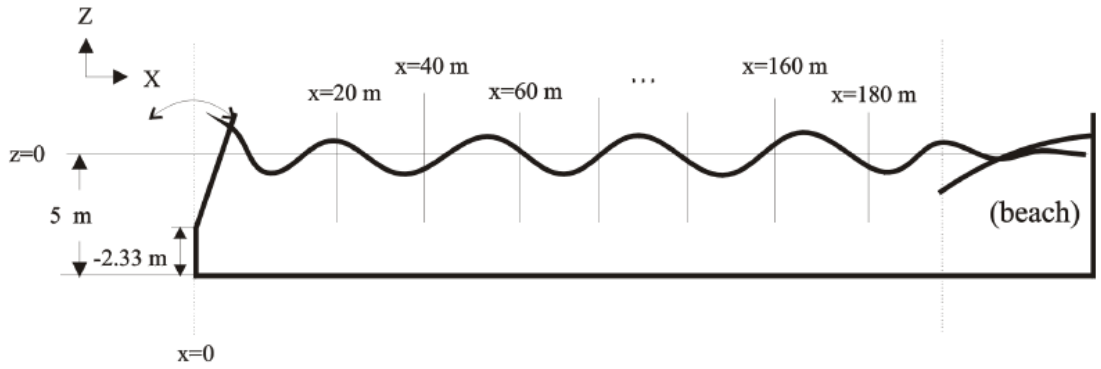

Figure 7.1.1 Experimental set up at MARIN high-speed basin

The experiments were performed around the central wave period of $T_c = 2\ [s]$ with different combinations of wave amplitudes amp_1 and amp_2 and periods T_1 and T_2 obtained by,

$$T_1 = T_c - \frac{1}{2}\Delta T \tag{7.1.1}$$

$$T_2 = T_c + \frac{1}{2}\Delta T \tag{7.1.2}$$

Here, the length of a carrier wave of the wave group satisfies deep water condition (L_c = 6.25m ~ 1.25d). For future reference and to interpret results, ΔT is termed as period bandwidth whereas wave steepness '$\bar{k}amp$' as 'q'.

The comparison of wave surface elevations predicted using numerical models with the measurements from a laboratory generated regular wave group at various positions in the tank are presented in Figure 7.1.2. Here, black dotted line ('…') represents experimental measurements whereas green dash ('- - -') and red solid ('-') line represents numerical results predicted by linear (LWT) and nonlinear (FNPT) wave model respectively.

It can be observed from the Figure 7.1.2 that the asymmetry of wave group and extreme wave associated with it is well predicted by QALE-FEM for x = 40m to 80m. At x = 100m and 120m the QALE-FEM seems to slightly underpredict the peak wave and overpredict the wave behind it, although further downstream the agreement becomes better again. As would be expected from the linear wave theory, in this case, no notable change in envelope was observed at x = 40m, however, the envelope significantly changed with increasing distance with maximum differences noted at x = 100m where surface elevations are underpredicted by linear wave theory by 90% and wave height by 60%. To see the effect of period bandwidth ΔT on the wave surface predictions, further comparisons of wave surface profiles are made for ΔT = 0.1, 0.15, and 0.4 and presented in Figure 7.1.3, Figure 7.1.4, and Figure 7.1.5 respectively.

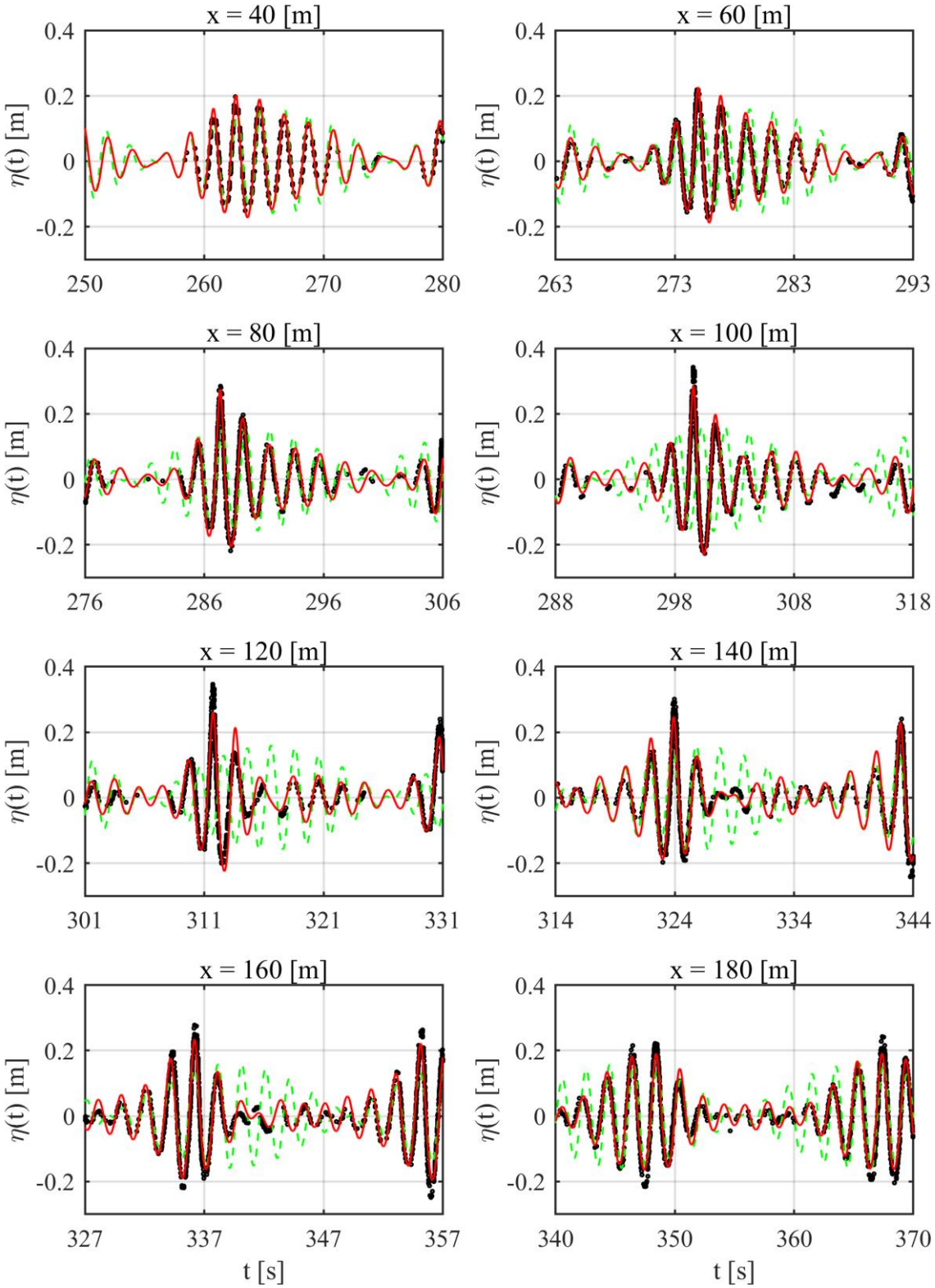

[Legend: (·····) Experimental, (- - - -) LWT, and (–) FNPT)]

Figure 7.1.2 Comparison of wave surface elevations η[m] for bichromatic wave group $\Delta T = 0.2, q = 0.08$ [$T_1 = 1.9sec, T_2 = 2.1sec, amp_1 = amp_2 = 0.08m, d = 5m$]

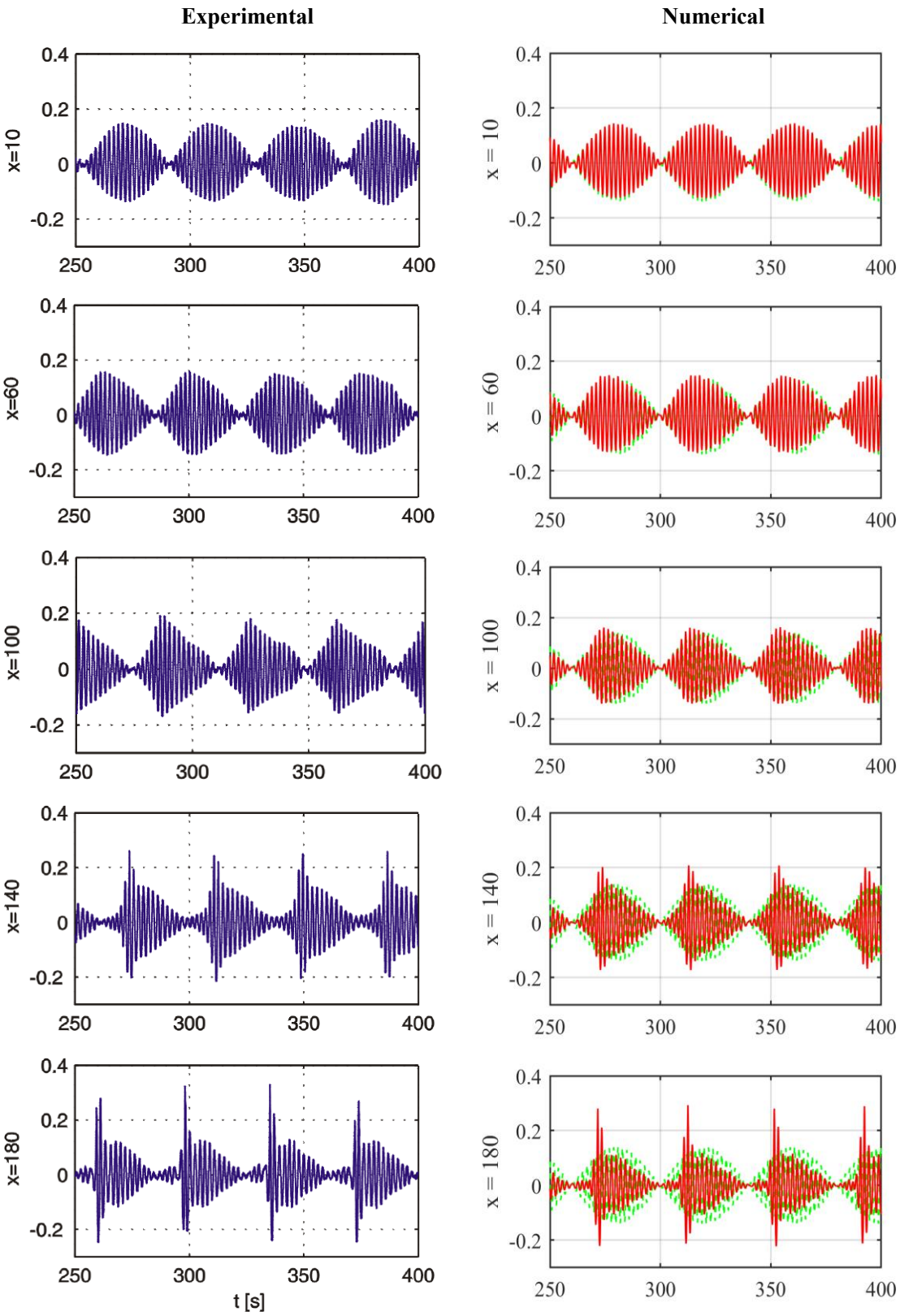

Legend: (- - - -) LWT, and (—) FNPT

Figure 7.1.3 Comparison of wave surface elevations η[m] for bichromatic wave group $\Delta T = 0.1, q = 0.07$ $[T_1 = 1.95sec, T_2 = 2.05sec, amp_1 = amp_2 = 0.07m, d = 5m]$

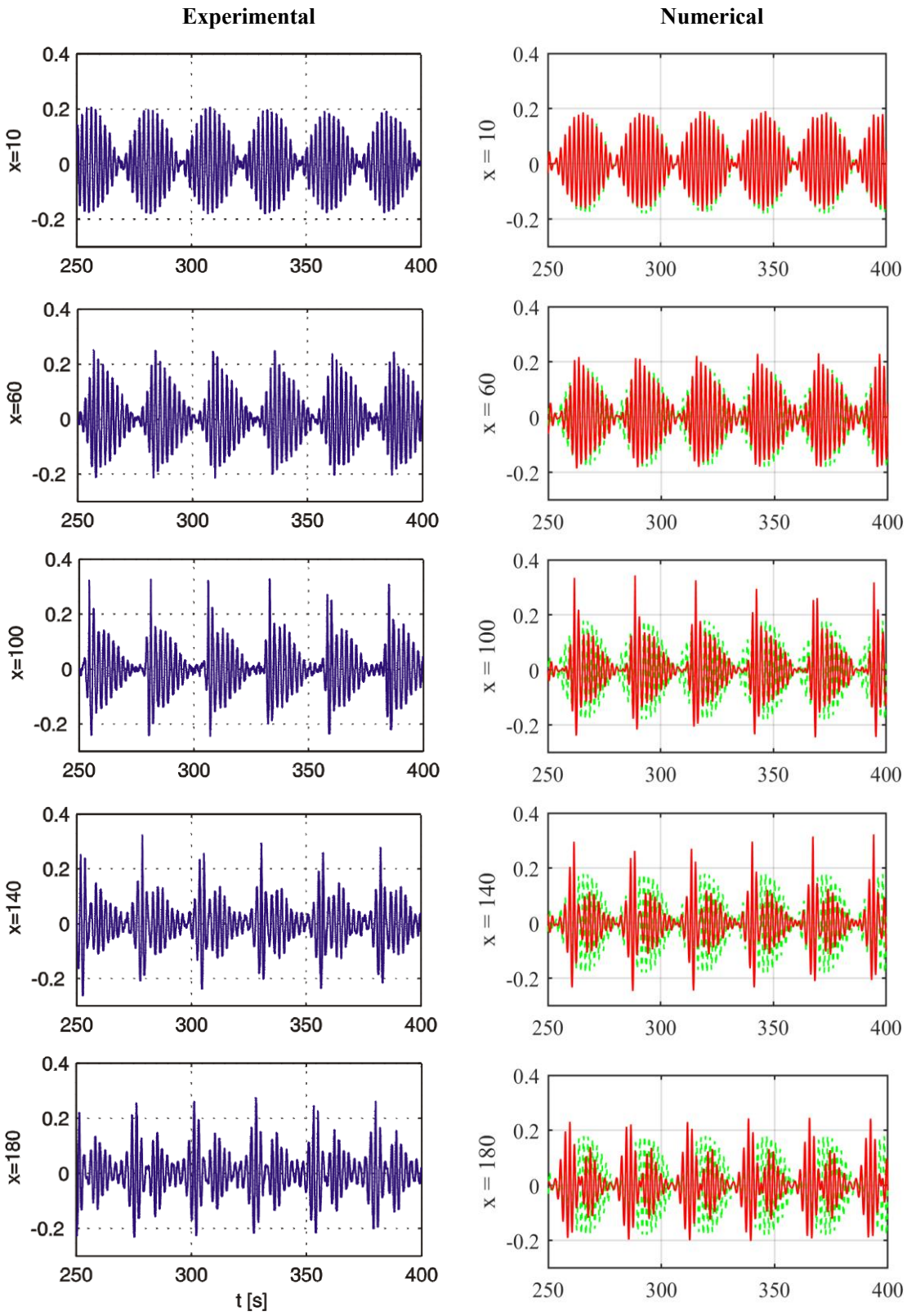

Legend: (- - - -) LWT, and (–) FNPT

Figure 7.1.4 Comparison of wave surface elevations η[m] for bi-chromatic wave group $\Delta T = 0.15, q = 0.09$ $[T_1 = 1.925sec, T_2 = 2.075sec, amp_1 = amp_2 = 0.09m, d = 5m]$

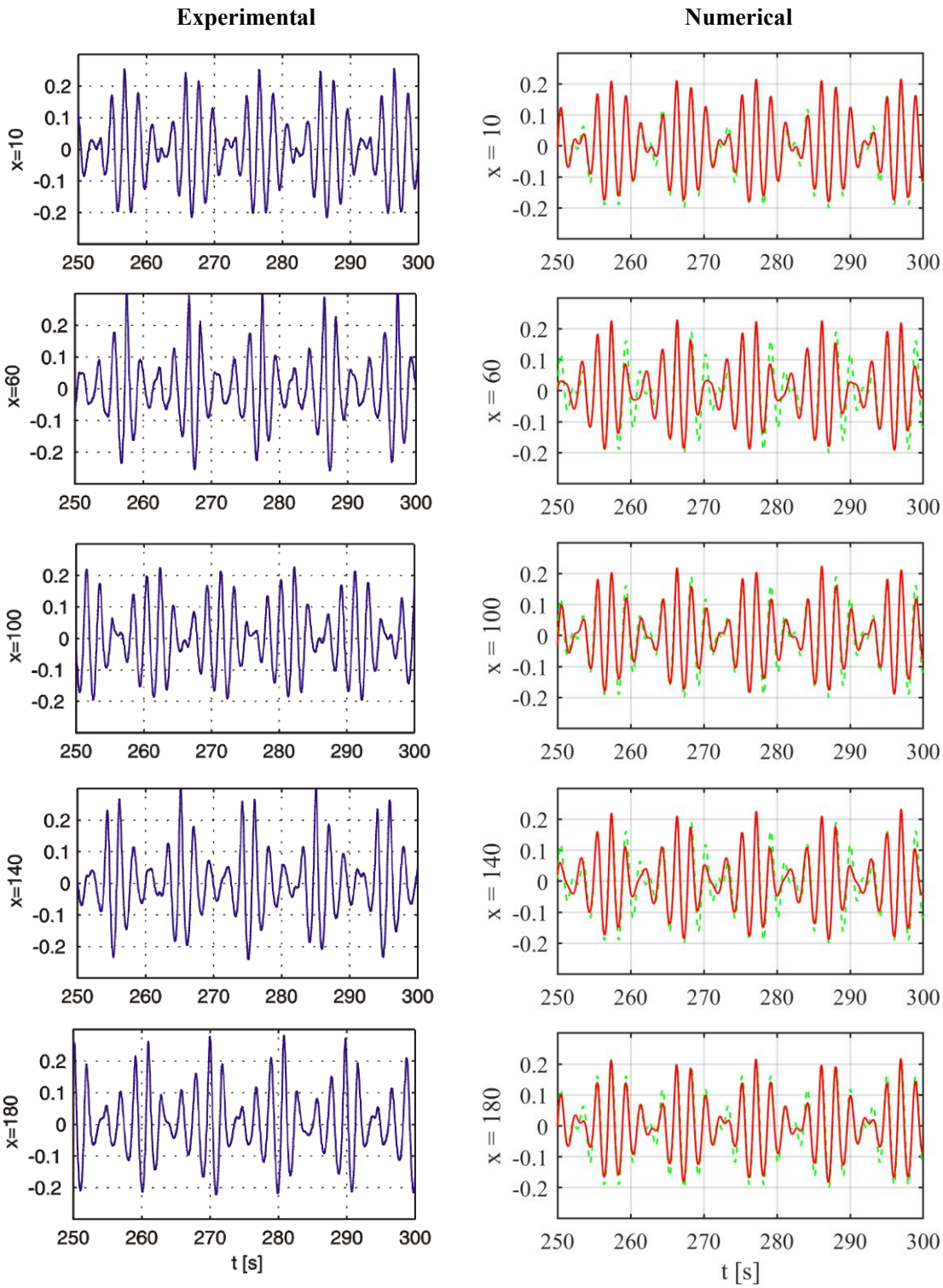

Legend: (- - - -) LWT, and (—) FNPT

Figure 7.1.5 Comparison of wave surface elevations η[m] for bi-chromatic wave group $\Delta T = 0.4, q = 0.1$ $[T_1 = 1.8sec, T_2 = 2.2sec, amp_1 = amp_2 = 0.1m, d = 5m]$

Figure 7.1.3 and Figure 7.1.4 clearly shows the significantly changed wave surface elevation with increasing distance for the lower value of period bandwidth, i.e., ΔT of 0.1 and 0.15, which is well predicted by QALE-FEM. The maximum crest elevations are seen at x = 180m for ΔT = 0.1 and at x = 100m for ΔT = 0.15. The maximum crest elevation is noted as 2.3 times and 1.8 times of crest elevations predicted by linear wave theory for ΔT = 0.1 and 0.15 respectively. However, for ΔT = 0.4, no notable change in wave surface elevations are observed in Figure 7.1.5. The wave surfaces are predicted well by both linear, LWT as well as nonlinear, FNPT wave models. The results presented in Figure 7.1.2 to Figure 7.1.5 confirms the accuracy of FNPT based QALE-FEM numerical scheme, in predicting wave surfaces of the propagating wave group. Based on the linear wave theory, the envelope of the periodic signals should be same at all the measurement locations; however, the comparison plot clearly shows that the linear wave theory is not valid for bichromatic wave groups having high period bandwidth (in this case ΔT > 0.4).

Having established this comparison between reliable FNPT based QALE-FEM wave model with traditional design-oriented analytical LWT wave model, QALE-FEM is further used for comparing wave surfaces of regular wave group in the practical water depths, where tension-leg-platform wind turbines are intended to be built.

7.1.2 Comparison of wave surface using numerical results

The performance of linear and nonlinear wave model in predicting extreme wave and its occurrences are examined in a water depth of 200m for regular (bichromatic) wave groups with various period bandwidths, ΔT and steepness q. The period of a carrier wave T_c is chosen as 12.65sec which is equivalent to the one used for experimental validation in the previous section. The length of the carrier wave satisfies deep water condition (L_c = 250m ~ 1.25d). The numerical simulations are performed around chosen carrier wave period of 12.65sec with different combinations of wave amplitudes, amp_1 and amp_2 and periods T_1 and T_2 obtained using normalised period bandwidth of $\Delta T''$ and steepness q listed in Table 7.1.1. Here normalised period bandwidth $\Delta T'' = \Delta T/2\pi$. This table provides list of limiting steepness of wave group q for each normalised period bandwidth $\Delta T''$ beyond which wave breaking occurs.

Table 7.1.1 Simulation cases for regular (bichromatic) wave group

Wave group steepness, q	**Normalised period bandwidth, $\Delta T''$**				
	0.4	0.3	0.2	0.15	0.1
0.08	NB	NB	NB	NB	NB
0.09	NB	NB	NB	NB	NB
0.10	NB	NB	NB	NB	B
0.11	NB	NB	NB	B	B
0.12	NB	NB	B	B	B
0.13	NB	NB	B	B	B
0.14	NB	B	B	B	B
0.15	NB	B	B	B	B
0.16	B	B	B	B	B

NOTE: 1. NB – Simulation run with non-breaking extreme wave.

2. B – Simulation run with breaking extreme wave.

As reported by Westhuis and Huijsmans (1999), evolution of wave group depends on both period bandwidth $\Delta T''$ and its steepness, q. Therefore, two sets of simulation cases are considered for analysing regular wave group. First set is grouped to see the effect of various period bandwidth $\Delta T''$ where steepness of wave group is maintained equal $q = 0.09$. The second set is grouped to see the effect of various wave group steepness, where period bandwidth of wave group is maintained equal $\Delta T'' = 0.1$. The time history and amplitude spectra of wave surface elevations predicted by Airy's LWT and FNPT based QALE-FEM are presented in Figure 7.1.6 and Figure 7.1.7 for equal q and $\Delta T''$ respectively. The crest and total height of an extreme wave predicted by both the wave models, and their occurrences in terms of carrier wave length L_c and carrier wave period, T_c are presented in Figure 7.1.8 and Figure 7.1.9 respectively. Here, wave surface elevation η is normalised by amplitude of regular (bichromatic) wave group components, i.e. $amp_1 = amp_2 = amp$.

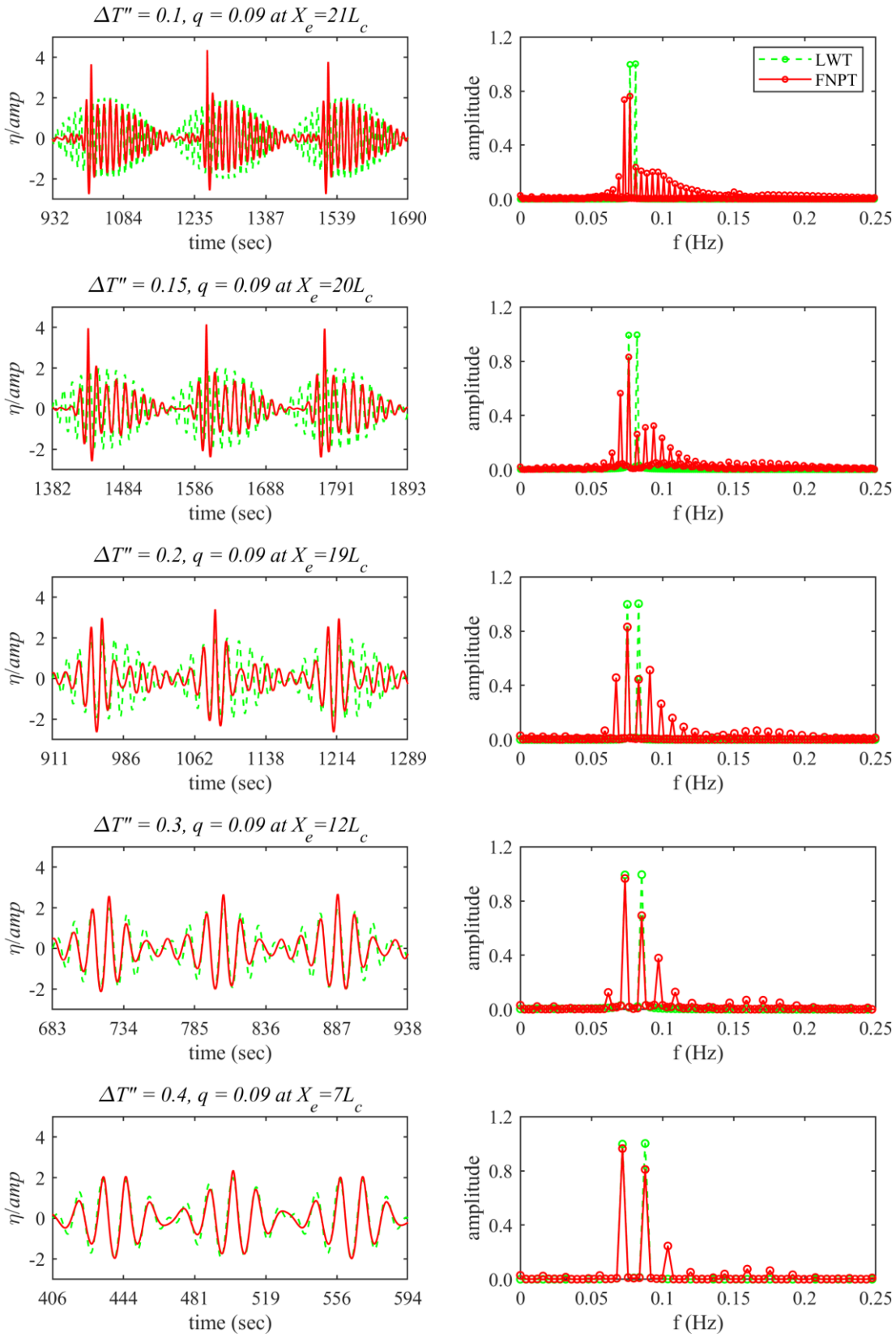

Figure 7.1.6 Time history and amplitude spectra of wave surface elevations for bichromatic wave group with various normalised period bandwidth $\Delta T''$ having equal steepness, $q = 0.09$

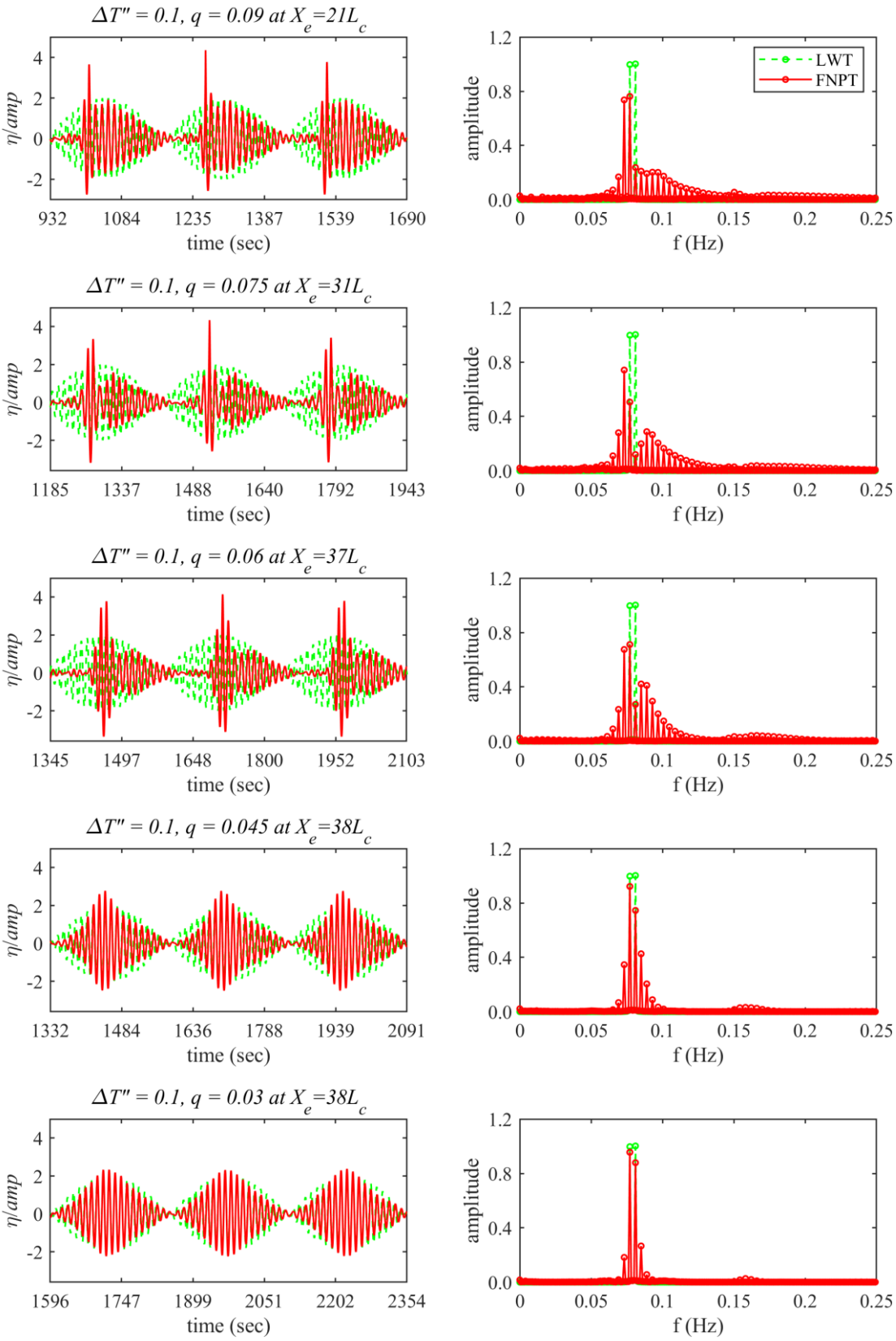

Figure 7.1.7 Time history and amplitude spectra of wave surface elevations for bichromatic wave group with various steepness, q having equal normalised period bandwidth $\Delta T'' = 0.1$

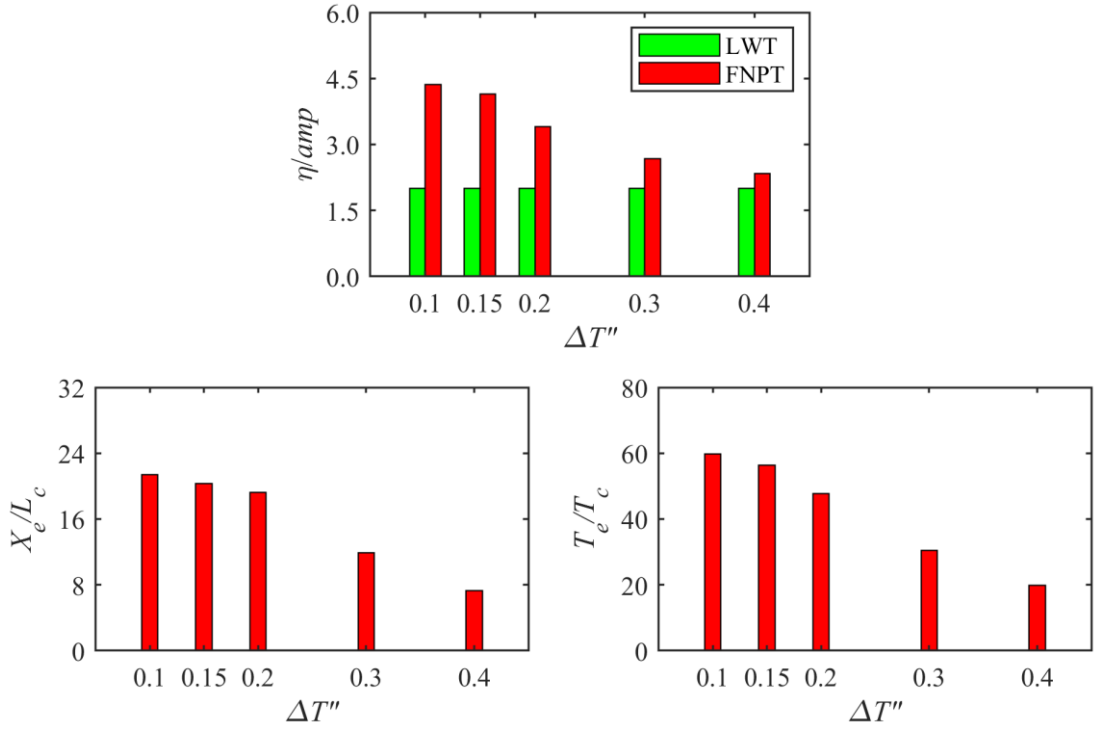

Figure 7.1.8 Extreme wave and its occurrence in bichromatic wave group with various normalised period bandwidth $\Delta T''$ and equal steepness $q = 0.09$

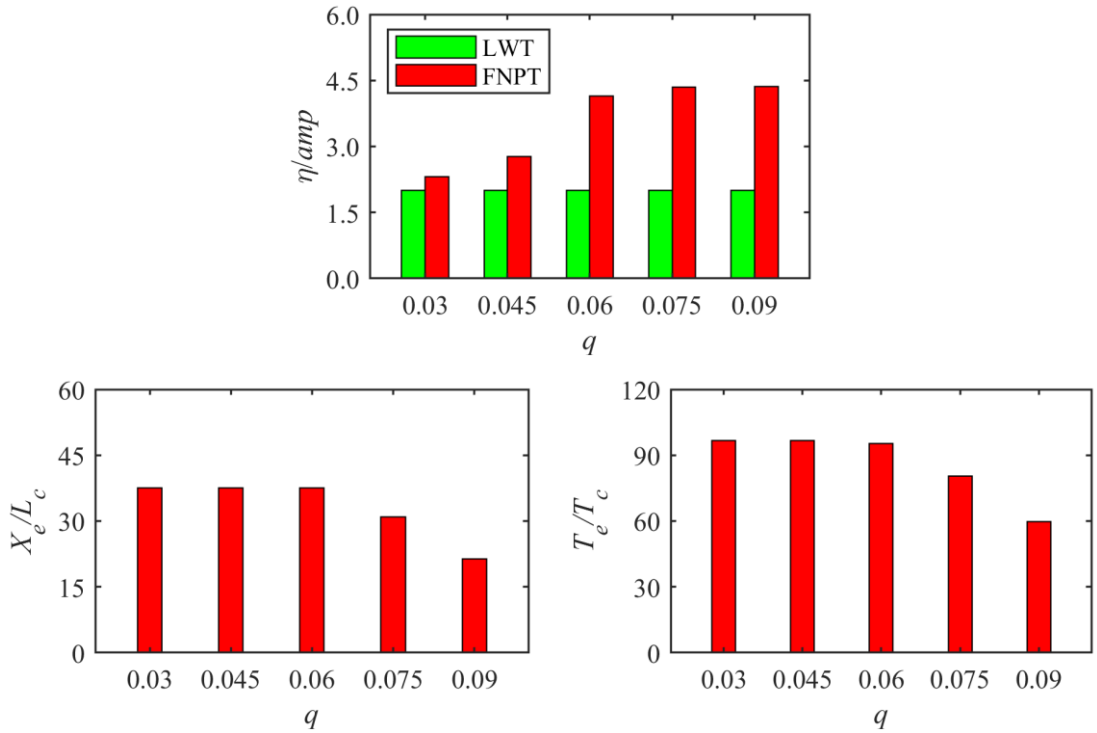

Figure 7.1.9 Extreme wave and its occurrence in bichromatic wave group with various steepness, q and equal normalised period bandwidth $\Delta T'' = 0.1$

Figure 7.1.6 shows the effect of period bandwidth $\Delta T''$ on the evolution of regular wave group where maximum difference in wave surface elevations predicted by both the wave models occurs for a low value of period bandwidth $\Delta T''$ of 0.1. The crest and height of an identified extreme wave predicted by nonlinear wave model are 2.3 and 1.8 times of the crest and height of an extreme wave predicted by the linear wave model respectively. The wave group evolution is predicted at 21 times of carrier wave length, L_c at a duration of 60 times of carrier wave period, T_c. With an increase in normalised period bandwidth $\Delta T''$, the effect of wave group evolution on the wave surface elevation and its occurrences as depicted in Figure 7.1.8 reduces, with minimum differences in wave surface elevations predicted by both the wave models are noted for $\Delta T''$ of 0.4. At period bandwidth $\Delta T''$ of 0.4, the differences in wave surface elevations predicted by both linear and nonlinear wave model are 15%. The occurrence of wave group evolution, i.e. distance, X_e and time, T_e also reduces with increase in period bandwidth $\Delta T''$. Amplitude spectra show a significant transfer of energy to the sidebands of both the input wave amplitudes for $\Delta T''$of 0.1. A significant increase in amplitude is seen at sideband frequency, $f_1 - df$ whereas a decrease in amplitude is seen at input amplitude frequency, f_2. With the increase in period bandwidth of $\Delta T''$, this effect reduces showing no significant transfer of energy for a high value of $\Delta T''$ of 0.4. The evolution of regular wave group at and beyond period bandwidth of 0.4 is seen almost linear.

A similar trend is observed for the effect of steepness q on the evolution of regular wave group and their occurrences presented in Figure 7.1.7 and Figure 7.1.9 respectively. For steepness, q of 0.09, 0.075 and 0.06, a significant difference in prediction of wave surface elevation by LWT and FNPT wave models are seen due to wave group evolution. Maximum crest and corresponding wave height are seen due to a non-uniform transfer of energy to sidebands. For steepness, q of 0.045 and below, no significant difference in prediction of wave surface elevation by LWT and FNPT model are seen due to less energy transfer to sidebands. For lower values of q, wave group evolution is seen almost linear. The occurrence of wave group evolution, i.e. distance, X_e and time, T_e also reduces with the increase in wave group steepness q. It demonstrates that the wave group evolution depends not only on the period bandwidth but also on its steepness. The results presented in this section showed how the evolution of regular wave group affects the prediction of wave surface elevation. The performance of both Airy's LWT and FNPT based QALE-FEM in predicting wave surface elevations are assessed by varying period bandwidth and steepness of wave group. The comparison showed a significant difference in prediction of wave surface elevations for limiting value of period bandwidth < 0.4 and steepness > 0.03. The effect of this difference in the prediction of extreme wave surface elevation on the response of a chosen floating wind turbine is studied next.

7.2 Effect of nonlinear wave surface evolution on motion response of TLPWT

Global motion analysis of a parameterized TLPWT is performed to study its motion responses under various environmental conditions comprising extreme regular (bi-chromatic) wave group. The analysis cases presented here uses an incident bi-chromatic waves with periods, T_1 and T_2 and amplitudes amp_1 and amp_2 obtained from the simulation cases presented in Table 7.1.1. The current speed is kept as zero and hydrodynamic coefficients in the wave force calculations are set as $C_a = 1.0$ and $C_d = 1.0$ based on Reynolds and Keulegan-Carpenter number (Chakrabarti, 2005). The wind and wave headings are considered as collinear and fixed at zero degrees with respect to the x-axis. With this assumption, the structure moves only in the x-z plane, hence the motions are surge, heave and pitch. At the beginning of the simulation, a cosine taper function is imposed on the forces and moments to reduce the transient effects produced by the impulsive loading. The motions resulting from the analysis are studied using their time history, amplitude spectra, range (minimum to maximum) and statistical parameters such as maximum and skewness. Three different load cases as detailed in Table 7.2.1 below, are chosen to investigate the impact of different wave models in predicting motion responses.

Table 7.2.1 Loading condition

Loading condition (LC)	Description
WO	TLPWT subjected to wave only
WW-O-V_w	TLPWT subjected to combined wave and wind (turbine in operating condition at wind speed V_w)
WW-P-V_w	TLPWT subjected to combine wave and wind (turbine in parked condition exposed to extreme wind speed V_w)

The motion responses of TLPWT are further compared using both linear and nonlinear wave models by varying normalised period bandwidth $\Delta T''$, and steepness q of the wave group to see range of applicability of linear wave model.

7.2.1 Motion response under wave excitation

Global motion analysis of a TLPWT under wave only (WO) loading condition is performed to see the clear difference in its motion predictions using different wave models from the state where the structure is at rest or in static equilibrium. The first case presented here uses an incident bichromatic wave with periods T_1 = 12.33sec and T_2 = 12.97sec and amplitudes $amp_1 = amp_2$ = 3.6m in a water depth of 200m. The normalised period bandwidth $\Delta T''$ and steepness q for this bichromatic wave group is 0.1 and 0.09 respectively. These wave parameters yield maximum difference in wave surface elevations predicted by linear and nonlinear wave models among all the cases listed in Table 7.1.1 as detailed in section 7.1.2. In the nonlinear wave model (FNPT based QALE-FEM), the structure is located at $X_e = 21L_c$ from the wave maker where extreme wave evolution occurs.

Time history and amplitude spectra of the motion response of concerned TLPWT are presented in Figure 7.2.1. Here, the translational motions such as surge and heave are normalised by amplitude of wave group components, i.e. $amp_1 = amp_2 = amp$, whereas pitch motion is normalised by its steepness q which is $\bar{k}.amp$.

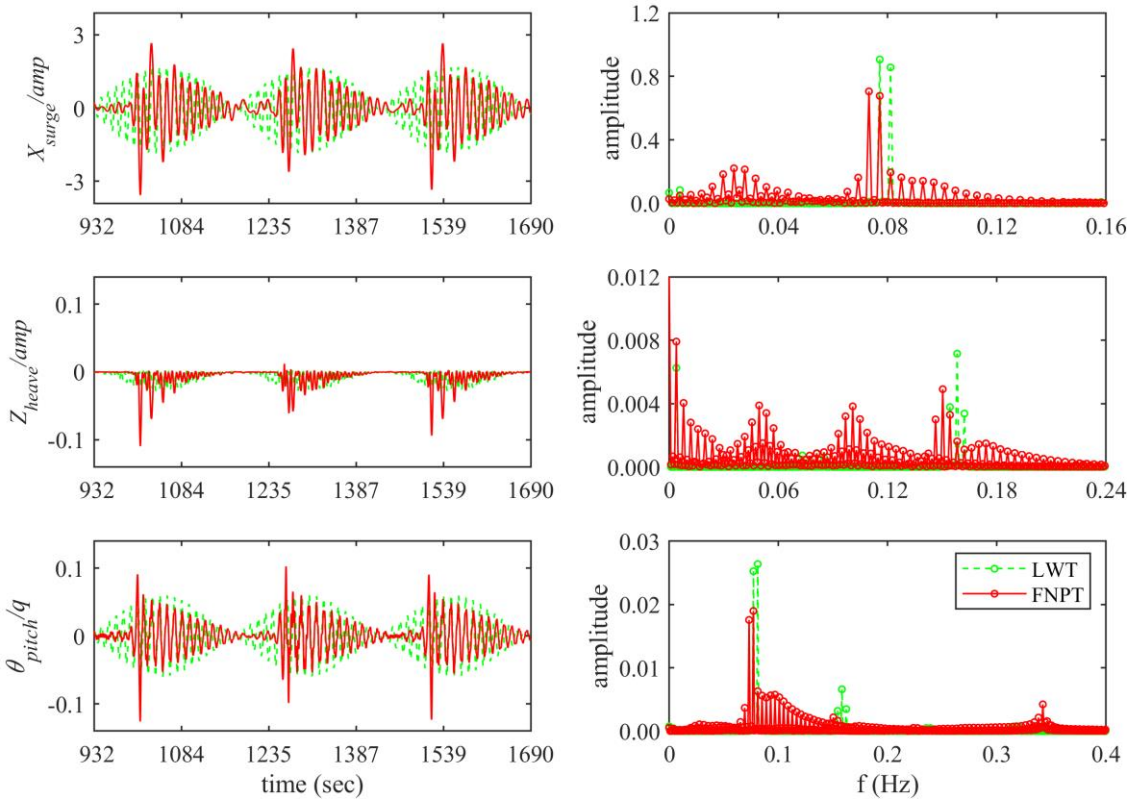

Figure 7.2.1 Time history and amplitude spectra of TLPWT motions for LC: WO

$\Delta T'' = 0.1, q = 0.09\ [T_1 = 12.33sec, T_2 = 12.97sec, amp_1 = amp_2 = 3.6m, d = 200m]$

The time history plots of TLPWT motions predicted by linear and nonlinear wave model presented for a wave only condition in Figure 7.2.1 showed positive mean for surge and pitch motion whereas negative mean for heave motion. This negative mean for heave motion is not only the result of wave loading but also due to the set-down effect resulting from positive surge and pitch motion of the platform. This difference in prediction of the mean value of TLPWT motions in each mode is a result of nonlinearity included in the numerical model. The numerical model with linear wave theory primarily constitutes nonlinearity in wave forces and the equations of motions whereas the numerical model with FNPT wave model constitutes an additional nonlinear effect of wave-wave interaction which severely affects the prediction of wave surface elevation.

The predominant peak responses predicted by FNPT wave model appeared at input wave frequency (fw_1), and its sideband frequency ($fw_1 - dfw$) for surge and pitch motions. The responses are also observed at surge and pitch natural frequency where magnitude of motion amplitudes is 40% and 20% of motion amplitudes at input wave frequencies respectively. For

heave motion, the peak responses appeared at input wave frequency and sum and difference of its several sideband frequencies. Contrary to this, peak responses predicted by LWT wave model appeared at input wave frequencies and difference of it for both surge and pitch motion whereas, for heave motion, responses appeared at input wave frequencies and its second harmonic frequencies. Although LWT wave model predicted motion responses higher at input wave frequencies in all the modes of motion, it failed to predict the motion responses at sideband frequencies and natural frequencies of the structure. The overall platform motions in each mode are predicted higher by nonlinear wave model as compared to predictions by linear wave model. The range of motions (measured from minimum to maximum) in the surge, heave and pitch mode predicted by FNPT wave model are 1.8, 4 and 1.9 times higher than the motions predicted by LWT wave model respectively.

This comparison shows that the TLPWT motions are predicted significantly higher by nonlinear wave model as compare to linear wave model which is mainly seen due to the difference in prediction of wave surface elevations as depicted in Figure 7.1.6. This difference in wave surface elevation is due to ability of the FNPT wave model in predicting extreme wave surfaces generated through nonlinear evolution of wave group. However, here differences in TLPWT motions are seen for a wave only loading condition where the structure is at rest in a static equilibrium condition. However, in practice floating wind turbines will always have an offset and heel angle due to wind loads acting on the turbine and its supporting tower; therefore, motion responses are studied next under combined wind and wave loading condition while the turbine is operating and in the parked condition.

7.2.2 Motion response under combined wind and wave excitation

Global motion analysis of a TLPWT under combined wind and wave loading condition is performed to see the difference in its motion predictions using linear and nonlinear wave models when the structure has a maximum offset and heel angle due to wind loads acting on the turbine and its supporting tower. As explained in section 6.3.1.2 of the previous chapter, maximum offset and heel angle for platform occurs when the wind turbine is operating at its rated wind speed or subjected to extreme wind speed when it is parked. Therefore, wind loads are considered while the turbine is operating at its rated wind speed of 21m/s and in a parked condition, an extreme wind speed of 30.5m/s is considered. The case presented here uses an incident bi-chromatic wave the same as used for wave only loading condition. Time history and amplitude spectra of motion response of TLPWT for turbine under operating (WW-O-21.8) and parked (WW-P-30.5) condition predicted by both linear LWT and nonlinear FNPT wave model are presented in Figure 7.2.2 and Figure 7.2.3 respectively.

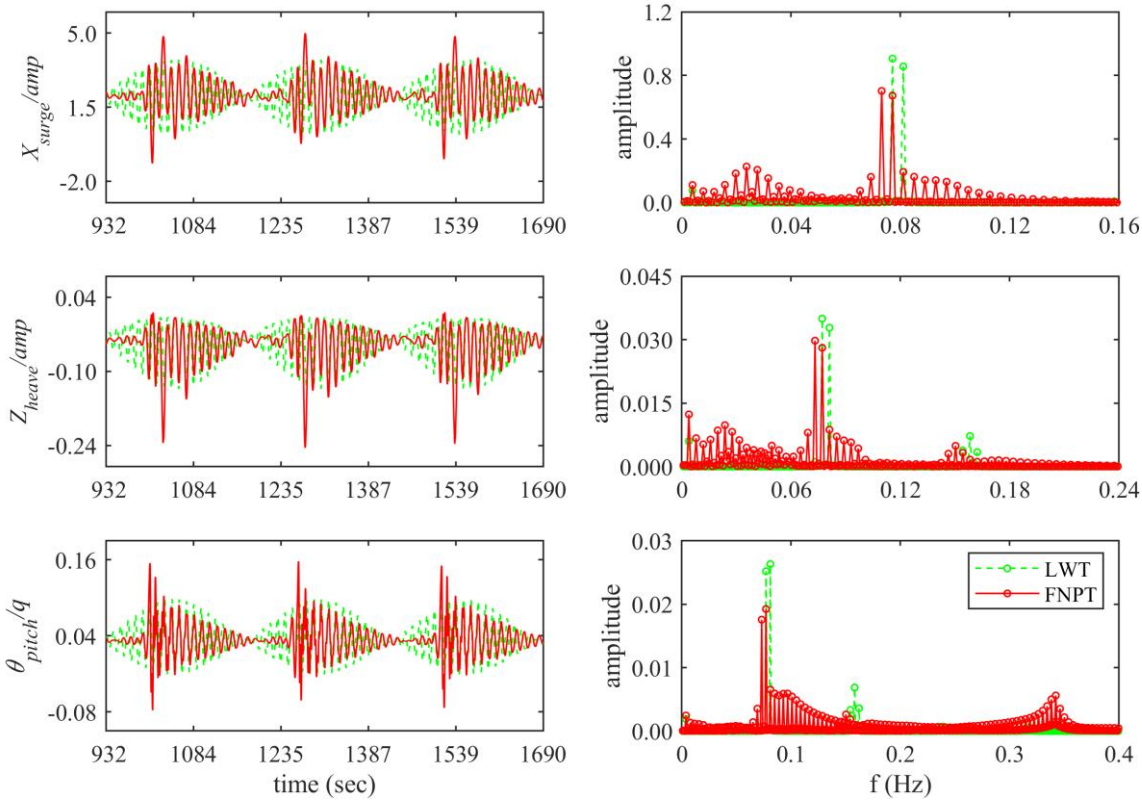

Figure 7.2.2 Time history and amplitude spectra of TLPWT motions for LC: WW-O-21

$\Delta T'' = 0.1, q = 0.09$ $[T_1 = 12.33sec, T_2 = 12.97sec, amp_1 = amp_2 = 3.6m, d = 200m]$

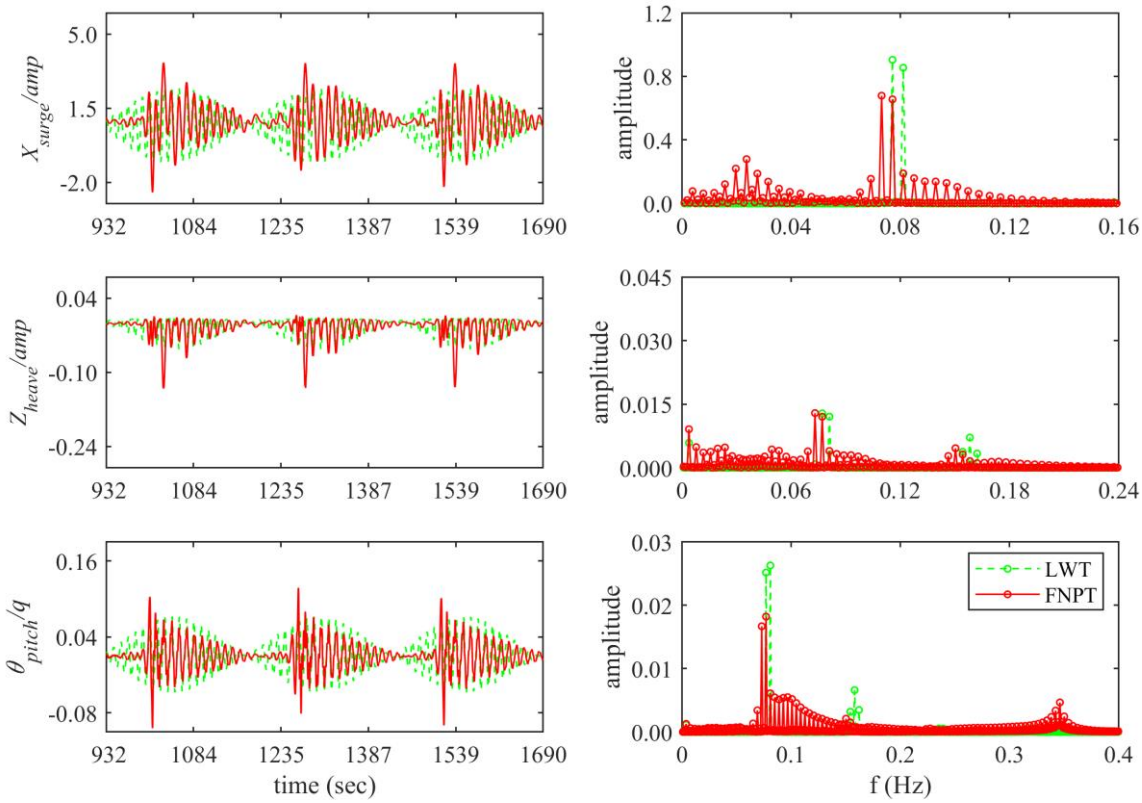

Figure 7.2.3 Time history and amplitude spectra of TLPWT motions for LC: WW-P-30.5

$\Delta T'' = 0.1, q = 0.09$ $[T_1 = 12.33sec, T_2 = 12.97sec, amp_1 = amp_2 = 3.6m, d = 200m]$

The time history plots of motions presented for co-existing wind and wave condition in Figure 7.2.2 and Figure 7.2.3 showed an increase in positive mean for surge and pitch motion of the platform as compared to wave only condition. This is expected due to the presence of wind turbine thrust and its large moment resulting due to its higher elevation from the centre of gravity of the structure. The heave time series also showed further increased in negative mean due to an additional set-down effect resulting from the increase in positive surge and pitch motion of the platform.

The predominant peak responses predicted by FNPT wave model appeared at input wave frequency (fw_1), and its sideband frequency ($fw_1 - dfw$) for surge and pitch motions. The responses are also observed at surge and pitch natural frequency. The magnitude of motion amplitude at surge natural frequency is 30% and 38% of motion amplitude at input wave frequency for loading condition WW-O-21 and WW-P-30.5 respectively, whereas the magnitude of motion amplitude at pitch natural frequency is 28% and 25% of motion amplitude at input wave frequency for loading condition WW-O-21 and WW-P-30.5 respectively. This reduction in motion amplitude at surge natural frequency as compared to wave only loading condition, is seen due to aerodynamic damping whereas increase in motion amplitude at pitch natural frequency is seen due to ringing and springing response resulting from the impact load by wind turbine thrust. The predominant peak response predicted by LWT wave model appeared at input wave frequencies and difference of it for all the modes of motion. Although LWT wave model predicted motion responses higher at input wave frequencies in all the modes of motion, it failed to predict the motion responses at sideband frequencies and natural frequencies of the structure and importantly ringing and spring response. The ringing and springing response predicted by FNPT wave model is mainly seen due to its ability to predict steep wave surface resulting from the evolution of regular wave group which LWT wave model failed to predict. These various motion responses predicted by FNPT wave model raises overall motion predictions as compared to predictions by LWT wave model. The range of motions (measured from minimum to maximum) in the surge, heave and pitch mode predicted by FNPT wave model are 1.7, 1.9 and 2.1 times higher than the motions predicted by LWT wave model for loading condition WW-O-21 respectively. For loading condition WW-P-30.5, FNPT wave model predicted motions in the surge, heave and pitch mode by 1.7, 2.4 and 1.9 times higher than the motions predicted by LWT wave model respectively.

We can further study the effect of nonlinear wave model on TLPWT motion response by studying its statistical parameters such as maximum (peak value) and skewness. The statistical parameters such as maximum and skewness of the platform motions considered in Figure 7.2.2 and Figure 7.2.3 are presented in Table 7.2.2.

Table 7.2.2 Normalised motion statistics for combined wind and wave loading condition

Loading condition	Motions	Maximum (peak)		Skewness	
		LWT	FNPT	LWT	FNPT
Wave only	Surge	1.679	2.659	-0.082	-0.298
	Heave	0.002	0.012	-1.093	-3.660
	Pitch	0.060	0.107	-0.014	-0.225
Wave + Wind (turbine operating)	Surge	3.740	4.995	-0.039	0.155
	Heave	0.133	0.245	-0.676	-1.950
	Pitch	0.098	0.172	0.212	0.640
Wave + Wind (turbine parked)	Surge	2.442	3.650	-0.052	-0.015
	Heave	0.056	0.130	-1.391	-2.939
	Pitch	0.072	0.129	0.091	0.186

The trend shown in Table 7.2.2 is consistent with that observed in Figure 7.2.1, Figure 7.2.2 and Figure 7.2.3. The maximum platform motions and its skewness (which is indicator of nonlinearity) in each mode are predicted significantly higher by nonlinear FNPT wave model as compared to linear LWT wave model for co-existing wind wave condition while the turbine is operating and in the parked condition.

This comparison shows that the platform motions under both the analysed co-existing wind, and wave loading conditions (WW-O-21 and WW-P-30.5) are predicted higher by nonlinear wave model (FNPT) as compared to predictions by linear wave model (LWT). This is mainly seen due to the ability of FNPT based QALE-FEM in predicting the evolution of wave group and corresponding steep wave surface elevation. However as seen in section 7.1, the evolution of wave group mainly depends upon period bandwidth, $\Delta T''$ and its steepness, q. Therefore, the effect of these parameters in predicting extreme wave surface and consequently motion responses are studied next.

7.2.3 Effect of period bandwidth, $\Delta T''$ on motion response

To study the influence of period bandwidth on motion response of concerned floating wind turbine, a set of bichromatic wave groups having normalised period band width $\Delta T''$ of 0.1,0.15,0.2,0.3, and 0.4 are generated. Loading condition of co-existing wave and wind with turbine in operating condition, (WW-O-21) is considered. The carrier wave period and water depth are used the same as used in the previous sub section 7.2.2 whereas steepness q of 0.09 is maintained equal for all the bi-chromatic wave groups. A range of steady state normalised motions in surge, heave and pitch modes are presented in Figure 7.2.4 through Figure 7.2.6 respectively. Here surge and heave motions are normalised by input wave amplitude amp and pitch motions are normalised by input wave steepness q which is $\bar{k}.amp$.

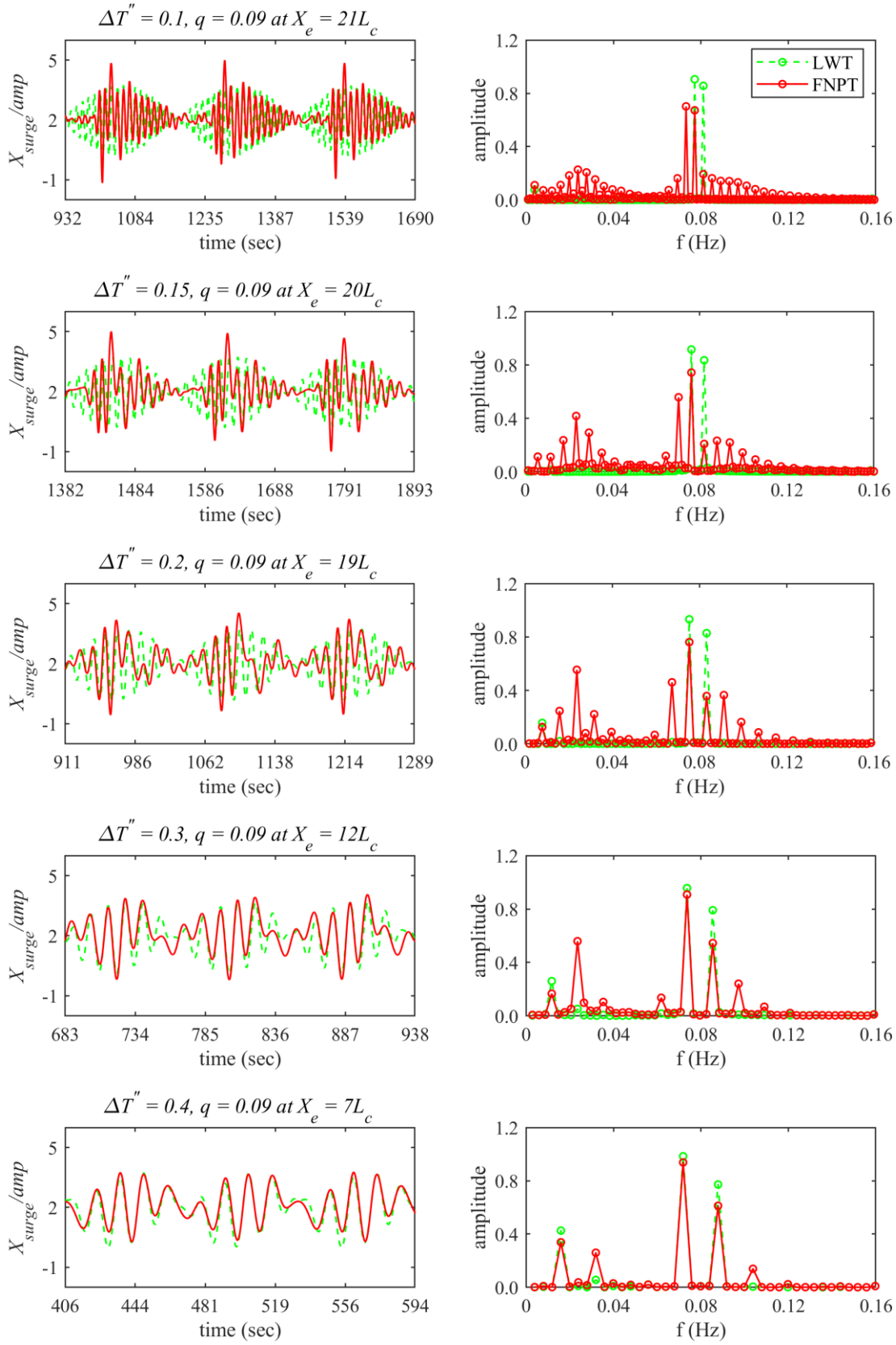

Figure 7.2.4 Time history and amplitude spectra of TLPWT surge motion for bichromatic wave group with various normalised period bandwidth $\Delta T''$ and equal steepness $q = 0.09$

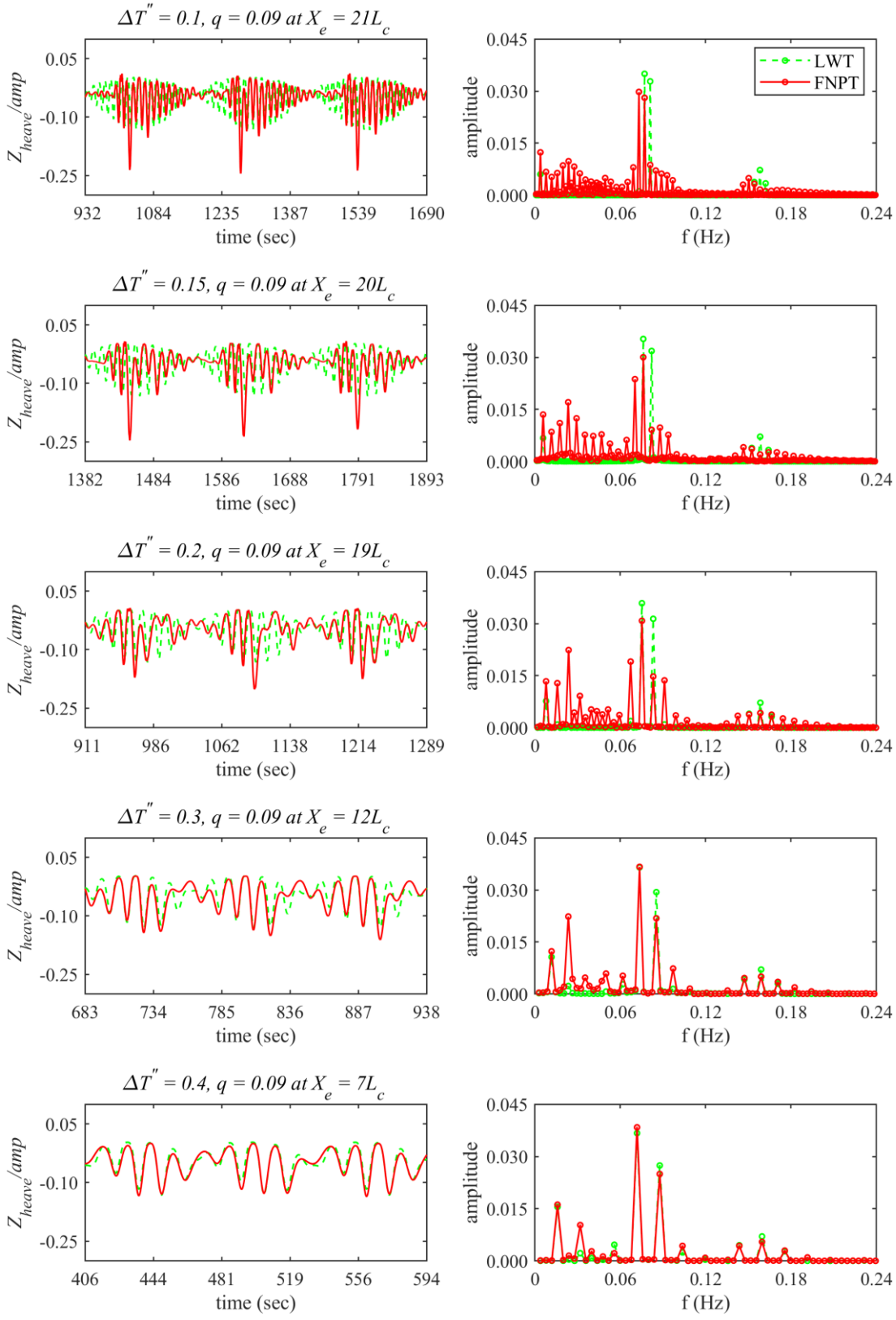

Figure 7.2.5 Time history and amplitude spectra of TLPWT heave motion for bichromatic wave group with various normalised period bandwidth $\Delta T''$ and equal steepness, $q = 0.09$

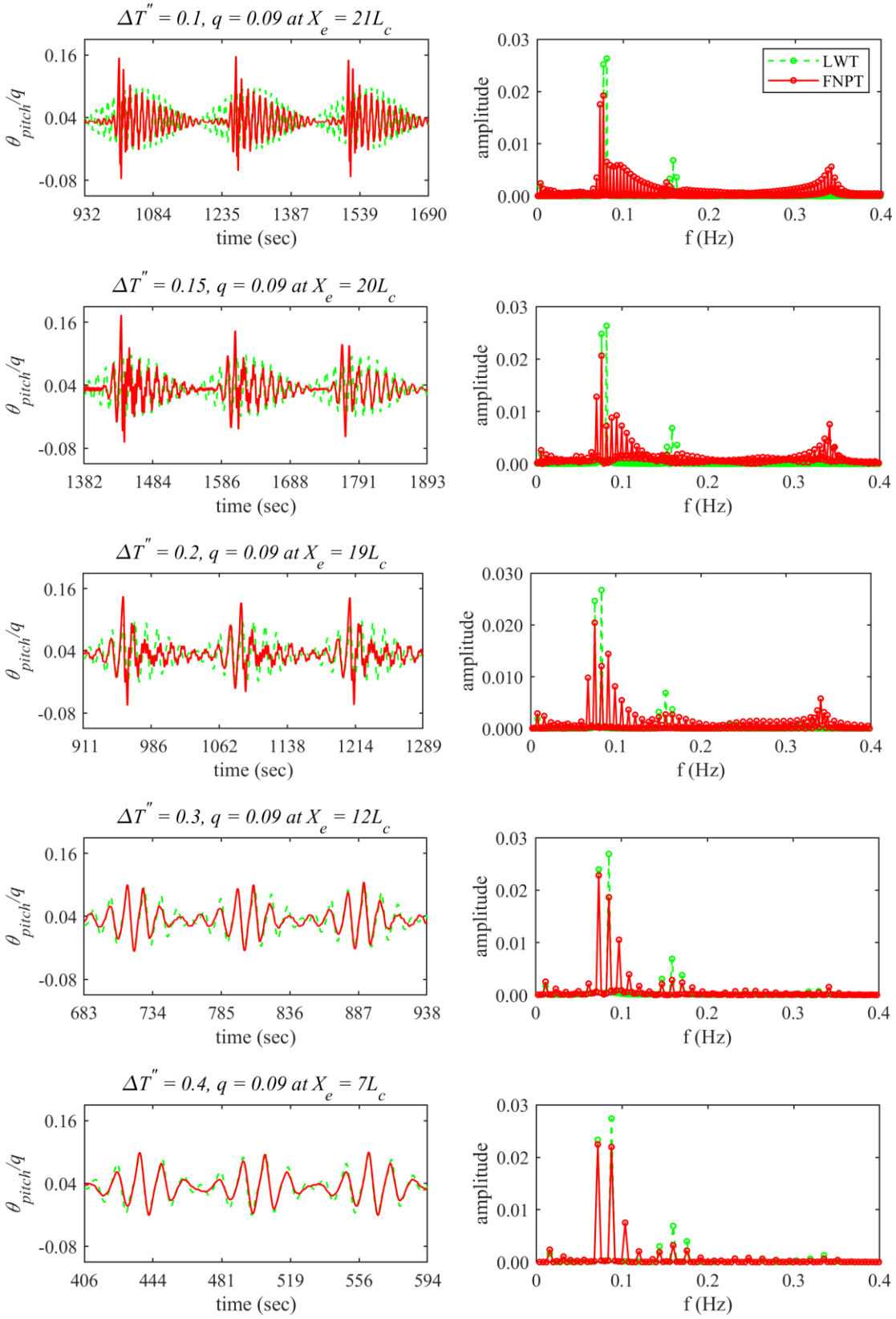

Figure 7.2.6 Time history and amplitude spectra of TLPWT pitch motion for bichromatic wave group with various normalised period bandwidth $\Delta T''$ and equal steepness, $q = 0.09$

The time history plots of surge motion predicted by linear (LWT) and nonlinear (FNPT) wave model presented in Figure 7.2.4 shows the effect of period bandwidth on surge motion of platform reflecting behaviour of extreme wave generated through evolution of regular wave group, as depicted in Figure 7.1.6. As difference in wave surface elevation predicted by both the wave model reduces with the increase in period bandwidth, consequently the differences in surge motion also seen reducing.

As seen in the previous section, for $\Delta T'' = 0.1$, predominant peak responses predicted by FNPT wave model appeared at input wave frequency (fw_1), its sideband frequency ($fw_1 - dfw$) and at surge natural frequency (fn_{surge}). The motion amplitude at sideband frequency ($fw_1 - dfw$) which were found significant seen reducing with an increase in period bandwidth whereas motion amplitudes which were found low at input wave frequency (fw_2) seen increasing with the increase in period bandwidth. At surge natural frequency (fn_{surge}), motion amplitudes are seen increasing with increase in $\Delta T''$ up to 0.2, and thereon it reduces with increase in $\Delta T''$. This motion amplitude at surge natural frequency is observed due to excitation of surge motion by difference in sideband frequencies generated through evolution of bichromatic wave group. For $\Delta T'' = 0.2$, difference in sideband frequency, ($fw_1 - dfw$) and ($fw_2 + dfw$) is seen 0.024Hz which is close to surge natural frequency of the structure, i.e. 0.026Hz. Linear wave model failed to predict this low-frequency surge motion due to its inability to predict wave group evolution. For $\Delta T'' = 0.4$, no significant transfer of energy to sideband is seen, hence the evolution of this bi-chromatic wave group is seen almost linear consequently showing no significant difference in prediction of surge motion by both the wave models. The time history plots of heave motion predicted by linear (LWT) and nonlinear (FNPT) wave model presented in Figure 7.2.5 showed a similar trend as seen for surge motion. The time history plots of pitch motion predicted by linear (LWT) and nonlinear (FNPT) wave model presented in Figure 7.2.6 shows a similar trend as seen for surge and heave motion. The motion amplitude at sideband frequency ($fw_1 - dfw$) which were found significant seen reducing with an increase in period bandwidth whereas motions amplitudes which were found low at input wave frequency (fw_2) seen increasing with increase in period bandwidth. At pitch natural frequency (fn_{pitch}), motion amplitudes are seen reducing with an increase in $\Delta T''$. For $\Delta T''$ = 0.1, 0.15, and 0.2 ringing and springing pitch motion are observed and beyond this, no significant difference in pitch motions are noted, reflecting an insignificant effect of bi-chromatic wave group evolution on wave surface elevation and consequently on platform motions.

The range of platform motions in each mode are presented in Figure 7.2.7. The maximum difference in the surge, heave and pitch motion predicted by linear and nonlinear wave model are seen for a low value of $\Delta T''$, where nonlinear wave model predicted it 1.8, 1.9 and 2.1 times as compared to linear wave model respectively. For higher value of $\Delta T'' = 0.4$, the differences in all the motions predicted by both the models are seen insignificant. This example demonstrates the

importance of fully nonlinear wave model while analysing structure subjected to extreme bi-chromatic wave group having low period bandwidth.

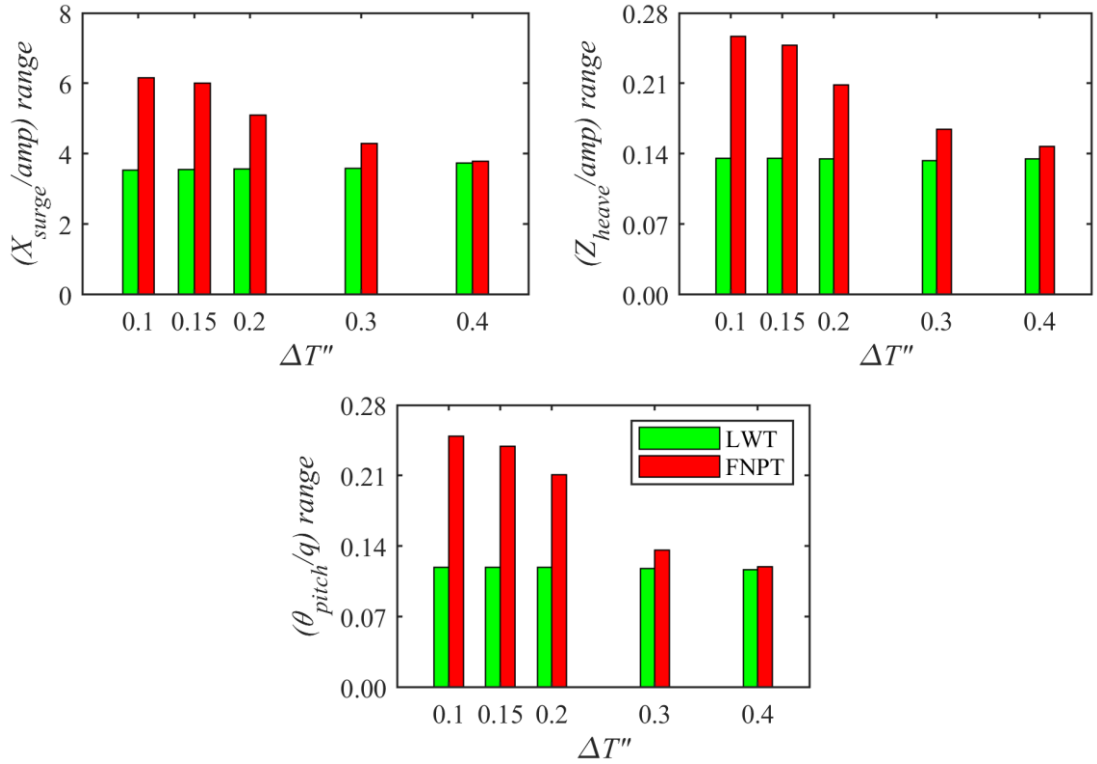

Figure 7.2.7 Range of TLPWT motions for bichromatic wave group with various normalised period bandwidth $\Delta T''$ and equal steepness $q=0.09$

7.2.4 Effect of wave group steepness, q on motion response

The nonlinearity of a regular (bichromatic) wave group is measured by amplitude of its components ($amp_1 = amp_2 = amp$) and carrier wavelength, L_c (or period, T_c) in a particular water depth, d. Wave group steepness q, which is linked to both the amplitude and length of a wave component is usually employed to describe the nonlinearity of a wave group. To study the influence of these parameters, the bichromatic wave groups are generated for five sets of q – 0.03, 0.045, 0.06, 0.075 and 0.09. Loading condition of co-existing wave and wind with the turbine in operating condition at its rated wind speed of 21m/sec is considered. The period of a carrier wave, T_c and water depth, d is used the same as used in section 7.2.2. The normalised period bandwidth $\Delta T''$ of 0.1 is used to obtain the periods of wave components, T_1 and T_2. A steady state normalised surge, heave and pitch motions of TLPWT for these bichromatic wave groups predicted by both linear LWT and nonlinear FNPT wave models are presented in Figure 7.2.8 through Figure 7.2.10 respectively.

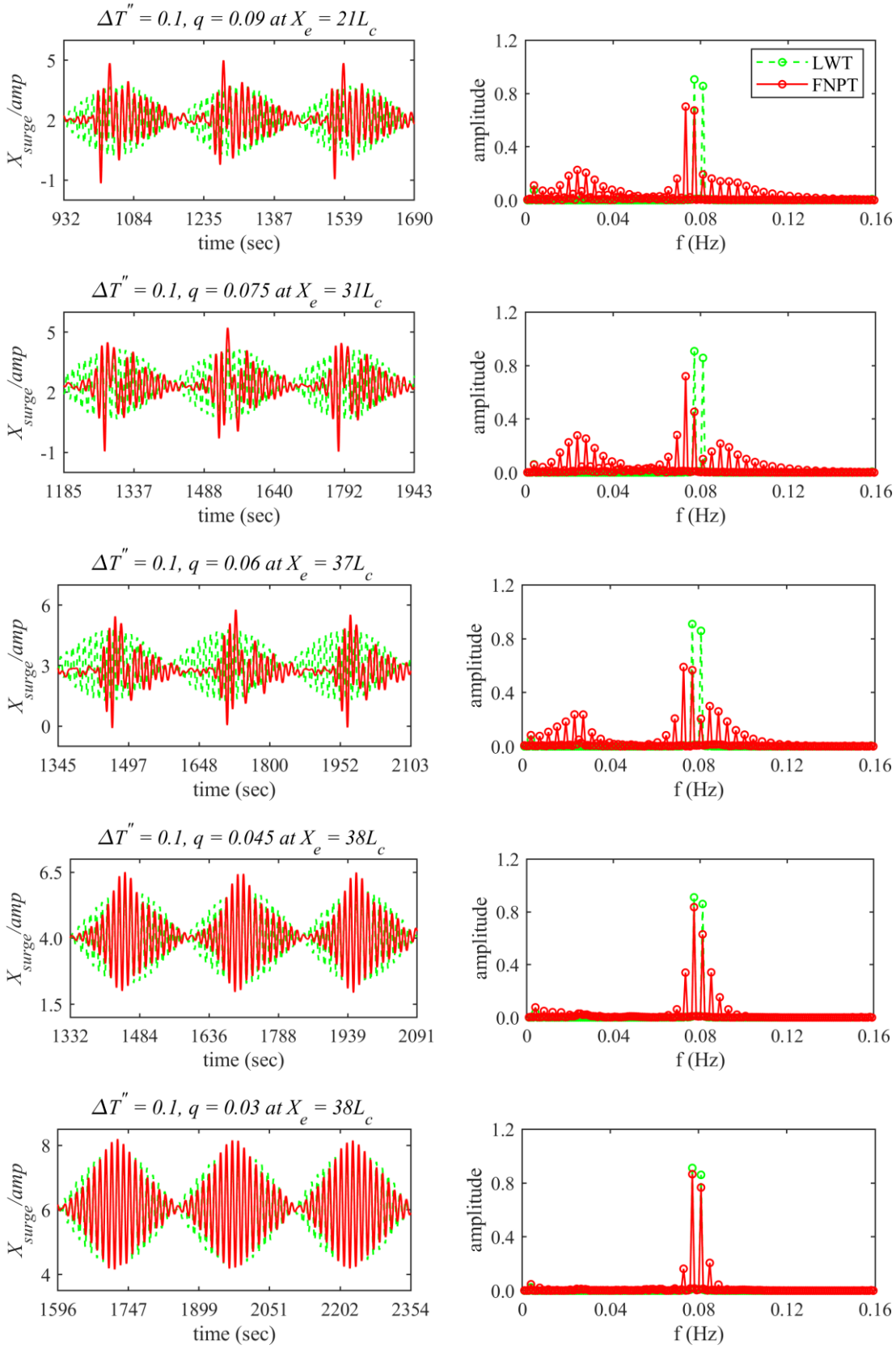

Figure 7.2.8 Time history and amplitude spectra of TLPWT surge motions for bichromatic wave group with various steepness q and equal normalised period bandwidth $\Delta T''=0.1$

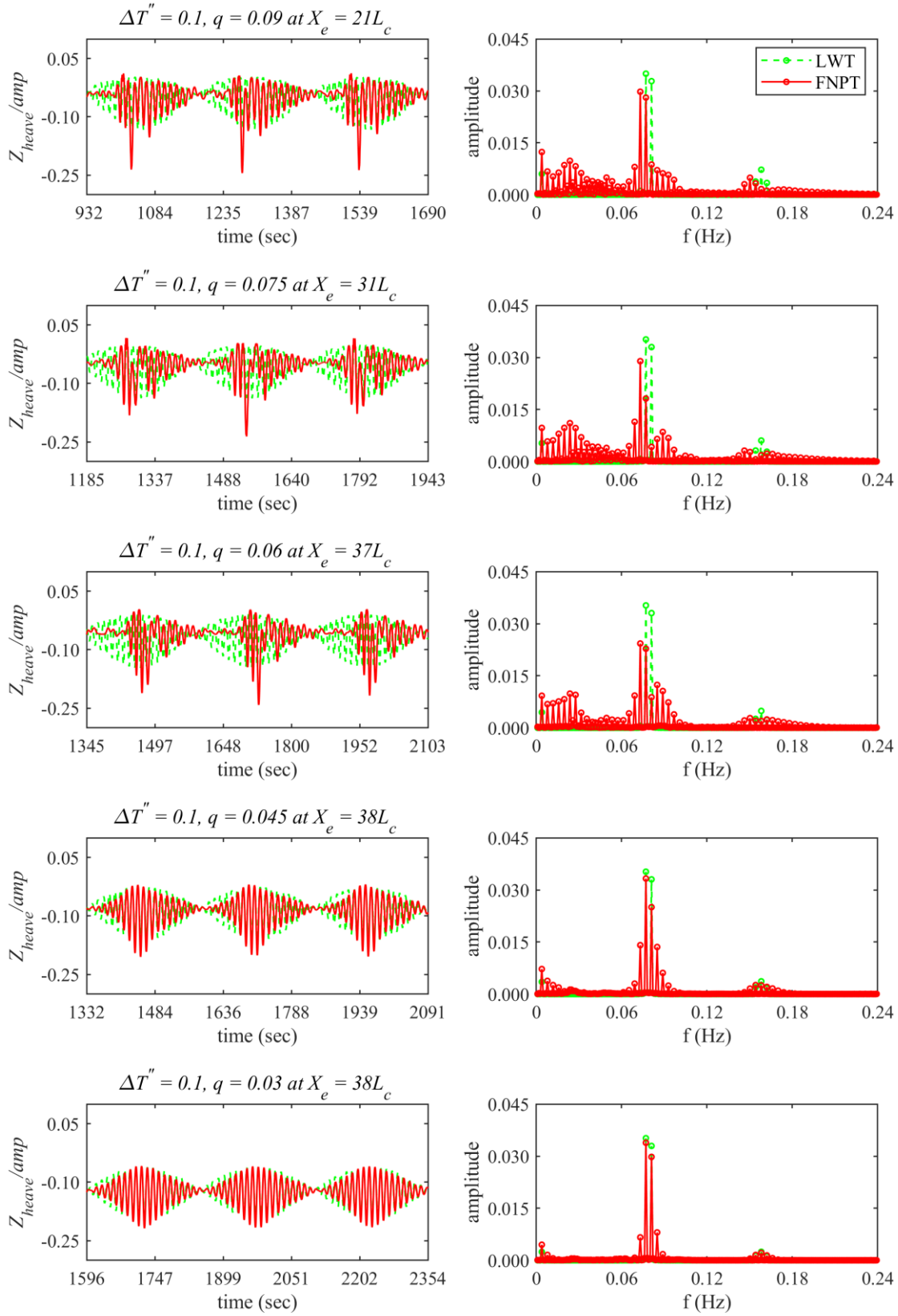

Figure 7.2.9 Time history and amplitude spectra of TLPWT heave motion for bichromatic wave group with various steepness q and equal normalised period bandwidth $\Delta T''=0.1$

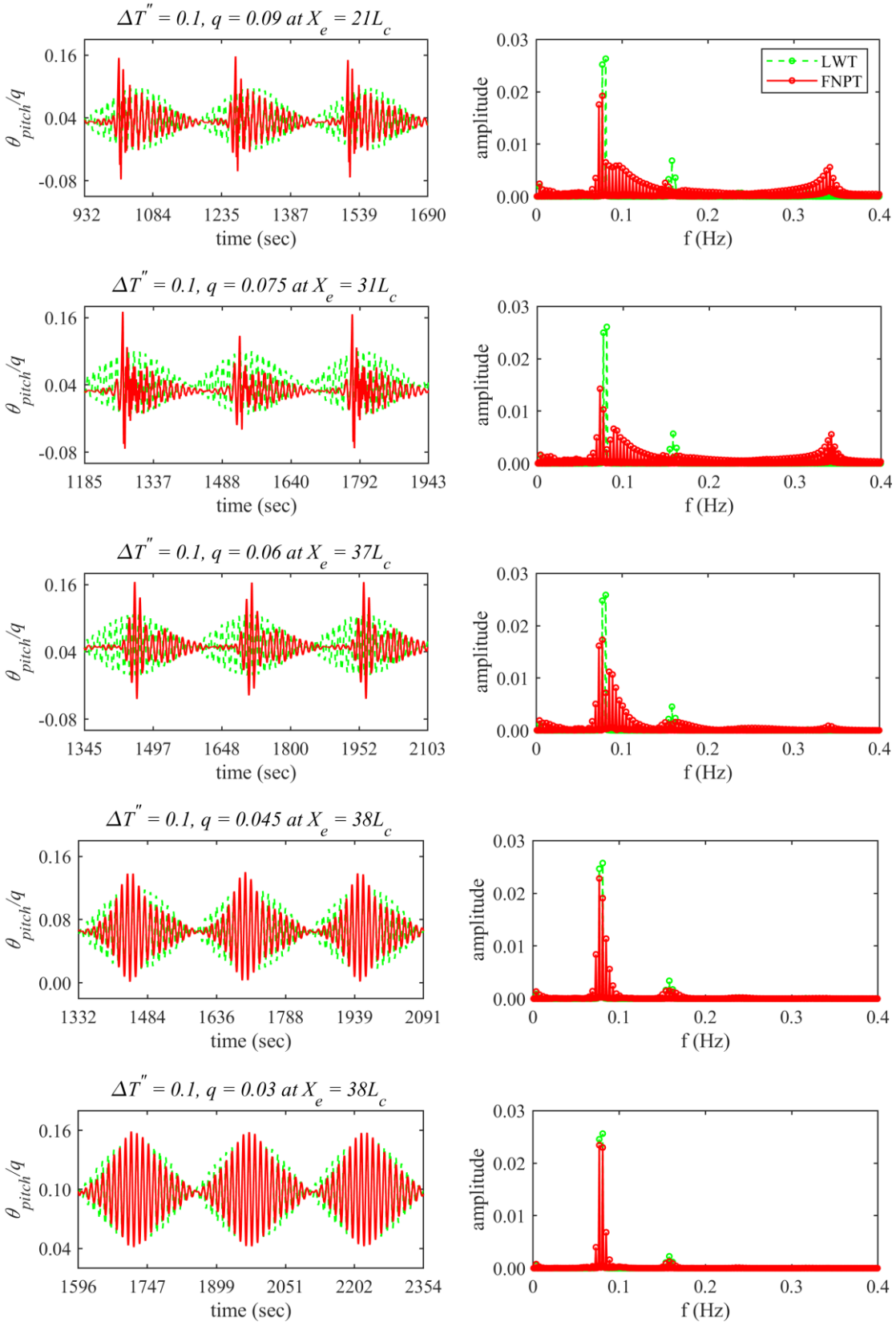

Figure 7.2.10 Time history and amplitude spectra of TLPWT pitch motions for bichromatic wave group with various steepness q and equal normalised period bandwidth $\Delta T''=0.1$

The time history plots of TLPWT motions presented in Figure 7.2.8 through Figure 7.2.10 shows the effect of wave group steepness on the difference in motion prediction using linear and nonlinear wave model reflecting the difference in extreme wave surface prediction depicted in Figure 7.1.7. The higher wave surface prediction by nonlinear FNPT wave model is seen due to the nonlinear evolution of wave group which linear LWT wave model failed to predict. As wave group steepness reduces, the difference in the height of an extreme wave and consequently the difference in TLPWT motions predicted by linear and nonlinear wave model decreases. The predominant peak responses for the translational surge and heave motions for bichromatic wave group $\Delta T'' = 0.1, q = 0.09$ appeared at input wave frequency (fw_1), sideband frequency ($fw_1 - dfw$) and surge natural frequency (fn_{surge}) as shown in Figure 7.2.8 and Figure 7.2.9 respectively. The surge response appeared at its natural frequency due to excitation by the difference in sideband frequencies generated through nonlinear evolution whereas the heave response at surge natural frequency appeared due to the set down effect resulting from the positive surge response. For wave group steepness q of 0.09, 0.075, and 0.06, a significant difference in TLPWT motions predicted by linear and nonlinear wave models are seen whereas, for steepness $q < 0.045$, the differences are seen insignificant showing wave group evolution is linear. A similar trend is seen for the pitch motion presented in Figure 7.2.10. The ringing and springing responses are seen for the wave group steepness q of 0.09, 0.075 and 0.06. For steepness $q < 0.045$, the difference in prediction of pitch motions by both the wave models are seen insignificant.

The range (measured from minimum to maximum) of TLPWT motions in each mode are presented in Figure 7.2.11. The maximum difference in the surge, heave and pitch motion predicted by linear and nonlinear wave model are seen for a high value of $q=0.09$, where nonlinear wave model predicted it 1.7, 1.9 and 2.1 times higher as compared to linear wave model respectively. For a lower value of q = 0.03, where effect of wave group evolution on wave surface prediction are seen less, the differences in all the modes of motions predicted by both the wave models are seen insignificant. This example demonstrates the importance of fully nonlinear wave model while analysing structure subjected to a bichromatic wave group with high steepness ($q >$ 0.03 for this case).

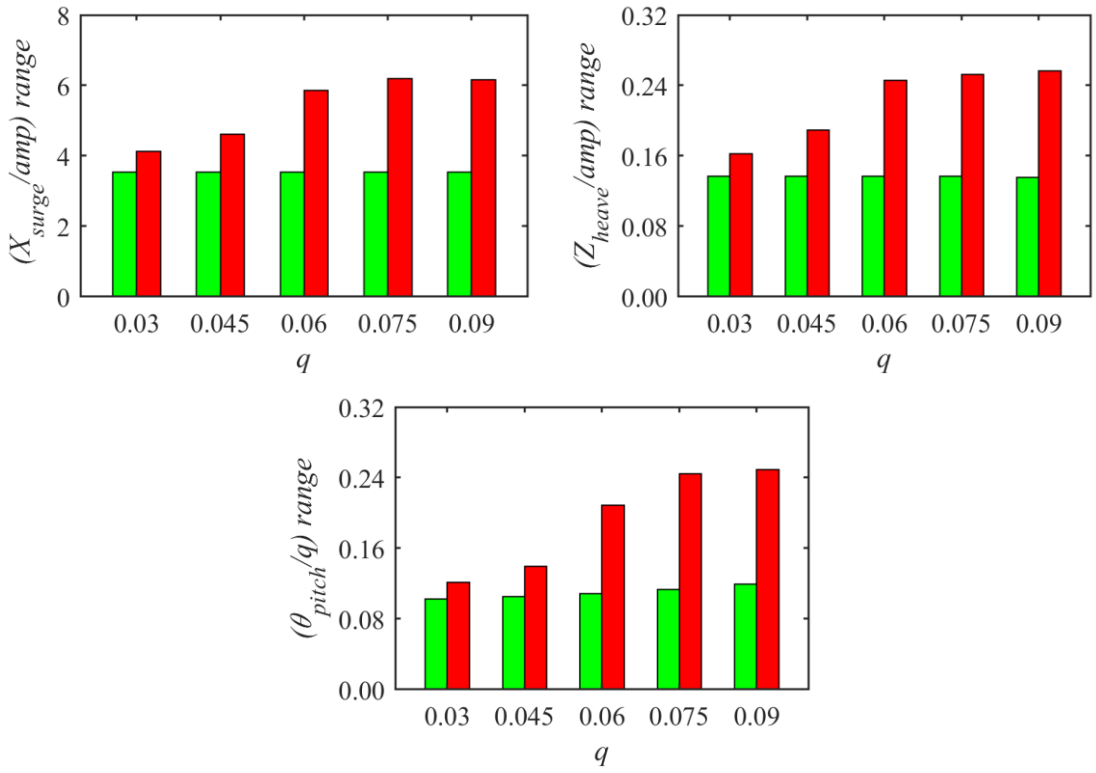

Figure 7.2.11 Range of TLPWT motions for bichromatic wave group with various steepness q and equal normalised period bandwidth $\Delta T''=0.1$

7.3 Effect of nonlinear motion response on global performance of TLPWT

Global performance of a TLPWT is assessed by investigating the effect of its nonlinear motions on the response parameters associated with its components, i.e., wind turbine, tall supporting tower, platform hull and mooring lines. Key response parameters associated with each component of a floating wind turbine are chosen to investigate their prediction using nonlinear wave model, i.e. FNPT based QALE-FEM. The response parameters are further compared using the most widely used linear wave theory (LWT) with wheeler stretching to examine its range of applicability. The response parameters chosen for the wind turbine are blade airgap, turbine fore-aft displacement, and thrust acting on it whereas, for a tower, the bending moment acting on it is chosen. For platform hull, the wave load acting in a predominant direction, i.e., the surge is chosen, and for station keeping system, tension in each mooring line is chosen for the investigation. All these parameters depend upon motion response of TLPWT.

As seen in previous section 7.2, the maximum difference in motions predicted by both the wave models, i.e. LWT and FNPT are observed for bichromatic wave group with period bandwidth of 0.1 and steepness of 0.09 (beyond which wave breaking occurs). Therefore, the effect of wave models in predicting response parameters are investigated for this bichromatic wave group. Loading condition where wind and wave are co-existing with the turbine in operating condition (WW-O-21) is considered for the investigation. Time history of response parameters associated with the wind turbine, tower, platform and mooring lines is presented in

Figure 7.3.1 through Figure 7.3.4 respectively. Here airgap, thrust, and tension in each mooring line are normalised by their steady-state values at simulation time $t = 0$, whereas turbine fore-aft displacement, surge wave force, and tower bending moment are normalised by wave amplitude, buoyancy force and product of buoyancy force and draft of the platform respectively.

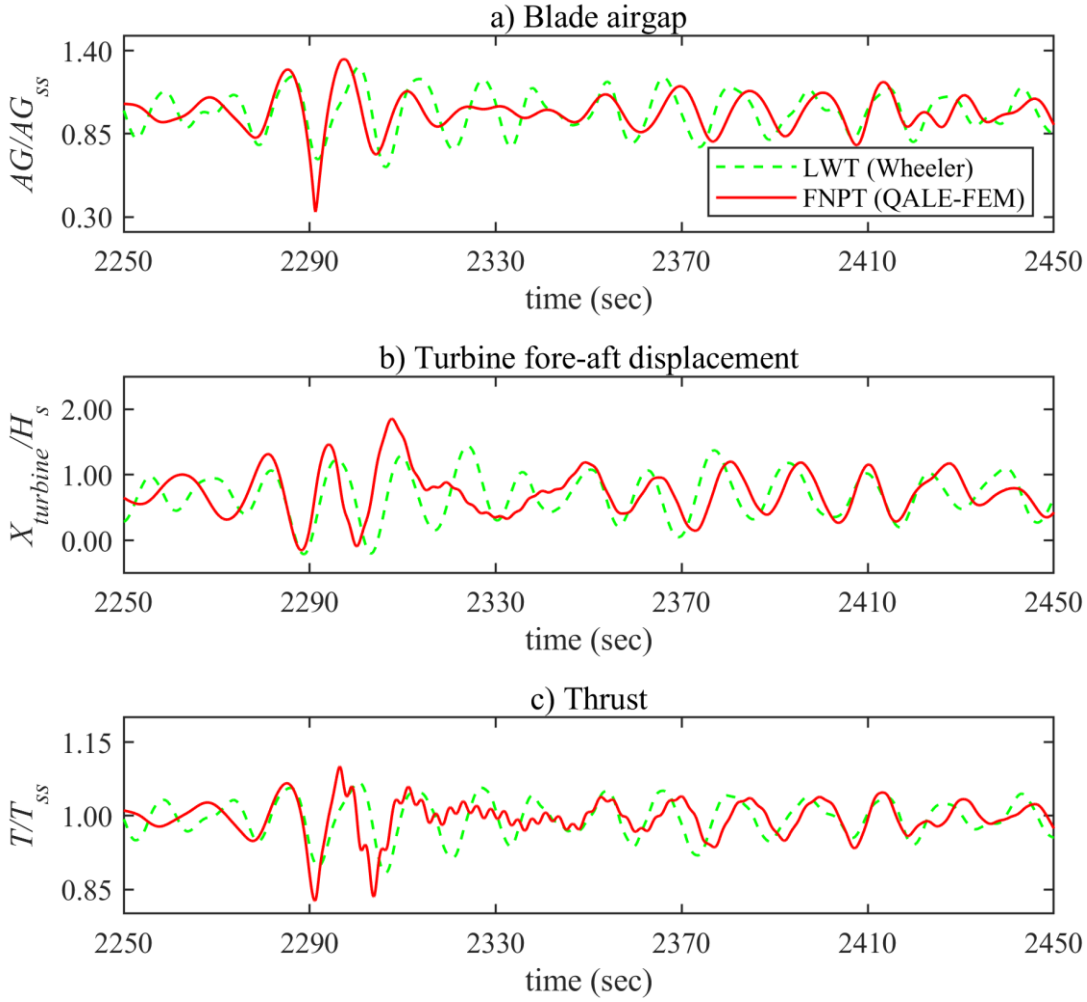

Figure 7.3.1 Time history of wind turbine response parameters for loading condition 'WW-O-21' in bichromatic wave group $\Delta T'' = 0.1$, $q = 0.09$

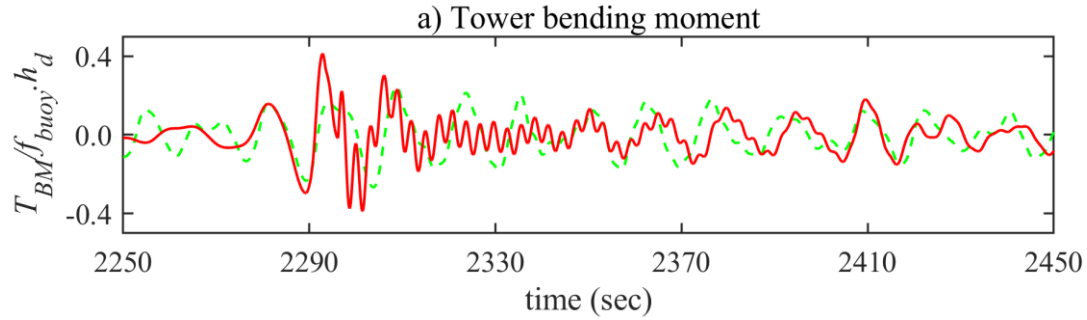

Figure 7.3.2 Time history of tower bending moment for loading condition 'WW-O-21' in bichromatic wave group $\Delta T'' = 0.1$, $q = 0.09$

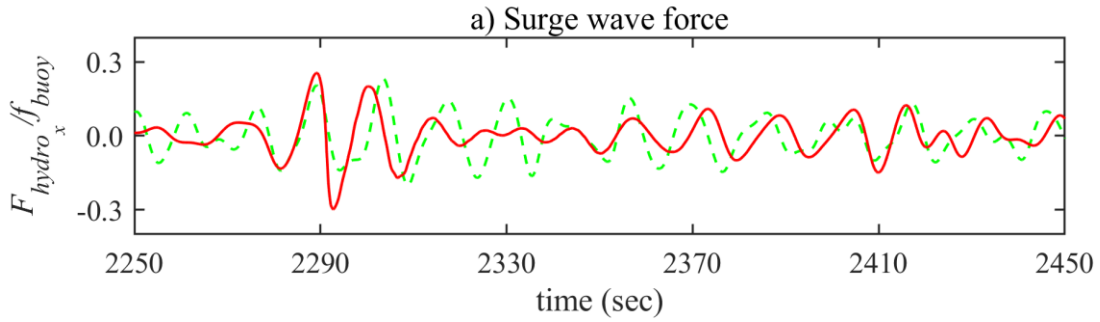

Figure 7.3.3 Time history of wave surge force for loading condition 'WW-O-21' in bichromatic wave group $\Delta T'' = 0.1$, $q = 0.09$

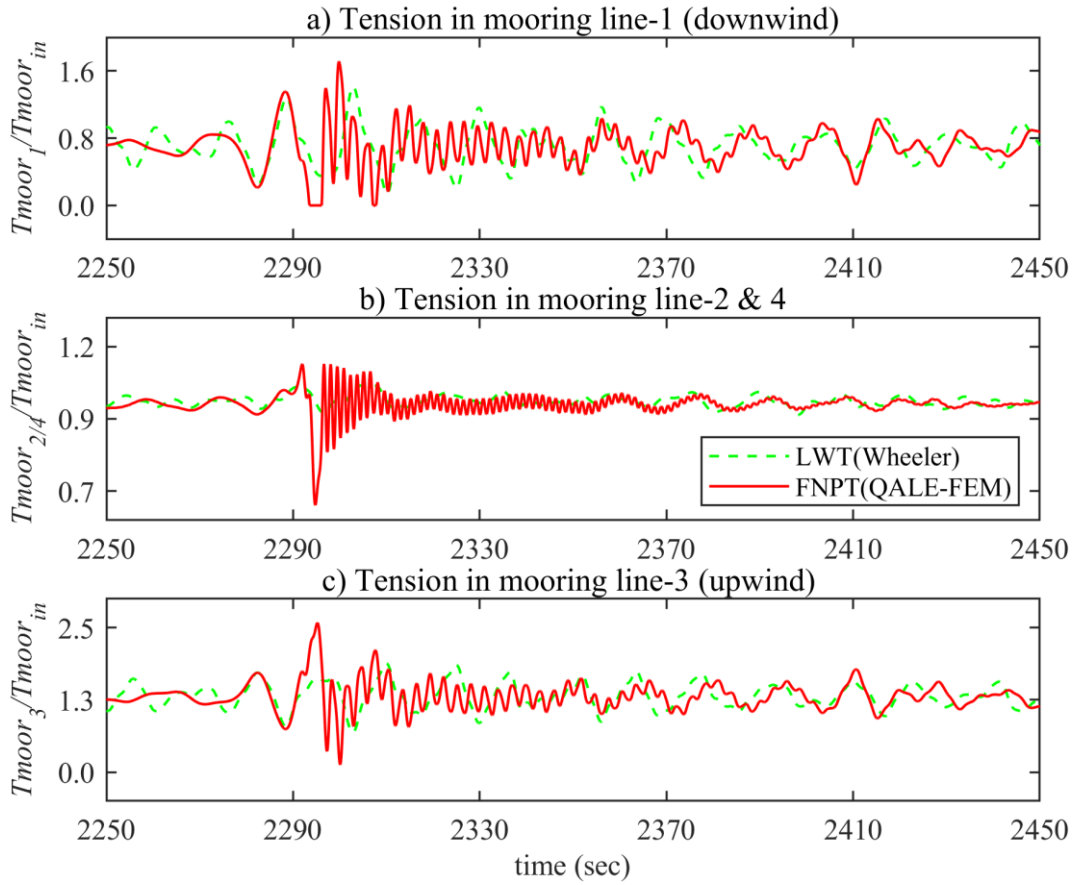

Figure 7.3.4 Time history of mooring line tensions for loading condition 'WW-O-21' in bichromatic wave group $\Delta T'' = 0.1$, $q = 0.09$

The time history plots presented in Figure 7.3.1 through Figure 7.3.4 reflects the difference in TLPWT motions predicted by both LWT and FNPT wave models in predicting response parameters for the wind turbine, tower, platform and mooring lines. All the response parameters are predicted higher by nonlinear wave model (FNPT) as compared to predictions by linear wave model (LWT). This overprediction is due to the ability of FNPT based QALE-FEM in predicting extreme wave generated through an evolution of bichromatic wave group that linear wave theory failed to predict. However, the difference in extreme wave surface and consequently TLPWT motions predicted by both the wave models is mainly controlled by period bandwidth and

steepness of the bichromatic wave group, as described in section 7.2.3 and 7.2.4. To investigate the influence of these parameters on the prediction of response parameters for the wind turbine, tower, platform and mooring lines, the calculations and comparisons are carried out for all the response parameters by varying period bandwidth and steepness of wave group. The range (measured from minimum to maximum) or maximum (peak) value of each parameter for varying period bandwidth and steepness is presented in Figure 7.3.5 and Figure 7.3.6 respectively.

It can be seen from Figure 7.3.5 and Figure 7.3.6 that the maximum difference in response parameters predicted by both the wave models occurs for low period bandwidth, $\Delta T''$ of 0.1 and maximum steepness, q of 0.09 (beyond which wave breaking occurs). As the period bandwidth $\Delta T''$ increases and steepness, q reduces, the differences in response parameters predicted by both the wave models decreases. For $\Delta T'' = 0.1$ and $q = 0.09$, the nonlinear wave model (FNPT) predicted minimum airgap, turbine fore-aft displacement, and thrust range higher by 75%, 75%, and 87% as compared to linear wave model respectively. For tower and platform, these predictions for bending moment and wave force are 75% and 60% higher whereas, for mooring system, tensions predicted in mooring line 1, 2/4 and 3 are 44%, 10%, and 24% higher respectively. For higher value of $\Delta T'' = 0.4$ with maximum steepness $q = 0.09$ and for lower value of $\Delta T'' = 0.1$ with low steepness, $q = 0.03$, the differences in predictions of response parameters are less than 10% which is limiting characteristics of bi-chromatic wave group up to which both linear and nonlinear wave model predict wave surface nearly equal and consequently responses of concerned floating wind turbine.

The response parameters investigated in Figure 7.3.5 and Figure 7.3.6 were for the wind speed of 21m/s which is corresponding to a rated speed of the turbine. However, to investigate the effect of wave group evolution on response parameters in more general cases, the calculation and comparisons are carried out for all the parameters for various wind speeds while the turbine is operating and in the parked condition. Each response parameters for various wind speeds are presented in Figure 7.3.7 for bichromatic wave group with period bandwidth $\Delta T''$ of 0.1 and steepness q of 0.09.

It can be seen from Figure 7.3.7 that all the response parameters are predicted higher by nonlinear wave model, FNPT as compared to linear wave model, LWT for all the wind speeds while the turbine is in operation and the parked condition. This significant difference in prediction of motion and global responses of the chosen TLPWT presented under section 7.2 and 7.3 demonstrates the importance of nonlinear wave model while performing global response analysis of a floating wind turbine subjected to extreme waves.

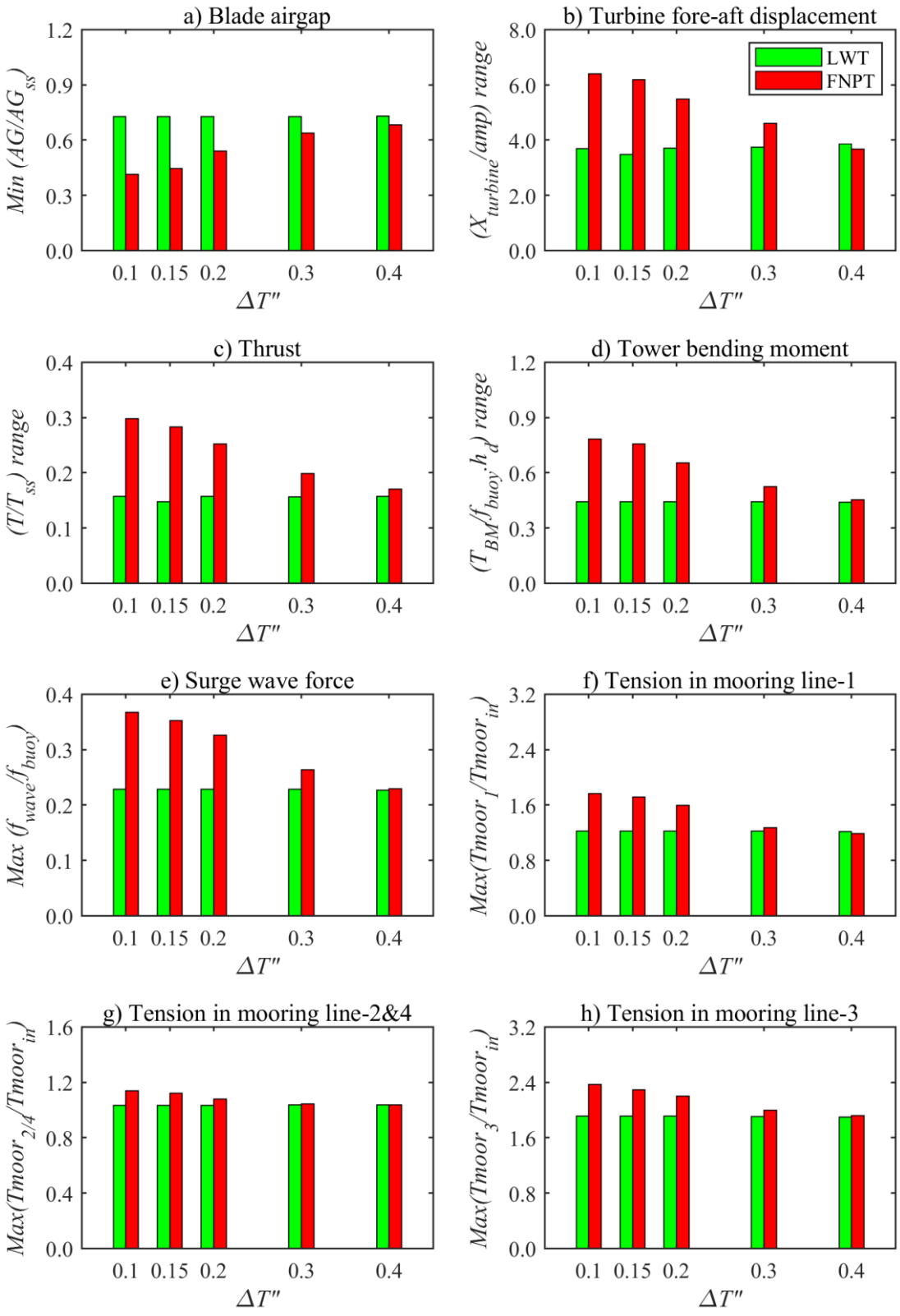

Figure 7.3.5 Response parameters for loading condition 'WW-O-21' in bichromatic wave with equal steepness, $q = 0.09$ and varying normalised period bandwidth $\Delta T''$

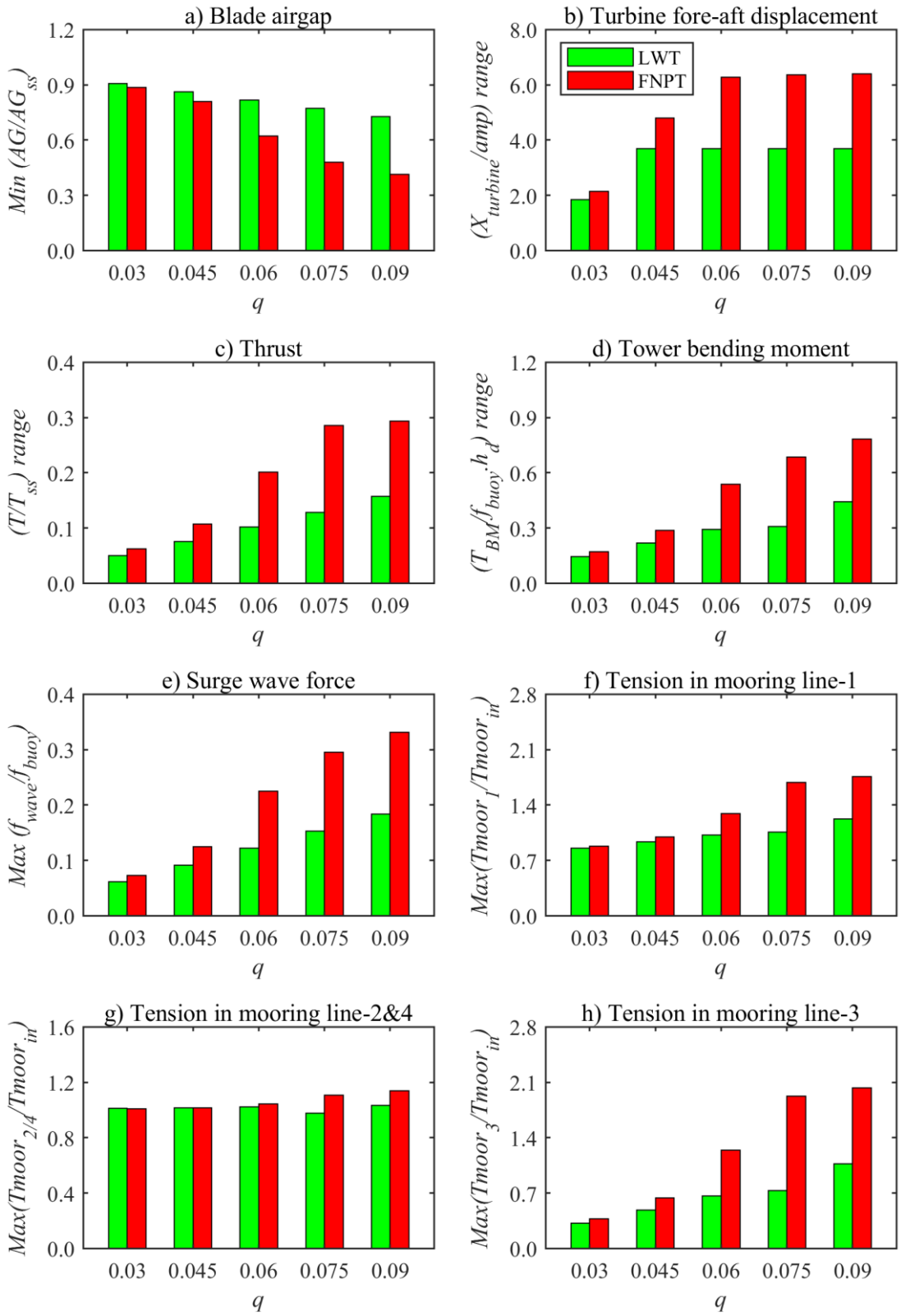

Figure 7.3.6 Response parameters for loading condition 'WW-O-21' in bichromatic wave with equal normalised period bandwidth $\Delta T'' = 0.1$ and varying steepness q

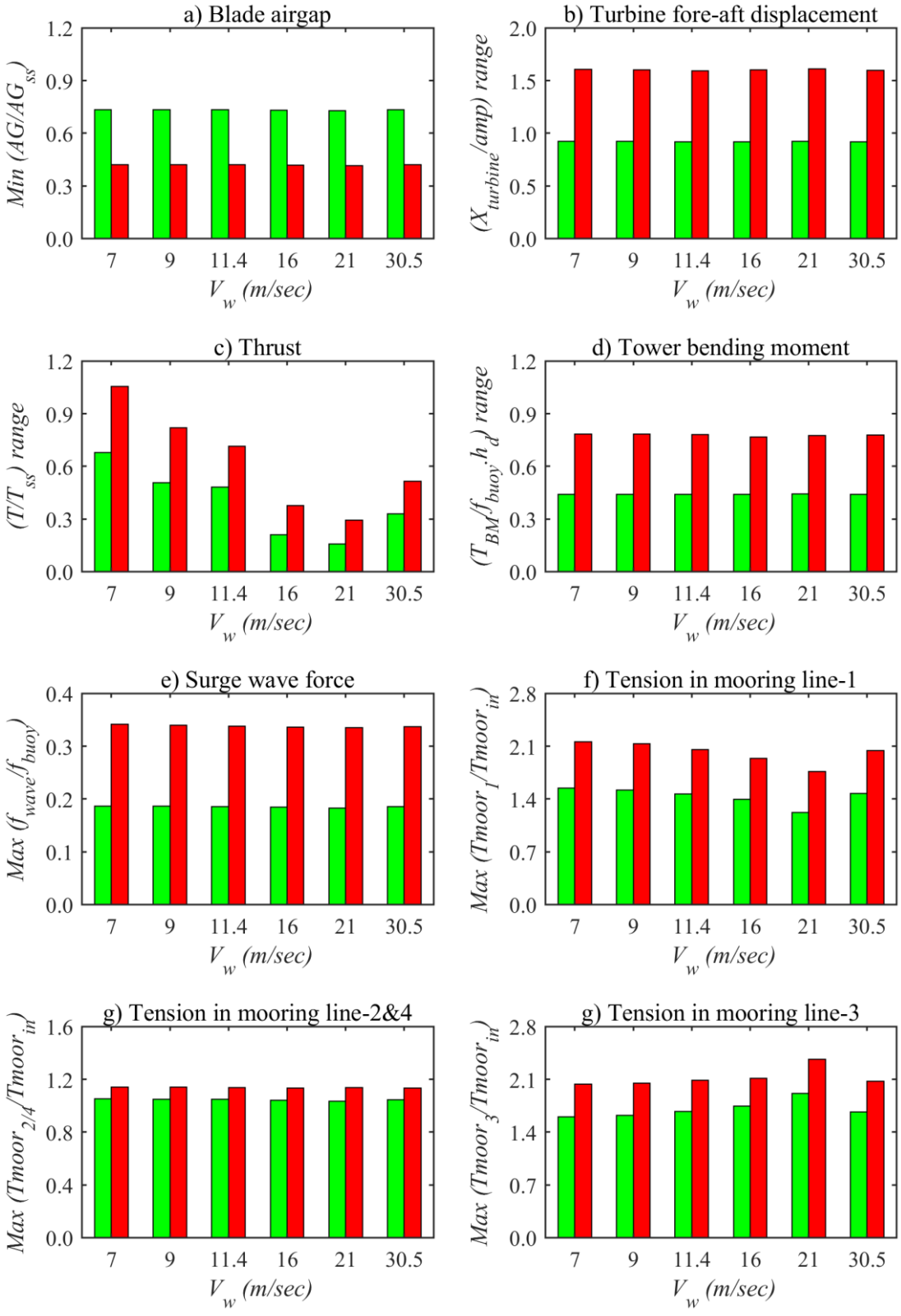

Figure 7.3.7 Response parameters for various wind speed V_w in bichromatic wave with normalised period bandwidth $\Delta T'' = 0.1$, and steepness $q = 0.09$

From the results presented in section 7.2 and 7.3, it appears that two closely spaced regular wave components can generate extreme wave through nonlinear evolution which may excite low-frequency surge motion and high-frequency ringing and springing pitch motion of the tension-leg-platform wind turbine. Both the phenomena are important as they significantly affect the global performance of the floating wind turbine. These motion responses and corresponding global response parameters for the chosen tension-leg-platform wind turbine are well predicted by the hybrid hydrodynamic wave model suggested in this thesis. However, such a tuned combination of wave components may not occur in practice but gives an idea of the possibility of such an event. Therefore, the response of TLPWT is studied next to the random wave group.

8 RESPONSE OF TLPWT TO EXTREME RANDOM WAVE GROUP

Waves in the real environment are random, and they can be effectively modelled in terms of energy spectra which describe ensembles of regular wave components combined in a random phase. An important advantage of such modelling is that the complete description of the wave motions including subsurface kinematics for the regular wave components can be linearly superimposed to provide the complete description of the combined wave motions. On this basis, spectra can be used to compute a wide range of statistical properties for waves and the responses of the structure subjected to it. There are methods of description for random waves other than spectra, including the use of wave height sequences defined by statistical laws such as those known as Markov or ARMA (Auto-Regressive Moving Average) processes (Box and Jenkins, 1970). These are less widely used, and hence here attention will be concentrated on the spectrum method commonly employed for modelling random waves.

A random wave group based on spectrum method is a periodic signal resulting from the linear superposition of N_c number of regular wave components combined in a random phase, $\emptyset_i$ with frequencies, ω_i and amplitude, amp_i derived from the energy spectra. The equation for wave surface elevation can be written as,

$$\eta(x,t) = \sum_{i=1}^{N_c} amp_i \cos(k_i\, x - \omega_i\, t + \emptyset_i) \tag{8.1}$$

where k_i is wave number of ith wave component and x is co-ordinate of a point along the wave direction.

Although for many practical purposes linear wave theory produces a satisfactory approximation of the underlying nonlinear process, this is not the case for the propagation of certain classes of random wave group which is demonstrated by several authors (Stansberg, 2000; Onorato, et al., 2006; Xia, et al., 2015) through experimental study in a wave tank. The measured wave groups that were generated using JONSWAP spectra showed a significant deviation from the linear wave theory at some distances from the wave maker. The crest height of an identified extreme wave in a random wave group was seen much higher than the crest height predicted by linear and second order wave theory. These observations motivated to investigate the effect of linear (Airy's LWT with wheeler stretching approximation) and nonlinear (FNPT based QALE-FEM) wave model considered in this thesis, in predicting responses of a chosen tension-leg-platform wind turbine (TLPWT) subjected to extreme wave in a random wave group.

The first section of the chapter compares characteristics of an extreme wave, and its occurrences predicted by both LWT and FNPT wave models. The subsequent sections of the chapter compare its effect on the motion response and global performance of a chosen tension-leg-platform wind turbine.

8.1 Nonlinear wave surface evolution in a freely propagating random wave group

To investigate the condition that is likely to induce higher TLPWT responses and might realistically occur in the offshore environment, an environmental condition from EU-FP7 marina platform project is chosen (Lin, et al., 2015). In this project, 3-D contour surfaces based on the long-term joint distribution of wind speed V_w, significant wave height H_s, and peak period T_p were generated for 18 European offshore sites as shown in Figure 8.1.1 for the development of offshore renewable energy concepts.

Figure 8.1.1 Location of potential European offshore sites for renewable energy development

The offshore site no. 14, Norway 5 in a water depth of 202m, situated 30miles from the shore in Northern North Sea is chosen to investigate the response of selected floating wind turbine. The slices of contour surfaces (H_s, T_p) for different wind speeds, V_w at turbine hub are plotted in Figure 8.1.2.

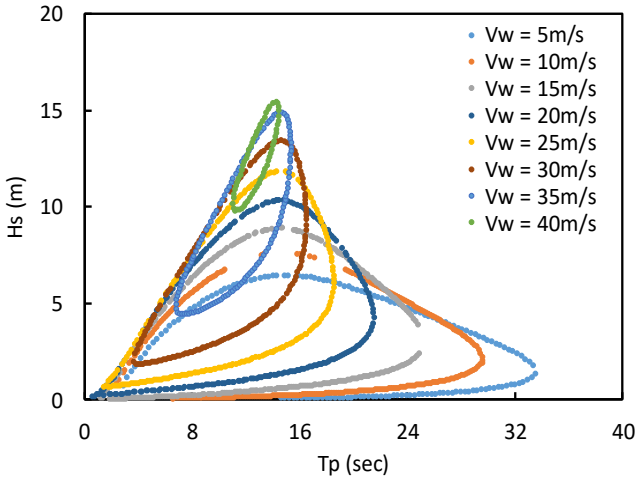

Figure 8.1.2 50-year contours of H_s and T_p for different wind speeds at site no.14

The steep random wave group identified at peak period T_p of 14.5s is chosen for the study. At this period, a maximum non-breaking significant wave height H_s is found through numerical simulation runs using a nonlinear (FNPT) wave model; and the corresponding wind speed V_w is obtained from the 3D-contour surface. For the site selected in this study, it is recommended to use the JONSWAP spectrum to estimate the extreme responses. This spectrum is formulated as a modification of the PM spectrum for a developing sea state in a fetch-limited situation. The spectrum was derived to account for a higher peak and a narrower spectrum in a storm situation for the same total energy as compared with the PM spectrum. Therefore, this spectrum is often used for the extreme event analysis.

The spectral density of the free surface elevation recommended by IEC 61400-3 (2009) is given by,

$$S_{JS}(f) = 0.3125 \cdot {H_s}^2 \cdot T_p \cdot \left(\frac{f}{f_p}\right)^{-5} \cdot exp\left(-1.25 \cdot \left(\frac{f}{f_p}\right)^{-4}\right) \cdot (1 - 0.287 \cdot \ln\gamma) \cdot \gamma^{exp\left(-0.5 \cdot \left(\frac{\frac{f}{f_p}-1}{\sigma}\right)^2\right)} \tag{8.1.1}$$

where,

H_s = significant wave height

T_p = peak wave period

f_p = peak frequency

σ = spectral width parameter which is 0.07 if $f \leq f_p$, else 0.09

γ = peak shape parameter varies between 1 to 5 with its mean value of 3.3

As seen in the previous chapter, extreme wave generated through nonlinear evolution in a regular (bichromatic) wave group was controlled by its steepness and period bandwidth. Similarly, for random wave group, evolution is controlled by Benjamin-Feir Index (BFI), as defined below in Eq. (8.1.2) which is basically a ratio between significant wave steepness S_p and spectral bandwidth $\Delta f/f_{\mathrm{p}}$.

$$BFI = \frac{\sqrt{2}\,\pi\, S_p}{2\Delta f/f_p}\sqrt{\frac{\beta_w}{\sigma_w}} \tag{8.1.2}$$

where,

S_p = the significant wave steepness defined as H_s/L_p

Δf = the spectral band width

f_{p} = the peak spectral frequency

$\frac{\beta_w}{\sigma_w}$ = ratio multiplied to include effect of finite water depth given by Onorato et al (2006)

For large BFI, the modulation instability will lead to a rogue sea which is highly intermittent sea state characterized by a high density of unstable modes as demonstrated through experimental

study by Onorato et al. (2006). Three different JONSWAP spectra with different values of peak shape parameter, γ are investigated for a period of 14.5s. Table 8.1.1 reports the parameters that characterized each JONSWAP spectrum including corresponding BFI.

Table 8.1.1 Simulation cases for random wave group

γ	$H_s(m)$	$S_p = H_s/L_p$	$\Delta f/f_{\mathrm{p}}$	BFI
1	11.382	0.0347	0.29	0.25
3.3	10.857	0.0331	0.10	0.70
5	10.660	0.0325	0.08	0.84

Above three different random wave group simulation runs will be called as BFI-0.25, BFI-0.7, and BFI-0.84 with an obvious meaning. The waves are generated using flap type wavemaker following the procedure detailed under section 3.3.2.3. An extreme wave resulting from the nonlinear evolution in these random wave groups are presented in Figure 8.1.3 in space domain where wave surface elevation η is normalised by significant wave height H_s, and distance x and time t by peak wave length L_p and peak wave period T_p respectively. An occurrence of extreme wave i.e., location X_e and duration T_e in terms of peak wave length L_p and peak wave period T_p are presented in Figure 8.1.4.

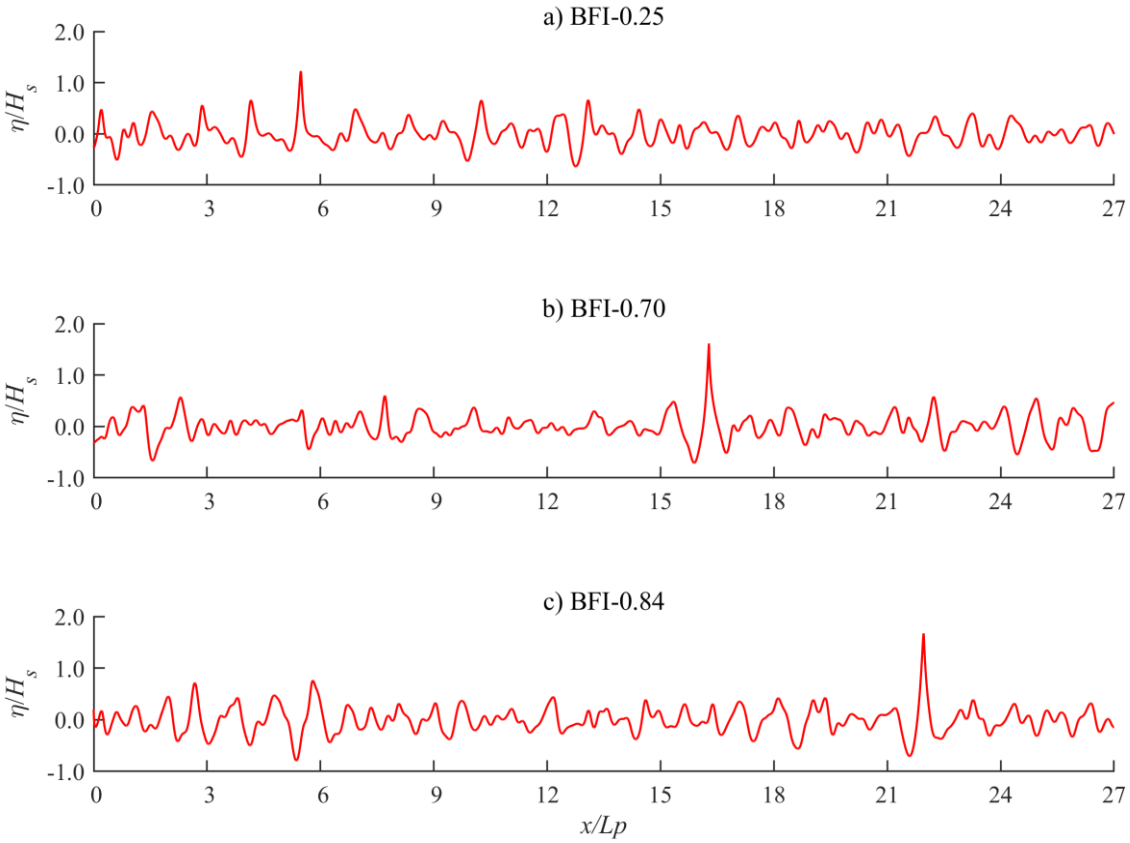

Figure 8.1.3 Extreme wave in space domain

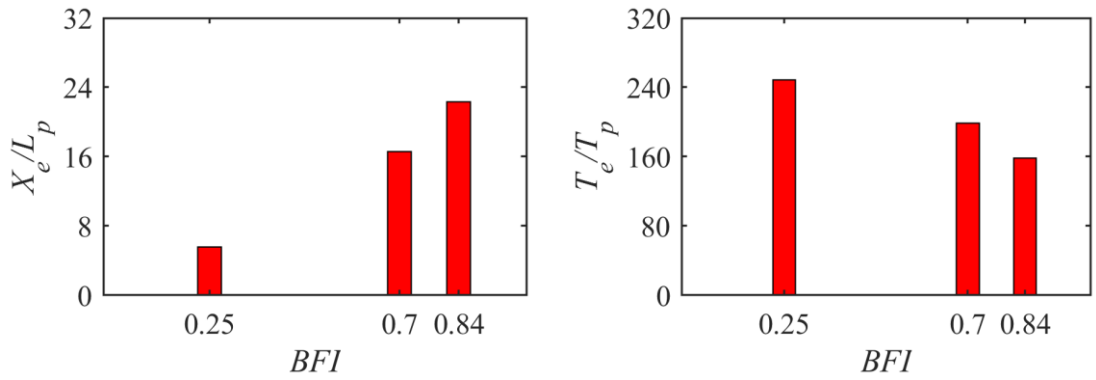

Figure 8.1.4 Extreme wave occurrence

An effect of *BFI* on the nonlinear evolution of random wave group and the resulting extreme wave can be clearly seen from Figure 8.1.3 and Figure 8.1.4. As value of *BFI* increases, the location of extreme wave increases in addition to increase in its crest and total height while its occurrence time reduces. The surface elevation of extreme wave predicted by fully nonlinear wave model (FNPT) is compared with the surface elevation predicted by linear wave model (LWT) by comparing their respective time histories in Figure 8.1.5. The crest and total wave height of extreme wave are compared in Figure 8.1.6.

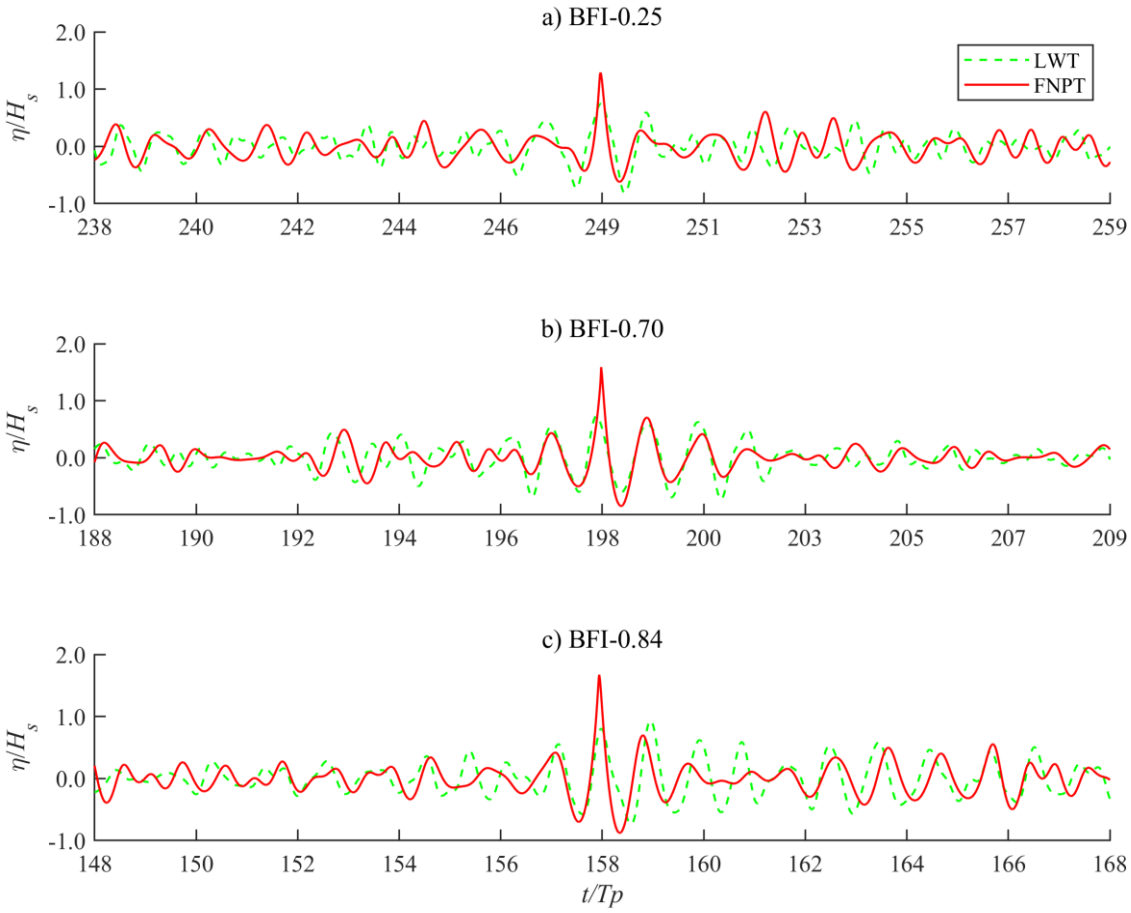

Figure 8.1.5 Extreme wave in time domain

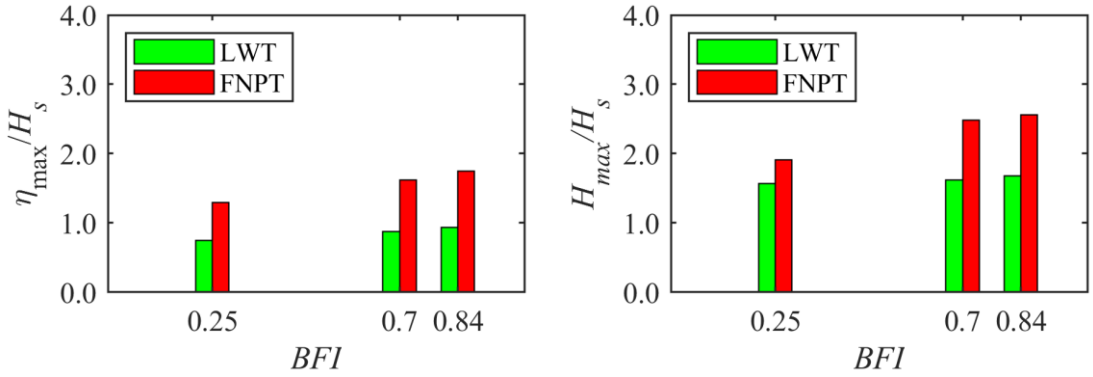

Figure 8.1.6 Extreme wave crest and height comparison

It can be seen from Figure 8.1.5 and Figure 8.1.6 that the maximum difference in extreme wave surface elevation predicted by both the wave models occurs for the high value of BFI of 0.84. The crest and height of an extreme wave identified in a random wave record predicted by nonlinear wave model are 1.9 and 1.6 times of predictions by linear wave model respectively. An extreme wave generated through nonlinear evolution is predicted at 22 times of peak wave length L_p at the duration of 158 times of peak wave period T_p. With the reduction in BFI value, the effect on nonlinear evolution and the resulting extreme wave surface as depicted in Figure 8.1.6 reduces with minimum difference in wave surface elevations predicted by both the wave models are seen for the low value of BFI of 0.25. At this BFI, the difference in wave crest and height predicted by both the wave models are 70% and 22% respectively. This difference is mainly seen due to an ability of FNPT wave model in predicting the nonlinear evolution. These results demonstrate that the crest and height of an extreme wave in random sea under certain conditions may be higher than predicted by Rayleigh distribution based on linear wave theory which is also observed during laboratory experiment reported by Stansberg (2000). An effect of this non-Rayleigh crest and height of an extreme wave on the response of TLPWT is studied next.

8.2 Effect of nonlinear wave surface evolution on motion response of TLPWT

Global motion analysis of a parameterized TLPWT is performed to study its motion responses under various environmental conditions comprising extreme random wave group. The analysis cases presented here, uses an incident random wave groups detailed in Table 8.1.1 chosen from the potential site identified for the renewable energy development in the Northern North Sea. The current speed is set as zero, while hydrodynamic coefficients in the wave force calculations are set as $C_a = 1.0$ and $C_d = 1.0$ based on Reynolds and Keulegan-Carpenter number (Chakrabarti, 2005). The wind and wave headings are considered as collinear and fixed at zero degree with respect to x-axis. With this assumption, the structure moves only in the x-z plane, hence the motions are surge, heave and pitch. At the beginning of the simulation, a cosine taper function is imposed on the forces and moments to reduce the transient effects produced by the impulsive loading. The motions resulting from the analysis are studied using their time history, amplitude spectra, range (minimum to maximum) and statistical parameters such as maximum (peak value) and skewness. Three different load conditions as detailed in Table 8.2.1 below, are chosen to investigate the impact of different wave models in predicting motion response.

Table 8.2.1 Loading condition

Loading condition (LC)	Description
WO	TLPWT subjected to wave only
WW-O-V_w	TLPWT subjected to combined wave and wind (turbine in operating condition at wind speed of V_w)
WW-P-V_w	TLPWT subjected to combine wave and wind (turbine in parked condition exposed to wind speed of V_w)

The motion responses of concerned structure are further compared using linear and nonlinear wave models for various BFI, to see range of applicability of LWT wave model.

8.2.1 Motion response under wave excitation

Global motion analysis of a TLPWT under wave only (WO) loading condition is performed to see the clear effect of extreme wave generated through nonlinear evolution on its motion response. The first case presented here uses an incident random wave group BFI-0.84. This case corresponds to Jonswap spectra with peak period T_p of 14.5sec, significant wave height H_s of 10.66m, and peak shape parameter γ of 5 in a water depth of 202m. This random wave group yields maximum difference in surface elevation of extreme wave predicted by LWT and FNPT wave models among all the BFI cases listed in Table 8.1.1 as illustrated in Figure 8.1.3 and Figure 8.1.5. In the nonlinear wave model (FNPT based QALE-FEM), the structure is located at $X_e = 22L_p$ from the wave maker where extreme wave evolution occurs.

Time history and amplitude spectra of TLPWT motion response is presented in Figure 8.2.1. Here, the translational motions such as surge and heave are normalised by significant wave height

H_s, whereas significant wave steepness S_p normalises rotational pitch motion. Amplitude spectra of normalised motions are obtained by performing FFT on the respective motions time history segment covering ringing and springing pitch motions.

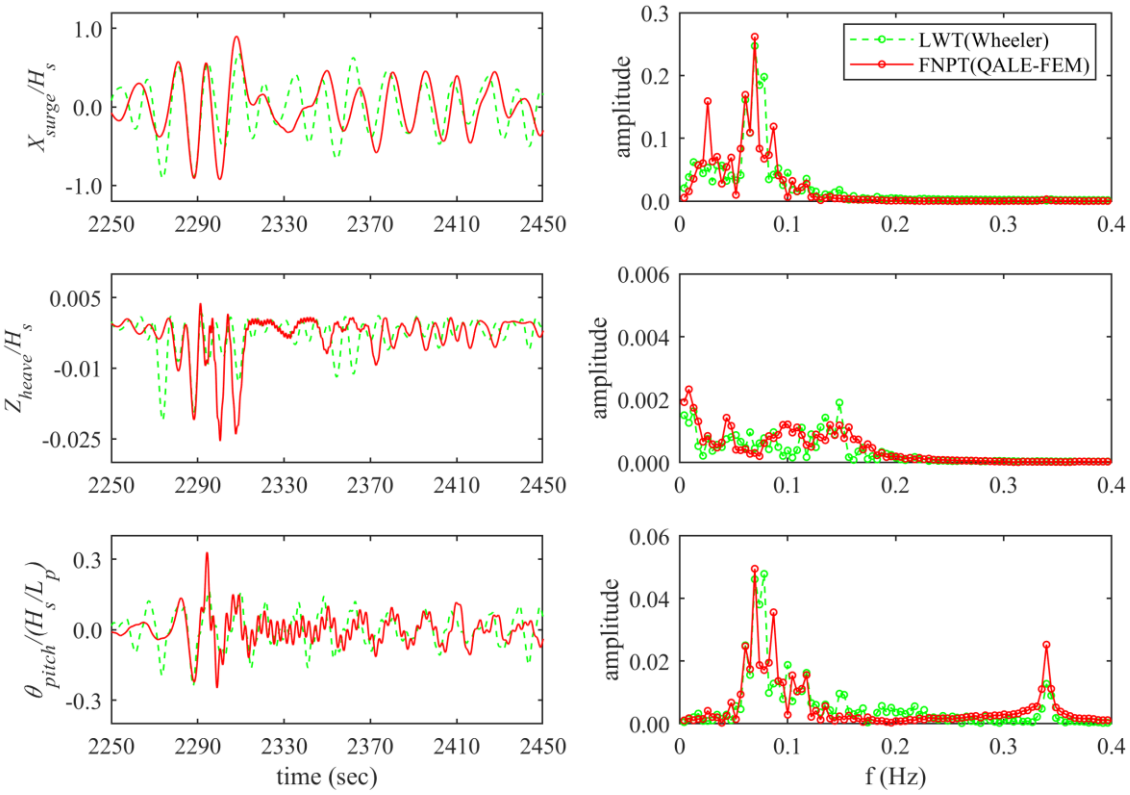

Figure 8.2.1 Time history and amplitude spectra of TLPWT motions under loading condition 'WO' in random wave group *BFI-0.84*

The time history plots of TLPWT motions predicted by linear and nonlinear wave model presented for wave only condition in Figure 8.2.1 showed positive mean for surge and pitch motion whereas negative mean for the heave motion. The positive mean for surge and pitch motion is mainly seen due to low-frequency surge and high-frequency ringing and springing pitch motion excited by an extreme wave. The negative mean for heave motion is not the only result of wave loading but also due to the set-down effect resulting from the positive surge and pitch motion of the TLPWT. The difference in prediction of mean and the range of motions in each mode are mainly result of difference in prediction of extreme wave surface elevation by both the wave models. The numerical model with linear wave theory primarily constitutes nonlinearity in wave forces and the equation of motions whereas the numerical model with FNPT wave model constitutes an additional nonlinear effect of wave-wave interaction which severely affects the prediction of extreme wave characteristics, i.e., crest and total height.

The predominant peak responses predicted by FNPT wave model appeared at peak wave frequency (fw_p), and at surge (fn_{surge}) and pitch natural frequency (fn_{pitch}) of the concerned structure. The magnitude of motion amplitudes at surge and pitch natural frequency are 70% and 50% of motion amplitudes at peak wave frequency respectively. The LWT wave model predicted

20% and 27%. For heave motion, the predominant peak responses predicted by FNPT wave model appeared at the difference in peak (fw_p), and surge natural frequency (fn_{surge}) of the concerned structure whereas LWT wave model predicted it at peak frequency. The LWT wave model predicted response lower at difference frequency ($fw_p - fn_{surge}$), and higher at peak frequency. Due to this underprediction of motion response by LWT wave model at concerned structures natural frequency, the overall platform motions in each mode are predicted higher by nonlinear wave model as compared to linear wave model. The range of motions (measured from minimum to maximum) predicted by FNPT wave model in the surge, heave and pitch mode are 1.15, 1.28 and 1.43 times higher as compared to the motions predicted by LWT wave model respectively.

This comparison demonstrates the importance of fully nonlinear wave model (FNPT) while analysing floating wind turbine subjected to extreme wave in random wave group. However, here the predictions of TLPWT motions are seen for the wave only loading condition where the structure is at rest in static equilibrium condition before wave approaches. In practice floating wind turbines will always have an offset and heel angle due to wind loads acting on the turbine and its supporting tower; therefore, motion responses are studied next under combined wind and wave loading condition while the turbine is operating and in the parked condition.

8.2.2 Motion response under combined wind and wave excitation

Global motion analysis of a TLPWT under combined wind and wave loading condition is performed to see the effect of extreme wave generated through nonlinear evolution on its motion response when the structure has a maximum offset and heel angle. As explained in section 6.3.1.2, the maximum offset and heel angle of structure occurs when the wind turbine is operating at its rated wind speed or subjected to extreme wind speed when it is parked. Therefore, wind loads are considered while the turbine is operating at its rated wind speed of 21m/s and in a parked condition, an extreme wind speed of 30.5m/s is considered. The case presented here uses an incident random wave group the same as used for wave only loading condition. Time history and amplitude spectra of motion response of TLPWT for turbine under operating (WW-O-21.8) and parked (WW-P-30.5) condition predicted by both linear LWT and nonlinear FNPT wave model are presented in Figure 8.2.2 and Figure 8.2.3 respectively.

The time history plots of TLPWT motions predicted by LWT and FNPT wave model presented for co-existing wind and wave condition in Figure 8.2.2 and Figure 8.2.3 showed an increase in positive mean for surge and pitch motion of the structure as compared to wave only condition. This is expected due to the presence of wind turbine thrust and its large moment resulting due to its higher elevation from the centre of gravity of the structure. The heave time series also showed further increased in negative mean due to an additional set-down effect resulting from the increase in positive surge and pitch motion of the structure.

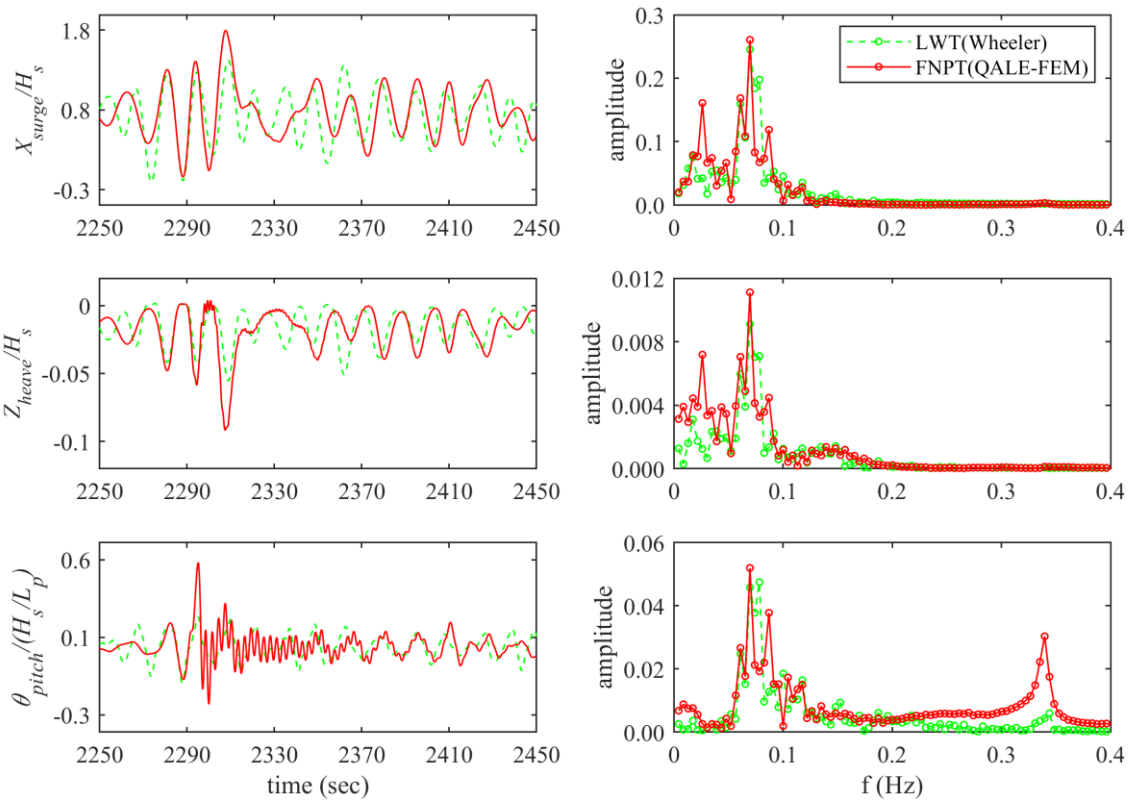

Figure 8.2.2 Time history and amplitude spectra of TLPWT motions under loading condition 'WW-O-21' in random wave group *BFI-0.84*

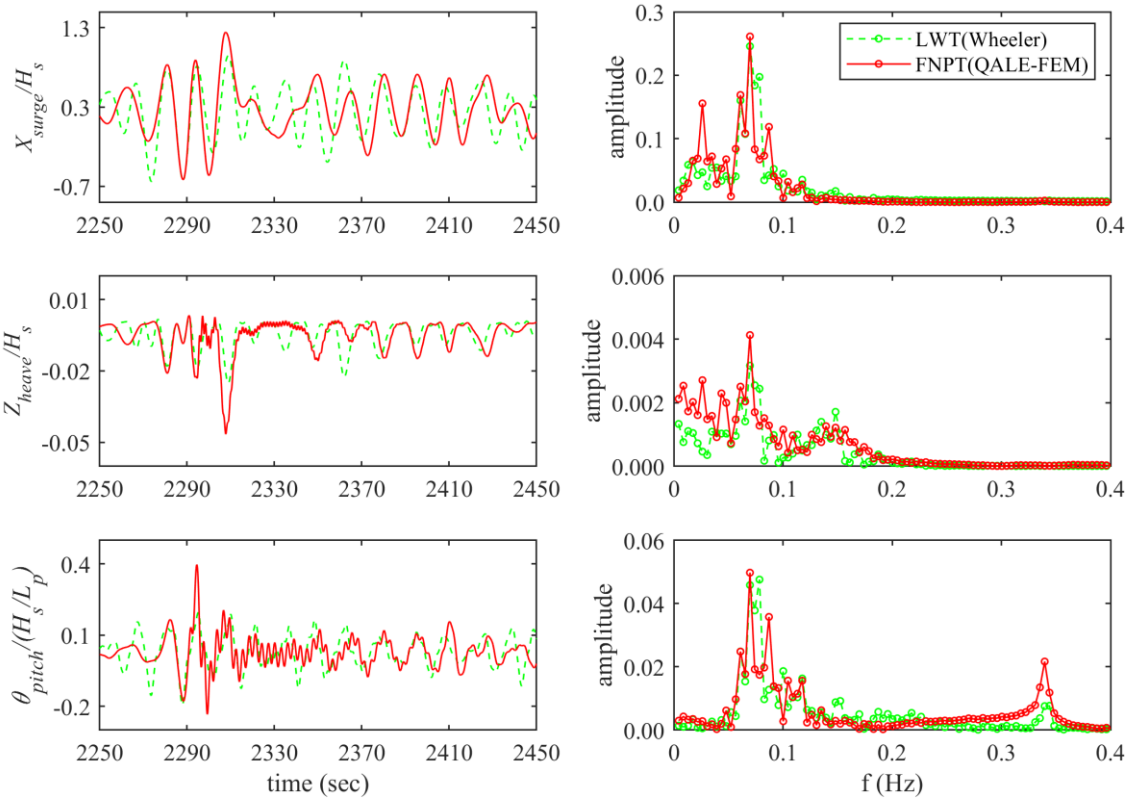

Figure 8.2.3 Time history and amplitude spectra of TLPWT motions under loading condition 'WW-P-30.5' in random wave group *BFI-0.84*

The predominant peak responses predicted by FNPT wave model for surge and pitch motions appeared at peak wave frequency (fw_p), and at surge (fn_{surge}) and pitch natural frequency (fn_{pitch}) of the concerned structure. The magnitude of motion amplitude at surge and pitch natural frequency is 58% and 62% of motion amplitude at peak wave frequency for loading condition WW-O-21 respectively. These predictions for WW-P-30.5 loading condition are noted as 60% and 53%. The reduction in motion amplitude at surge natural frequency with an increase in turbine loading is seen due to aerodynamic damping whereas, increase in motion amplitude at pitch natural frequency is seen due to high ringing and springing pitch motion resulting from the higher impact load. The predominant peak responses for heave motion appeared at peak wave frequency (fw_p), and at surge (fn_{surge}) natural frequency of the concerned structure reflecting set-down effect resulting from the positive surge motion. The LWT wave model also predicted these motion responses but underpredicted it for all the modes of motions. The range of motions (measured from minimum to maximum) in the surge, heave and pitch mode predicted by FNPT wave model are 1.21, 1.67 and 2.15 times higher than the motions predicted by LWT wave model for loading condition WW-O-21 respectively. For loading condition WW-P-30.5, FNPT wave model predicted motions in the surge, heave and pitch mode by 1.17, 1.53 and 1.62 times higher than the motions predicted by LWT wave model.

We can further study the effect of both the wave models on motion response of concerned structure by studying its statistical parameters such as maximum and skewness. The statistical parameters such as maximum and skewness of the motions predicted for combined wind and wave loading condition WW-O-21 and WW-P-30.5 are presented in Table 8.2.2.

Table 8.2.2 Normalised motion statistics for combined wind and wave loading condition

Load case	Motion	Maximum		Skewness	
		LWT	FNPT	LWT	FNPT
Wave + Wind (turbine operating)	Surge	1.402	1.823	-0.271	0.361
	Heave	0.055	0.095	-0.890	-2.191
	Pitch	0.270	0.608	-0.023	1.490
Wave + Wind (turbine parked)	Surge	0.948	1.261	-0.300	0.089
	Heave	0.025	0.048	-1.789	-3.358
	Pitch	0.196	0.406	-0.193	0.729

The trend shown in Table 8.2.2 is consistent with what is observed in Figure 8.2.2 and Figure 8.2.3. The maximum TLPWT motions and its skewness (which is an indicator of nonlinearity), in each mode are predicted higher by nonlinear FNPT wave model as compared to LWT wave model for both the loading condition. This is mainly seen due to the ability of FNPT based QALE-FEM in predicting the evolution of random wave group and generated steep wave surface elevation. However as seen in section 8.1, the evolution of wave group mainly depends upon

Benjamin Feir Index (BFI). Therefore, an effect of this parameter in predicting extreme wave surface and consequently TLPWT motions are studied next.

8.2.3 Effect of Benjamin Feir Index, BFI on motion response

To study the influence of BFI on motion response of TLPWT, a set of random wave groups having BFI of 0.25, 0.70, and 0.84 as detailed in Table 8.1.1 are generated. Loading condition of co-existing wave and wind with turbine in operating condition, (WW-O-21) is considered. A time history and corresponding amplitude spectra of normalised TLPWT motions in surge, heave and pitch modes are presented in Figure 8.2.4 through Figure 8.2.6 respectively.

The time history plots presented in Figure 8.2.4 and Figure 8.2.5 shows the effect of BFI on the translational surge and heave motion of TLPWT reflecting effect of extreme wave generated through nonlinear evolution of random wave group, as depicted in Figure 8.1.5. As elevation of extreme wave and difference in its predictions by both the wave models reduces with reduction in BFI, the differences in surge and heave motion also reducing. For high BFI of 0.7 and 0.84, a significant difference in surge and heave motion responses at surge natural frequency are seen. The high heave motion response at surge natural frequency is mainly seen due to set-down effect resulting from the positive surge motion.

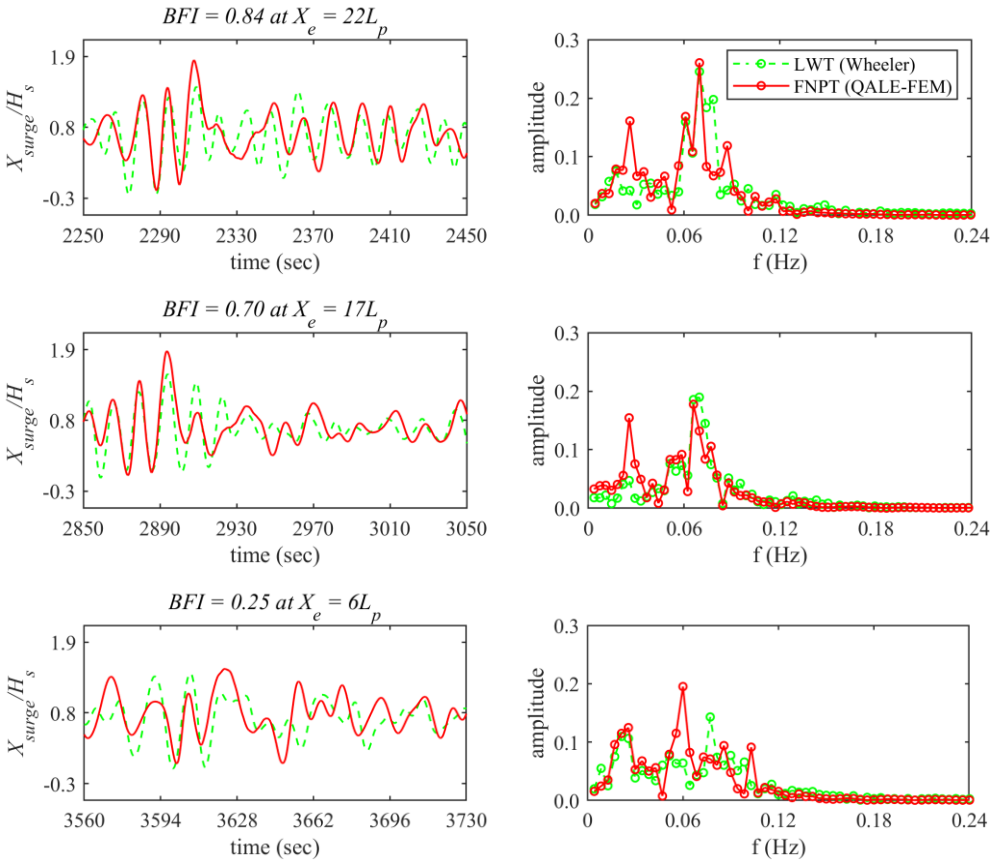

Figure 8.2.4 Time history and amplitude spectra of TLPWT surge motion for random wave group with *BFI-0.25, 0.70, and 0.84*

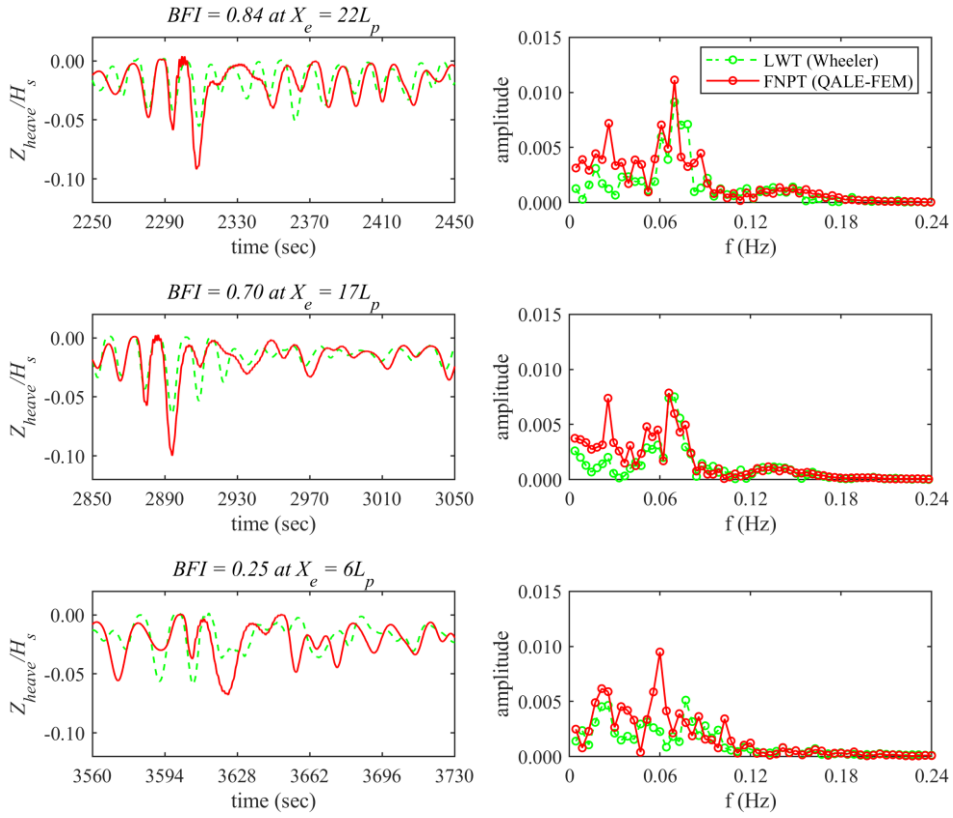

Figure 8.2.5 Time history and amplitude spectra of TLPWT heave motion for random wave group with *BFI-0.25, 0.70, and 0.84*

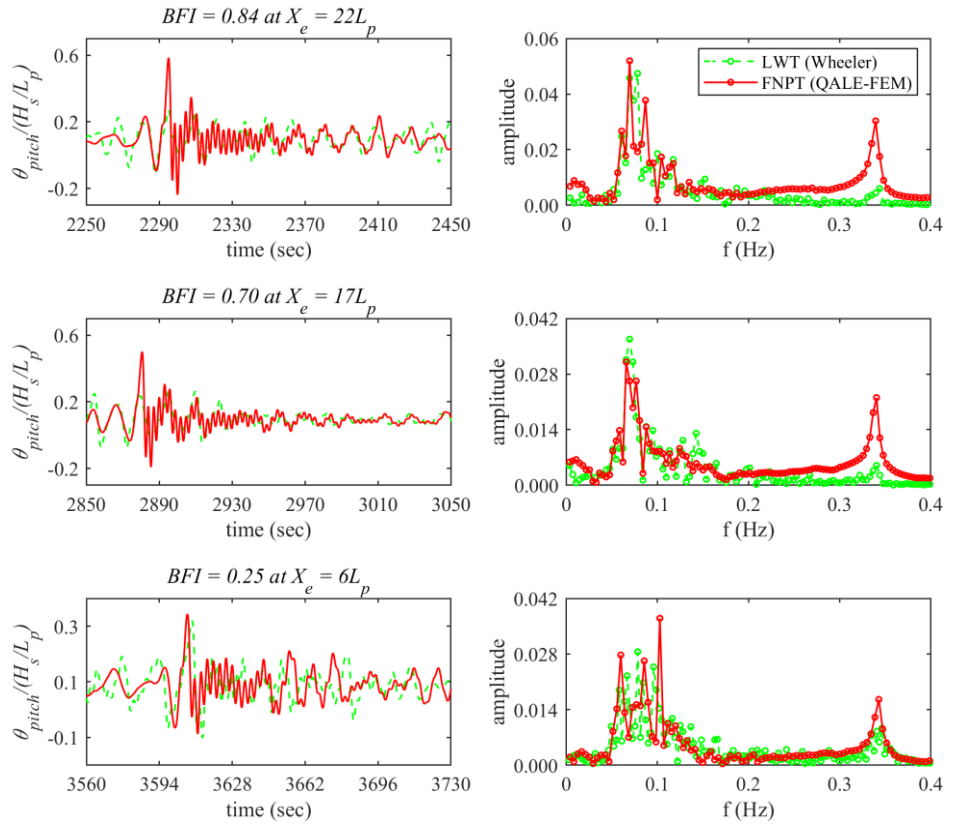

Figure 8.2.6 Time history and amplitude spectra of TLPWT pitch motion for random wave group with *BFI-0.25, 0.70, and 0.84*

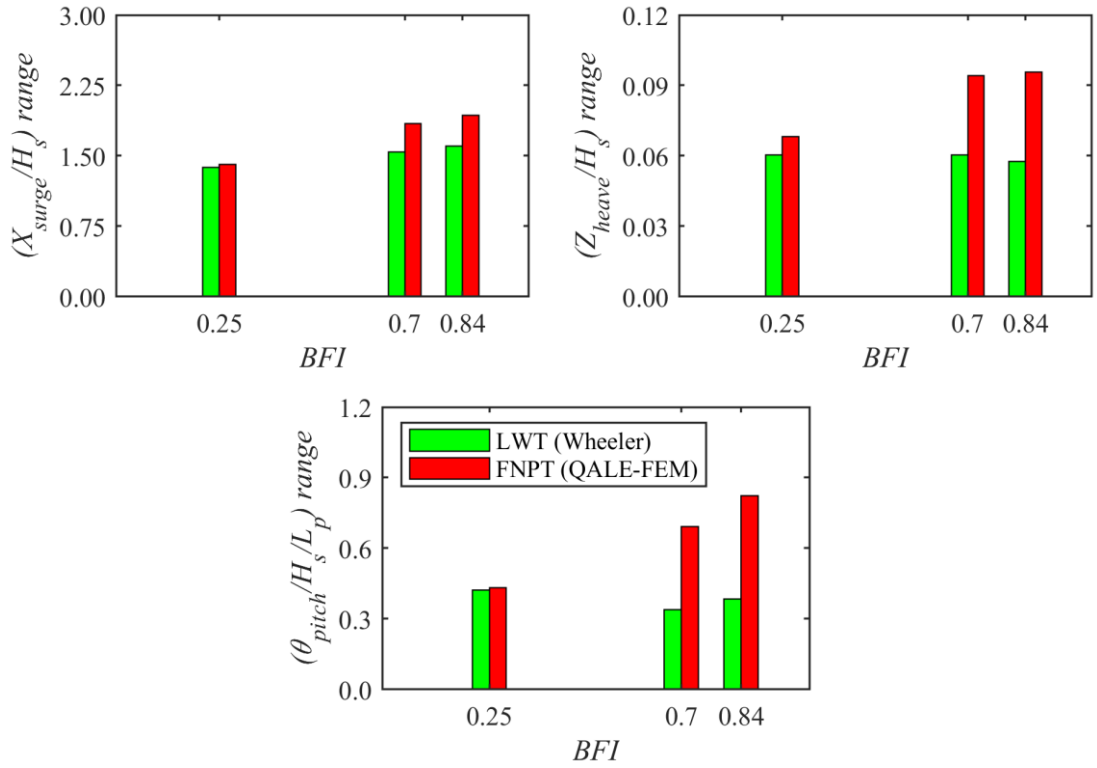

Figure 8.2.7 Range of normalised motions for random wave group with various *BFI*

The time history plots of rotational pitch motion presented in Figure 8.2.6 shows similar trend as seen for surge and heave motion. For low BFI of 0.25, the ringing and springing pitch motions predicted by both the wave models are seen nearly identical. As BFI increases, the ringing and springing pitch motion amplitudes and the difference in their predictions by LWT and FNPT wave models are also increasing.

The range of TLPWT motions in each mode are presented in Figure 8.2.7. The maximum difference in surge, heave and pitch motion predicted by linear, LWT and nonlinear, FNPT wave model are seen for high value of *BFI*, where nonlinear wave model predicted it 1.8, 1.9 and 2.1 times as compared to linear wave model respectively. For low value of *BFI* of 0.25, the differences in all the motions predicted by both the wave models are seen insignificant. This example demonstrates the importance of fully nonlinear wave model while analysing structure subjected to extreme wave in a random wave group having high *BFI* value.

8.3 Effect of nonlinear motion response on global performance of TLPWT

Global performance of a TLPWT is assessed by investigating the effect of its nonlinear motions on the response parameters associated with its components, i.e., wind turbine, tall supporting tower, platform hull and mooring lines. Key response parameters associated with each component of a floating wind turbine are chosen to investigate their predictions using nonlinear wave model, i.e. FNPT based QALE-FEM. The response parameters are further compared using the most widely used linear wave theory (LWT) with wheeler stretching to examine its range of applicability. The response parameters chosen for the wind turbine are blade airgap, turbine fore-

aft displacement, and thrust acting on it whereas, for a tower, the bending moment acting on it is chosen. For platform hull, the wave load acting in a predominant direction, i.e., the surge is chosen, and for station keeping system, tension in each mooring line is chosen for the investigation. All these parameters depend upon motion response of TLPWT.

As seen in previous section 8.2.3, the maximum differences in TLPWT motions predicted by both the wave models, i.e., LWT and FNPT are observed for random wave group with BFI of 0.84, hence this wave case is chosen for the investigation of global response parameters. Loading condition where wind and wave are co-existing with turbine in operating condition is considered for the investigation. Time history of response parameters associated with the wind turbine, tower, platform and mooring lines are presented in Figure 8.3.1 through Figure 8.3.4 respectively. Here airgap, thrust, and tension in each mooring line is normalised by their steady state values at simulation time $t = 0$, whereas turbine fore-aft displacement and surge wave force are normalised by significant wave height and platform buoyancy respectively. The tower bending moment is normalised by product of buoyancy and draft of the platform.

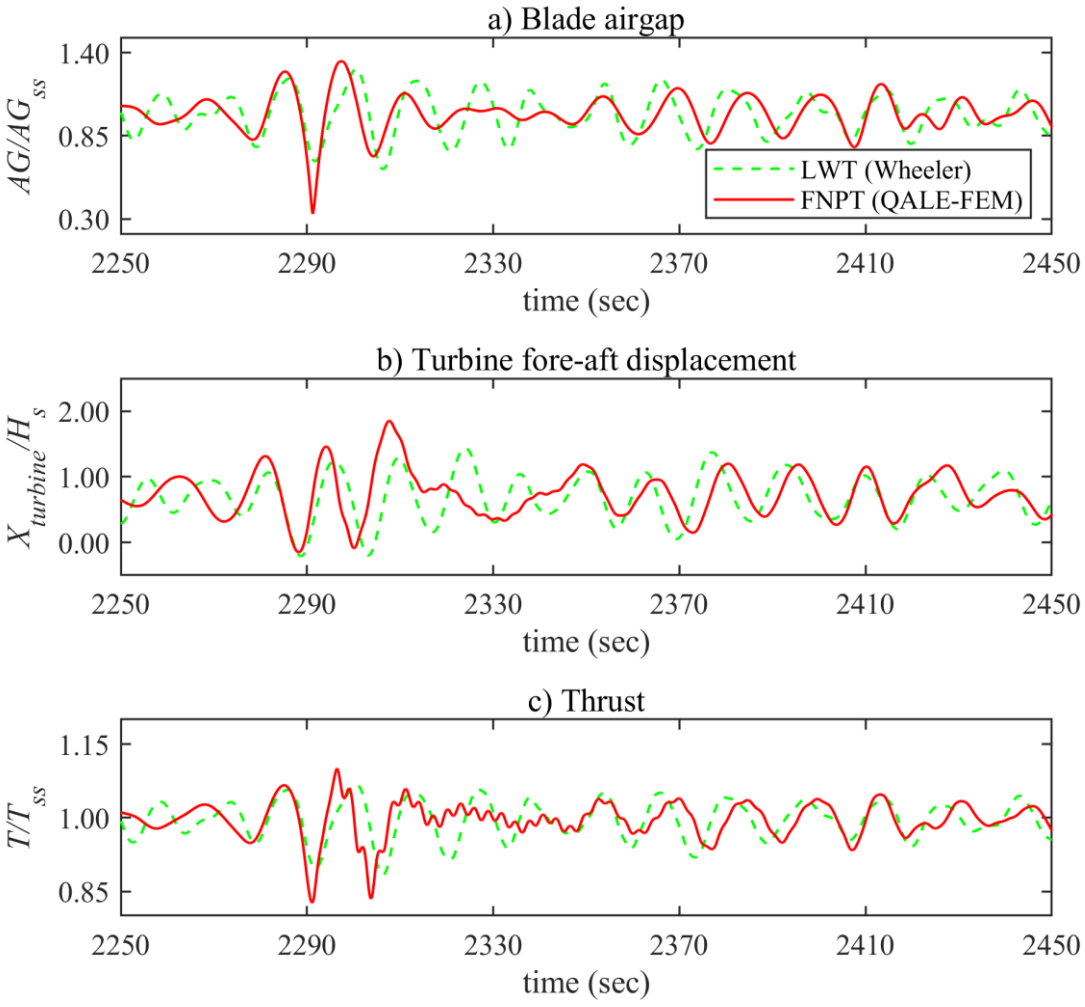

Figure 8.3.1 Time history of wind turbine response parameters for loading condition 'WW-O-21' in random wave group with BFI-0.84

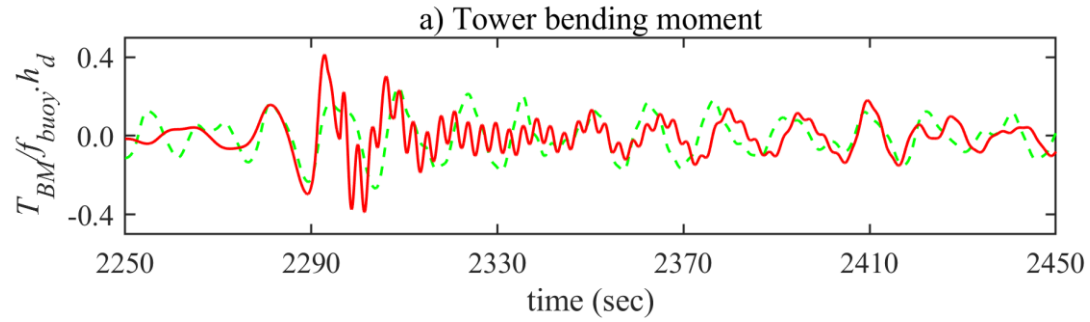

Figure 8.3.2 Time history of tower bending moment for loading condition 'WW-O-21' in random wave group with BFI-0.84

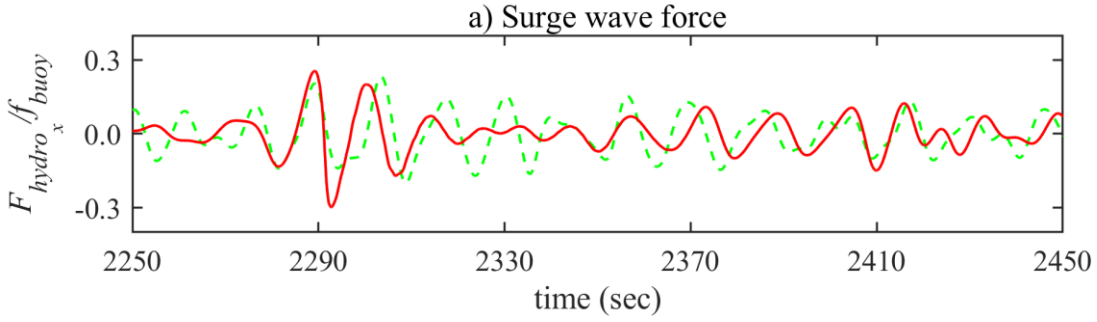

Figure 8.3.3 Time history of surge wave force for loading condition 'WW-O-21' in random wave group with BFI-0.84

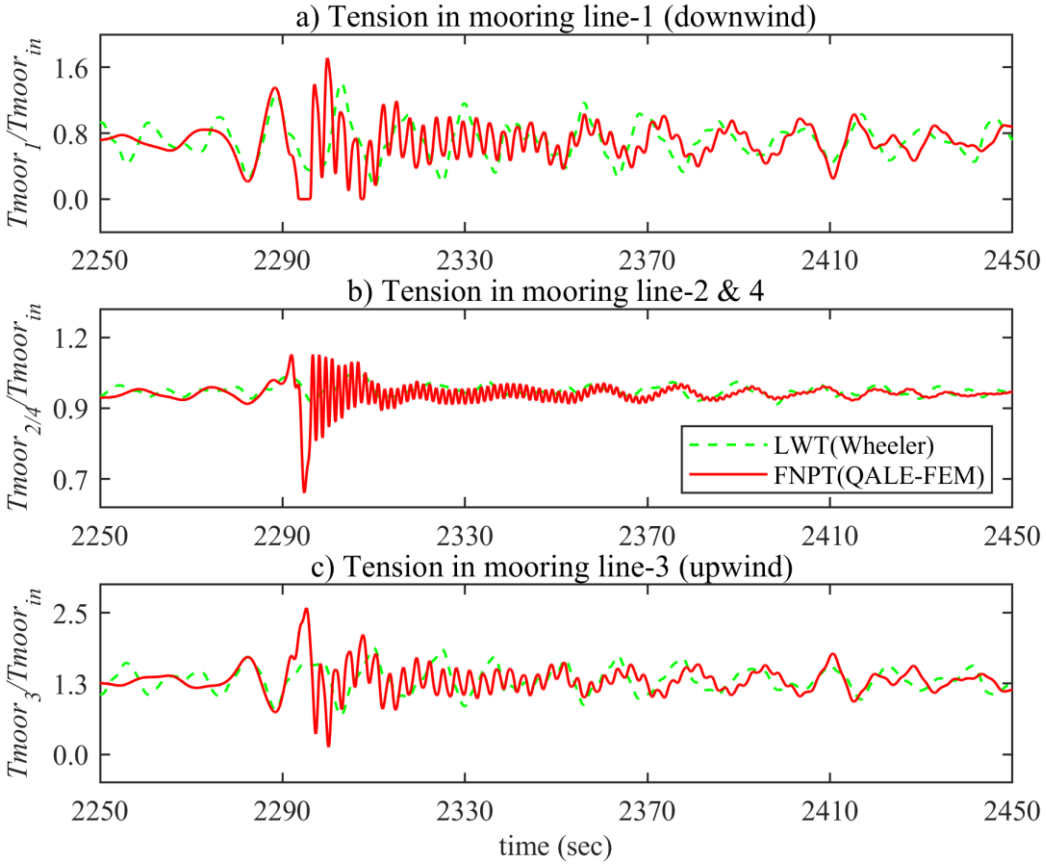

Figure 8.3.4 Time history of mooring line tensions for loading condition 'WW-O-21' in random wave group with BFI-0.84

The time history plots presented in Figure 8.3.1 through Figure 8.3.4 reflects the difference in TLPWT motions predicted by both LWT and FNPT wave models in predicting response parameters for the wind turbine, tower, platform, and mooring lines. All the response parameters are predicted higher by FNPT as compared to predictions by LWT wave models. This overprediction is mainly seen due to the ability of FNPT based QALE-FEM of predicting extreme wave generated through the evolution of random wave group which linear wave theory failed to predict. However, the difference in extreme wave surface and consequently TLPWT motions predicted by both the wave models are mainly controlled by BFI, as described in section 8.2.3. To investigate the influence of BFI on these response parameters, calculations and comparisons are carried out for all the response parameters for various BFI. Each parameter for varying BFI is presented in Figure 8.3.5.

It can be seen from Figure 8.3.5 that the maximum difference in response parameters predicted by both the wave models occurs for high BFI of 0.84. As the BFI reduces, the difference in response parameters predicted by both the wave models reduces. For BFI = 0.84, the nonlinear wave model (FNPT) predicted airgap, turbine displacement, and thrust higher by 85%, 22%, and 48% as compared to linear wave model respectively. For tower and platform, these predictions for bending moment and wave force are 60% and 30% higher respectively whereas, for mooring system, tensions predicted in mooring line 1, 2&4 and 3 are 20%, 10%, and 41% higher respectively. For lower value of BFI = 0.25, the differences in predictions of response parameters are less than 10% which is limiting characteristics of random wave group up to which linear wave theory failed to predict wave group evolution and consequently response of a concerned floating wind turbine.

The response parameters presented in Figure 8.3.5 were for wind speed of 21m/s which is corresponding to rated speed of turbine. However, to investigate the effect of extreme wave on the response parameters in more general cases, the calculation and comparisons are carried out for all the response parameters for various wind speeds while turbine is in operating and in the parked condition. Each parameter for various wind speeds are presented in Figure 8.3.6.

It can be seen from Figure 8.3.6 that all the response parameters are predicted higher by nonlinear wave model, FNPT as compared to linear wave model, LWT for all the wind speeds while turbine is in operation and in the parked condition. This example clearly demonstrates the importance of nonlinear wave model in predicting motion responses of a floating wind turbine and associated global responses of its components.

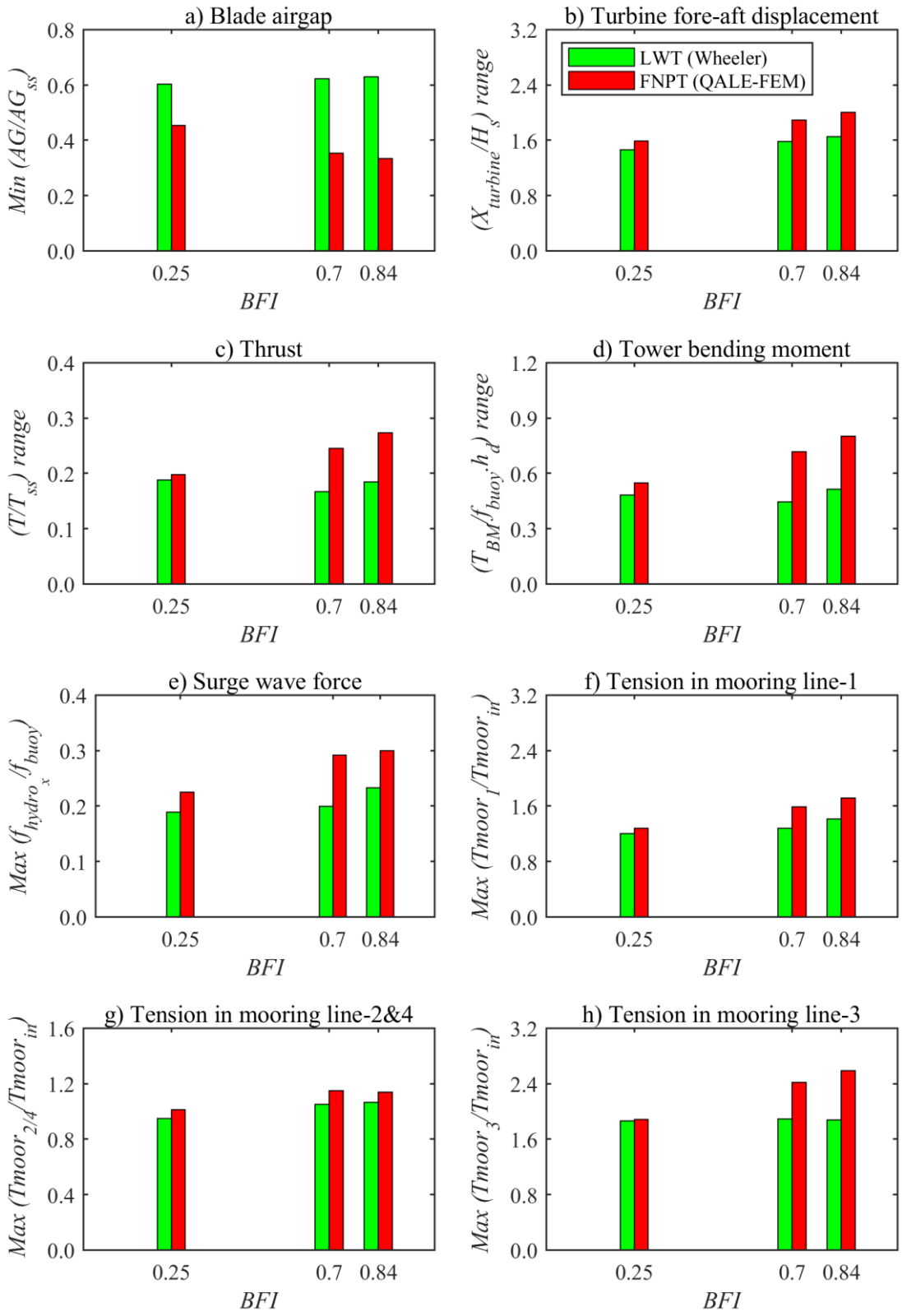

Figure 8.3.5 Response parameters for loading condition ‘WW-O-21’ in random wave group with various *BFI*

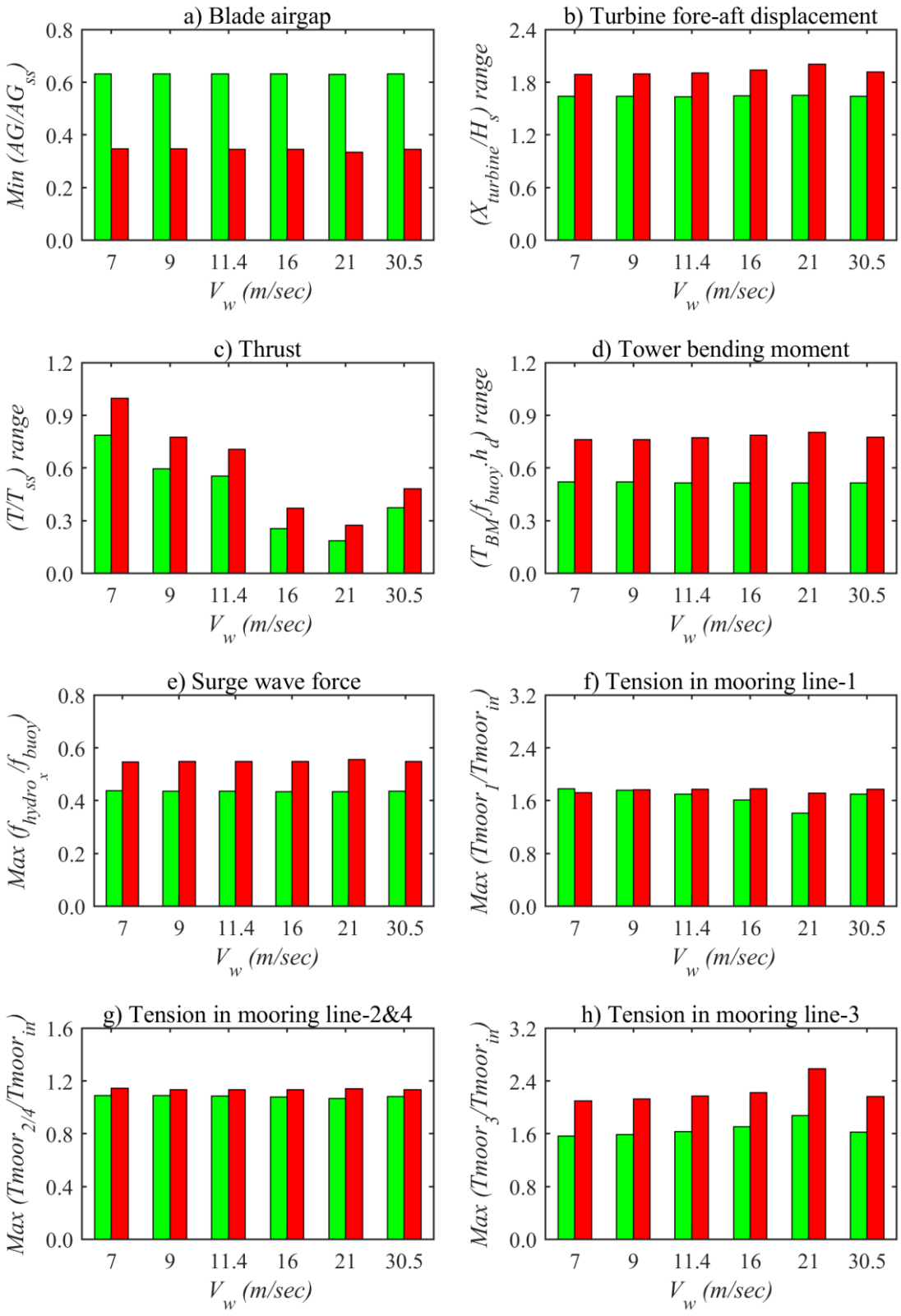

Figure 8.3.6 Response parameters for various wind speed V_w in random wave group with BFI-0.84

9 EFFECT OF NONLINEAR WAVE FORCES ON RESPONSE OF TLPWT

This chapter presents the effect of nonlinear wave forces on the response of a tension leg platform wind turbine (TLPWT). In the numerical model, wave forces acting on the members of the structure are evaluated using Rainey′s (1995) slender body approach (also known as non-diffracting potential theory, NDPT) where he modified the inertia term of the Morison′s (1950) equation by including axial divergence and centrifugal force terms acting on the member cross-section and by introducing an additional point forces at both the ends of the immersed members. This chapter investigates the effect of these additional nonlinear force terms on the overall response of a chosen structure (i.e., tension leg platform wind turbine). The first part of the chapter investigates nonlinear forces acting on the structure and latter parts of the chapter investigate its effect on the motion response and global performance of the structure under various wave conditions including resonance.

9.1 Investigation of nonlinear wave forces

The nonlinear wave forces acting on the structure are investigated by comparing the aforementioned nonlinear force terms derived by Rainey (1995) with the nonlinear force component from fluid acceleration present in the conventional Morrison (1950) equation. The nonlinear force component from fluid acceleration is obtained by subtracting the linear part from the total force obtained by integrating the whole acceleration term acting on the members of the structure at its instantaneous position. The linear part of the force from fluid acceleration is an integration of the temporal acceleration of fluid at the mean position of the structure. Figure 9.1.1 and Figure 9.1.2 presents the time histories of nonlinear forces and their moment components in surge and pitch direction acting on the vertical spar buoy and all the horizontal pontoons respectively when the structure is excited by a monochromatic wave with a period of 14sec having steepness (H/L_0) of 0.1 in a water depth of 100m. Here, term f_{fk-nl} represents the nonlinear force component from fluid acceleration, term f_{div} is axial divergence force, term f_{cf} is centrifugal force, and term f_{bp} is point force at the bottom end of the immersed member. Other force terms such as surface intersection force f_{int} and nonlinear added mass force f_{adm-nl} appearing in the wave force equation (3.3.27) are very small as compared to f_{fk-nl} and hence not considered here for the investigation. All the forces are normalised by platform buoyancy force f_{buoy} and moments are normalised by the product of platform buoyancy force f_{buoy} and draft h_d.

From the nonlinear force and moment comparison plot presented for vertical spar buoy in Figure 9.1.1, it can be seen that the amplitude of axial divergence force, f_{div} and its moment, m_{div} is about 20% and 35% of amplitude of nonlinear acceleration force f_{fk-nl} and its moment

m_{fk-nl} whereas amplitude of bottom point force, f_{bp} and its moment, m_{bp} is about 1.25 and 1.75 times of amplitude of f_{fk-nl} and moment m_{fk-nl} respectively.

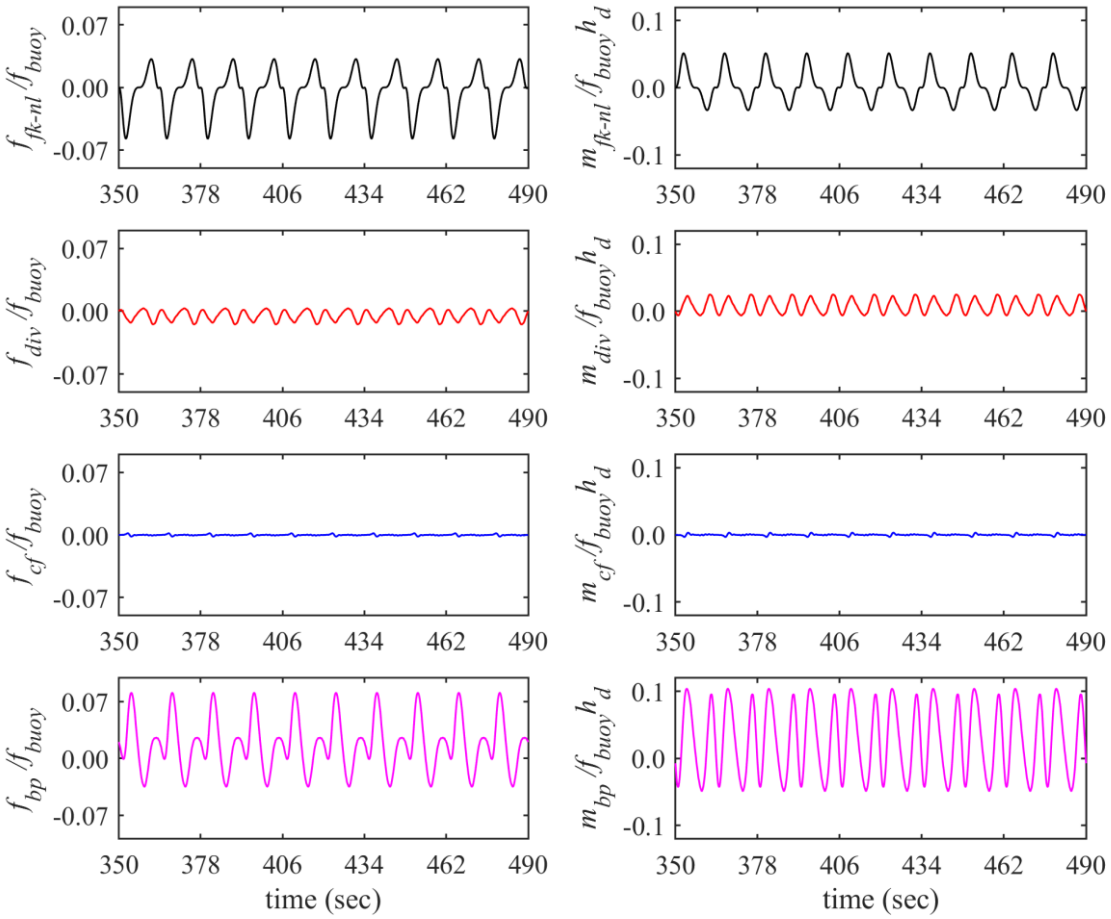

Figure 9.1.1 Nonlinear wave force and moment components in 'surge' and 'pitch' direction respectively for vertical spar buoy

The amplitude of centrifugal force f_{cf} and moment m_{cf} is seen very less (< 5%) as compared to a nonlinear acceleration force, f_{fk-nl} and moment m_{fk-nl} respectively. The bottom point force, f_{bp} and its moment component, m_{bp} dominate over all other nonlinear force and moment components. This is mainly observed due to the shallow draft of the structure where wave-induced water particle velocities (horizontal and vertical) are high and the bottom point force is a function of the product of both horizontal and vertical water particle velocity whereas axial divergence and centrifugal force terms are the functions of horizontal water particle velocity alone. In the past, Ma and Patel (2001) have investigated these nonlinear force components for the floating spar having deep draft, where they have shown this f_{bp} component as insignificant as compared to f_{div} and f_{cf}. This is observed due to the lower water particle velocity at the deep end of the spar.

The nonlinear force and moment comparison plot presented for the horizontal pontoons in Figure 9.1.2 shows that the amplitude of force and moment component due to axial divergence and bottom point force is significantly higher as compared to the amplitude of nonlinear

acceleration force and moment component. Here the force and moment component due to axial divergence term also dominates nonlinear force and moment due to acceleration. The lower value of acceleration force is mainly seen due to the deeper location of pontoons where horizontal water particle accelerations significantly reduces as compared to their high values near the sea surface.

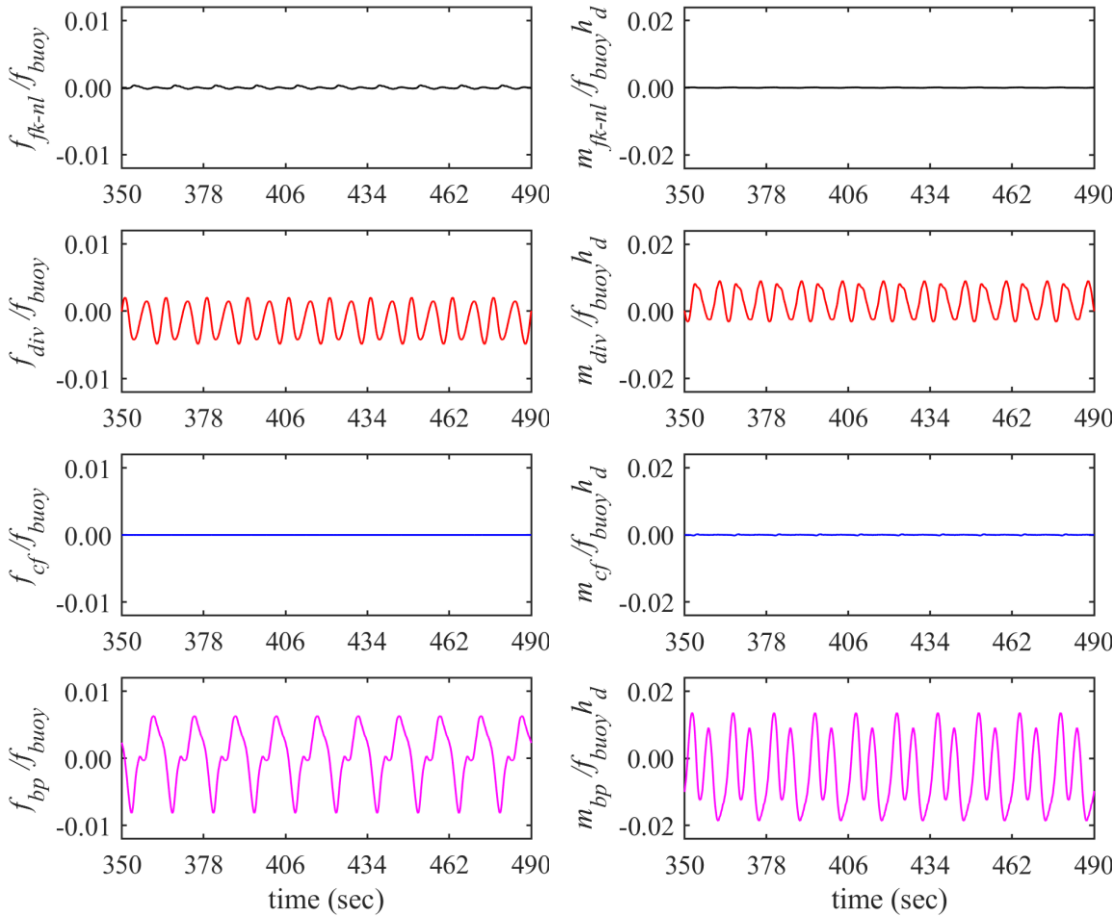

Figure 9.1.2 Nonlinear wave force and moment components in ‘surge’ and ‘pitch’ direction respectively for all the horizontal pontoons (combined)

This is one example which demonstrates the importance of the additional nonlinear force terms while evaluating wave forces acting on the floating structure. The nonlinear wave forces investigated here were for the wave only condition where the structure was at rest in its equilibrium position before the wave approaches. However, in practice floating wind turbines may have an offset and heel angle due to wind loads acting on the turbine and its supporting tower, therefore the nonlinear forces and moments due to waves are further examined under combined wind and wave loading condition while the turbine is operating at its rated wind speed and in the parked condition exposed to extreme wind speed. These two loading conditions are expected to cause maximum offset and heel angle for the floating wind turbines as explained in section 6.3.1.2.

9.1.1 Effect of platform offset and heel angle on the nonlinear wave forces

The nonlinear wave forces acting on the structure are further compared when the structure is having a maximum offset and heel angle. The maximum offset and heel angle for the concerned floating wind turbine found occurring when the turbine is operating at its rated wind speed of 21m/s as compared to parked condition with an extreme wind speed of 30.5m/s. Therefore, an effect of platform offset and heel angle on the nonlinear wave forces are investigated for the combined loading condition of wave and wind with turbine operating at its rated wind speed of 21m/s. The case presented here uses an incident monochromatic wave with a period of 14sec having steepness (H/L_0) of 0.1 in a water depth of 100m. The time history of normalised nonlinear forces and their moment components in surge and pitch direction are presented in Figure 9.1.3 and Figure 9.1.4 for vertical spar buoy and horizontal pontoons respectively.

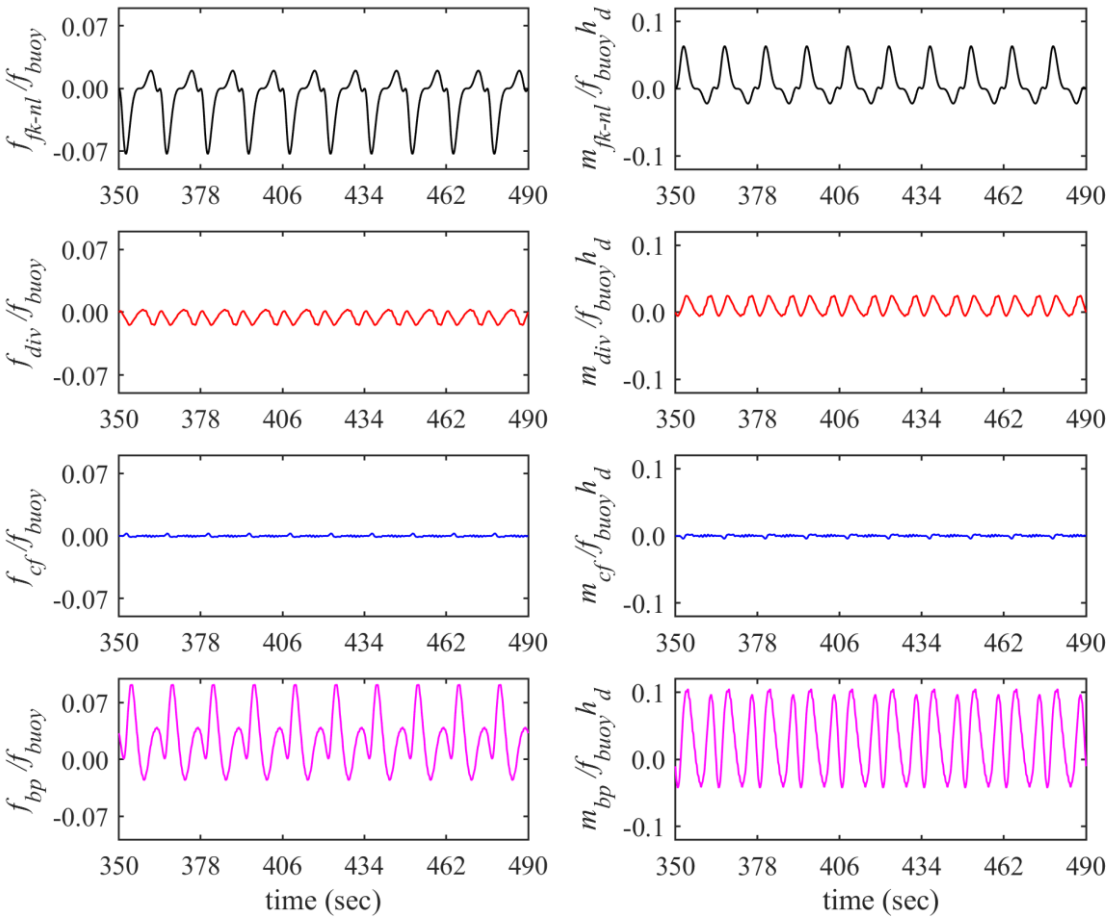

Figure 9.1.3 Nonlinear wave force and moment components in 'surge' and 'pitch' direction respectively for vertical spar buoy

The time history plots presented for co-existing wind and wave condition in Figure 9.1.3 and Figure 9.1.4 showed an increase in mean for surge force and pitch moment acting on the platform as compared to wave only condition. A slight increase in force and moment amplitudes are also seen but the differences are noted less than 10% for the chosen structure. Hence, the relative values of these additional nonlinear force components, f_{div}, f_{cf}, and f_{bp} as compared to f_{fk-nl}

clearly depends upon the wave parameters for any given structure. To investigate the behaviour of these nonlinear forces in a more general case, the calculations and comparisons have been carried out for various wave periods with their extreme amplitudes. The incident waves detailed in Table 6.1.1 are used in the calculations. To usefully compare the nonlinear forces for various extreme regular wave cases, the range of normalised nonlinear forces and their moment components are measured from minimum to maximum during steady part of their time histories. Figure 9.1.5 and Figure 9.1.6 presents the various nondimensionalised nonlinear components of the surge force and pitch moments corresponding to different wave periods for vertical spar buoy and horizontal pontoons respectively.

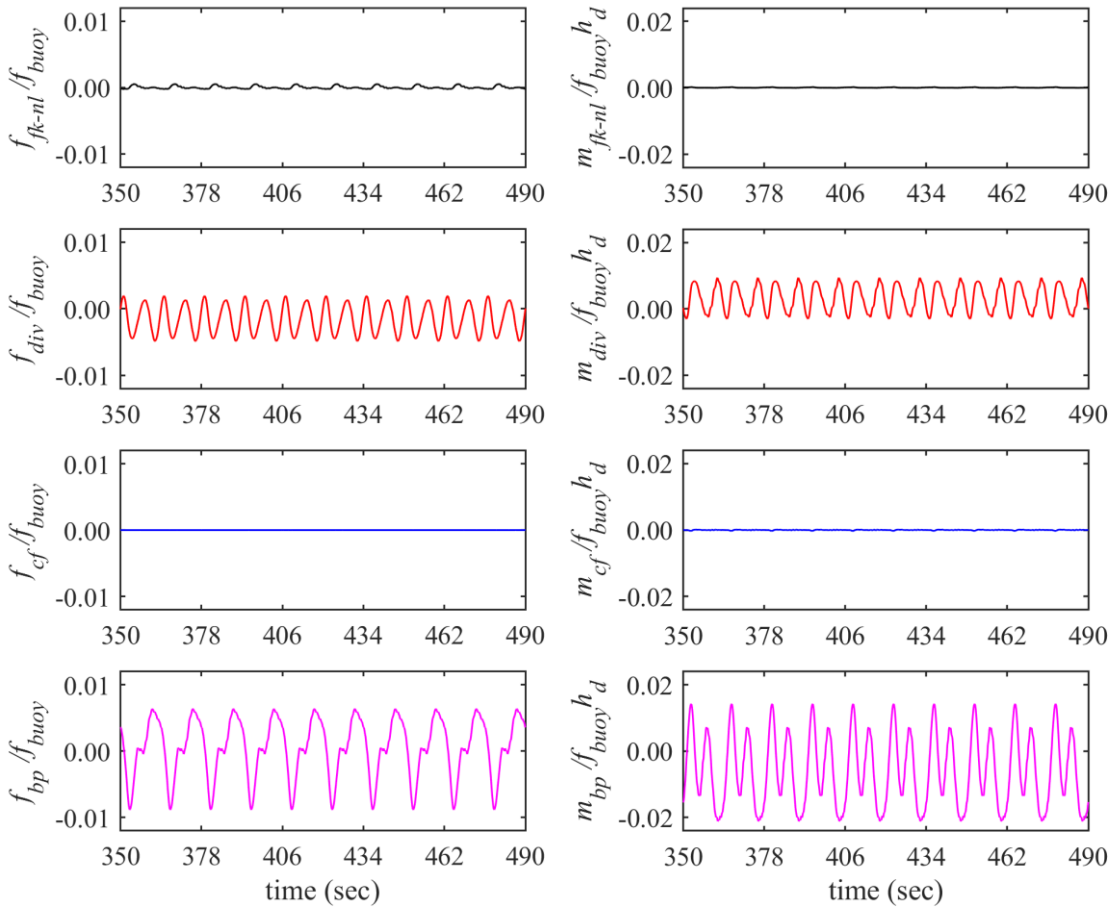

Figure 9.1.4 Nonlinear wave force and moment components in 'surge' and 'pitch' direction respectively for all the pontoons (combined)

From the result plots presented for vertical spar buoy in Figure 9.1.5, it can be seen that for the shorter range of periods, f_{fk-nl} dominates over all other nonlinear surge force components; and f_{div} is smaller than f_{fk-nl} but evidently larger than the other two. With an increase in wave period, f_{bp} dominates f_{fk-nl} and other nonlinear terms f_{div} and f_{cf}. The force component f_{fk-nl} is smaller than f_{bp} but evidently dominates the other two components f_{div} and f_{cf}. A similar trend is noticed for pitch moment components. The result plots presented for horizontal pontoons in Figure 9.1.6 shows that the nonlinear surge force component f_{bp} dominates f_{fk-nl},

f_{div}, and f_{cf} for the whole range of periods. f_{div} is smaller than f_{bp} but evidently dominates the other two. Similar behaviour has been noticed in the case of pitch moments for the pontoons as well.

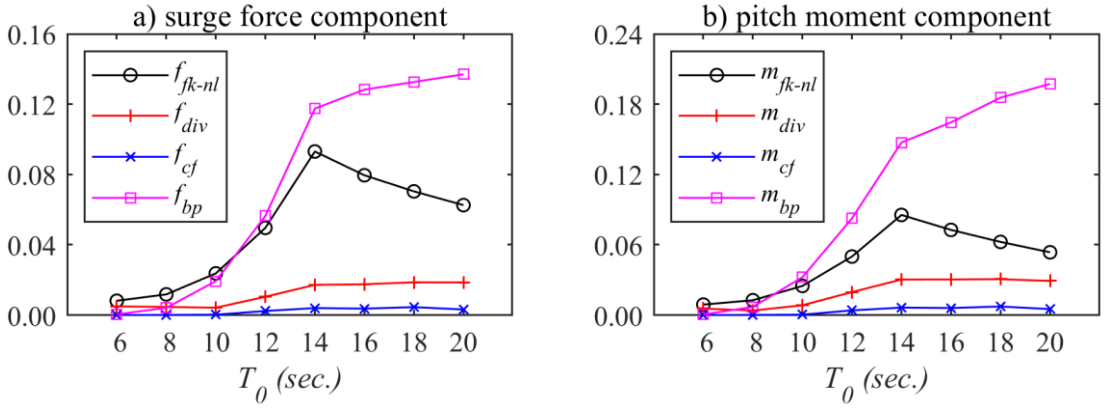

Figure 9.1.5 Normalised nonlinear wave force and moment components in 'surge' and 'pitch' direction respectively under various wave periods, T_0 for vertical spar buoy

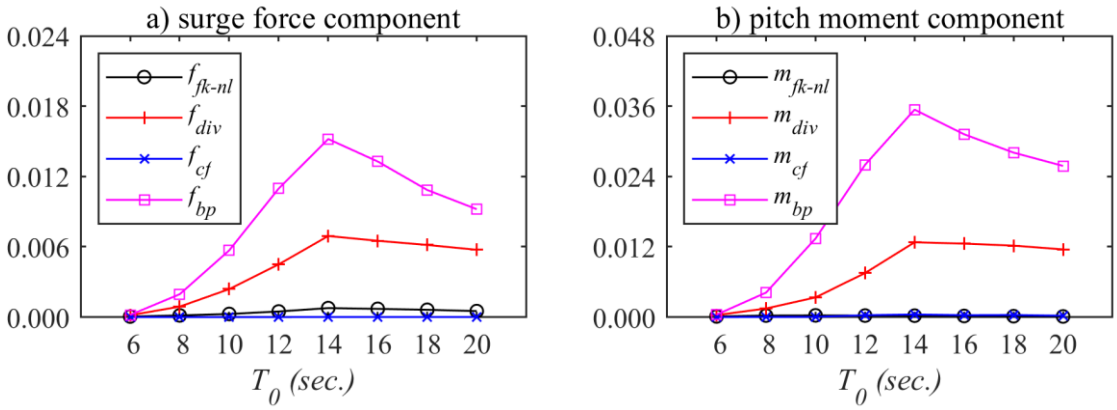

Figure 9.1.6 Normalised nonlinear wave force and moment components in 'surge' and 'pitch' direction respectively under various wave periods, T_0 for horizontal pontoons

It can be seen that the importance of each nonlinear wave force component largely depends on the wave period and the axial divergence and bottom point forces may not always be negligible as compared to the nonlinear component of acceleration force.

9.1.2 Effect of wave steepness on the nonlinear wave forces

The effect of wave steepness on nonlinear wave forces is examined by comparing them for waves with various steepness′s. Figure 9.1.7 and Figure 9.1.8 presents the range of non-dimensionalized nonlinear components of the surge force and pitch moments corresponding to different wave steepness′s for vertical spar buoy and horizontal pontoons respectively. Here wind speed is chosen as 21m/s whereas wave period as 14sec and the water depth as 100m.

Figure 9.1.7 and Figure 9.1.8 shows a similar behaviour of nonlinear wave forces as seen in Figure 9.1.5 and Figure 9.1.6. For vertical spar buoy, the dominance of nonlinear wave forces and their moment components are seen in the order of f_{bp}, f_{fk-nl}, f_{div} and f_{cf} whereas for

horizontal pontoons dominance order is seen as f_{bp}, f_{div}, f_{fk-nl}, and f_{cf}. All the nonlinear wave force components and the differences among them increases with the increase in wave steepness. Continuous domination of the bottom point force and its moment component is seen over other nonlinear force and moment components. Similar observations are made for the force and moment components for the horizontal pontoons.

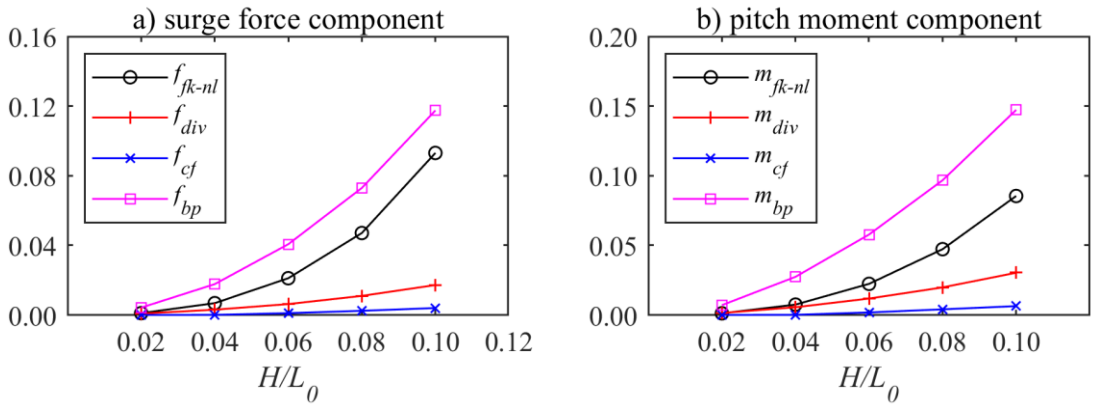

Figure 9.1.7 Normalised nonlinear wave force and moment components in 'surge' and 'pitch' direction respectively under waves with various steepness (H/L_0) for vertical spar buoy

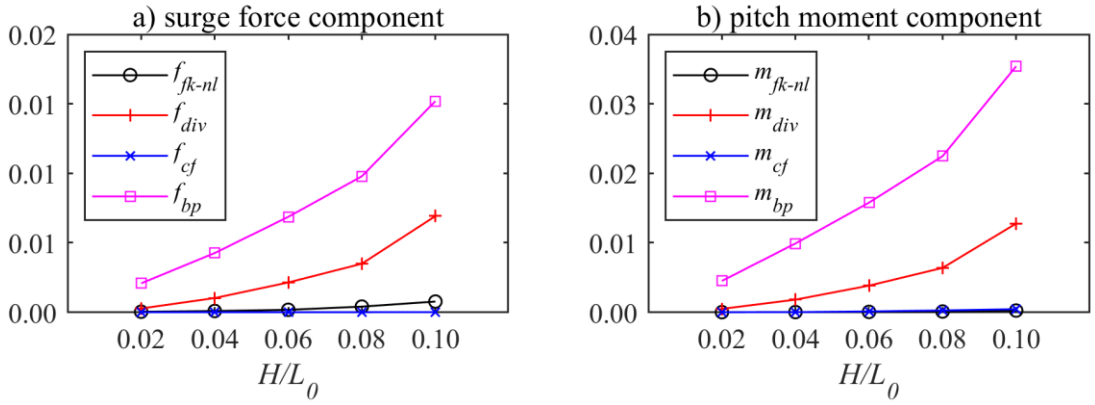

Figure 9.1.8 Normalised nonlinear wave force and moment components in 'surge' and 'pitch' direction respectively under waves with various steepness (H/L_0) for horizontal pontoons

9.1.3 Effect of water depth on the nonlinear wave forces

As chosen floating wind turbine is the most favourable structure in the water depth of 100m–200m, the effect of water depth on the nonlinear wave forces are examined by comparing them for the structure located in various water depths. No changes in platform configuration were implemented other than extending tendon lengths. However, there was a decrease in tendon stiffness due to increase in its length and that may affect the platform motions and the corresponding nonlinear forces and their moment components.

Figure 9.1.9 and Figure 9.1.10 presents the range of non-dimensionalized nonlinear components of the surge force and pitch moments corresponding to different water depths for

vertical spar buoy and horizontal pontoons respectively. Here wind speed is chosen as 21m/s whereas the period of a wave is chosen as 14sec with its steepness (H/L_0) of 0.1.

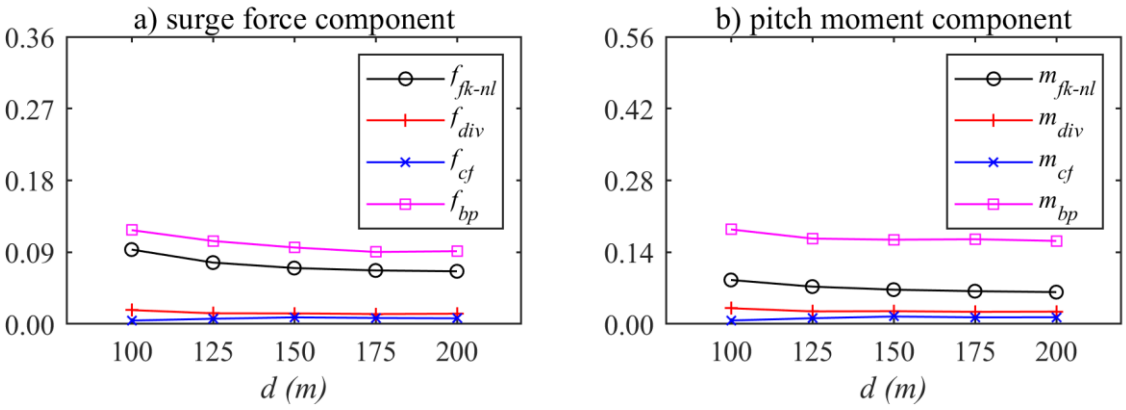

Figure 9.1.9 Normalised nonlinear wave force and moment components in 'surge' and 'pitch' direction respectively under waves in various water depths, d for vertical spar

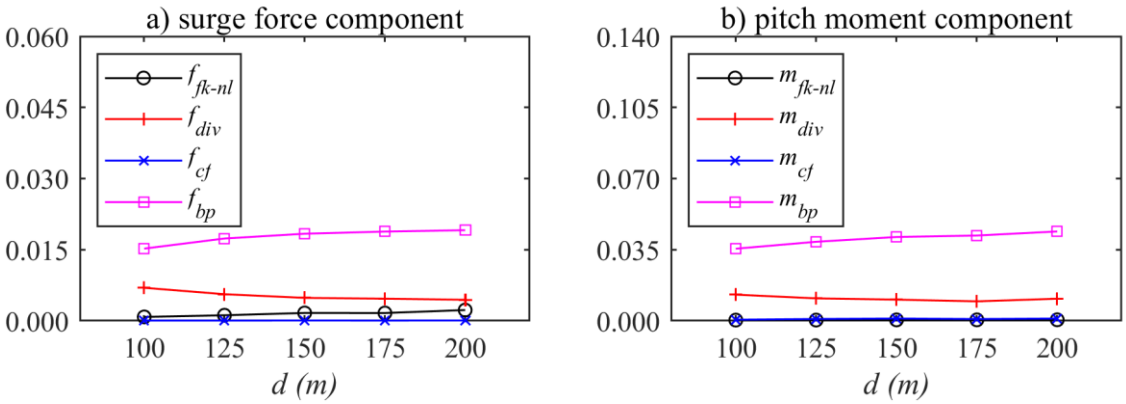

Figure 9.1.10 Normalised nonlinear wave force and moment components in 'surge' and 'pitch' direction respectively under waves in various water depths, d for horizontal pontoons

Figure 9.1.9 and Figure 9.1.10 shows a similar behaviour of nonlinear forces as seen in Figure 9.1.7 and Figure 9.1.8. Continuous dominance of bottom point force and its moment component is seen over other terms for both vertical spar buoy and horizontal pontoons in all the analysed water depths. For vertical spar buoy, slight decrease in force and moment components are seen with the increase in water depth but clear differences among them do exist. This set of results demonstrates that the water depth has a small effect on the nonlinear forces and should be considered while evaluating wave forces acting on the structure in deeper water depths too.

The results presented in this section demonstrates that the magnitude of nonlinear force components, f_{div} and f_{bp} derived by Rainey are significant as compared to the nonlinear force components due to flow acceleration, f_{fk-nl} present in the conventional Morison′s equation. It is also seen that the magnitude of these nonlinear force components is strongly dependent on the wave conditions. These force components are small in some circumstances but cannot be ignored in general. The inclusion of these components in the wave force calculations does not cause any additional computational penalty which makes it worthwhile using for simulation purpose.

9.2 Effect of nonlinear wave forces on motion response of TLPWT

The wave induced motion responses of a chosen tension-leg-platform wind turbine generally categorise as first order motions at wave frequency, low-frequency or slowly varying surge, sway, and yaw motions and high-frequency ringing and springing roll, heave and pitch motions. An effect of nonlinear wave forces in predicting such motion responses are examined next by comparing them without considering each nonlinear force term.

9.2.1 First order response

An effect of nonlinear wave forces on the first order motion response of the chosen TLPWT is examined by comparing motions without considering each nonlinear force term. As seen in section 9.1.1 maximum amplitude of nonlinear wave force and moment components are seen when the platform had maximum offset and heel angle. Therefore, loading condition with co-existing wind and wave with the turbine in operating condition at its rated wind speed of 21m/s is chosen to investigate the effect of nonlinear wave forces on the motion responses of the structure. The case presented here uses an incident wave with a period of 14sec having steepness of 0.1 in a water depth of 100m. Time history and amplitude spectra of motion response of the structure are presented in Figure 9.2.1 and Figure 9.2.2 without axial divergence f_{div} and bottom point force f_{bp} respectively. Here, the surge and heave motions are normalised by input wave amplitude, amp whereas pitch motion is normalised by input wave steepness, H/L_0.

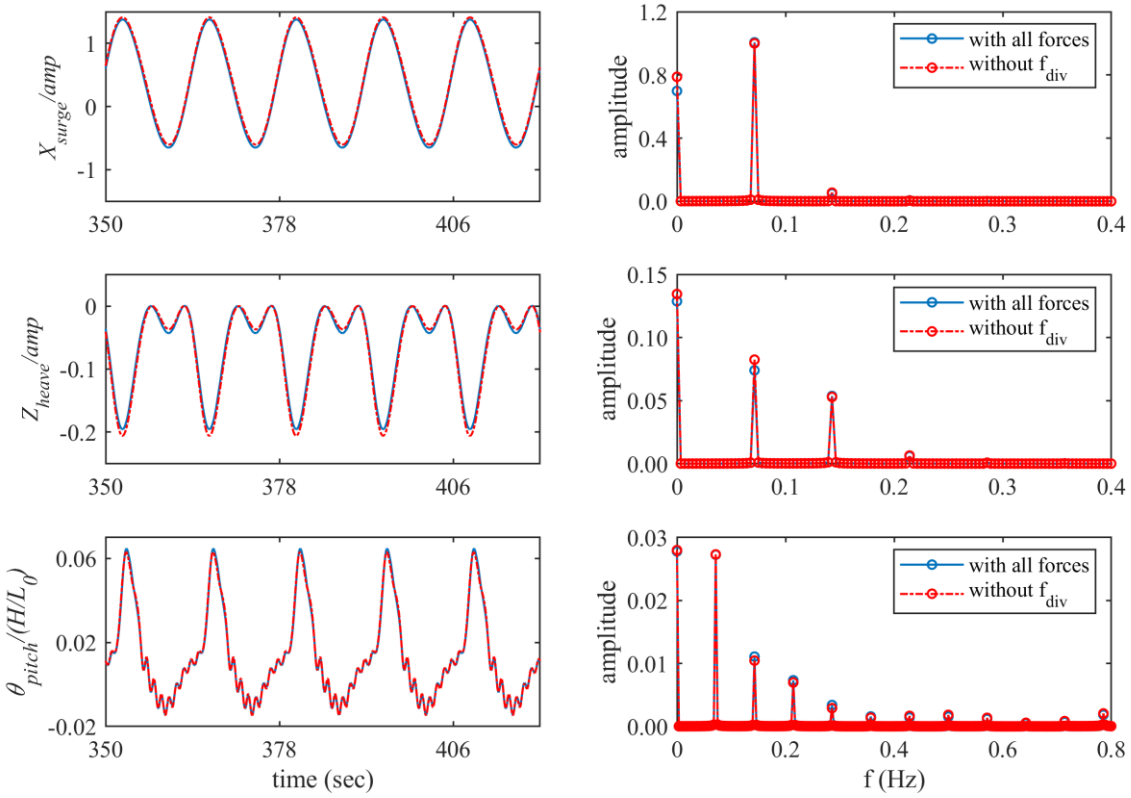

Figure 9.2.1 Time history and amplitude spectra of motion response of TLPWT without axial divergence force, f_{div} and its moment m_{div}

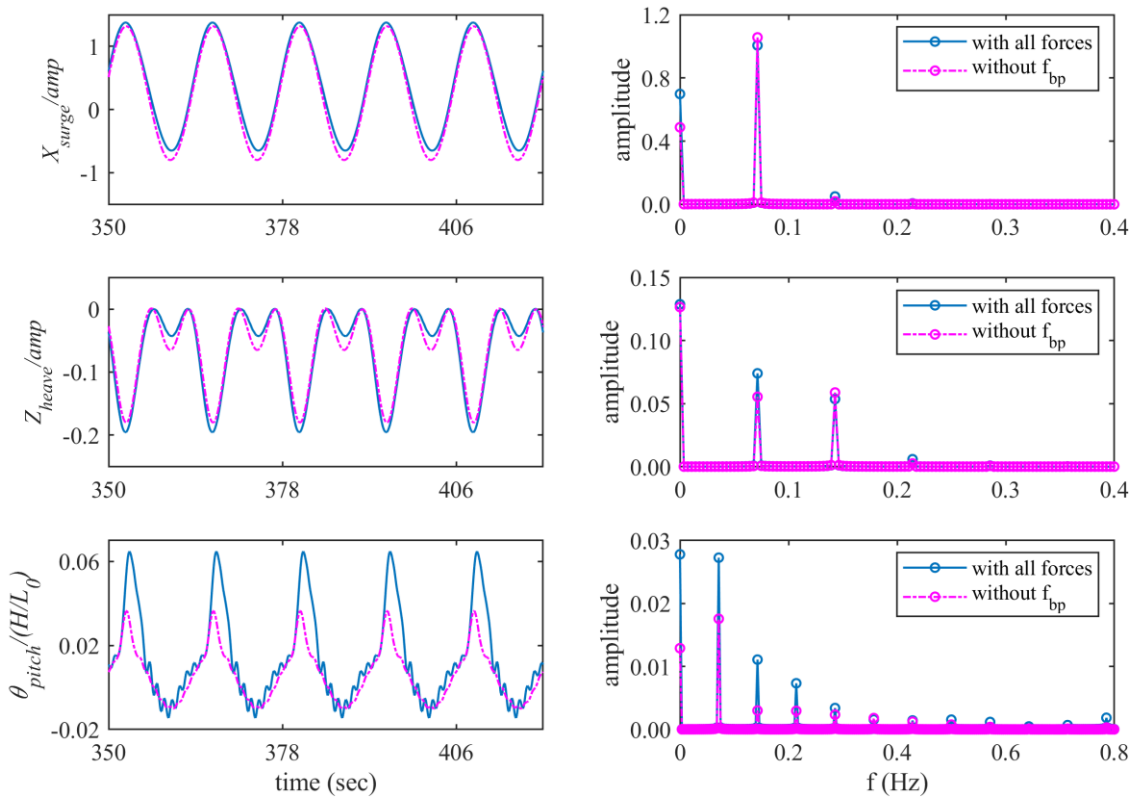

Figure 9.2.2 Time history and amplitude spectra of motion response of TLPWT without bottom point force, f_{bp} and its moment m_{bp}

It can be seen from the time history plots presented in Figure 9.2.1 that the motions of the platform are very similar when axial divergence force and its moment is not included in the wave loads, however, the exclusion of bottom point force and its moment has shown significant difference in pitch motions presented in Figure 9.2.2. The amplitude spectra of pitch motion presented in Figure 9.2.2 shows underprediction of pitch amplitude at input wave frequency and at multiple harmonics of input wave frequency. The underprediction of overall pitch motion without bottom point force is noticed as 55%. This significant difference in pitch motion is mainly seen due to high pitching moment resulting from the dominant nonlinear bottom point force and its high lever arm (location of force from the platform's centre of gravity). The differences are also seen for the surge and heave motions but less than 15%.

To investigate the effect of bottom point force in more general cases, the calculations and comparisons have been carried out for the platform pitch motion under various wave cases. The cases considered are waves with various periods having extreme amplitude, waves with various steepness and waves in various water depths. The range of steady state normalised platform pitch motion with and without including f_{div} and f_{bp} for various extreme waves are presented in Figure 9.2.3 whereas for varying steepness and water depth are presented in Figure 9.2.4 and Figure 9.2.5 respectively.

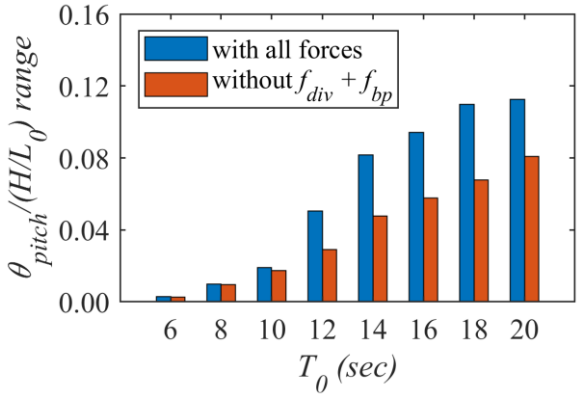

Figure 9.2.3 Range of normalised pitch motion for various wave periods

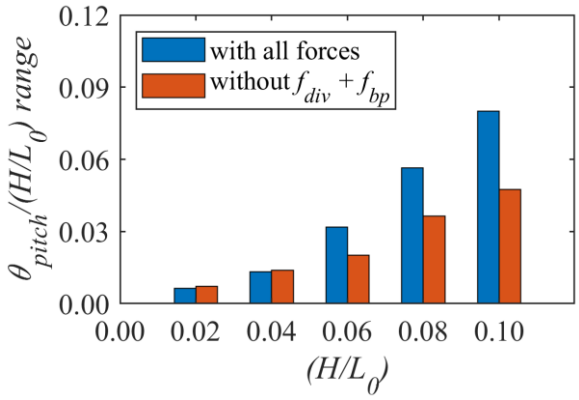

Figure 9.2.4 Range of normalised pitch motion for various wave steepness

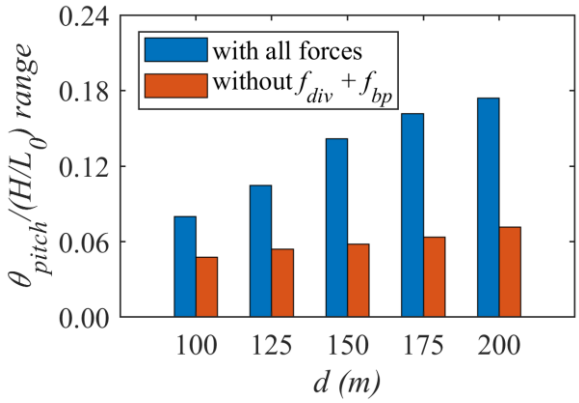

Figure 9.2.5 Range of normalised pitch motion for various water depths

It can be seen from the Figure 9.2.3 that the difference in normalised pitch motion with and without considering nonlinear force component f_{div} and f_{bp} are significant for larger wave periods with maximum differences are noticed for the steep wave with a period of 14sec and thereon differences remain nearly equal. This increase in differences in pitch motions with an increase in wave period clearly reflects the behaviour of bottom point force depicted in Figure 9.1.5 for vertical spar buoy. A similar trend is seen for platform pitch motion presented in Figure 9.2.4 for varying wave steepness. The difference in pitch motion with and without considering nonlinear force component f_{div} and f_{bp} are increasing with an increase in wave steepness reflecting the behaviour of bottom point force depicted in Figure 9.1.7. As the dominance of

bottom point force over other nonlinear force terms increases with an increase in wave steepness, the differences in pitch motions also increase exponentially. However, the normalised platform pitch motions presented in Figure 9.2.5 are contradictory to the behaviour of nonlinear forces depicted in Figure 9.1.9. The difference in pitch motion with and without considering nonlinear force terms f_{div} and f_{bp} are seen increasing with an increase in water depth though nonlinear forces f_{div} and f_{bp} are seen reducing with an increase in water depth. This behaviour is mainly seen due to the reduction of mooring stiffness with an increase in water depth. As per Figure 9.1.9, the reduction in nonlinear forces and its moment is seen less with an increase in water depth but the differences among them are nearly uniform. These uniform differences in nonlinear forces combined with the reduction in mooring stiffness yield higher pitch motions. This example demonstrates that the effect of nonlinear forces on motion response of the floating platform not only depend on wave parameters but also on its mooring stiffness. Hence, they should be included while evaluating wave forces acting on the floating platform in deep water depth too.

Although bottom point force dominated over other nonlinear force components for both vertical spar buoy and horizontal pontoons, their effect on the translational motions of the structure such as surge and heave are not seen significant for regular waves with predominant periods ranging from 6 to 20sec. However, there are also components of nonlinear forces that arise at frequencies given by the difference in frequency components in the incident wave spectrum. Effect of these nonlinear forces at the difference in frequencies can be significant because they can excite lateral translational motions such as surge/sway motion of the structure in question which tends to have relatively long natural period compared to predominant wave periods. This lateral translational motion responses at resonance, when excited by the difference in wave frequency components, is the most critical design case for TLP mooring system. The resonance response and the consequential mooring loads limited by damping makes this a particularly important parameter requiring accurate estimation in the design case. The effect of nonlinear wave forces on the surge motion of the structure at the difference in frequencies are examined next by considering bichromatic incident waves.

9.2.2 Low-frequency resonance response

Low-frequency resonance response (also referred as slowly varying motion) of a tension- leg-platform wind turbine is mainly induced by nonlinear components present in the hydrodynamic interaction of such structures with the extreme ocean waves. The effect of nonlinear wave forces in predicting such low-frequency resonance responses of the chosen floating wind turbine is examined by comparing motions without considering nonlinear force terms, f_{div} and f_{bp} and their moment components m_{div} and m_{bp}. Here the structure is excited by two monochromatic waves with amplitude and periods expressed by (amp_1, amp_2) and (T_1, T_2) respectively, in a water depth of 200m. In the case presented here wave parameters are taken as $amp_1 = amp_2 =$

5m and $T_1 = 11.320$s and $T_2 = 16.217$s. The period corresponding to the difference in frequency of these two waves is about 37.48s, which is close to the natural period of the surge motion with the tethered moorings providing system stiffness. The wind speed, $V_w = 21$m/s corresponding to rated speed of turbine is considered.

To investigate the nonlinear effect of the resultant wave forces, Fourier analysis on the time history of the surge motion is performed to obtain the slowly varying surge motion (corresponding to the difference in wave frequencies). The result is presented in Figure 9.2.6 where legend 'without f_{div}' denotes that the surge motion is calculated by wave forces that exclude axial divergence force term f_{div}. A similar meaning is used for 'without f_{bp}' and without '$f_{div} + f_{bp}$' term.

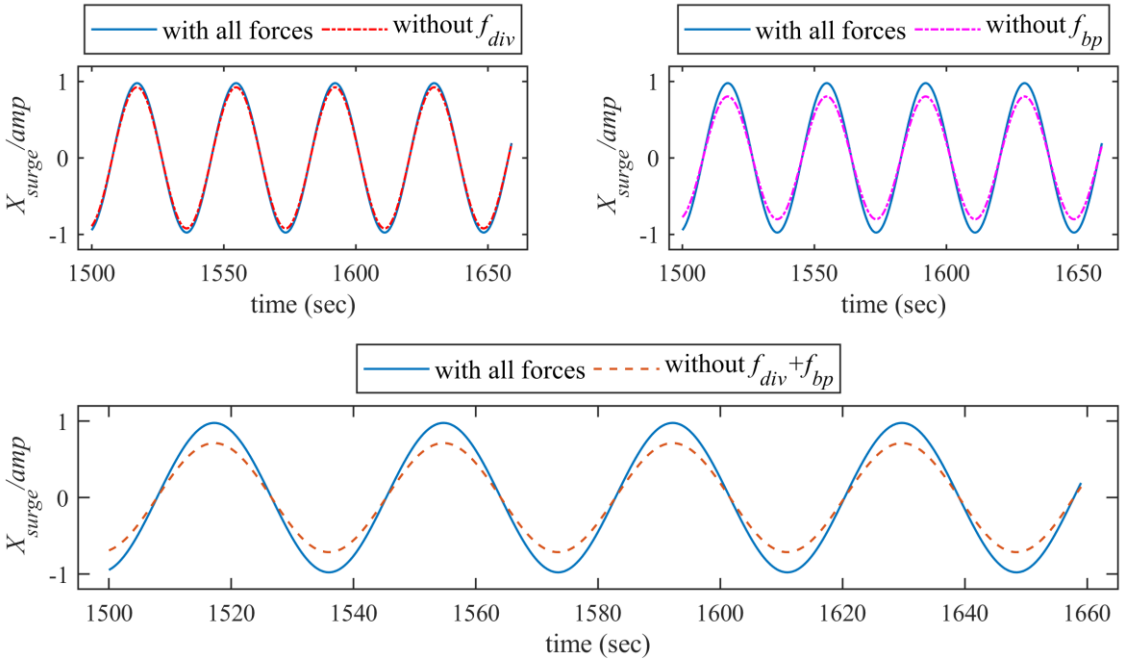

Figure 9.2.6 Low-frequency resonant surge motion due to bi-chromatic wave

It can be seen from the above figure that when all the nonlinear force terms are included, the slow surge motion is much larger than the motion without f_{div} and f_{bp}. When the axial divergence force is not included, the difference in slow surge motion is also visible but is not as marked. When bottom point force is not included, the slow surge motion is much smaller than the motion when the structure is excited by wave force including all the nonlinear force terms. This figure demonstrates that the influence of f_{div} and f_{bp} on the surge motion may be important in many cases when the period corresponding to the difference frequency of incident waves is close to the surge natural period of the structure in question. The influence of centrifugal force f_{cf}, on the surge motion corresponding to the above case, has also been investigated but its effect is not as large as that of f_{div} and f_{bp}. This may be because the amplitude of f_{cf} for this structure is much smaller as compared to amplitude of f_{div} and f_{bp}. In addition to this, difference in pitch

motion with and without considering nonlinear force components f_{div} and f_{bp} is seen very little in this case. This is primarily because of the period of nonlinear forces which are very different from that of pitch natural period of the structure. However, an extreme wave with a frequency in the order of pitch natural frequency may excite pitch response of the concerned structure (as demonstrated in section 6.3.2) which tend to have relatively short natural period compared to predominant wave period. An effect of nonlinear forces in predicting such responses are examined next by considering extreme regular wave.

9.2.3 High-frequency resonance response

High-frequency resonance response (also referred as springing) of tension-leg-platform wind turbine is mainly induced by nonlinear components present in the hydrodynamic interaction of such structures with the extreme ocean waves. Here springing refers to a resonance response to a harmonic oscillation and major contribution to it comes from the second order potential and viscous drag effect. Like low-frequency forces, high-frequency forces are generally small in amplitude and become important only when they excite a resonance response of the structure. For floating wind turbines, especially for TLPs, which, owing to the high axial stiffness of tethers, have lightly damped natural periods of about 1 to 3 seconds in heave, roll and pitch. Though heave natural period of a chosen structure is very low, pitch/roll natural period of the structure is closer to the lower limit of predominant wave period range and can get excited due to the extreme wave. The effect of nonlinear wave forces in predicting such high-frequency resonance responses of the chosen floating wind turbine is examined by comparing motions without considering nonlinear force terms, f_{div} and f_{bp} and their moment components m_{div} and m_{bp}.

The high-frequency pitch resonance response of a chosen floating wind turbine is studied in a water depth of 200m as such platforms tend to have pitch natural period close to the lower limit of predominant wave period of 3sec. The mooring line stiffness is set at 2750kN which yields a natural period of the structure as 37.5sec, 1.4sec, and 2.9sec for a surge, heave and pitch motions respectively. These natural periods are within the design limits set under section 6.2. The case presented here uses an incident monochromatic wave with a period of 8.7sec which is 3 times of pitch natural period of the structure. A height of a wave is obtained by limiting its steepness (H/L_0) to 0.1. Time history and amplitude spectra of pitch motion of the structure are presented in Figure 9.2.7 without considering axial divergence and bottom point force and their moment components.

It can be seen from Figure 9.2.7 that when all the moment components due to nonlinear forces are included pitch motion of the structure is much larger than pitch motion without them. When moment component due to axial divergence force is not included, the difference is also visible but is not as marked. However, when the moment component due to bottom point force is not

included a significant difference in pitch motions are seen. The overall pitch motion is seen underpredicted by 50%.

The amplitude spectra show peaks at input wave frequency and at second and third harmonics of input wave frequency. The third harmonic of input wave frequency coincides with the pitch natural period of the structure where motion amplitude is significantly underpredicted when nonlinear moment component due to bottom end force is not included. The exclusion of moment component due to axial divergence force also under predicts pitch motion amplitude but differences are seen less than 10%.

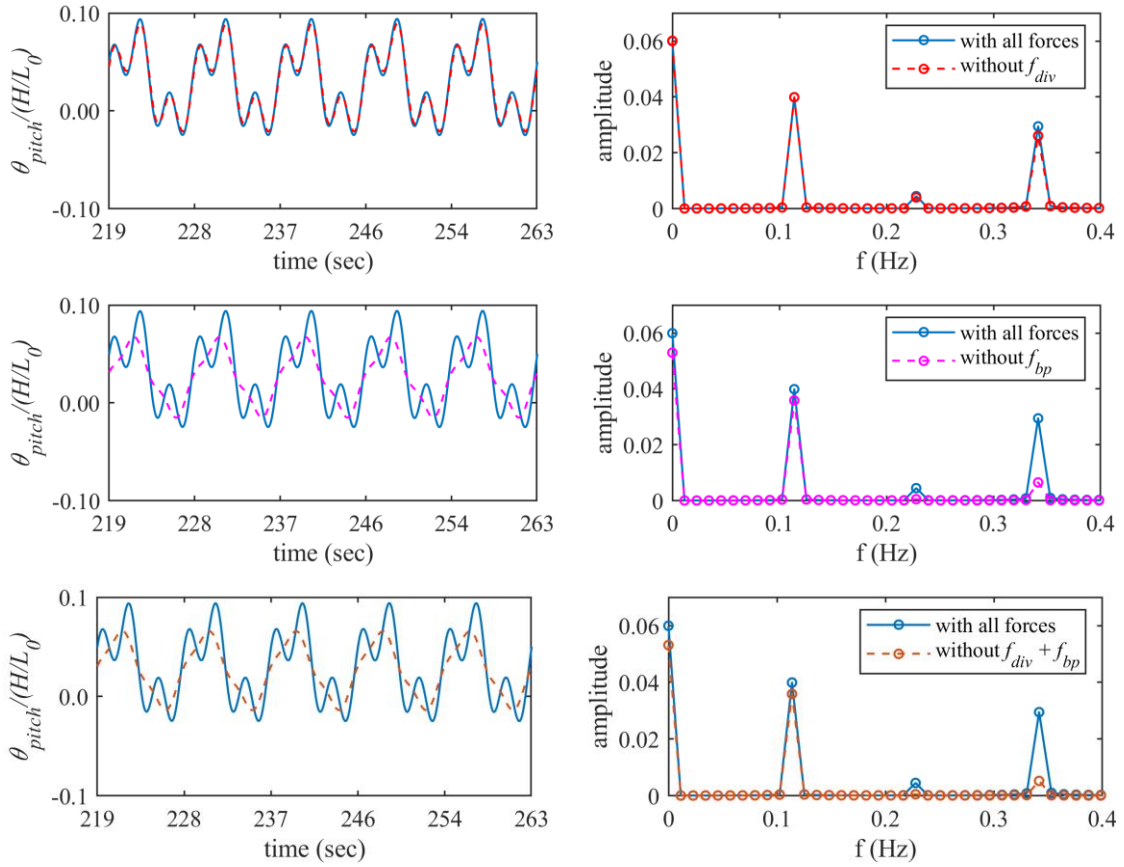

Figure 9.2.7 High-frequency resonant pitch motion due to extreme regular wave $H=11.8m$, $T_0=8.7s$, and $V_w=21m/s$

To see the effect of wind load on pitch motion of the chosen floating wind turbine, calculations are repeated for various wind speeds while the turbine is under operating and in the parked condition. The range of normalised pitch motion (measured from minimum to maximum) for various wind speeds during the steady part of their time history are presented in Figure 9.2.8.

It can be seen from Figure 9.2.8 that the increase in wind speed up to a rated speed of turbine produces higher turbine loads and hence higher damping that reduces pitch motion amplitude. The pitch motions are underpredicted by 33% without nonlinear force terms f_{div} and f_{bp} for a wind speed of 21m/s which is corresponding to a rated speed of the turbine. This results further

demonstrates the importance of inclusion of axial divergence and bottom point force while evaluating wave forces acting on the floating structure.

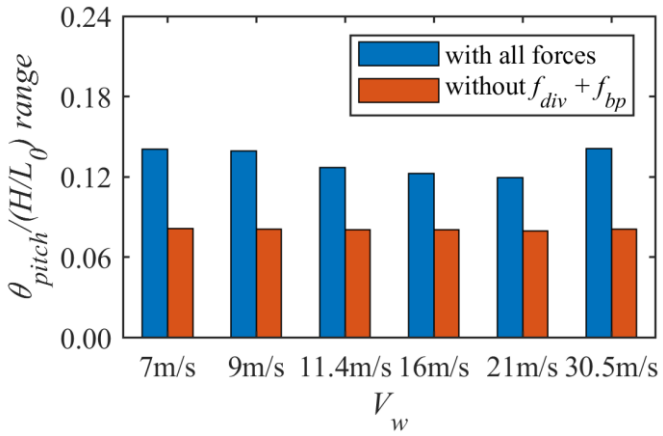

Figure 9.2.8 Effect of wind load on high-frequency resonant pitch motion

9.2.4 Ringing and springing response

Impulsive wave loads on the floating structure are generated when they are suddenly engulfed by very steep waves. Because the loads are applied impulsively they generate a global transient response, called as ringing and springing, which is superimposed on to the wave frequency response. The loads act so rapidly that it results in a characteristic burst of structural vibration even though the natural frequency of the structure is well away from the input wave frequency. Such motions are results of higher order potential slam and drag forces. The effect of nonlinear wave forces in predicting such responses for the chosen tension-leg-platform wind turbine is examined by comparing motions without considering nonlinear force terms, f_{div} and f_{bp} and their moment components m_{div} and m_{bp}.

The ringing and springing response of the chosen floating wind turbine is studied in a water depth of 200m where mooring line stiffness is set at 2750kN and wind speed V_w is considered as 21m/s corresponding to a rated speed of the wind turbine. The case presented here uses an incident bichromatic wave with amplitude $amp_1 = amp_2 = 3.6$m, and period $T_1 = 12.33$sec and $T_2 = 12.97$sec. These wave parameters generate an extreme wave of steepness (H/L_0) of 0.12 due to an evolution of regular wave group (i.e., bichromatic wave components). Time history of wave surface elevation and corresponding pitch motion of the structure with and without considering axial divergence and bottom point force are presented in Figure 9.2.9. Here wave surface elevation is normalised by input wave amplitude ($amp_1 = amp_2 = amp$) and pitch motion of the structure by steepness q which is $\bar{k}.amp$, where $\bar{k}$ is wave number corresponding to an average frequency of input wave components.

It can be seen from wave surface elevations presented in Figure 9.2.9 that at $t = 1758$sec normalised wave surface elevation is 0.64 and then after 10 sec a wave with an elevation of 4.19 is passing a structure. Such steep wave suddenly approaching structure generates a high impact

load and results in ringing and springing response of the structure as shown in Figure 9.2.9. When all the nonlinear force terms are included pitch motion of the structure predicted is much larger than the pitch motion without them. When axial divergence force and its moment component is not included, the difference is also visible but is not as marked. However, when bottom point force and its moment is not included a significant difference in pitch motion are observed. The maximum pitch motion is underpredicted by 60% whereas the range of pitch motion (measured from minimum to maximum) is underpredicted by 65%.

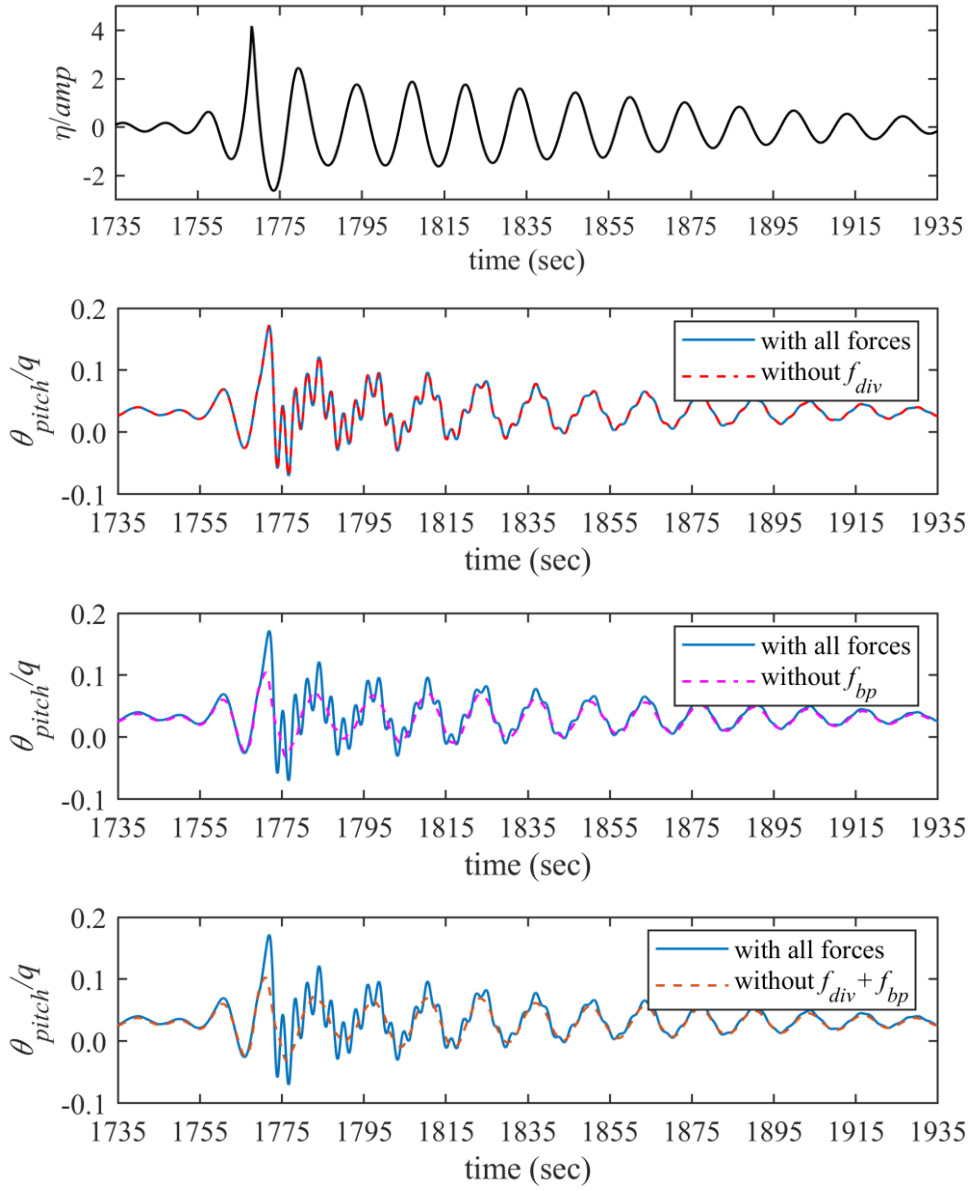

Figure 9.2.9 Time history of wave surface elevation and corresponding ringing and springing pitch motion due to bi-chromatic wave

The amplitude spectra of pitch motion presented in Figure 9.2.10 show peaks at input wave frequencies, fw_1 and fw_2 and at its several sideband frequencies. The magnitude of motion amplitude at input wave frequencies and its sideband frequencies are slightly underpredicted but

at pitch natural frequency, motion amplitudes are underpredicted significantly when nonlinear force terms are not included.

To investigate the effect of wind load on ringing pitch motion of the chosen floating wind turbine, calculations are performed for various wind speeds detailed in Table 5.1.3, while the turbine is operating and in the parked condition. The maximum pitch motion and its range (measured from minimum to maximum) for various wind speeds are presented in Figure 9.2.11.

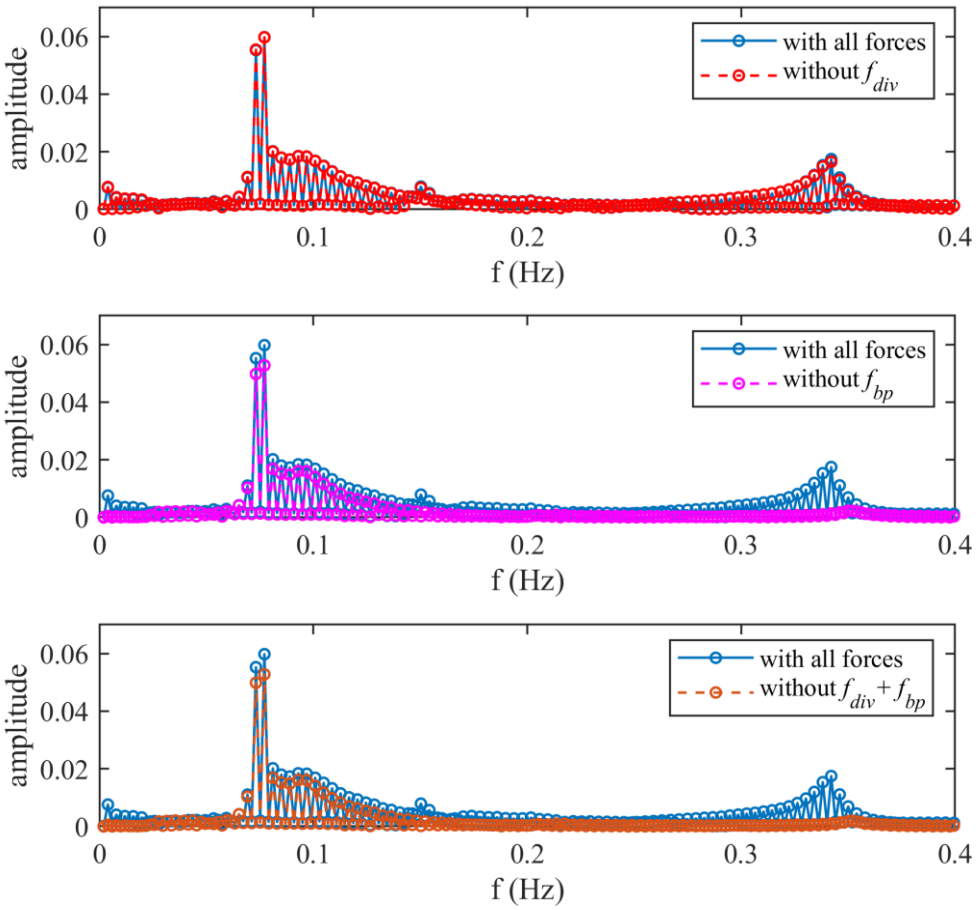

Figure 9.2.10 Amplitude spectra of ringing and springing pitch motion due to bi-chromatic wave

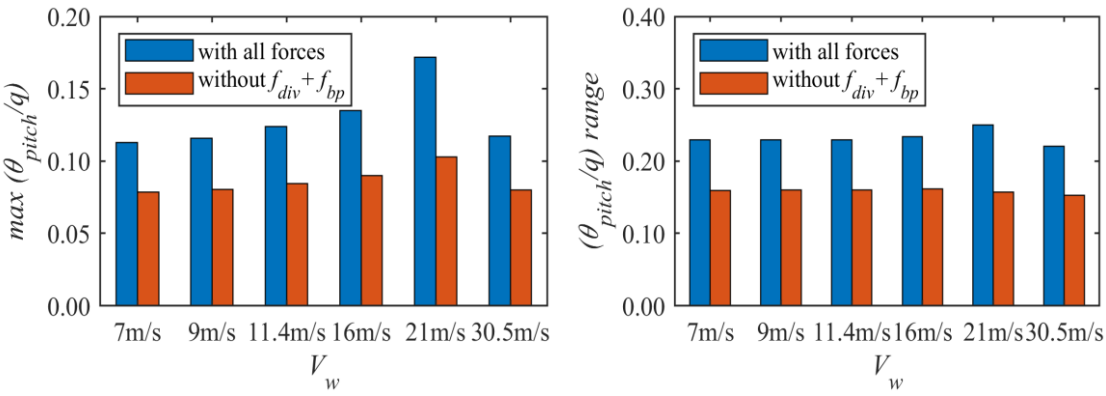

Figure 9.2.11 Effect of wind load on ringing pitch motion

It can be seen from Figure 9.2.11 that the increase in wind speed up to a rated speed of turbine produces higher turbine loads and hence higher impact load that increases the maximum pitch motion and its range. The minimum difference in maximum pitch motion and its range predicted without nonlinear force terms f_{div} + f_{bp} are 44% and 46% respectively, for the lowest analysed operating wind speed of 7m/s. This results further demonstrates the importance of inclusion of axial divergence and bottom point force while evaluating wave forces acting on the floating structure.

9.3 Effect of nonlinear wave forces on global performance of TLPWT

Global performance of TLPWT is assessed by investigating the effect of nonlinear wave forces on the response parameters associated with its components, such as wind turbine, tall supporting tower, platform hull and mooring system. Key response parameters associated with each component of floating wind turbine are chosen to investigate their predictions without considering nonlinear force terms f_{div} and f_{bp} and their moment components m_{div} and m_{bp} in the wave load calculation. Here global response parameters such as thrust acting on the wind turbine, bending moment in tower, and the mooring line tensions are chosen for the investigation. As seen in the previous section 9.2, nonlinear wave forces have a significant impact on the first order pitch motion, low-frequency resonance surge motion, high-frequency resonance pitch motion, and high-frequency ringing pitch motion. Among these, high-frequency resonance and ringing pitch motion affected the most due to exclusion of nonlinear force components f_{div} and f_{bp} and hence the wave conditions associated with these motion responses are chosen for investigating global response parameters. Low operating wind speed of 7m/s is chosen for the resonance pitch motion case whereas rated operating wind speed of 21m/s is chosen for the ringing pitch motion case as these wind speeds yield maximum difference in motion predictions when nonlinear force components are excluded from the wave force calculations. Time history of global response parameters such as wind turbine thrust, tower bending moment and upwind mooring line tension corresponding to high-frequency resonance and ringing pitch motion are presented in Figure 9.3.1 and Figure 9.3.2 respectively. Here, the wind turbine thrust, and mooring line tensions are normalised by their mean value at t = 0sec, whereas tower bending moment is normalised by product of buoyancy force f_{buoy} and draft of the platform h_d.

The time history plots presented in Figure 9.3.1 and Figure 9.3.2 clearly reflect the effect of nonlinear wave forces in predicting global response parameters. All the response parameters are predicted lower when the nonlinear force terms f_{div} and f_{bp} are not included as compared to the response parameters predicted including them. When concerned structure is subjected to extreme regular wave exciting pitch resonance, the differences in prediction of response parameters, such as wind turbine thrust, tower bending moment and upwind mooring line tensions are seen 27%, 55%, and 67% respectively.

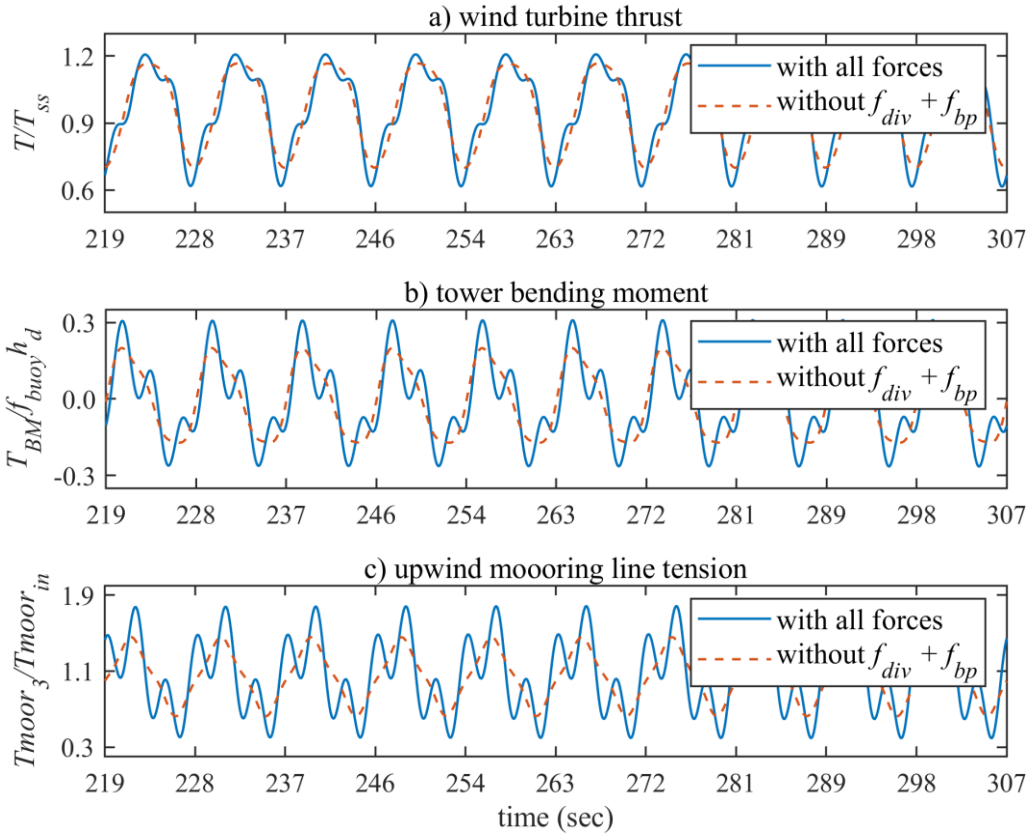

Figure 9.3.1 Global response parameters for resonant pitch motion due to regular wave (H = 11.8m, T_0 = 8.7sec, V_w = 7m/sec)

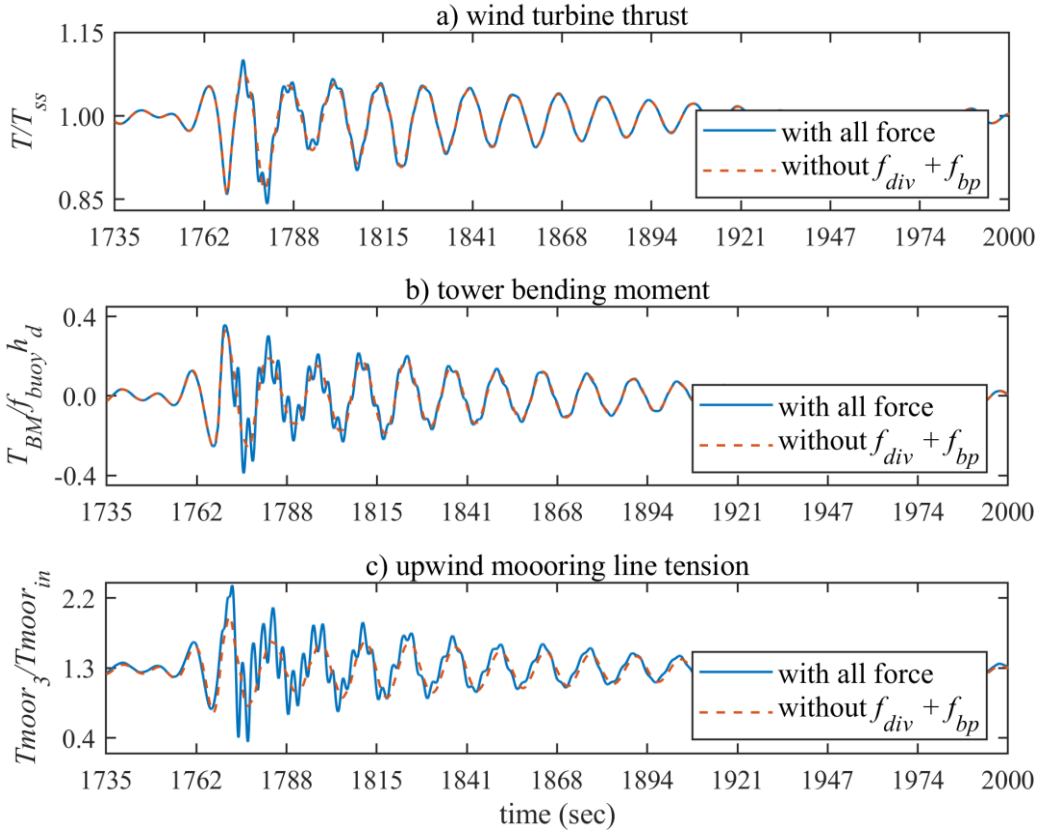

Figure 9.3.2 Global response parameters for ringing pitch motion due to bi-chromatic wave ($amp_1 = amp_2$ = 3.6m, T_1 = 12.33sec, T_2 =12.97sec, V_w = 21m/sec)

The difference in prediction of platform pitch motion with and without including nonlinear force terms in the wave load calculations are also influenced by wind loads acting on the turbine and its supporting tower as shown in Figure 9.2.8 and Figure 9.2.11. To investigate the influence of wind load in predicting global response parameters, the calculations and comparisons are carried out for all the chosen response parameters for various wind speeds while the turbine is operating and in the parked condition. The range of each parameter (measured from minimum to maximum) for high-frequency resonance and ringing pitch motion is presented in Figure 9.3.3.

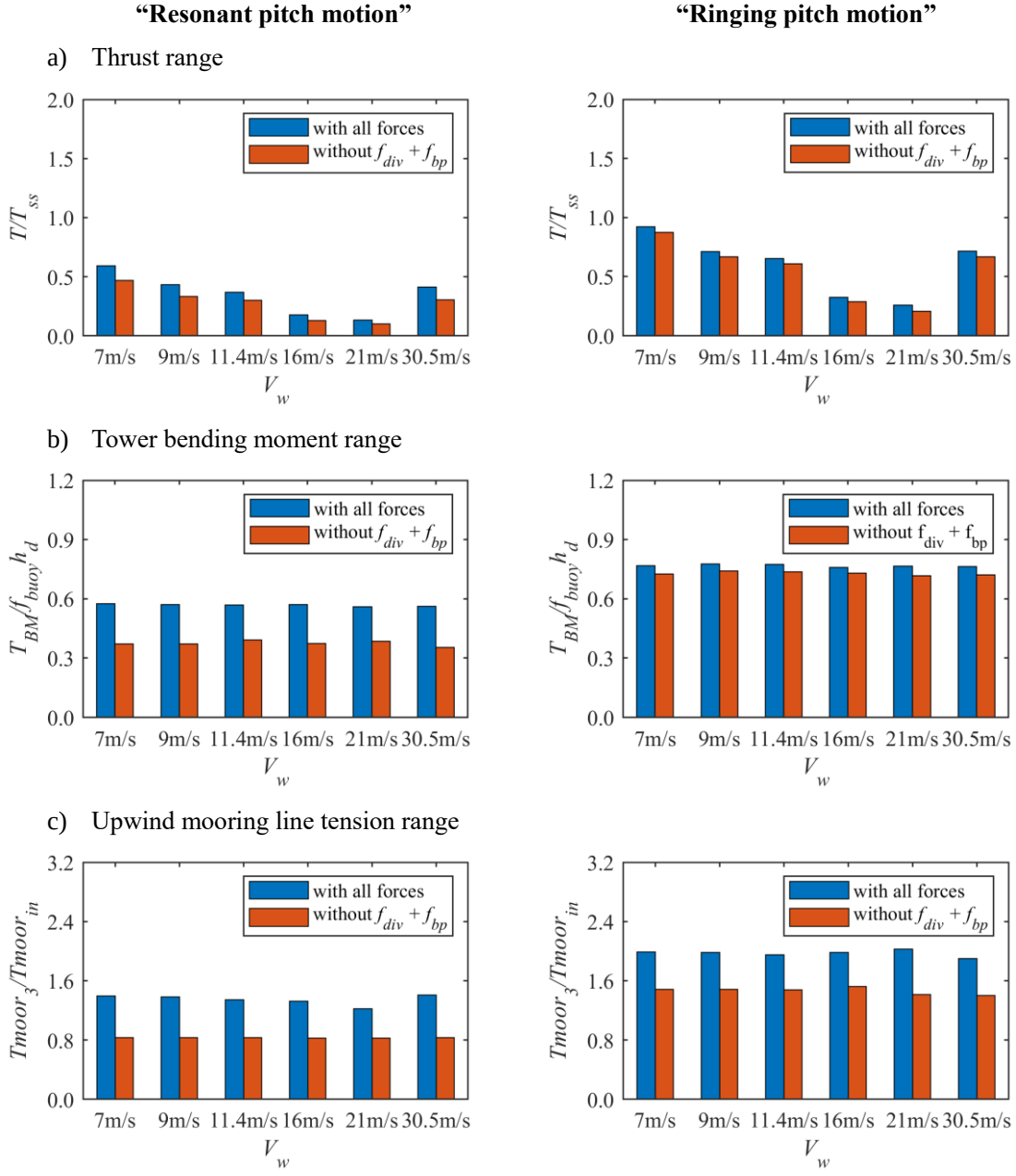

Figure 9.3.3 Range of global response parameters for resonant and ringing pitch motion

It can be seen from Figure 9.3.3 that the maximum difference in global response parameters predicted with and without considering nonlinear force terms occur for low wind speed of 7m/s when structure is subjected to high frequency resonance pitch motion and for rated wind speed

of 21m/s when structure is subjected to ringing pitch motion that follows the trend in prediction of pitch motion depicted in Figure 9.2.8 and Figure 9.2.11. The maximum difference in predictions are seen for mooring line tension for both high frequency resonance and ringing pitch motion as it mainly depends on platform motions.

This investigation on effect of nonlinear forces in predicting motion responses as well as global performance of TLPWT shows the importance of nonlinear wave forces while evaluating wave loads acting on the floating structure in intermediate to deep water depth. The nonlinear force term f_{div}, and f_{cf} may be important for deep draft structure whereas f_{bp} is important for the shallow draft structure which is most likely to be the case for floating wind turbine especially for the chosen tension leg platform, as they will be deployed the most in the intermediate to deep water depth (100m-200m) in near future.

10 CONCLUSIONS AND RECOMMENDATIONS

10.1 Conclusions

This thesis has presented an integrated nonlinear modelling of floating wind turbine system. The main technical development, as presented in chapter 3, is the development of the formulation for evaluating various external forces and moments acting on the floating wind turbine system. The external forces considered under this study constitute, aerodynamic forces due to wind, hydrodynamic forces due to wave and current, and the restoring forces due to mooring system. The forces due to wind acting on the turbine rotor and its supporting tower are calculated using modified BEM theory and quadratic drag force equation respectively. The forces due to wave and current are calculated using Rainey's non-diffracting potential theory (NDPT), where QALE-FEM numerical scheme based on fully nonlinear potential theory (FNPT) is employed to predict the wave kinematics (i.e., free surface and underlying water particle kinematic). The forces due to mooring system are calculated using the quasi-static approach. Evaluation of these forces and their moment components considered the interaction between wind turbine, tower, platform, and mooring system. Equations for all these forces and moments and the motions were set up and solved using numerical procedure developed and presented under chapter 4. Further, the model is validated using published experimental results which showed that the model yields satisfactory results for steady wind, regular wave, and combined steady wind and irregular wave environment.

The most distinguishing feature of this model is its numerical procedure which evaluates forces acting on each component of the floating wind turbine considering nonlinear interaction among them at each time step during the simulation. As platform supports tall tower with a heavy wind turbine at high elevation, it will be subjected to a large aerodynamic force which may affect the platform's motions and subsequently mooring line tension. In return, the motions of the platform due to waves and current may affect the performance of wind turbine and alter the loads acting on the rotor, tower and mooring system. The main sources of nonlinearity considered while incorporating this interaction effect includes, nonlinearity in the equations of motions, nonlinear wind forces, nonlinear wave forces due to potential and viscous effect, nonlinear wave kinematics with convective and temporal acceleration terms, nonlinear mooring line forces, and nonlinearity arising while computing forces up to instantaneous free surface for the displaced position of the structure at each instant of time. Among all the nonlinearities mentioned above, the nonlinearities associated with the wave kinematics and wave forces has not been considered adequately in the past or shown to be of less importance. The work presented in this thesis demonstrated that the effect of both nonlinear wave kinematic and nonlinear wave forces is significant by assessing the global response of tension-leg-platform wind turbine (TLPWT) that is being considered as a most promising concept to harness wind energy in a moderate water depth. The primary results from

the global response analysis includes global motions, blade airgap, turbine fore-aft displacement for RNA design and selection, and loads on the wind turbine, tower, platform, and mooring system. These results provide the input required for the structural design of floating wind turbine components. To be more specific, the conclusions drawn using nonlinear wave kinematic (FNPT) and nonlinear wave force (NDPT) models adopted in this thesis are summarised separately as follows,

10.1.1 Effect of nonlinear wave kinematic model (FNPT based QALE-FEM)

An effect of FNPT based QALE-FEM on the prediction of wave kinematics, and consequently, global responses of TLPWT are investigated in extreme regular, bichromatic and random waves. The wave kinematics and global responses are further compared with the most commonly used analytical Airy's linear wave theory (LWT) with wheeler's stretching approximation and Fenton's nonlinear steady wave theory (NLSWT), where the latter is employed for modelling regular wave only, to examine their suitability. The wave kinematics, i.e., free surface elevation and underlying water particle kinematics are compared using their steady-state profiles whereas global responses are compared using their time history, amplitude spectra and statistical parameters. The major findings concerning wave kinematics and global responses of TLPWT are listed below,

A. Effect of nonlinearity on wave kinematics

i) A distinct nonlinear free surface and water particle kinematics for an extreme regular wave

An effect of FNPT based QALE-FEM on the prediction of wave kinematics is assessed by comparing free surface elevation, and underlying water particle kinematics predicted by it with the laboratory generated experimental data. The wave kinematics are further compared using analytical LWT & NLSWT wave models to examine their suitability. This comparison is further extended using numerical results for predominant wave frequencies with their extreme amplitudes in a moderate water depth (100m-200m) where chosen tension-leg-platform wind turbines are expected to be built.

- The comparison of **free surface elevation** revealed that the numerical FNPT based QALE-FEM predicted free surface with sufficient accuracy as compared to experiment, demonstrating the nonlinear behaviour of a wave is well captured for both short (deep water) and long (intermediate water) waves. The comparison using analytical wave models, i.e., LWT and NLSWT revealed distinct predictions for intermediate and deep-water waves. For deep water waves, LWT and NLSWT models predicted both crest and total wave height higher as compared to predictions by FNPT and experiment. For intermediate water waves, the crest is predicted lower by LWT model and higher by NLSWT model as compared to FNPT based QALE-FEM and experiment whereas, total wave height is predicted higher by

both LWT and NLSWT wave models. These distinct differences in the prediction of free surface elevations by both the analytical wave models (LWT and NLSWT) with respect to numerical FNPT based QALE-FEM are mainly seen due to their inherent assumption of the uniform waveform and ignorance of wave dispersion.

- The comparison of **water particle kinematics** revealed that the numerical FNPT based QALE-FEM predicted horizontal water particle velocity with sufficient accuracy as compared to experiment. The LWT model underpredicted velocity at the crest and overpredicted at trough whereas, NLSWT model slightly overpredicted velocity at the crest but predicted well at the trough. The comparison is further extended for predominant wave frequencies with their extreme amplitude for all the water particle kinematic parameters. The comparison revealed that except horizontal water particle velocity, all other kinematic parameters were predicted higher by LWT and NLSWT model as compared to FNPT based QALE-FEM. The difference in prediction by LWT model is seen due to wheeler stretching technique used for approximating water particle kinematics whereas the difference in prediction by NLSWT model is seen due to higher predicted crest used for the evaluation of water particle kinematics. These conclusions are applicable for freely propagating predicted wave surface whereas for target wave surface (equal steepness waves) the differences in water particle kinematics predicted by LWT and FNPT based QALE-FEM are seen growing and the differences in prediction by NLSWT and FNPT based QALE-FEM are seen reducing to negligible and hence confirming an accuracy of NLSWT model for modelling extreme waves in moderate water depth.

ii) A non-Rayleigh height of an extreme wave generated through nonlinear evolution in bichromatic and random wave group

An effect of FNPT based QALE-FEM on the prediction of the free surface of the bichromatic wave group is assessed by comparing free surface elevation predicted by it with the laboratory generated experimental data. The free surface is further compared using analytical LWT wave model to examine its suitability. For random wave group, this comparison is performed numerically using site-specific spectra.

- The comparison for **bichromatic wave group** revealed that the FNPT based QALE-FEM predicted free surface with sufficient accuracy as compared to experiment demonstrating its ability to predict the nonlinear evolution of wave group, with the significant increase in wave height above a critical value for the quotient of wave amplitude and period bandwidth. The amplitude spectra of the free surface revealed several sideband frequency components showing a significant transfer of energy. Contrary to this, the LWT wave model failed to predict large wave height and associated sideband frequency components. However, this difference in predictions by both the wave models are seen for wave group having high steepness and low period bandwidth. As wave group steepness reduces and period bandwidth

increases, an evolution of wave group is seen becoming linear showing an insignificant difference in prediction of the free surface by both the wave models.

- The comparison for **random wave group** revealed that the FNPT based QALE-FEM predicted the non-Rayleigh crest and height of an extreme wave identified in a random wave group. Like the bichromatic wave group, LWT model failed to predict both large wave height and associated sideband frequency components. However, the nonlinear evolution of the random wave group mainly depends upon the Benjamin-Feir index, BFI which is a ratio of significant wave steepness and spectral bandwidth. An effect of this BFI on wave group evolution is studied by varying it and found that for lower BFI value, an evolution of random wave group is nearly linear and the difference in prediction of the wave surface by LWT and FNPT based QALE-FEM is insignificant.

B. Effect of nonlinear wave kinematic on global response of TLPWT

i) A distinct first order response caused by nonlinear wave kinematics for highly loaded wind turbine

A distinct first order response of a TLPWT predicted by FNPT based QALE-FEM is observed when excited by extreme regular waves with predominant frequencies ranging from 6 to 20sec having steepness (H/L_0) of 0.1 while the turbine is operating at its rated wind speed. An analytical NLSWT wave model predicted motions in all the modes higher as compared to FNPT based QALE-FEM that is mainly seen due to the higher prediction of free surface elevation and the corresponding water particle kinematics. However, these differences were seen for predicted wave surface whereas for target wave surface differences in motion prediction by both the nonlinear wave models are seen insignificant confirming that the Fenton's NLSWT model can be used to model extreme regular wave. Airy's LWT model predicted motions considerably higher as compared to both the nonlinear wave models (i.e., Fenton and QALE-FEM). It is seen because in the case presented here, inertia part of the wave force dominated total wave force acting on the structure. This inertia force is mainly dependent on the water particle accelerations, which are predicted higher by LWT model as compared to both the nonlinear wave models for the entire wetted length of platform members over which forces are integrated to obtain the total force acting on the structure. This wetted length is a function of wave surface profile variation which is also predicted higher by LWT model that further contributes to higher wave loading and hence the higher platform motions. The drag part of the wave force is dependent upon the water particle velocity. Though LWT model underpredicted it at wave crest as compared to nonlinear wave models, the difference gets reduced with depth and reverses the sign before the keel of the platform. Therefore, the effect of higher horizontal water particle velocity predicted by nonlinear wave models is not seen for the chosen structure.

ii) High-frequency resonance response caused by third harmonic force component for low loaded wind turbine

A high-frequency resonance response of a TLPWT predicted by FNPT based QALE-FEM is observed when excited by an extreme regular wave with a frequency, f_w equal to three times of pitch natural frequency, $f_{n-pitch}$ of the structure having target steepness, (H/L_0) of 0.1. The response is observed for a low loaded turbine that occurs when the turbine operates at low wind speed or in the parked condition. The NLSWT wave model predicted resonant pitch motion very close to predictions by FNPT based QALE-FEM showing it can predict the higher-order wave kinematic very close to fully nonlinear QALE-FEM for target wave surface. The LWT model underpredicted pitch motion significantly as compared to both the nonlinear wave models, i.e., NLSWT and FNPT. This higher pitch motion predicted by both the nonlinear wave models is mainly seen due to the nonlinear force component generated at third harmonics which LWT model failed to predict. However, this difference in pitch motion predicted by linear and nonlinear wave models is seen decreasing with an increase in turbine load with a minimum difference is noticed while the turbine is operating at its rated wind speed due to high aerodynamic damping.

iii) Low-frequency resonance response caused by the difference in sideband frequency components for low loaded wind turbine

A significant low-frequency resonance response of a TLPWT predicted by FNPT based QALE-FEM is observed when excited by the non-Rayleigh height of an extreme wave generated through nonlinear evolution in bichromatic and random wave group. For the bichromatic wave group, low-frequency surge response is observed when surge natural frequency, $f_{n-\mathrm{surge}}$ of the structure coincided with the difference in sideband frequency components associated with an extreme wave. For random wave group, low-frequency surge response is observed when surge natural frequency, $f_{n-\mathrm{surge}}$ of the structure coincided with both, the difference in frequency components from input wave spectrum and sideband frequency components associated with non-Rayleigh height of an extreme wave. For both the wave groups, surge motions are predicted significantly higher by FNPT based QALE-FEM as compared to LWT model for the low loaded turbine. This difference is seen reducing with an increase in turbine loads due to aerodynamic damping. As this low-frequency surge response is dependent on the sideband frequency components associated with a non-Rayleigh extreme wave, a generation of such wave is mainly dependent upon steepness and period bandwidth for bichromatic wave group and BFI value for the random wave group. For bichromatic wave group, as the steepness of wave components reduces, and period bandwidth increases, the difference in prediction of surge motion by LWT and FNPT based QALE-FEM is seen decreasing, as an evolution of wave group becoming linear showing no

transfer of energy to sideband frequency components. A similar effect is observed for random wave group with low BFI value.

iv) High ringing response caused by the non-Rayleigh height of an extreme wave for highly loaded wind turbine

A high ringing response of a TLPWT predicted by FNPT based QALE-FEM is observed when excited by the non-Rayleigh height of an extreme wave generated through nonlinear evolution in bichromatic and random wave group. As ringing refers to a transient response to an impulsive load, an extreme ringing pitch response is observed when the turbine is highly loaded that occurs when the turbine operates at its rated wind speed. Due to high ringing behaviour, pitch motion of a TLPWT predicted by FNPT based QALE-FEM is seen significantly higher as compared to predictions by LWT model which failed to predict large wave height and hence the high ringing response. As this high ringing response is dependent on the non-Rayleigh height of an extreme wave, a generation of such wave is mainly reliant on steepness and period bandwidth for bichromatic wave group and BFI value for random wave group. For bichromatic wave group, as the steepness of wave components reduces, and period bandwidth increases, the difference in prediction of ringing pitch motion by LWT and FNPT based QALE-FEM is seen decreasing as the evolution of wave group becoming linear showing no significant difference in prediction of wave surface elevation. A similar effect is observed for random wave group with low BFI value.

v) Reduction in blade airgap due to set-down of structure and non-Rayleigh crest height of an extreme wave

A reduction in the blade airgap for a TLPWT predicted by FNPT based QALE-FEM is observed when excited by the non-Rayleigh height of an extreme wave generated through nonlinear evolution in bichromatic and random wave group. Airgap primarily depends upon heave motion of the structure and crest height of an extreme wave. High negative heave motion occurs not only due to wave heave force but also due to an additional set-down effect resulting from the positive surge and pitch motion of the structure and both are high when turbine operates at its rated wind speed. FNPT based QALE-FEM predicted both negative heave motion and crest height significantly higher as compared to predictions by LWT wave model due to its ability to predict an extreme wave through nonlinear evolution and corresponding negative heave force. As this blade airgap is dependent on non-Rayleigh crest height of an extreme wave, a generation of such wave is mainly reliant upon steepness and period bandwidth for bichromatic wave group and BFI value for random wave group. For bichromatic wave group, as the steepness of wave components reduces, and period bandwidth increases, the difference in prediction of blade airgap by LWT and FNPT wave model is seen decreasing as the evolution of wave group becoming linear showing no

significant difference in prediction of crest height and consequently heave motion. A similar effect is observed for random wave group with low BFI value.

vi) ***Large fore-aft displacement of turbine due to high surge and pitch motion induced by non-Rayleigh height of an extreme wave***

Large fore-aft displacement of the turbine predicted by FNPT based QALE-FEM is observed when the structure is excited by the non-Rayleigh height of an extreme wave generated through nonlinear evolution in bichromatic and random wave group. For both the wave groups, a peak as well as a range of turbine displacement is predicted significantly higher by FNPT based QALE-FEM as compared to LWT model. This is mainly seen due to the ability of FNPT based QALE-FEM in predicting the non-Rayleigh height of an extreme wave and hence corresponding high surge and pitch motion of the structure which LWT model failed to predict. However, this significant difference in prediction of turbine fore-aft displacement is only applicable to a certain class of bichromatic and random wave group. For bichromatic wave group, as the steepness of wave components reduces, and period bandwidth increases, the difference in prediction of turbine fore-aft displacement by LWT and FNPT based QALE-FEM is seen decreasing as the evolution of wave group becoming linear showing no significant difference in prediction of wave surface and consequently surge and pitch motions. A similar effect is observed for random wave group with low BFI value.

vii) ***Increase in loads acting on TLPWT components due to high ringing and springing response***

An increase in loads acting on the TLPWT components due to high-frequency ringing and springing response predicted by FNPT based QALE-FEM is observed when the structure is excited by extreme regular, bichromatic and random wave. The loads observed comprises, thrust acting on wind turbine, bending moment in tower, wave loads on platform hull and tension in each mooring line.

- For an extreme regular wave, a range of all the afore-mentioned loads are predicted higher by both the nonlinear wave models (NLSWT & FNPT based QALE-FEM) as compared to LWT wave model when pitch motion of the structure is excited by third harmonic force component while the turbine is operating at low wind speed and in the parked condition. However, as the turbine load increases, this difference in predictions by linear and nonlinear wave models is seen decreasing due to increase in aerodynamic damping.
- For an extreme bichromatic and random wave group, a peak and range of all the afore-mentioned loads are predicted significantly higher by FNPT based QALE-FEM as compared to LWT wave model when the high ringing response of the structure is excited by the non-Rayleigh height of an extreme wave for a highly loaded wind turbine. It occurs when the turbine is operating at its rated wind speed. However, this significant difference in load predictions is only applicable to a certain class of bichromatic and random wave group. For

bichromatic wave group, as the steepness of wave components reduces, and period bandwidth increases, the difference in prediction of loads by LWT and FNPT wave model is seen decreasing as the evolution of wave group becoming linear showing no significant difference in prediction of wave surface and consequently loads acting on the TLPWT components. A similar effect is observed for random wave group with low BFI value.

These conclusions confirm the importance of considering a fully nonlinear wave model while performing load and response analyses of the floating wind turbine to extreme waves.

10.1.2 Effect of nonlinear wave force model (NDPT)

In the numerical model, Rainey's non-diffracting potential wave theory (NDPT) is used to calculate the wave loads acting on the floating platform. Rainey modified the inertia term of the Morrison's equation by including axial divergence f_{div} and centrifugal force f_{cf} terms acting on the member cross-section and by introducing an additional point forces f_{int} and f_{bp} at top and bottom end of the immersed members. In the past several authors have used this equation for wave force evaluation where the last force component i.e., point force at the bottom end of the immersed member f_{bp} is shown to be small and neglected thereafter. The results presented in this thesis demonstrated that the effect of this force component can be significant as compared to the other nonlinear force components including nonlinear force component due to wave acceleration present in the conventional Morison′s equation. It is also shown that the magnitude of this force component is strongly dependent on the wave conditions and may be small in some circumstances but cannot be neglected in general especially for the load and response analysis of the chosen TLPWT to extreme waves. The exclusion of this force component has a significant effect on the chosen floating wind turbine′s motion response at wave frequency, low-frequency surge and high-frequency pitch resonance, and ringing pitch response while the turbine is operating or in the parked condition. The underprediction of motion responses due to exclusion of this nonlinear force component also has an adverse effect on the global response parameters for the chosen floating wind turbine system that includes wind turbine thrust, a bending moment in the tower, and tension in the mooring lines.

There is no significant difficulty or computational penalty in including this force component and hence it is recommended that it must be included in the formulation of wave loads acting on the floating structure having a shallow draft.

10.2 Recommendations for future work

Although nonlinear wave kinematic and force model is suggested to be included in the integrated numerical model for analysing floating wind turbine responses, there are still some issues unresolved and hence they are summarised here as future work scope.

I. In the numerical model, floating wind turbine components such as wind turbine blades, tower and floating platform are assumed as rigid body components of the whole rigid

floating wind turbine system. However, the rotor blades and tall slender tower are flexible elements and hence the flexibility effect of these structural elements shall be included either by developing dedicated structural dynamic code or by coupling it with existing structural dynamic code such as ADAM's.

II. In the numerical model, mooring lines are modelled using a quasi-static approach without considering a wave and current forces acting on it. However, in the future, wave and current load calculations shall be extended to mooring system enabling full dynamic modelling of mooring lines.

III. In the numerical model, wave kinematics are predicted using FNPT based numerical scheme QALE-FEM that uses 2-D numerical wave tank as fluid domain, however, nonlinear wave group evolution also depends upon directional spreading, and hence the model shall be updated including 3-D numerical wave tank.

Finally, the numerical model shall be extended including the number of floating wind turbine units with their locations and spacing among them so that the multiple floating wind turbine units subjected to the same random wave environment can be studied at a time.

REFERENCES

Adcock, T. et al., 2011. Did the Draupner wave occur in a crossing sea?. *Proceedings of the Royal Society A: Mathematical, Physical and Engineering Sciences,* 467(2134), pp. 3004-3021.

Airy, G. B., 1845. *Tides and waves.* London: Encyclopaedia Metropolitana.

Azcona, J., Palacio, D., Munduate, X. & Leo, G., 2016. Impact of mooring lines dynamics on the fatigue and ultimate loads of three offshore floating wind turbines computed with IEC 61400-3 guideline. *WIND ENERGY,* 20(5), pp. 797-813.

Baldock, T. E., Swan, C. & Taylor, P. H., 1996. A Laboratory Study of Nonlinear Surface Waves on Water. *Philosophical Transactions of the Royal Society of London A: Mathematical, Physical and Engineering Sciences,* 354(1707), pp. 649-676.

Benard, P. et al., 2018. Large-Eddy Simulation of wind turbines wakes including geometrical effects. *Computers & Fluids,* Volume 173, pp. 133-139.

Benjamin, T. B. & Feir, J. E., 1967. The disintegration of wave trains on deep water Part 1. Theory. *J. Fluid Mech.,* Volume 2, pp. 417-430.

Benjamin, T. B. & Hasselmann, K., 1967. Instability of periodic wavetrains in nonlinear dispersive systems. *Proceedings of the Royal Society of London A: Mathematical, Physical and Engineering Sciences,* 299(1456), pp. 59-76.

Bossanyi E.A., 2003. *GH Bladed Theory Manual,* Bristol, UK.: Garrad Hassan and Partners Limited,.

Buckley, W. H., 1983. *A study of extreme waves and their effects on ship structure,* Washington, D.C.: The ship Structure Committee Report No. SSC-320.

Buckley, W. H. & Stavovy, A. B., 1981. *Progress in the development of structural criteria for extreme waves.* New York, N.Y, Proc. Extreme Loads Response Symp.

Buhl, M. J., 2004. *A New Empirical Relationship between Thrust Coefficient and Induction Factor for the Turbulent Windmill State,* Golden, CO: National Renewable Energy Laboratory: NREL/TP-500-36834.

Bulder BH, et al., 2002. *Study to feasibility of and boundary conditions for floating offshore wind turbines,* Lagerwey the Windmaster, TNO, TUD: Delft, The Netherlands: Public Report 2002-CMC-R43, ECN, MARIN, MSC.

Casale, C., Lembo, E., Serri, L. & Viani, S., 2010. Preliminary Design of a Floating Wind Turbine Support Structure and Relevant System Cost Assessment. *WIND ENGINEERING,* 34(1), p. 29–50..

Cermelli, C., Roddier, D. & Aubault, A., 2009. *WindFloat: A Floating Foundation for Offshore Wind Turbines, Part II Hydrodynamic Analysis.* May 31-June 5, Honolulu, Hawaii, USA., 28th International Conference on Ocean, Offshore and Arctic Engineering.

Chakrabarti, S. K., 2005. *Handbook of offshore engineering Vol 1 & 2.* Plainfield, Illinois, USA:

ELSEVIER.

Chappelear, J. E., 1961. Direct Numerical Calculation of Nonlinear Ocean Waves. *J. Geophys. Res.,* 66(2), pp. 501-508.

Chitrapu, A. S., Saha, S. & Salpekar, V. Y., 1998. *Time-domain simulation of spar platform response in random waves and current.* Lisbon, Portugal, OMAE' 98.

Clamond, D., 2003. Cnoidal-type surface waves in deep water. *Journal of Fluid Mechanics,* Volume 489, pp. 101-120.

Clamond, D., Francius, M., Grue, J. & Kharif, C., 2006. Long time interaction of envelope solitons and freak wave formations. *European Journal of Mechanics B/Fluids,* Volume 25, pp. 536-553.

Clauss, G. F. & Kuehnlein, W. L., 1994. Seakeeping Tests of Marine Structures with Deterministic Wave Groups and Tank Side Wall Wave Absorbers. *7th Intl. Conf. on the Behaviour of Offshore Structures,* Volume 2, pp. 769-785.

Cokelet, E. D., 1977b. Steep gravity waves in water of arbitrary uniform depth. *Philosophical Transactions of the Royal Society of London A: Mathematical, Physical and Engineering Sciences,* 286(1335), pp. 183-230.

Dean, R. G., 1965. Stream Function Representation of Nonlinear Ocean Waves. *J. Geophys. Res.,* 70(18), pp. 4561-4572.

Dean, R. G., 1974. *Evaluation and development of water wave theories for engineering application (Vol. 2),* Gainesville, Florida, USA: US Coastal Engineering Research Center.

Dean, R. G. & Dalrymple, R. A., 1991. *Water Wave Mechanics for Engineers and Scientists.* Advanced Series on Ocean Engineering-Vol. 2 ed. Singapore: World Scientific Publishing Co..

Dean, R. G. & Perlin, M., 1986. Intercomparison of near bottom kinematics by several wave theories and field and laboratory data. *Coastal Engineering,* 9(5), pp. 399-437.

De, S. C., 1955. Contributions to the theory of Stokes waves. *Mathematical Proceedings of the Cambridge Philosophical Society,* 51(4), pp. 713-736.

Dias, F. & Kharif, C., 1999. Nonlinear gravity and capillary-gravity waves. *Annual review of fluid mechanics,* 31(1), pp. 301-346.

DNV-GL, 2014. *Control of Floating Wind Turbines: The Challenge and the Stakes-Presentation,* Aberdeen: Patrick Rainey - All Energy Exhibition and Conference.

DNVGL-RP-C205, 2017. *Environmental conditions and environmental loads,* August 2017: DNV GL AS.

Dysthe, K. B., 1979. Note on a modification to the nonlinear Schrödinger equation for application to deep water waves. *Proc. R. Soc. Lond. A,* Volume 369, pp. 105-114.

EESI, 2010. *Offshore Wind Energy,* Fact Sheet: Environmental and Energy Study Institute.

Eppler, R., 1990. *Airfoil Design and Data.* 1st ed. Berlin: Springer-Verlag.

ETI, 2015. *Options, Choices, Actions,* UK scenarios for a low carbon energy system transition:

Energy Technologies Institute.

EWEA, 2013. *Deep water-The next step for offshore wind energy,* : A report by European Wind Energy Association.

Faltinsen, O.M., 1990. *Sea loads on Ships and Offshore structures.* 1st ed. New York: Cambridge University Press.

Fedele, F., 2015. On the kurtosis of deep-water gravity waves. *Journal of Fluid Mechanics,* Volume 782, pp. 25-36.

Fenton, J. D., 1979. A high-order cnoidal wave theory. *Journal of Fluid Mechanics,* 94(1), pp. 129-161.

Fenton, J. D., 1985. A fifth-order Stokes theory for steady waves. *Journal of Waterway Port Coastal and Ocean Engineering,* 111(2), pp. 216-234.

Fenton, J. D., 1985. A fifth-order Stokes theory for steady waves. *J. Waterway Port Coastal and Ocean Engineering,* 111(2), p. 216–234..

Fenton, J. D., 1988. The numerical solution of steady water wave problems. *Comp. Geosci.,* 14(3), pp. 357-368.

Fenton, J. D., 1990. Nonlinear wave theories. *The Sea,* 9(1), pp. 3-25.

Forristall, G. Z., 1985. Irregular wave kinematics from a kinematic boundary condition fit (KBCF). *Appl. Ocean Res.,* 7((4)), pp. 202-212.

Forristall, G. Z., 2000. Wave crest distributions: Observations and second-order theory. *Journal of Physical Oceanography,* 30(8), pp. 1931-1943.

Froude, R. E., 1889. On the part played in propulsion by differences of fluid pressure. *Trans. Inst. Naval Arch,* Volume 30, p. 390.

Fylling, I., Mo, K., Merz, K. & Luxcey, N., 2009. *Floating wind turbine - Response analysis with rigid-body model.* Stockholm, Sweden, European Offshore Wind.

Gibson, R. & Swan, C., 2007. The evolution of large ocean waves: the role of local and rapid spectral changes. *Proceedings of the Royal Society of London A: Mathematical, Physical and Engineering Sciences,* 463(2077), pp. 21-48.

Gibson, R., Swan, C. & Tromans, P., 2007. Fully nonlinear statistics of wave crest elevation calculated using a spectral response surface method: Applications to unidirectional sea states. *Journal of physical oceanography,* 37(1), pp. 3-15.

Glauert, H., 1926. *The analysis of experimental results in the windmill brake and vortex ring states of an airscrew,* London: Aeronautical Research Committee: Reports and Memoranda No. 1026.

Glauert, H., 1935. *"Airplane propellers", in Aerodynamic Theory.* W. F. Durand ed. Berlin: Springer Verlag.

Goullet, A. & Choi, W., 2011. A numerical and experimental study on the nonlinear evolution of long-crested irregular waves. *Physics of Fluids,* 23(016601), pp. 1-15.

GWEC, 2017. *A Snapshot of Top Wind Markets in 2017-Global Wind Report,* : Global Wind Energy Council.

GWEC, 2018. Global Wind Statistics 2017 (PDF). *GWEC.net.*

Hansen, M. et al., 2006. State of the art in wind turbine aerodynamics and aeroelasticity. *Progress in Aerospace Sciences,* 42(4), pp. 285-330.

Henderson, K. L., Peregrine, D. H. & Dold, J. W., 1999. Unsteady water wave modulations: fully nonlinear solutions and comparison with the nonlinear Schrodinger equation. *Wave motion,* 29(4), pp. 341-361.

Hildebrandt, A. & Sriram, V., 2014. *Pressure Distribution and Vortex Shedding Around a Cylinder due to a Steep Wave at the Onset of Breaking from Physical and Numerical Modeling.* Busan, Korea, The Twenty-fourth International Ocean and Polar Engineering Conference.

Hu, S. J. & Zhao, D., 1993. Non-Gaussian Properties of Second Order Random Waves. *Journal of Engineering Mechanics,* 119(2), pp. 344-364.

Hu, Z., Tang, W., Xue, H. & Zhang, X., 2015. Numerical study of Rogue waves as nonlinear Schrödinger breather solutions under finite water depth. *Wave Motion,* Volume 52, pp. 81-90.

Ian Baring-Gould, 2013. *Offshore wind energy market review,* : NREL/PR-7A20-58974.

IEC 61400-1, 2005. *Wind turbines – Part 1: Design Requirements.* 3rd ed. Geneva,Switzerland: International Electrotechnical Commission (IEC).

IEC 61400-3, 2009. *Wind turbines - Part 3: Design Requirements for Offshore Wind Turbines.* 1st ed. Geneva, Switzerland: International Electrotechnical Commission (IEC).

Jagdale, S. & Ma, Q. W., 2010. *Practical Simulation on Motions of a TLP-Type Support Structure for Offshore Wind Turbines.* Beijing, China, 20th International Offshore and Polar Engineering Conference.

Jagdale, S. & Ma, Q. W., 2012. *Effect of Non-linear Wave Forces on Dynamic Response of Floating Offshore Wind Turbine.* Rhodes, Greece, 22nd International Offshore and Polar Engineering Conference.

Johnson, R., 1997. *A modern introduction to the mathematical theory of water waves.* Cambridge: Cambridge University Press.

Jonkman, J. et al., 2010. *Offshore Code Comparison Collaboration within IEA Wind Task 23: Phase IV Results Regarding Floating Wind Turbine Modelling,* Warsaw, Poland: NREL/CP-500-47534.

Jonkman, J. M., 2007. *Dynamic Modeling and Loads Analysis of an Offshore Floating Wind Turbine,* Colorado: NREL/TP-500-41958.

Jonkman, J. M., 2009. Dynamics of Offshore Floating Wind Turbines-Model Development and Verification. *Wind Energy 12,* 12(5), pp. 459-492.

Jonkman, J. & Matha, D., 2011. Dynamics of offshore floating wind turbines-analysis of three concepts. *Wind Energy,* 14(4), pp. 557-569.

Kaimal, J. C., Wyngaard, J. C., Izumi, Y. & Cote, Y. R., 1972. Spectral characteristics of surface layer turbulence. *Q.J.R. Meteorol. Soc. ,* Volume 98, pp. 563-598.

Kashiwagi, M., 2000. Nonlinear simulations of wave-induced motions of a floating body by means of the mixed Eulerian-Lagrangian method. *Proceedings of the Institution of Mechanical Engineers. Part C, Journal of Mechanical Engineering Science,* Volume 214, pp. 841-855.

Kelvin, L., 1887. On the waves produced by a single impulse in water of any depth, or in a dispersive medium. *Proceedings of the Royal Society of London. Ser. A.,* Volume 42, pp. 80-85.

Kharif, C., Pelinovsky, E. & Slunyaev, A., 2009. *Rogue Waves in the Ocean.* Berlin Heidelberg: Springer-Verlag.

Kim M H & Chen W, 1994. Slender body approximation for slowly varying wave loads in multi-directional waves. *Applied Ocean Research,* 16(3), pp. 141-163.

Kim, C. H., 2008. *Nonlinear Waves and Offshore Structure.* Singapore: World Scientific Publishing Co. Pte. Ltd.

Kim, C. H., Randall, R. E., Boo, S. Y. & Krafft, M. J., 1992. Kinematics of 2-D Transient Water Waves Using Laser Doppler Anemometry. *Journal of Waterways, Port, Coastal, and Ocean Engineering, ASCE,* 118(2), pp. 147-165.

Kim, C., Randall, R., Boo, S. & Kraft, M., 1990. *Experimental Study of Kinematics of Large Transient Wave in 2-D Wave Tank.* 7-10 May, Houston, Texas, Proc. 22nd Annual Offshore Tech Conf - OTC 6364.

Kim, M., 1991. Second-Order Sum-Frequency Wave Loads on Large-Volume Structures. *Appl. Ocean Res.,* 13(6), pp. 287-296.

Kjeldsen, S. P., 1982. *2- and 3- Dimensional Deterministic Freak Waves.* Cape Town, South Africa, Int Conf on Coastal Eng.

Kjeldsen, S. P., 1990. "Breaking Waves",. In: O. T. Gudmestad & A. Torum, eds. *Water Wave Kinematics.* A. Torum and O.T. Gudmestad ed. Trodheim, Norway: Kluwer Academic Publishers, pp. 453-473.

Knauer, A. & Hagen, E., 2007. *Simulation of Floating Wind Turbine Concept.* Berlin, Germany, 2nd European Offshore Wind Conference.

Koo, W. & Kim, M., 2004. Freely floating body simulation by a 2D fully nonlinear numerical wave tank. *Ocean Engineering,* 31(16), p. 2011–2046..

Koo, B., Goupee, A. J., Lambrakos, K. & Kimball, R. W., 2012. *Model Tests for a Floating Windturbine on Three Different Floaters.* New York, Proceedings of the 31st International Conference on Ocean, Offshore and Artic Engineering, American Society of Mechanical Engineers.

Kraft, M. J. & Kim, C. H., 1987. *Extreme transient water waves generation at Texas A&M University,* Houston,Texas: COE report 294..

Kriebel , D. L., 2000. Efficient simulation of extreme waves in a random sea. *Abstract of*

Workshop, "Rogue Waves 2000", pp. 29-39.

Kriebel, D. L. & Alsina, M. V., 2000. *Simulation of Extreme Waves in a Background Random Sea.* Seatle, USA, The Tenth International Offshore and Polar Engineering Conference, pp.31-37.

Kühn, M., Schmidt, A. & Gutiérrez, M., 2017. *Wind Energy Fundamentals.* First edition ed. Oldenburg: Carl von Ossietzky University of Oldenburg.

Lamb, H., 1916. *Hydrodynamics (Fourth Edition).* Cambridge: Cambrige University Press.

Larsen, T. J. & Hansen, A. M., 2015. *How 2 HAWC2, The User's Manual.,* Roskilde, Denmark: Risø National Laboratory,Technical University of Denmark.

Larsen, T. J. & Hanson, T. D., 2007. A method to avoid negative damped low frequent tower vibrations for a floating, pitch controlled wind turbine. *Journal of Physics,* 75(1), pp. 1-11.

Le Méhauté, B., 1976. *An Introduction to Hydrodynamics and Water Waves.* Berlin: Springer Berlin Heidelberg.

Lee, K. H., 2005. *Responses of Floating Wind Turbines to Wind and Wave Excitation,* Massachusetts Institute of Technology, Dept. of Ocean Engineering: Msc Thesis,.

Lee, C. & Newman, J., 2006. *WAMIT (R) User Manual Version 6.4S.* Chestnut Hill, MA, USA: WAMIT, Inc..

Li , J., Liu, S. & Hong, K. Y., 2008. Numerical study of two-dimensional focusing waves. *China Ocean Engineering,* 22(2), p. 253–266.

Lighthill, M.J., 1986b. Fundamentals concerning wave loading on offshore structures. *Journal of Fluid Mechanics,* Volume 173, pp. 667-681.

Lighthill, J., 1979. *Waves and hydrodynamic loading.* Cranfield, Bedford, England., Proc. 2nd Int. Conf. Behaviour of Off-Shore Structures, pp. 1-40.

Lighthill, M., 1979. Waves and hydrodynamic loading. *Proc. 2nd Int. Conf. on Behaviour of Offshore Structures,* Volume 1, pp. 1-40.

Lin, L., Zhen, G. & Moan, T., 2015. Joint distribution of environmental condition at five European offshore sites for design of combined wind and wave energy devices. *Journal of Offshore Mechanics and Arctic Engineering,* 137(3), pp. 1-16.

Liu, P. C., 2007. A chronology of freauqe wave encounters. *Geofizika,* 24(1), pp. 57-70.

Liu, S. & Hong, K. Y., 2004. The generation method of three-dimensional focusing wave and its properties. *Acta Oceanologica Sinica,* 26(6), pp. 133-142.

Longuet-Higgins, M. S., 1952. On the statistical distribution of the heights of sea waves. *Journal of Marine Research,* 11(3), pp. 245-266.

Longuet-Higgins, M. S., 1963. The effect of non-linearities on statistical distributions in the theory of sea waves. *J. Fluid Mech.,* Volume 17, pp. 459-480.

Longuet-Higgins, M. S., 1974. *Breaking Waves in Deep or Shallow Water.* MIT, Proc. 10th Conf. on Naval Hydrodynamics.

Low Y.M., 2009. Frequency domain analysis of a tension leg platform with statistical linearization of the tendon restoring forces. *Journal of Marine Structures,* 22(3), pp. 480-503..

Lukomsky, V. P., Gandzha, I. & Lukomsky, D., 2002a. Steep sharp-crested gravity waves on deep water. *Physical review letters,* 89(16), p. 164502.

Lukomsky, V. P., Gandzha, I. S. & Lukomsky, D. V., 2002b. Computational analysis of the almost-highest waves on deep water. *Computer physics communications,* 147(1), pp. 548-551.

Maciel, J. G., 2012. *The WindFloat Project: Deep Offshore Wind - An Opportunity for Europe,* Brest, France: The Atlantic Forum organized by European Commission.

Madsen & Krogsgaard, 2010. Offshore Wind Power 2010, Archived June 30, 2011, at the Wayback Machine. *BTM consult*.

Manners, W. & Rainey, R., 1992. Hydrodynamic-forces on fixed submerged cylinders. *Proc. R Soc. London Ser A – Math Phys Engineering Science,* Volume 436, pp. 13-32..

Mansard, E. & Funke, E., 1982. *A New Approach to Transient Wave Generation.* Cape Town, South Africa, Proc. 18th Int. Conf. on Coastal Eng.

Manwell J, McGowan J & Rogers A, 2009. *Wind Engery Explained: Theory, Design and Application.* 2nd ed. University of Massachusetts, USA: John Wiley and Sons Ltd.

Ma, Q. W., 1998. *Numerical simulation of nonliear interaction between structures and steep waves (PhD Thesis).* London: Department of Mechanical Enginieering, University College London, UK.

Ma, Q. W., 2007. Numerical generation of freak waves using MLPG_R and QALE-FEM methods. *CMES-Computer Modelling in Engineering & Sciences,* 18(3), pp. 223-234.

Ma, Q. W., 2008a. A new meshless interpolation scheme for MLPG_R method. *Computer Modeling in Engineering & Sciences,* 23(2), pp. 75-90.

Ma, Q. W. & Patel, M. H., 2001. On the non-linear forces acting on a floating spar platform in ocean waves. *Applied Ocean Research,* 23(1), p. 29–40.

Ma, Q. W. & Patel, M. H., 2001. On the non-linear forces acting on a floating spar platform in ocean waves. *Applied Ocean Research,* 23(1), pp. 29-40.

Ma, Q. W., Wu, G. X. & Eatock-Taylor, R., 2001b. Finite element simulation of fully non-linear interaction between vertical cylinders and steep waves. Part 2: Numerical results and validation. *Int. J. Numer. Meth. Fluids,* Volume 36, pp. 287-308.

Ma, Q. W. & Yan, S., 2006. Quasi ALE finite element method for nonlinear water waves. *Journal of Computational Physics,* Volume 212, pp. 52-72.

Ma, Q. W. & Yan, S., 2009. QALE-FEM for numerical modelling of non-linear interaction between 3D moored floating bodies and steep waves. *International Journal for Numerical Methods in Engineering,* 78(6), pp. 713-756.

Ma, Q. W. & Yan, S., 2009. QALE-FEM for numerical modelling of non-linear interaction between 3D moored floating bodies and steep waves. *International journal for numerical*

methods in engineering, 78(6), pp. 713-756.

Ma, Q. W. & Zhou, J. T., 2009. MLPG_R method for numerical simulation of 2D breaking waves. *Computer Modeling in Engineering & Sciences,* 43(3), pp. 277-304.

Marine Scotland, 2014. *Potential Scottish Test Sites for Deep Water Floating Wind Technologies,* : Regional Location Guidance.

MARINTEK, 2008. *SIMO - Theory Manual Version 3.6, rev: 1,* Trondheim, Norway: SINTEF.

MARINTEK, 2010. *RIFLEX - Theory Manual Finite Element Formulation,* Trondheim, Norway: SINTEF, P.O.Box 4125 Valentinlyst NO-7450.

Marion, J. B., 1965. *Classical Dynamics of Particles and Systems.* 1st ed. London: Academic Press.

Matha, D, 2009. *Model Development and Loads Analysis of an Offshore Wind Turbine on a Tension Leg Platform,* University of Colorado - Boulder: NREL/SR-500-45891.

Mei, C.C., 1989. *The Applied Dynamics of Ocean Surface waves.* 15th ed. Singapore: World Scientific.

Mei, C., 1983. *The applied dynamics of ocean surface waves.* New York: Wiley.

Mekha, B. B., Weggel, D. C., Johnson, C. P. & Rosset, J. M., 1996. *Effect of second order diffraction forces on the global response of spars.* Los Angeles, CA, USA, ISOPE 96.

Mori, N. & Yasuda, T., 2000. *Effects of high-order nonlinear wave–wave interactions on gravity waves.* Brest, France, In Proceedings of the Rogue Waves 2000.

Morison, J. R., O'Brien, M. P., Johnson, J. W. & Schaaf, S. A., 1950. The force exerted by surface waves on piles. *Petroleum Transactions, American Institute of Mining Engineers,* 189(:), pp. 149-154.

Musial, W., Butterfield, S. & Boone, A., 2003. *Feasibility of Floating Platform Systems for Wind Turbine,* National Renewable Energy Laboratory, Golden CO: NREL/CP-500-34874.

Myhr, A., Maus, K. J. & Nygaard, T. A., 2011. *Experimental and Computational Comparisons of the OC3-HYWIND and Tension-Leg-Buoy (TLB) Floating Wind Turbine Conceptual Designs.* Maui, Hawaii, USA, 21st International Offshore and Polar Engineering Conference.

Naess, A. & Ness, G., 1992. Second-Order, Sum-Frequency Response Statistics of Tethered Platforms in Random Waves. *Appl.Ocean Res,* 14(1), pp. 23-32.

Nelder, J. A. & Mead, R., 1965. A simplex method for function minimization. *The Computer Journal,* 7(4), pp. 308-313.

Nihei, Y. & Fujioka, H., 2011. Aerodynamic Effects of TLP type Wind Turbines and Predictions of the Electricity They Generate. *Journal of Marine Science and Applications,* 10(2), pp. 139-149.

Nikolkina, I. & Didenkulova, I., 2012. Catalogue of rogue waves reported in media in 2006-2010. *Natural hazards,* 61(3), pp. 989-1006.

Ning, D. Z. et al., 2009. Free-surface evolution and wave kinematics for nonlinear uni-directional

focused wave groups. *Ocean Engineering,* 36(15), pp. 1226-1243.

Onorato, M. et al., 2006. Extreme waves, modulational instability and second order theory: wave flume experiments on irregular waves. *European Journal of Mechanics-B/Fluids,* 25(5), pp. 586-601.

ORECCA, 2011. *European Offshore Renewable Energy Roadmap,* : ORECCA (Offshore Renewable Energy Conversion platforms Coordination Action) Project.

Patterson, M. M., 1974. *Oceanographic Data from Hurricane Camille.* Houston, Texas, Offshore Technology Conference.

Paulling, J. R. & Webster, W. C., 1986. *A Consistent Large-Amplitude Analysis of the Coupled Response of a TLP and Tension System.* Tokyo, Japan, Proceedings of the fifth International Offshore Mechanics and Arctic Engineering Symposium.

Pei, Y., Zhang, N. & Zhang , Y., 2007. Efficient generation of freak waves in laboratory. *China Ocean Engineering,* 21(3), pp. 515-523.

Peyard, C., 2015. *Offshore Wind Turbine Foundations.* Laboratoire d'Hydraulique St Venant: EDF R&D - LNHE.

Phillips, O. M., 1960. On the dynamics of unsteady gravity waves of finite amplitude. Part 1. The elementary interactions. *Journal of Fluid Mechanics,* 9(2), pp. 193-217.

Phillips, O. M., 1981. Wave interactions - the evolution of an idea. *Journal of Fluid Mechanics,* Volume 106, pp. 215-227.

Price, W. G. & Bishop, R., 1974. *Probabilistic Theory of Ship Dynamics.* N.Y., John Wiley and Sons.

Prowell, I. et al., 2013. *Numerical Prediction of Experimentally Observed Behavior of a Scale Model of an Offshore Wind Turbine.* Houston, Texas, Offshore Technical Conference.

Rainey RCT, 1989. A new equation for wave loads on offshore structures. *Journal of Fluid Mechanics,* Volume 204, pp. 295-324.

Rainey RCT, 1995. Slender-body expressions for the wave load on offshore structures. *Proc. R Soc. London Ser A – Math Phys Sci,* 450(1939), pp. 391-416.

Rankine, W. J., 1865. On the mechanical principles of the action of ship propellers. *Trans. Inst. Naval Arch.,* Volume 6, pp. 13-39.

Rapp, R. J. & Melville, W. K., 1990. Laboratory measurements of deep water breaking waves. *Phil. Trans. R. Soc. London,* A(331), pp. 735-800.

Rayleigh, L., 1876. On waves. *Phil. Mag,* 1(5), pp. 257-279.

Reid, R. O., 1958. *Correlation of water level variations with wave forces on a vertical pile for non-periodic waves.* Gainesville, Florida, Proceedings of 6th Conference on Coastal Engineering.

Rienecker, M. M. & Fenton, J. D., 1981. A Fourier approximation method for steady water waves. *Journal of Fluid Mechanics,* Volume 104, pp. 119-137.

Rocha, P. C. et al., 2014. k–ω SST (shear stress transport) turbulence model calibration: A case

study on a small scale horizontal axis wind turbine. *Energy,* Volume 65, pp. 412-418.

Roddier, D., Cermelli, C. & Weinstein, A., 2009. *WindFloat: A Floating Foundation for Offshore Wind Turbines, Part I Design Basis and Qualification Process.* Honolulu, Hawaii, USA, 28th International Conference on Ocean, Offshore and Arctic Engineering-OMAE2009-79229.

Rodenbusch, G. & Forristall, G. Z., 1986. *An empirical model for random directional wave kinematics near the free surface.* Houston, Proc. Offshore Technology Conf. OTC-5097.

Rosenthal, W. & Lehner, S., 2008. Rogue Waves: Results of the MaxWave Project. *J. Offshore Mech. Arct. Eng,* 130(2), pp. 1-8.

Sand, S. et al., 1990. Freak Wave Kinematics. In: A. Torum and O.T. Gudmestad, ed. *Water Wave Kinematics.* Trondheim, Norway: Kluwer Academic, Publishers, pp. 535-549.

Sarpkaya, T. & Isaacson, M., 1981. *Mechanics of wave forces on offshore structures.* 1st ed. University of California: Van Norstrand Reinhold.

Schwartz, L. W., 1974. Computer extension and analytic continuation of Stokes' expansion for gravity waves. *Journal of Fluid Mechanics,* 62(3), pp. 553-578.

Schwartz, L. W. & Vanden-Broeck, J. M., 1979. Numerical solution of the exact equations for capillary–gravity waves. *Journal of Fluid Mechanics,* 95(1), pp. 119-139.

Sclavounos, P, Tracy, C & Lee, S, 2007. *Floating Offshore Wind Turbines: Responses in a Seastate Pareto Optimal Designs and Economic Assessment.* Estoril, Portugal, Proc of 27th Int Conf on Offshore Mechanics and Arctic Engineering,OMAE 2008-57056.

Scottish Enterprise, 2015. *Floating Offshore Wind Scotland's Opportunity,* Glasgow: All-Energy Exhibition and Conference.

Sebastian, T. & Lackner, M., 2011. *Offshore Floating Wind Turbines - An Aerodynamic Perspective.* Orlando, Florida, 49th AIAA Aerospace Sciences Meeting including the New Horizons Forum and Aerospace Exposition.

Sedaghatizadeh, N. et al., 2018. Modelling of wind turbine wake using large eddy simulation. *Renewable Energy,* Volume 115, pp. 1166-1176.

Sharma, J. N. & Dean, R. G., 1979. *Development and evaluation of a procedure for simulating a random directional second order sea surface and associated wave forces.* Newark, USA: University of Delaware.

Shim S., 2007. *Coupled Dynamic Analysis of Floating Offshore Wind Farm,* Texas A&M University: MS Thesis.

Shim, S. & Kim, M. H., 2008. *Rotor-Floater-Tether Coupled Dynamic Analysis of Offshore Floating Wind Turbines.* Vancouver, BC, Canada, 18th International Offshore and Polar Engineering Conference.

Skaare, B. et al., 2007. *Integrated Dynamic Analysis of Floating Offshore Wind Turbines.* Milan, Italy, European Wind Energy Conference (EWEC).

Skourup, J., Ottensen Hansen , N. & Andreasen, K., 1996. Non-Gaussian Extreme Waves in the

Central North Sea. *Proc. Offshore Mechanics and Arctic Engineering Conf.,* Volume I-A, pp. 25-32.

Slunyaev, A. et al., 2013. Super rogue waves in simulations based on weakly nonlinear and fully nonlinear hydrodynamic equations. *Physical Review E,* 88(1), pp. 012909-1 to 012909-10.

Snel, H. et al., 1993. *Sectional prediction of 3-D effects for stalled flow on rotating blades.* Germany, Proc. Eur. Community Wind Energy.

Snel, H. & Schepers, J. G., 1995. *Joint Investigation of Dynamic Inflow Effects and Implementation of an Engineering Method,* Petten: Energy Research Centre of the Netherlands: ECN-C-94-107.

Sorensen, J. N., 2019. *Viscwind. Viscous effects on wind turbine blades,* Technical University of Denmark: final report for the Joule III Project. ET-AFN-9902. Department of Energy Engineering.

Sorensen, J.N. & Mikkelsen, R., 2001. *On the validity of the blade element momentum method.* Copenhagen, Denmark, Proc. Eur. Wind Energy Conf.

Sriram, V., Ma, Q. W. & Schlurmannc, T., 2014. A hybrid method for modelling two dimensional non-breaking and breaking waves. *Journal of Computational Physics,* Volume 272, pp. 429-454.

Sriram, V., Schlurmann, T. & Schimmels, S., 2013. *Focused Wave Evolution in Intermediate Water Depth Using First and Second Order Wave Maker Theory.* Anchorage, Alaska, The Twenty-third International Offshore and Polar Engineering Conference.

Stansberg, C. T., 1993. *On Spectral Instabilities and Development of Nonlinearities in Deep-Water Propagating Wave Trains.* Venice, Italy, Proc. Vol. I, 23rd ASCE Int. Conf. on Coastal Engineering.

Stansberg, C. T., 1998a. *On the Nonlinear Behaviour of Ocean Wave Groups.* Virginia Beach, VA, USA, Proc. 3rd Int. ASCE Symp. on Wave Measurement and Analysis (WAVES'97).

Stansberg, C. T., 2000. *Nonlinear Extreme Wave Evolution in Random Wave Groups.* Trondheim, Norway, Proceedings of the Tenth (2000) International Offshore and Polar Engineering Conference.

Stoddard, F. S. & Eggleston, D. M., 1987. *Wind turbine engineering design.* 1st ed. : Kluwer Academic Publishers.

Stoker, J. J., 2011. *Water waves: The mathematical theory with applications.* New York: John Wiley & Sons.

Stokes G. G., 1847. On the theory of oscillatory waves. *Transactions of the Cambridge Philosophical Society,* Volume 8, pp. 441-455.

Sun, Y., Liu, S. & Zang , J., 2009. Experimental study of 2-D focused wave in flume. *Journal of Dalian University of Technology,* 49(6), pp. 951-957.

Takezawa, S. & Hirayama, T., 1977. Advanced Experimental Techniques for Testing Ship Models in Transient Water Waves-Part 2. The Controlled Transient Water Waves for Using in Ship Motion Tests. *Inst. of Mech. Eng.,* pp. 37-54.

Tanizawa, K & Minami, M, 2001. *Development of a 3D-NWT for simulation of running ship motions in waves.* Hiroshima, Japan., International Workshop on Water Waves and Floating Bodies.

Tillessen, T., 2010. High demand for wind farm installation vessels. *Hansa International Maritime Journal,* 147(8), pp. 170-171.

Toffoli, A. et al., 2010. Evolution of weakly nonlinear random directional waves: laboratory experiments and numerical simulations. *Journal of Fluid Mechanics,* Volume 664, pp. 313-336.

Toffoli, A. et al., 2006. Second-Order Theory and Setup in Surface Gravity Waves: A Comparison with Experimental Data. *Journal of Physical Oceanography,* Volume 37, pp. 2726-2739.

Trulsen, K. & Dysthe, K. B., 1996. A modified nonlinear Schrödinger equation for broader bandwidth gravity waves on deep water. *Wave motion,* Volume 24, pp. 281-298.

Trulsen, K., Stansberg, C. & Velarde, M., 1999. Laboratory evidence of three-dimensional frequency downshift of waves in a long tank. *Physics of Fluids,* 11(1), pp. 235-237.

Tucker, M. J., Challenor, P. G. & Carter, D. T., 1984. Numerical simulation of a random sea: a common error and its effect upon wave group statistics. *Applied Ocean Research,* 6(2), pp. 118-122.

Vijfhuizen, W. J. M. J, 2006. *Design of a Wind and Wave Power Barge,* Universities of Glasgow and Strathclyde, Glasgow, Scotland: M.S. Dissertation, Department of Naval Architecture and Mechanical Engineering,.

Ward, E. G., 1979. *Ocean data gathering program-An overview..* Houston, Texas, Proc. 6th Annual Offshore Tech. Conference.

Westhuis, J., Groesen, E. v. & Huijsmans, R., 2001. The numerical simulation of nonlinear waves in a hydrodynamic model test basin. *Journal of Waterway, Port, Coastal, and Ocean Engineering,* 127(6), pp. 334-342.

Wheeler J. D., 1969. *Method for calculating forces produced by irregular waves.* 18-21 May, Houston, Texas, Offshore Technology Conference.

Whitham, G. B., 1967. Non-linear dispersion of water waves. *Journal of Fluid Mechanics,* 27(2), pp. 399-412.

Wilson, R. E. & Lissaman, P. B. S., 1974. *Applied aerodynamics of wind power machines,* Oregon State Univ: Report NSF/RA/N-7413. NTIS PB 238594.

Wu, G. X. & Taylor, E. R., 2003. The coupled finite element and boundary element analysis of nonlinear interactions between waves and bodies. *Ocean Engineering,* Volume 30, pp. 387-400.

Wu, X., 2017. Inflow Turbulence Generation Methods. *Annual Review of Fluid Mechanics,* Volume 49, pp. 23-49.

Xia, W., Ma, Y. & Dong, G., 2015. *Numerical simualtion of freak waves in random sea state.* IIT Madras, Chennai, India, 8th International Conference on Asian and Pacific Coasts (APAC 2015).

Yan, S., 2006. Numerical simulation on nonlinear response of moored floating structures to steep

waves. *PhD thesis. School of Engineering and Mathematical Sciences. City University London.*

Yan, S. & Ma, Q. W., 2007. Numerical simulation of fully non-linear interaction between steep waves and 2D floating bodies using the QALE-FEM method. *Journal of Computational Physics,* 221(2), pp. 666-692.

Yan, S. & Ma, Q. W., 2009. Nonlinear simulation of 3-D freak waves using a fast numerical method. *International Journal of Offshore and Polar Engineering,* 19(3), pp. 168-175.

Yan, S. & Ma, Q. W., 2010. QALE-FEM for modelling 3D overturning waves. *International Journal for Numerical Methods in Fluids,* 63(6), pp. 743-768.

Yan, S., Ma, Q. W. & Adcock, T. A. A. A., 2010. *Investigation of freak waves on uniform current.* Harbin, Proc. 25th Int Workshop on Water Waves and Floating Bodies.

Yan, S. et al., 2015. *Numerical and Experimental Studies of Moving Cylinder in Unidirectional Focusing Waves.* Kona, Hawaii, USA, Proceedings of the 25th International Offshore and Polar Engineering Conference.

Yan, S. et al., 2013. *Fully Nonlinear Simulation of Tsunami Wave Impacts on Onshore Structures.* Alaska, USA, The Twenty-third International Offshore and Polar Engineering Conference.

Yasuda, T., Mori, N. & Nakayama, S., 1998. *Characteristics of Giant Freak Waves Observed in the Sea of Japan.* Virginia Beach, VA, USA, Proc. 3rd Int. ASCE Symp. on Wave Measurement and Analysis (WAVES'97).

Zakharov, V. E., 1968. Stability of periodic waves of finite amplitude on the surface of a deep fluid. *Sov. Phys. J. Appl. Mech. Tech. Phys,* Volume 9, pp. 86-94.

Zhang, J., Randall, R. E. & Spell, C. A., 1991. *On Wave Kinematics Approximate Methods.* Houston, Texas, 23rd Annual Offshore Technology Conference, OTC 6522.

Zhao, X., Sun, Z. & Liang, S. ., 2009. Efficient focusing models for generation of freak waves. *China Ocean Engineering,* 23(3), pp. 429-440.

Zhou, J. T. & Ma, Q. W., 2010. MLPG method based on rankine source solution for modelling 3D breaking waves. *CMES - Computer Modeling in Engineering and Sciences,* 56((2)), pp. 179-210.

Zou, J. & Kim, C. H., 2000. *Generation of Strongly Asymmetric Wave in Random Seaway.* Seattle, Proceeding of The 10th International Offshore and Polar Engineering Conference, pp. 95-102.

APPENDIX A

Transformation Matrix

This Appendix presents the transformation matrix derived to transfer co-ordinate from body-fixed axis system (b-system) to space fixed axis system (g-system) based on Euler angles. In addition, a transformation matrix derived to transfer co-ordinate from member fixed axis system (m-system) to body fixed axis system (b-system) is also presented. Furthermore, a relationship derived between angular velocity and Euler angles is also presented. A similar procedure mentioned by Marion (1965) is employed.

A.1. Transformation between body (b-system) to space (g-system) fixed axis system

First space fixed axis system $o_g x_g y_g z_g$ is defined. This axis system moves with the translation of body and is always parallel to X-, Y-, and Z-axis. This axis system coincides with the body fixed axis system $o_b x_b y_b z_b$ when the body is at rest. However, they will not coincide if the body has rotations, as shown in Figure A-1.

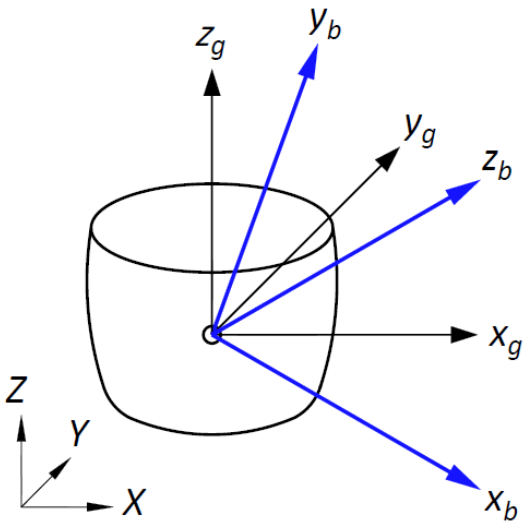

Figure A-1 Two reference axis system

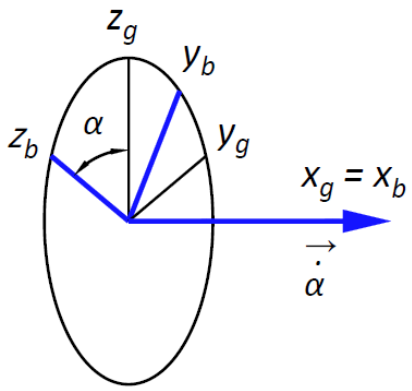

Figure A-2 Rotation about X

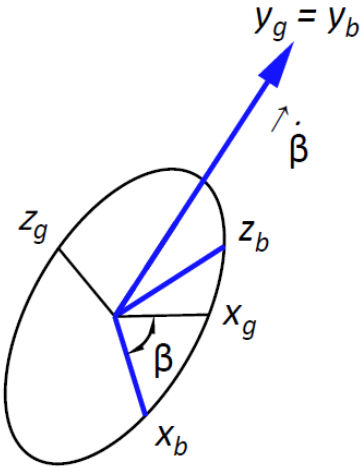

Figure A-3 Rotation about Y

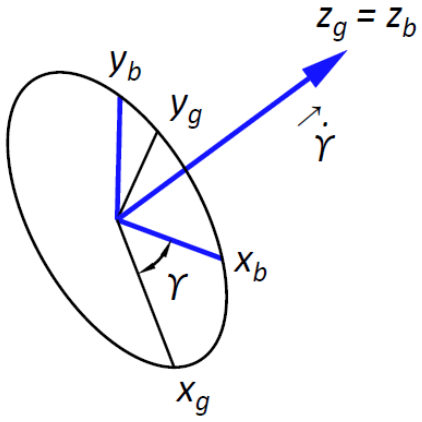

Figure A-4 Rotation about Z

A co-ordinate from body fixed $o_b x_b y_b z_b$ axis system to space fixed $o_g x_g y_g z_g$ axis system can be transformed by following three successive rotations:

1. The first rotation is about x-axis ($o_b x_b y_b z_b$ to $o_g x_g y_g z_g$) by an angle α. After the rotation, y_b and z_b axis lies on a plane determined by x-axis as shown in Figure A-2. The transformation relationship is given by,

$$\begin{Bmatrix} x_g \\ y_g \\ z_g \end{Bmatrix} = \begin{bmatrix} 1 & 0 & 0 \\ 0 & \cos\alpha & -\sin\alpha \\ 0 & \sin\alpha & \cos\alpha \end{bmatrix} \begin{Bmatrix} x_b \\ y_b \\ z_b \end{Bmatrix} = [T_1] \begin{Bmatrix} x_b \\ y_b \\ z_b \end{Bmatrix} \tag{A.1}$$

2. The second rotation is about y-axis ($o_b x_b y_b z_b$ to $o_g x_g y_g z_g$) by an angle β. After the rotation, x_b and z_b axis lies on a plane determined by y-axis as shown in Figure A-3. The transformation relationship is given by,

$$\begin{Bmatrix} x_g \\ y_g \\ z_g \end{Bmatrix} = \begin{bmatrix} \cos\beta & 0 & \sin\beta \\ 0 & 1 & 0 \\ -\sin\beta & 0 & \cos\beta \end{bmatrix} \begin{Bmatrix} x_b \\ y_b \\ z_b \end{Bmatrix} = [T_2] \begin{Bmatrix} x_b \\ y_b \\ z_b \end{Bmatrix} \tag{A.2}$$

3. The third rotation is about z-axis ($o_b x_b y_b z_b$ to $o_g x_g y_g z_g$) by an angle γ. After the rotation, x_b and y_b axis lies on a plane determined by z-axis as shown in Figure A-4. The transformation relationship is given by,

$$\begin{Bmatrix} x_g \\ y_g \\ z_g \end{Bmatrix} = \begin{bmatrix} \cos\gamma & -\sin\gamma & 0 \\ \sin\gamma & \cos\gamma & 0 \\ 0 & 0 & 1 \end{bmatrix} \begin{Bmatrix} x_b \\ y_b \\ z_b \end{Bmatrix} = [T_3] \begin{Bmatrix} x_b \\ y_b \\ z_b \end{Bmatrix} \tag{A.3}$$

where, α, β, and γ are Euler angles corresponding to roll, pitch and yaw motions. The combined transformation matrix can be expressed as,

$$[T_{bg}] = [T_1][T_2][T_3] \tag{A.4}$$

Substituting Eq. (A.1), (A.2), and (A.3) into (A.4) gives,

$$[T_{bg}] = \begin{bmatrix} \cos\beta\cos\gamma & -\cos\beta\sin\gamma & \sin\beta \\ \sin\alpha\sin\beta\cos\gamma + \cos\alpha\sin\gamma & -\sin\alpha\sin\beta\sin\gamma + \cos\alpha\cos\gamma & -\sin\alpha\cos\beta \\ -\cos\alpha\sin\beta\cos\gamma + \sin\alpha\sin\gamma & \cos\alpha\sin\beta\sin\gamma + \sin\alpha\cos\gamma & \cos\alpha\cos\beta \end{bmatrix} \tag{A.5}$$

The matrices in equations (A.1) to (A.3) have the following properties,

$$\underbrace{\left[T_{bg_i}\right]^{-1}}_{inverse} = \underbrace{[T_{bg}]'}_{transpose} \quad (i = 1,2,3) \tag{A.6}$$

Noting the transformation matrix derive in Eq. (A.5), a co-ordinate can be transferred from body-fixed to space-fixed axis system using following relationship,

$$\begin{Bmatrix} x_g \\ y_g \\ z_g \end{Bmatrix} = \begin{Bmatrix} x_c \\ y_c \\ z_c \end{Bmatrix} + [T_{bg}] \begin{Bmatrix} x_b \\ y_b \\ z_b \end{Bmatrix} \tag{A.7}$$

A.2 Transformation between member fixed (m-system) to body fixed (b-system) axis system

The member fixed axis system $o_m x_m y_m z_m$ is defined for horizontal members with its x-axis fixed along its length. With this assumption, it has two rotational axes, i.e., about y_m and z_m axis as shown in Figure A-5.

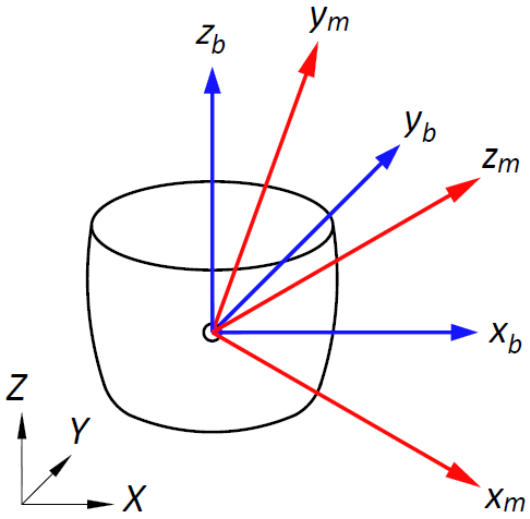

Figure A-5 Two reference axis system

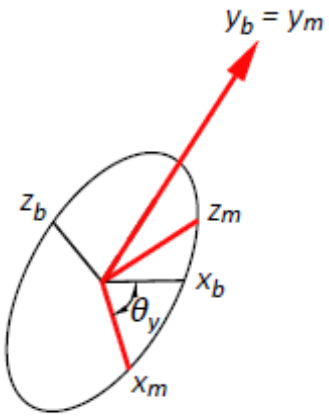

Figure A-6 Rotation about Y

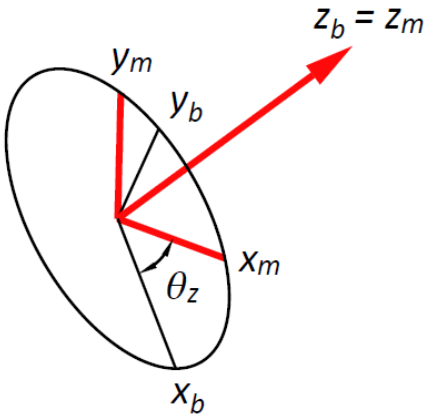

Figure A-7 Rotation about Z

A co-ordinate from member fixed $o_m x_m y_m z_m$ axis system to body fixed $o_b x_b y_b z_b$ axis system can be transformed by following two successive rotations:

The first rotation is about y-axis ($o_m x_m y_m z_m$ to $o_b x_b y_b z_b$) by an angle θ_y. After the rotation, x_m and z_m axis lies on a plane determined by y_m -axis as shown in Figure A-6. The transformation relationship is given by,

$$\begin{Bmatrix} x_b \\ y_b \\ z_b \end{Bmatrix} = \begin{bmatrix} \cos\theta_y & 0 & \sin\theta_y \\ 0 & 1 & 0 \\ -\sin\theta_y & 0 & \cos\theta_y \end{bmatrix} \begin{Bmatrix} x_m \\ y_m \\ z_m \end{Bmatrix} = [T_1] \begin{Bmatrix} x_m \\ y_m \\ z_m \end{Bmatrix} \quad \text{(A.8)}$$

The second rotation is about z-axis ($o_m x_m y_m z_m$ to $o_b x_b y_b z_b$) by an angle θ_z. After the rotation, x_m and y_m axis lies on a plane determined by z_m-axis as shown in Figure A-7. The transformation relationship is given by,

$$\begin{Bmatrix} x_b \\ y_b \\ z_b \end{Bmatrix} = \begin{bmatrix} \cos\theta_z & -\sin\theta_z & 0 \\ \sin\theta_z & \cos\theta_z & 0 \\ 0 & 0 & 1 \end{bmatrix} \begin{Bmatrix} x_m \\ y_m \\ z_m \end{Bmatrix} = [T_2] \begin{Bmatrix} x_m \\ y_m \\ z_m \end{Bmatrix} \tag{A.9}$$

where, θ_y and θ_z are angles with respect to body-fixed axis system. The combined transformation matrix can be expressed as,

$$[T_{mb}] = [T_1][T_2] \tag{A.10}$$

Substituting Eq. (A.8) and (A.9) into (A.10) gives,

$$[T_{mb}] = \begin{bmatrix} \cos\theta_y \cos\theta_z & -\cos\theta_y \sin\theta_z & \sin\theta_y \\ \sin\theta_z & \cos\theta_z & 0 \\ -\sin\theta_y \cos\theta_z & \sin\theta_y \sin\theta_z & \cos\theta_y \end{bmatrix} \tag{A.11}$$

Noting the transformation matrix derived in Eq. (A.11), a co-ordinate can be transferred from member-fixed to body-fixed axis system using following relationship,

$$\begin{Bmatrix} x_b \\ y_b \\ z_b \end{Bmatrix} = [T_{mb}] \begin{Bmatrix} x_m \\ y_m \\ z_m \end{Bmatrix} \tag{A.12}$$

A.3. Transformation between angular velocity Ω and Euler's angles (α, β, and γ)

Next the relationship between angular velocity and the Euler angles is derived. It is noted that, like the finite rotation above, a general infinitesimal rotation associated with the angular velocity Ω can also be considered as consisting of three successive infinitesimal rotations with angular velocities $\dot{\alpha}$, $\dot{\beta}$, and $\dot{\gamma}$. Therefore, the angular velocity Ω can be determined by the sum of three separate angular velocity vectors.

$$\Omega = \dot{\alpha} + \dot{\beta} + \dot{\gamma} \tag{A.13}$$

where, $\dot{\alpha}$, $\dot{\beta}$, and $\dot{\gamma}$ are in the direction of x-axis, y-axis and z-axis respectively, as shown in Figure A-2, Figure A-3, and Figure A-4. From the rotational process discussed under A.1, $\dot{\alpha}$, $\dot{\beta}$, and $\dot{\gamma}$ can be written in the moving body fixed axis system $o_b x_b y_b z_b$ as,

$$\begin{Bmatrix} \dot{\alpha_1} \\ \dot{\alpha_2} \\ \dot{\alpha_3} \end{Bmatrix} = [T_1]^{-1} \begin{Bmatrix} \dot{\alpha} \\ 0 \\ 0 \end{Bmatrix} \tag{A.14}$$

$$\begin{Bmatrix} \dot{\beta_1} \\ \dot{\beta_2} \\ \dot{\beta_3} \end{Bmatrix} = [T_2]^{-1}[T_3]^{-1} \begin{Bmatrix} 0 \\ \dot{\beta} \\ 0 \end{Bmatrix} \tag{A.15}$$

$$\begin{Bmatrix} \dot{\gamma_1} \\ \dot{\gamma_2} \\ \dot{\gamma_3} \end{Bmatrix} = [T_3]^{-1} \begin{Bmatrix} 0 \\ 0 \\ \dot{\gamma} \end{Bmatrix} \tag{A.16}$$

Hence, the matrix for angular velocities can be written as,

$$\begin{Bmatrix} \Omega_1 \\ \Omega_2 \\ \Omega_3 \end{Bmatrix} = \begin{Bmatrix} \dot{\alpha} cos\beta cos\gamma + \dot{\beta} sin\gamma \\ \dot{\beta} cos\gamma - \dot{\alpha} cos\beta sin\gamma \\ \dot{\gamma} + \dot{\alpha} sin\beta \end{Bmatrix} \tag{A.17}$$

APPENDIX B

Iterative Blade Element and Momentum Theory

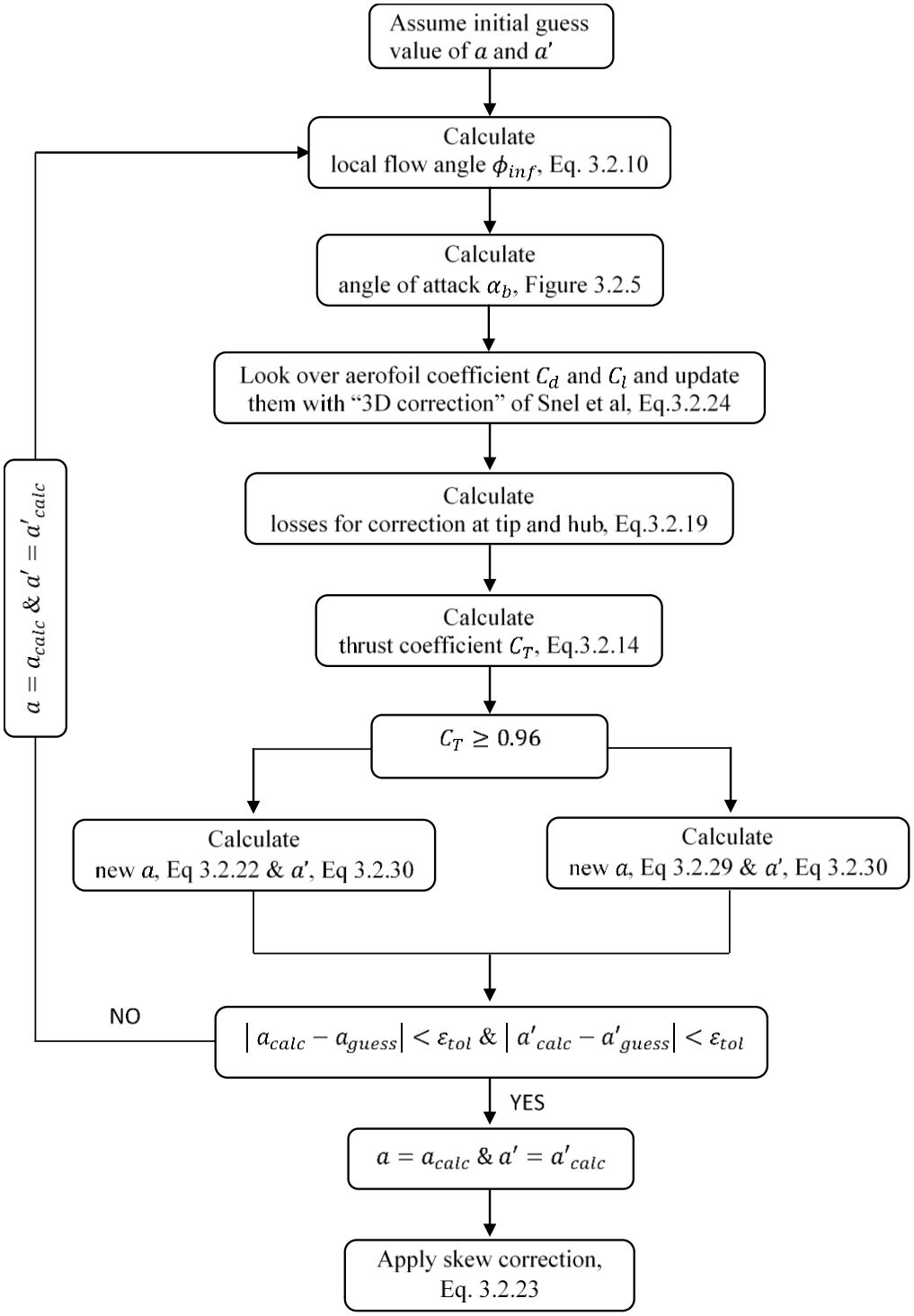

APPENDIX C

Forces and Moments in Matrix form

Following formulation for calculating various forces and moments acting on the chosen floating wind turbine are derived for its practical use in the simulation model presented in this thesis.

C-1 Wind load

The wind load acting on the chosen floating wind turbine system in matrix form is given by,

$$\overrightarrow{F_{aero}} = \begin{Bmatrix} F_x \\ F_y \\ F_z \end{Bmatrix} = [T_{bg}][T_{mb}] \begin{Bmatrix} T\cos(\theta_{wi}) \\ T\sin(\theta_{wi}) \\ 0 \end{Bmatrix} + [T_{bg}][T_{mb}] \int_{l_t} \begin{Bmatrix} dT_{drag}\cos(\theta_{wi}) \\ dT_{drag}\sin(\theta_{wi}) \\ 0 \end{Bmatrix} dl_t \tag{C.1}$$

$$\overrightarrow{N_{aero}} = \begin{Bmatrix} N_x \\ N_y \\ N_z \end{Bmatrix} = [T_{mb}]\,\overrightarrow{r_{hub}} \times \begin{Bmatrix} T\cos(\theta_{wi}) \\ T\sin(\theta_{wi}) \\ 0 \end{Bmatrix} + [T_{mb}] \int_{l_t} \vec{r} \times \begin{Bmatrix} dT_{drag}\cos(\theta_{wi}) \\ dT_{drag}\sin(\theta_{wi}) \\ 0 \end{Bmatrix} dl_t \tag{C.2}$$

where, θ_{wi} is wind approach angle with respect to x-axis of TLPWT system, and $[T_{mb}]$ and $[T_{bg}]$ are transformation matrix for converting vector from member-fixed to body-fixed axis system and body-fixed to space-fixed axis system respectively.

C-2 Wave load

The wave load acting on the chosen floating wind turbine system in matrix form is given by,

Froude-Krylov force, F_{fk}

$$F_{fk-spar} = \begin{Bmatrix} F_x \\ F_y \\ F_z \end{Bmatrix}_g = [T_{bg}][T_{mb}] \int_{l_w} (1 + C_a)\rho_w S \left[[\Gamma_{Fz}] [T_{mb}]^{-1} [T_{bg}]^{-1} \begin{Bmatrix} a_{w_x} \\ a_{w_y} \\ a_{w_z} \end{Bmatrix} dl_w \right] \tag{C.3}$$

$$N_{fk-spar} = \begin{Bmatrix} N_x \\ N_y \\ N_z \end{Bmatrix}_b = [T_{mb}] \int_{l_w} (1 + C_a)\rho_w S \left[[\Gamma_{Mz}][T_{mb}]^{-1} [T_{bg}]^{-1} r_z \begin{Bmatrix} a_{w_x} \\ a_{w_y} \\ a_{w_z} \end{Bmatrix} dl_w \right] \tag{C.4}$$

$$\begin{aligned} F_{fk-pontoon_i} &= \begin{Bmatrix} F_x \\ F_y \\ F_z \end{Bmatrix}_g \\ &= [T_{bg}][T_{mb}] \int_{l_{wi}} (1 + C_a)\rho_w S \left[[\Gamma_{Fx}] [T_{mb}]^{-1} [T_{bg}]^{-1} \begin{Bmatrix} a_{w_x} \\ a_{w_y} \\ a_{w_z} \end{Bmatrix} dl_{w_i} \right] \end{aligned} \tag{C.5}$$

$$\begin{aligned} N_{fk-pontoon_i} &= \begin{Bmatrix} N_x \\ N_y \\ N_z \end{Bmatrix}_b \\ &= [T_{mb}] \int_{l_{wi}} (1 + C_a)\rho_w S \left[[\Gamma_{Mx}] [T_{mb}]^{-1} [T_{bg}]^{-1} r_x \begin{Bmatrix} a_{w_x} \\ a_{w_y} \\ a_{w_z} \end{Bmatrix} dl_{w_i} \right. \\ &\quad \left. + [\Gamma_{Mz}][T_{mb}]^{-1} [T_{bg}]^{-1} r_z \begin{Bmatrix} a_{w_x} \\ a_{w_y} \\ a_{w_z} \end{Bmatrix} dl_{w_i} \right] \end{aligned} \tag{C.6}$$

where, l_w is wetted length of member; r_x and r_z are vector components with respect to centre of gravity of TLPWT system.

$$\Gamma_{Fz} = \begin{bmatrix} 1 & 0 & 0 \\ 0 & 1 & 0 \\ 0 & 0 & 0 \end{bmatrix}; \Gamma_{Mz} = \begin{bmatrix} 0 & -1 & 0 \\ 1 & 0 & 0 \\ 0 & 0 & 0 \end{bmatrix};$$

$$\Gamma_{Fx} = \begin{bmatrix} 0 & 0 & 0 \\ 0 & 1 & 0 \\ 0 & 0 & 1 \end{bmatrix}; \Gamma_{Mx} = \begin{bmatrix} 0 & 0 & 0 \\ 0 & 0 & -1 \\ 0 & 1 & 0 \end{bmatrix}; \Gamma_{Mz} = \begin{bmatrix} 0 & -1 & 0 \\ 1 & 0 & 0 \\ 0 & 0 & 0 \end{bmatrix}$$

Static buoyancy force, F_{sb}

$$F_{sb-spar} = \begin{Bmatrix} F_x \\ F_y \\ F_z \end{Bmatrix}_g = [T_{bg}][T_{mb}] \int_{l_w} \rho_w S \left[[\Gamma_{Fz}] [T_{mb}]^{-1} [T_{bg}]^{-1} \begin{Bmatrix} g_x \\ g_y \\ g_z \end{Bmatrix} dl_w \right] \tag{C.7}$$

$$N_{sb-spar} = \begin{Bmatrix} N_x \\ N_y \\ N_z \end{Bmatrix}_b = [T_{mb}] \int_{l_w} \rho_w S \left[[\Gamma_{Mz}][T_{mb}]^{-1} [T_{bg}]^{-1} r_z \begin{Bmatrix} g_x \\ g_y \\ g_z \end{Bmatrix} dl_w \right] \tag{C.8}$$

$$F_{sb-pontoon_i} = \begin{Bmatrix} F_x \\ F_y \\ F_z \end{Bmatrix}_g = [T_{bg}][T_{mb}] \int_{l_{wi}} \rho_w S \left[[\Gamma_{Fx}] [T_{mb}]^{-1} [T_{bg}]^{-1} \begin{Bmatrix} g_x \\ g_y \\ g_z \end{Bmatrix} dl_{w_i} \right] \tag{C.9}$$

$$N_{sb-pontoon_i} = \begin{Bmatrix} N_x \\ N_y \\ N_z \end{Bmatrix}_b$$

$$= [T_{mb}] \int_{l_{wi}} \rho_w S \left[[\Gamma_{Mx}] [T_{mb}]^{-1} \left[T_{bg}\right]^{-1} r_x \begin{Bmatrix} g_x \\ g_y \\ g_z \end{Bmatrix} dl_{w_i} \right. \tag{C.10}$$

$$\left. + [\Gamma_{Mz}][T_{mb}]^{-1} \left[T_{bg}\right]^{-1} r_z \begin{Bmatrix} g_x \\ g_y \\ g_z \end{Bmatrix} dl_{w_i} \right]$$

Axial divergence force, F_{div}

$$F_{div-spar} = \begin{Bmatrix} F_x \\ F_y \\ F_z \end{Bmatrix}_g$$

$$= \left[T_{bg}\right][T_{mb}][M_a] \left[\int_{l_w} [\Gamma_{Fz}][T_{mb}]^{-1} \left[T_{bg}\right]^{-1} (l.Vl) \begin{Bmatrix} u - U_x \\ v - U_y \\ w - U_z \end{Bmatrix} dl_w \right] \tag{C.11}$$

$$- \left[T_{bg}\right][M_a] \left[[-\Gamma_{Mz}] \begin{Bmatrix} \Omega_x \\ \Omega_y \\ \Omega_z \end{Bmatrix} [T_{mb}] \int_{l_w} [T_{mb}]^{-1} \left[T_{bg}\right]^{-1} (l \cdot Vl)\, r_z\, dl_w \right]$$

$$N_{div-spar} = \begin{Bmatrix} N_x \\ N_y \\ N_z \end{Bmatrix}_b$$

$$= [T_{mb}][M_a] \left[\int_{l_w} [\Gamma_{Mz}]\, [T_{mb}]^{-1} \left[T_{bg}\right]^{-1} (l \cdot Vl) r_z \begin{Bmatrix} u - U_x \\ v - U_y \\ w - U_z \end{Bmatrix} dl_w \right] \tag{C.12}$$

$$- [M_a] \left[\begin{Bmatrix} \Omega_x \\ \Omega_y \\ 0 \end{Bmatrix} [T_{mb}] \int_{l_w} [T_{mb}]^{-1} \left[T_{bg}\right]^{-1} (l \cdot Vl) r_z{}^2 dl_w \right]$$

$$
\begin{aligned}
F_{div-pontoon_i} &= \begin{Bmatrix} F_x \\ F_y \\ F_z \end{Bmatrix}_g \\
&= \left[T_{bg}\right][T_{mb}][M_a]\left[\int_{l_{w_i}} [\Gamma_{Fx}][T_{mb}]^{-1}\left[T_{bg}\right]^{-1}(l.Vl)\begin{Bmatrix} u-U_x \\ v-U_y \\ w-U_z \end{Bmatrix} dl_{w_i}\right. \\
&\quad \left. + \int_{l_{w_i}} [\Gamma_{Fz}][T_{mb}]^{-1}\left[T_{bg}\right]^{-1}(l\cdot Vl)\begin{Bmatrix} u-U_x \\ v-U_y \\ w-U_z \end{Bmatrix} dl_{w_i}\right] \\
&\quad - \left[T_{bg}\right][M_a]\left[[-\Gamma_{Mx}]\begin{Bmatrix} \Omega_x \\ \Omega_y \\ \Omega_z \end{Bmatrix}[T_{mb}]\int_{l_{w_i}} [T_{mb}]^{-1}\left[T_{bg}\right]^{-1}(l\cdot Vl)r_x dl_{w_i}\right. \\
&\quad \left. + [-\Gamma_{Mz}]\begin{Bmatrix} \Omega_x \\ \Omega_y \\ \Omega_z \end{Bmatrix}[T_{mb}]\int_{l_{w_i}} [T_{mb}]^{-1}\left[T_{bg}\right]^{-1}(l\cdot Vl)r_z dl_{w_i}\right]
\end{aligned} \tag{C.13}
$$

$$
\begin{aligned}
N_{div-pontoon_i} &= \begin{Bmatrix} N_x \\ N_y \\ N_z \end{Bmatrix}_b \\
&= [T_{mb}][M_a]\left[\int_{l_{w_i}}\left[[\Gamma_{Mx}]\,[T_{mb}]^{-1}\left[T_{bg}\right]^{-1}(l.Vl)r_x\begin{Bmatrix} u-U_x \\ v-U_y \\ w-U_z \end{Bmatrix} dl_{w_i}\right.\right. \\
&\quad \left.\left. + [\Gamma_{Mz}]\,[T_{mb}]^{-1}\left[T_{bg}\right]^{-1}(l\cdot Vl)r_z\begin{Bmatrix} u-U_x \\ v-U_y \\ w-U_z \end{Bmatrix} dl_{w_i}\right]\right] \\
&\quad - [M_a]\left[\begin{Bmatrix} 0 \\ \Omega_y \\ \Omega_z \end{Bmatrix}[T_{mb}]\int_{l_{w_i}} [T_{mb}]^{-1}\left[T_{bg}\right]^{-1}(l\cdot Vl){r_x}^2 dl_{w_i}\right. \\
&\quad + \begin{Bmatrix} \Omega_x \\ \Omega_y \\ 0 \end{Bmatrix}[T_{mb}]\int_{l_{w_i}} [T_{mb}]^{-1}\left[T_{bg}\right]^{-1}(l\cdot Vl){r_z}^2 dl_{w_i} \\
&\quad \left. + \begin{Bmatrix} -\Omega_z \\ 0 \\ -\Omega_x \end{Bmatrix}[T_{mb}]\int_{l_{w_i}} [T_{mb}]^{-1}\left[T_{bg}\right]^{-1}(l\cdot Vl)r_x r_z dl_{w_i}\right]
\end{aligned} \tag{C.14}
$$

Added mass force, F_{adm}

The linear added mass force and moment equations can be written as,

$$F_{adm\_l-spar} = \begin{Bmatrix} F_x \\ F_y \\ F_z \end{Bmatrix}_g$$

$$= -[T_{bg}][T_{mb}][M_a]\left[\int_{l_w} [T_{mb}]^{-1}[T_{bg}]^{-1}\begin{Bmatrix} \dot{U}_x \\ \dot{U}_y \\ \dot{U}_z \end{Bmatrix} dl_w \right. \tag{C.15}$$

$$\left. + \int_{l_w} -[\Gamma_{Mz}][T_{mb}]^{-1}\begin{Bmatrix} \dot{\Omega}_x \\ \dot{\Omega}_y \\ \dot{\Omega}_z \end{Bmatrix}[T_{bg}]^{-1} r_z \, dl_w \right]$$

$$N_{adm\_l-spar} = \begin{Bmatrix} N_x \\ N_y \\ N_z \end{Bmatrix}_b$$

$$= -[T_{mb}][M_a]\left[[\Gamma_{Mz}]\,[T_{mb}]^{-1}[T_{bg}]^{-1}\begin{Bmatrix} \dot{U}_x \\ \dot{U}_y \\ \dot{U}_z \end{Bmatrix}\int_{l_w} r_z \, dl_w \right. \tag{C.16}$$

$$\left. + \int_{l_w} [\Gamma_{Fz}]\,[T_{mb}]^{-1}\begin{Bmatrix} \dot{\Omega}_x \\ \dot{\Omega}_y \\ \dot{\Omega}_z \end{Bmatrix}[T_{bg}]^{-1} {r_z}^2 \, dl_w \right]$$

$$F_{adm\_l-pontoon_i} = \begin{Bmatrix} F_x \\ F_y \\ F_z \end{Bmatrix}_g$$

$$= -[T_{bg}][T_{mb}][M_a]\left[\int_{l_{w_i}} [T_{mb}]^{-1}[T_{bg}]^{-1}\begin{Bmatrix} \dot{U}_x \\ \dot{U}_y \\ \dot{U}_z \end{Bmatrix} dl_{w_i} \right.$$

$$+ \int_{l_{w_i}} -[\Gamma_{Mx}]\,[T_{mb}]^{-1}\begin{Bmatrix} \dot{\Omega}_x \\ \dot{\Omega}_y \\ \dot{\Omega}_z \end{Bmatrix}[T_{bg}]^{-1} r_x \, dl_{w_i} \tag{C.17}$$

$$\left. + \int_{l_{w_i}} -[\Gamma_{Mz}][T_{mb}]^{-1}\begin{Bmatrix} \dot{\Omega}_x \\ \dot{\Omega}_y \\ \dot{\Omega}_z \end{Bmatrix}[T_{bg}]^{-1} r_z \, dl_{w_i} \right]$$

$$
\begin{aligned}
N_{adm\_l-pontoon_i} &= \begin{Bmatrix} N_x \\ N_y \\ N_z \end{Bmatrix}_b \\
&= -[T_{mb}][M_a]\Bigg[[\Gamma_{Mx}]\,[T_{mb}]^{-1}\big[T_{bg}\big]^{-1}\begin{Bmatrix} \dot{U}_x \\ \dot{U}_y \\ \dot{U}_z \end{Bmatrix}\int_{l_{w_i}} r_x\, dl_{w_i} \\
&+ [\Gamma_{Mz}]\,[T_{mb}]^{-1}\big[T_{bg}\big]^{-1}\begin{Bmatrix} \dot{U}_x \\ \dot{U}_y \\ \dot{U}_z \end{Bmatrix}\int_{l_{w_i}} r_z\, dl_{w_i} \\
&+ \int_{l_{w_i}} [\Gamma_{Fx}][T_{mb}]^{-1}\begin{Bmatrix} \dot{\Omega}_x \\ \dot{\Omega}_y \\ \dot{\Omega}_z \end{Bmatrix}\big[T_{bg}\big]^{-1} r_x{}^2\, dl_{w_i} \\
&+ \int_{l_{w_i}} [\Gamma_{Fz}][T_{mb}]^{-1}\begin{Bmatrix} \dot{\Omega}_x \\ \dot{\Omega}_y \\ \dot{\Omega}_z \end{Bmatrix}\big[T_{bg}\big]^{-1} r_z{}^2\, dl_{w_i} \\
&+ \int_{l_{w_i}} -[\Gamma_{Fxz}][T_{mb}]^{-1}\begin{Bmatrix} \dot{\Omega}_x \\ \dot{\Omega}_y \\ \dot{\Omega}_z \end{Bmatrix}\big[T_{bg}\big]^{-1} r_x r_z\, dl_{w_i}\Bigg]
\end{aligned}
\tag{C.18}
$$

where, $[\Gamma_{Fxz}] = \begin{bmatrix} 0 & 0 & 1 \\ 0 & 0 & 0 \\ 1 & 0 & 0 \end{bmatrix}$

The nonlinear added mass force and moment equations can be written as,

$$
\begin{aligned}
F_{adm\_nl-spar} &= \begin{Bmatrix} F_x \\ F_y \\ F_z \end{Bmatrix}_g \\
&= -\big[T_{bg}\big][T_{mb}][M_a]\Bigg[\int_{l_w} [T_{mb}]^{-1}\begin{Bmatrix} \Omega_x\Omega_z \\ \Omega_y\Omega_z \\ -\Omega_x{}^2 - \Omega_y{}^2 \end{Bmatrix}\big[T_{bg}\big]^{-1} r_z\, dl_w\Bigg]
\end{aligned}
\tag{C.19}
$$

$$
\begin{aligned}
F_{adm\_nl-pontoon_i} &= \begin{Bmatrix} F_x \\ F_y \\ F_z \end{Bmatrix}_g \\
&= -\big[T_{bg}\big][T_{mb}][M_a]\Bigg[\int_{l_{w_i}} [T_{mb}]^{-1}\begin{Bmatrix} -\Omega_y{}^2 - \Omega_z{}^2 \\ \Omega_x\Omega_y \\ \Omega_x\Omega_z \end{Bmatrix}\big[T_{bg}\big]^{-1} r_x\, dl_{w_i} \\
&+ \int_{l_{w_i}} [T_{mb}]^{-1}\begin{Bmatrix} \Omega_x\Omega_z \\ \Omega_y\Omega_z \\ -\Omega_x{}^2 - \Omega_y{}^2 \end{Bmatrix}\big[T_{bg}\big]^{-1} r_z\; dl_{w_i}\Bigg]
\end{aligned}
\tag{C.20}
$$

$$
N_{adm\_nl-spar} = \begin{Bmatrix} N_x \\ N_y \\ N_z \end{Bmatrix}_b = -[T_{mb}][M_a]\Bigg[\int_{l_w} [T_{mb}]^{-1}\begin{Bmatrix} -\dot{\Omega}_y\dot{\Omega}_z \\ \dot{\Omega}_x\dot{\Omega}_z \\ 0 \end{Bmatrix}\big[T_{bg}\big]^{-1} r_z{}^2\, dl_w\Bigg] \tag{C.21}
$$

$$N_{adm\_nl-pontoon_i} = \begin{Bmatrix} N_x \\ N_y \\ N_z \end{Bmatrix}_b$$

$$= -[T_{mb}][M_a]\left[\int_{l_{w_i}} [T_{mb}]^{-1}\begin{Bmatrix} 0 \\ -\dot{\Omega}_x\dot{\Omega}_z \\ \dot{\Omega}_x\dot{\Omega}_y \end{Bmatrix}[T_{bg}]^{-1} {r_x}^2\, dl_{w_i}\right.$$

$$+ \int_{l_{w_i}} [T_{mb}]^{-1}\begin{Bmatrix} -\dot{\Omega}_y\dot{\Omega}_z \\ \dot{\Omega}_x\dot{\Omega}_z \\ 0 \end{Bmatrix}[T_{bg}]^{-1} {r_z}^2\, dl_{w_i} \quad (C.22)$$

$$\left. + \int_{l_{w_i}} [T_{mb}]^{-1}\begin{Bmatrix} -\dot{\Omega}_x\dot{\Omega}_y \\ {\dot{\Omega}_x}^2 - {\dot{\Omega}_z}^2 \\ \dot{\Omega}_y\dot{\Omega}_z \end{Bmatrix}[T_{bg}]^{-1} r_x r_z\, dl_{w_i}\right]$$

To combine linear added mass force and its moment to mass $[M]$ and inertia $[I]$ matrices of equations of motions, they are expressed in matrix form as follows,

$$[M_{adm}] = \begin{bmatrix} a_{11} & a_{12} \\ a_{21} & a_{22} \end{bmatrix} \quad (C.23)$$

where, a_{11}, a_{12}, a_{21}, and a_{22} are added mass matrix extracted from Eq. (C.15) through (C.18) and can be written as,

$$a_{11-spar} = -[T_{bg}][T_{mb}][M_a]\left[\int_{l_w} [T_{mb}]^{-1}[T_{bg}]^{-1} dl_w\right]$$

$$a_{11-pontoon_i} = -[T_{bg}][T_{mb}][M_a]\left[\int_{l_{w_i}} [T_{mb}]^{-1}[T_{bg}]^{-1}\begin{Bmatrix} \dot{U}_x \\ \dot{U}_y \\ \dot{U}_z \end{Bmatrix} dl_{w_i}\right]$$

$$a_{12-spar} = -[T_{bg}][T_{mb}][M_a]\left[\int_{l_w} -[\Gamma_{Mz}][T_{mb}]^{-1}[T_{bg}]^{-1} r_z\, dl_w\right]$$

$$a_{12-pontoon_i} = -[T_{mb}][M_a]\left[[\Gamma_{Mx}]\,[T_{mb}]^{-1}[T_{bg}]^{-1}\int_{l_{w_i}} r_x\, dl_{w_i}\right.$$

$$\left. + [\Gamma_{Mz}]\,[T_{mb}]^{-1}[T_{bg}]^{-1}\int_{l_{w_i}} r_z\, dl_{w_i}\right]$$

$$a_{22-spar} = -[T_{mb}][M_a]\left[\int_{l_w} [\Gamma_{Fz}]\,[T_{mb}]^{-1}[T_{bg}]^{-1} {r_z}^2\, dl_w\right]$$

$$a_{22-pontoon_i} = -[T_{mb}][M_a]\left[\int_{l_{w_i}} [\Gamma_{Fx}][T_{mb}]^{-1}[T_{bg}]^{-1} {r_x}^2\, dl_{w_i} + \int_{l_{w_i}} [\Gamma_{Fz}][T_{mb}]^{-1}[T_{bg}]^{-1} {r_z}^2\, dl_{w_i}\right.$$

$$\left. + \int_{l_{w_i}} -[\Gamma_{Fxz}][T_{mb}]^{-1}[T_{bg}]^{-1} r_x r_z\, dl_{w_i}\right]$$

Centrifugal force, F_{cf}

$$F_{cf-spar} = \begin{Bmatrix} F_x \\ F_y \\ F_z \end{Bmatrix}_g = -2[M_a]\left[T_{bg}\right]\left[[-\Gamma_{Mz}] \begin{Bmatrix} \Omega_x \\ \Omega_y \\ \Omega_z \end{Bmatrix} [T_{mb}] \int_{l_w} [T_{mb}]^{-1}\left[T_{bg}\right]^{-1} \begin{Bmatrix} 0 \\ 0 \\ w - U_z \end{Bmatrix} dl_w \right] \tag{C.24}$$

$$N_{cf-spar} = \begin{Bmatrix} N_x \\ N_y \\ N_z \end{Bmatrix}_b = -2[M_a][T_{mb}]\left[[\Gamma_{Fz}] \begin{Bmatrix} \Omega_x \\ \Omega_y \\ \Omega_z \end{Bmatrix} \int_{l_w} [T_{mb}]^{-1}\left[T_{bg}\right]^{-1} r_z \begin{Bmatrix} 0 \\ 0 \\ w - U_z \end{Bmatrix} dl_w \right] \tag{C.25}$$

$$F_{cf-pontoon_i} = \begin{Bmatrix} F_x \\ F_y \\ F_z \end{Bmatrix}_g$$

$$= -2[M_a]\left[T_{bg}\right]\left[[-\Gamma_{Mx}] \begin{Bmatrix} \Omega_x \\ \Omega_y \\ \Omega_z \end{Bmatrix} [T_{mb}] \int_{l_{w_i}} [T_{mb}]^{-1}\left[T_{bg}\right]^{-1} \begin{Bmatrix} u - U_x \\ 0 \\ 0 \end{Bmatrix} dl_{w_i} \right. \tag{C.26}$$

$$\left. + [-\Gamma_{Mz}] \begin{Bmatrix} \Omega_x \\ \Omega_y \\ \Omega_z \end{Bmatrix} [T_{mb}] \int_{l_{w_i}}^{0} [T_{mb}]^{-1}\left[T_{bg}\right]^{-1} \begin{Bmatrix} 0 \\ 0 \\ w - U_z \end{Bmatrix} dl_{w_i} \right]$$

$$N_{cf-pontoon_i} = \begin{Bmatrix} N_x \\ N_y \\ N_z \end{Bmatrix}_b$$

$$= -2[M_a][T_{mb}]\left[[\Gamma_{Fx}] \begin{Bmatrix} \Omega_x \\ \Omega_y \\ \Omega_z \end{Bmatrix} \int_{l_{w_i}} [T_{mb}]^{-1}\left[T_{bg}\right]^{-1} r_x \begin{Bmatrix} u - U_x \\ 0 \\ 0 \end{Bmatrix} dl_{w_i} \right. \tag{C.27}$$

$$\left. + [\Gamma_{Fz}] \begin{Bmatrix} \Omega_x \\ \Omega_y \\ \Omega_z \end{Bmatrix} \int_{l_{w_i}} [T_{mb}]^{-1}\left[T_{bg}\right]^{-1} r_z \begin{Bmatrix} 0 \\ 0 \\ w - U_z \end{Bmatrix} dl_{w_i} \right]$$

Bottom point force, F_{bp}

$$F_{bp-spar} = \begin{Bmatrix} F_x \\ F_y \\ F_z \end{Bmatrix}_g = \left[T_{bg}\right][T_{mb}] \begin{Bmatrix} F_{normal,x} \\ F_{normal,y} \\ F_{axial,z} \end{Bmatrix}_m \tag{C.28}$$

$$F_{bp-pontoon_i} = \begin{Bmatrix} F_x \\ F_y \\ F_z \end{Bmatrix}_g = \left[T_{bg}\right][T_{mb}] \begin{Bmatrix} F_{axial,x_i} \\ F_{normal,y_i} \\ F_{normal,z_i} \end{Bmatrix}_m \tag{C.29}$$

where,

For vertical member,

$$\{F_{axial,z}\}_m = \left[P\,S - \frac{1}{2}[M_a]\left\{(u - U_x)^2 + \left(v - U_y\right)^2\right\}\right]$$

For horizontal member,

$$\{F_{axial,x}\}_m = \left[P\ S - \frac{1}{2}[M_a]\left\{(v-U_y)^2 + (w-U_z)^2\right\}\right]$$

For vertical member,

$$\begin{Bmatrix} F_{normal,x} \\ F_{normal,y} \end{Bmatrix}_m = -[M_a](w-U_z)_m \begin{Bmatrix} u-U_x \\ v-U_y \end{Bmatrix}_m$$

For horizontal member,

$$\begin{Bmatrix} F_{normal,y} \\ F_{normal,z} \end{Bmatrix}_m = -[M_a](u-U_x)_m \begin{Bmatrix} v-U_y \\ w-U_z \end{Bmatrix}_m$$

$$N_{bp-spar} = \begin{Bmatrix} N_x \\ N_y \\ N_z \end{Bmatrix}_b = -[M_a][T_{mb}]\left[(w-U_z)_m\ r_z\ [\Gamma_{Mz}] \begin{Bmatrix} u-U_x \\ v-U_y \\ w-U_z \end{Bmatrix}_m\right] \quad \text{(C.30)}$$

$$N_{bp-pontoon_i} = \begin{Bmatrix} N_x \\ N_y \\ N_z \end{Bmatrix}_b = -[M_a][T_{mb}]\left[(u-U_x)_m\ r_x\ [\Gamma_{Mx}] \begin{Bmatrix} u-U_x \\ v-U_y \\ w-U_z \end{Bmatrix}_m + (w-U_z)_m\ r_z\ [\Gamma_{Mz}] \begin{Bmatrix} u-U_x \\ v-U_y \\ w-U_z \end{Bmatrix}_m\right] \quad \text{(C.31)}$$

Intersection point force, F_{int}

$$F_{int-spar} = \begin{Bmatrix} F_x \\ F_y \\ F_z \end{Bmatrix}_g = [T_{bg}][T_{mb}] \begin{Bmatrix} f_x \\ f_y \\ f_z \end{Bmatrix}_m \quad \text{(C.32)}$$

$$M_{int-spar} = \begin{Bmatrix} N_x \\ N_y \\ N_z \end{Bmatrix}_b = [T_{mb}][\Gamma_{Mz}] \begin{Bmatrix} f_x \\ f_y \\ f_z \end{Bmatrix}_m \quad \text{(C.33)}$$

where,

$$f_{int-spar} = \begin{Bmatrix} f_x \\ f_y \\ f_z \end{Bmatrix}_m = \left[\frac{1}{2}\tan\alpha\left[\left(t \cdot \begin{Bmatrix} (u-U_x) \\ (v-U_y) \\ 0 \end{Bmatrix}_m\right)[M_a] \begin{Bmatrix} (u-U_x) \\ (v-U_y) \\ 0 \end{Bmatrix}_m - \left(t \cdot [M_a] \begin{Bmatrix} -(v-U_y) \\ (u-U_x) \\ 0 \end{Bmatrix}_m\right) \begin{Bmatrix} -(v-U_y) \\ (u-U_x) \\ 0 \end{Bmatrix}\right]\right]$$

Drag force, F_{drag}

$$F_{drag-spar} = \begin{Bmatrix} F_x \\ F_y \\ F_z \end{Bmatrix}_g = [T_{bg}][T_{mb}]\left[\int_{l_w} C_d \frac{1}{2}\ \rho_w\ D\ [\Gamma_{Fz}] \begin{Bmatrix} (u-U_x)\ |u-U_x| \\ (v-U_y)\ |v-U_y| \\ (w-U_z)\ |w-U_z| \end{Bmatrix}_m dl_w\right] \quad \text{(C.34)}$$

$$N_{drag-spar} = \begin{Bmatrix} N_x \\ N_y \\ N_z \end{Bmatrix}_b = [T_{mb}] \left[\int_{l_w} C_d \frac{1}{2} \rho_w D [\Gamma_{Mz}] r_z \begin{Bmatrix} (u - U_x)|u - U_x| \\ (v - U_y)|v - U_y| \\ (w - U_z)|w - U_z| \end{Bmatrix}_m dl_w \right] \tag{C.35}$$

$$\begin{aligned} F_{drag-pontoon_i} &= \begin{Bmatrix} F_x \\ F_y \\ F_z \end{Bmatrix}_g \\ &= [T_{bg}][T_{mb}] \left[\int_{l_{wi}} C_d \frac{1}{2} \rho_w D [\Gamma_{Fx}] \begin{Bmatrix} (u - U_x)|u - U_x| \\ (v - U_y)|v - U_y| \\ (w - U_z)|w - U_z| \end{Bmatrix}_m dl_{w_i} \right] \end{aligned} \tag{C.36}$$

$$\begin{aligned} N_{drag-pontoon_i} &= \begin{Bmatrix} N_x \\ N_y \\ N_z \end{Bmatrix}_b \\ &= [T_{mb}] \left[\int_{l_{wi}} C_d \frac{1}{2} \rho_w D \left[[\Gamma_{Mx}] r_x \begin{Bmatrix} (u - U_x)|u - U_x| \\ (v - U_y)|v - U_y| \\ (w - U_z)|w - U_z| \end{Bmatrix}_m dl_{w_i} \right. \right. \\ &\quad \left. \left. + [\Gamma_{Mz}] r_z \begin{Bmatrix} (u - U_x)|u - U_x| \\ (v - U_y)|v - U_y| \\ (w - U_z)|w - U_z| \end{Bmatrix}_m dl_{w_i} \right] \right] \end{aligned} \tag{C.37}$$

C-3 Mooring system load

The procedure to evaluate mooring line loads acting on the chosen floating wind turbine system in the matrix form is given in this section. The procedure described is applicable to N_m number of mooring lines and N_p number of pontoons. Figure C-1 shows layout of the mooring lines for a chosen floating wind turbine system where, A_p is the bottom end of mooring line anchored to the seabed and F_p is the top end of mooring line attached to the platform at fairlead.

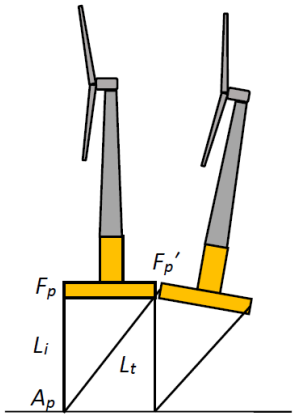

Figure C-1 Mooring layout

Due to arbitrary platform motions, the point F_p is displaced to a new position F_p' which will develop tension in the mooring lines. Hence tension in each mooring line at instantaneous time t can be calculated by,

$$Tmoor_j = \begin{cases} Tmoor_{in} + \dfrac{EA}{Li_j}\left(Lt_j - Li_j\right) \;\; if\;\left(Lt_j > Li_j\right) \\ 0 \qquad\qquad\qquad otherwise \end{cases} \tag{C.38}$$

where, $Tmoor_{in}$ is initial tension in mooring line, EA is axial stiffness of mooring line, Li_j and Lt_j are un-stretched and stretched length of mooring line respectively. The procedure for calculating stretched length of mooring line Lt_j and its directional vector $\vec{e}$ is given below,

The fairlead and anchor point position vector for each mooring line in member fixed axis system is given by,

$$\left\{\overrightarrow{F_{p_j}}\right\}_m = \begin{Bmatrix} F_p x_j \\ F_p y_j \\ F_p z_j \end{Bmatrix}_m \qquad \left\{\overrightarrow{A_{p_j}}\right\}_m = \begin{Bmatrix} A_p x_j \\ A_p y_j \\ A_p z_j \end{Bmatrix}_m \tag{C.39}$$

The fairlead and anchor point position vector for each mooring line in body fixed axis system is given by,

$$\left\{\overrightarrow{F_{p_j}}\right\}_b = [T_{bm}] \begin{Bmatrix} F_p x_j \\ F_p y_j \\ F_p z_j \end{Bmatrix}_m , \quad \left\{\overrightarrow{A_{p_j}}\right\}_b = [T_{bm}] \begin{Bmatrix} A_p x_j \\ A_p y_j \\ A_p z_j \end{Bmatrix}_m \tag{C.40}$$

Displacement of fairlead in space fixed axis system is given by,

$$\left\{\overrightarrow{F_{p_j}}\right\}_g = \left\{\overrightarrow{U_c}\right\}_g + \left[T_{gb}\right] \left\{\overrightarrow{F_{p_j}}\right\}_b \tag{C.41}$$

Stretched mooring line length at instantaneous time t is given by,

$$Lt_j = \sqrt{\left[\left(F_p x_j\right)_g - \left(A_p x_j\right)_b\right]^2 + \left[\left(F_p y_j\right)_g - \left(A_p y_j\right)_b\right]^2 + \left[\left(F_p z_j\right)_g - \left(A_p z_j\right)_b\right]^2} \tag{C.42}$$

Direction vector $\vec{e}$ for each mooring line at instantaneous time t is given by,

$$\vec{e} = \begin{Bmatrix} e_x \\ e_y \\ e_z \end{Bmatrix} = \begin{Bmatrix} \left[\left(F_p x_j\right)_g - \left(A_p x_j\right)_b\right]/Lt_j \\ \left[\left(F_p y_j\right)_g - \left(A_p y_j\right)_b\right]/Lt_j \\ \left[\left(F_p z_j\right)_g - \left(A_p z_j\right)_b\right]/Lt_j \end{Bmatrix} \tag{C.43}$$

Once stretched length of mooring line is computed, tension in each mooring line can be calculated using Eq. (C.38).

The restoring force acting on the platform due to N_m number of mooring lines for each pontoon in body fixed axis system is given by,

$$\left\{\overrightarrow{F_{pontoon,\iota}}\right\}_b = \begin{Bmatrix} f_x \\ f_y \\ f_z \end{Bmatrix}_b = [T_{bm}] \sum_{j=1}^{N_m} Tmoor_j . \vec{e} \tag{C.44}$$

The restoring moment acting on the platform due to N_m number of mooring lines for each pontoon is given by,

$$\left\{\overrightarrow{N_{pontoon,\iota}}\right\}_b = \begin{Bmatrix} N_x \\ N_y \\ N_z \end{Bmatrix}_b = \begin{Bmatrix} f_z \cdot F_p y - f_y \cdot F_p z \\ f_x \cdot F_p z - f_z \cdot F_p x \\ f_y \cdot F_p x - f_x \cdot F_p y \end{Bmatrix} \tag{C.45}$$

Total restoring forces acting on the platform due to all the mooring lines in space fixed axis system is given by,

$$\overrightarrow{F_{moor}} = \begin{Bmatrix} F_x \\ F_y \\ F_z \end{Bmatrix}_g = \left[T_{gb}\right] \sum_{i=1}^{N_p} \left\{\overrightarrow{F_{pontoon,\iota}}\right\}_b \tag{C.46}$$

Total restoring moment acting on the platform due to all the mooring lines in body fixed axis system is given by,

$$\overrightarrow{N_{moor}} = \begin{Bmatrix} N_x \\ N_y \\ N_z \end{Bmatrix}_b = \sum_{i=1}^{N_p} \left\{\overrightarrow{N_{pontoon,\iota}}\right\}_b \tag{C.47}$$

APPENDIX D

Aerodynamic Properties of Wind Turbine Blade

This Appendix presents the distributed aerodynamic properties of wind turbine blade used in this thesis.

Table D.1 Distributed aerodynamic properties of wind turbine blade

Node	RNodes r (m)	DRNodes, dr (m)	Chord c (m)	Aero twist β (deg.)	Aerofoil
1	2.8667	2.7333	3.542	13.308	Cylinder1
2	5.6000	2.7333	3.854	13.308	Cylinder1
3	8.3333	2.7333	4.167	13.308	Cylinder2
4	11.7500	4.1000	4.557	13.308	DU40
5	15.8500	4.1000	4.652	11.480	DU35
6	19.9500	4.1000	4.458	10.162	DU35
7	24.0500	4.1000	4.249	9.011	DU30
8	28.1500	4.1000	4.007	7.795	DU25
9	32.2500	4.1000	3.748	6.544	DU25
10	36.3500	4.1000	3.502	5.361	DU21
11	40.4500	4.1000	3.256	4.188	DU21
12	44.5500	4.1000	3.010	3.125	NACA64
13	48.6500	4.1000	2.764	2.319	NACA64
14	52.7500	4.1000	2.518	1.526	NACA64
15	56.1667	2.7333	2.313	0.863	NACA64
16	58.9000	2.7333	2.086	0.370	NACA64
17	61.6333	2.7333	1.419	0.106	NACA64

The aerodynamic lift and drag coefficient corresponding to the aerofoil sections noted in Table D.1 are given in Figure D.1. For cylindrical section, the lift coefficient is 0.0 and the drag coefficient is 1.0 for all the angles of attacks.

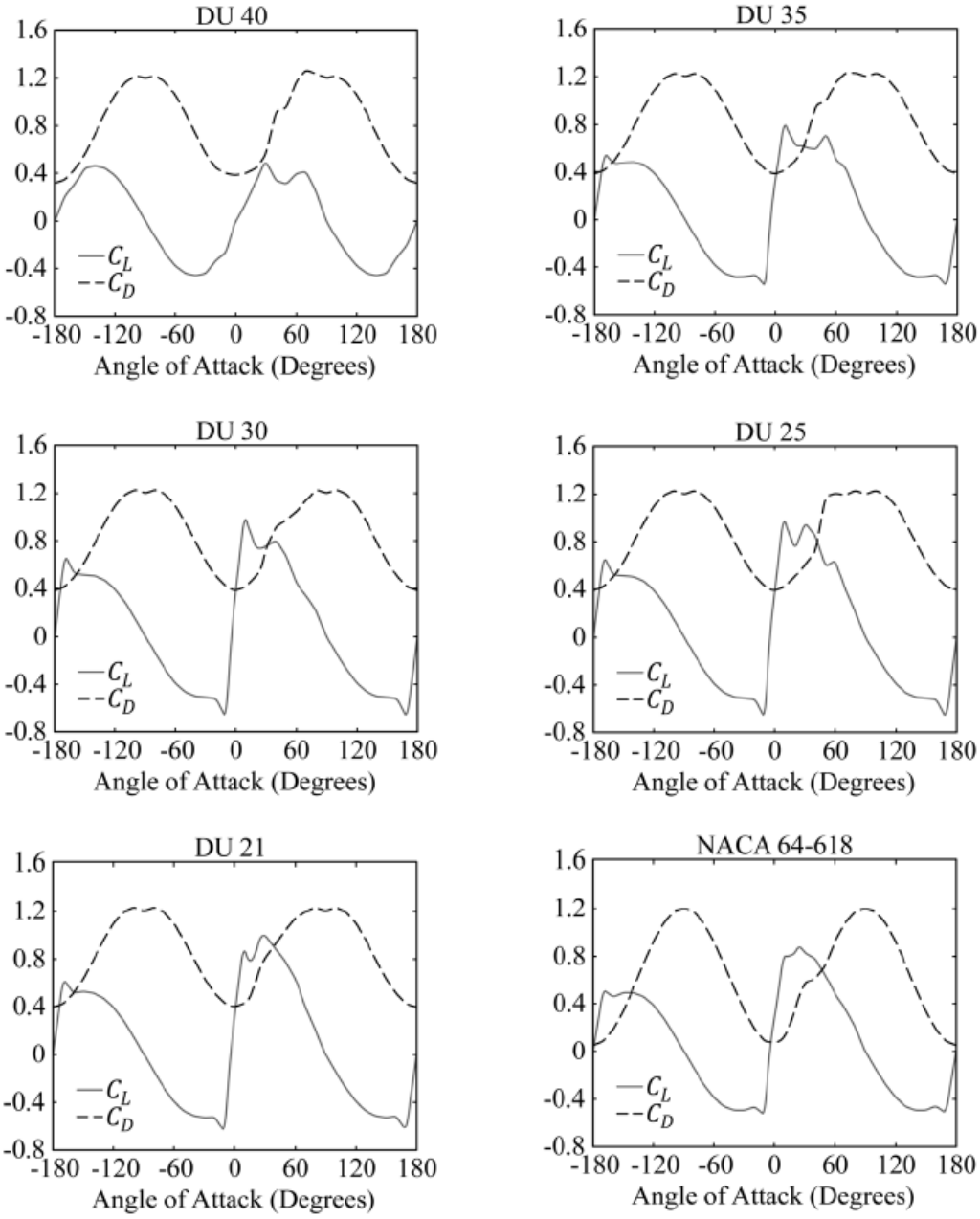

Figure D.1 Aerofoil lift and drag coefficient for a) DU 40, b) DU 35, c) DU 30, d) DU 25, e) DU 21, f) NACA 61-618

APPENDIX E

The author's publications by the date of submitting this thesis are listed below:

[1] Jagdale,S. & Ma, Q. W., 2010. Practical simulation on motions of a TLP-Type support structure for offshore wind turbine. Proceedings of the Twentieth International Offshore and Polar Engineering Conference, Beijing, China, pp. 692-698.

[2] Jagdale,S. & Ma, Q. W., 2012. Effect of Non-linear Wave Forces on Dynamic Response of Floating Offshore Wind Turbine. Proceedings of the Twenty-second International Offshore and Polar Engineering Conference, Rhodes, Greece, pp. 316-323.